UNIVERSITEIT ANTWERPEN
UNIVERSITAIRE INSTELLING ANTWERPEN
DEPARTEMENT SCHEIKUNDE

Chemical Characterization of Individual Particles by Electron Probe X-Ray Microanalysis and Electron Energy-Loss Spectrometry

Proefschrift voorgelegd tot het behalen van de graad van doctor in de wetenschappen aan de Universitaire Instelling Antwerpen te verdedigen door Chris Xhoffer.

Promotor : Prof. Dr. R. Van Grieken

Antwerpen, 1993

5771

IZWO
Instituut voor Zeewetenschappelijk Onderzoek (vzw)
Institute for Marine Scientific Research
VICTORIALAAN 3 - B - 8400 OOSTENDE BELGIUM
Tel. +32 - (0) 59 - 32 10 45 -- Fax: +32 - (0) 59 - 32 11 35

UNIVERSITEIT ANTWERPEN
UNIVERSITAIRE INSTELLING ANTWERPEN
DEPARTEMENT SCHEIKUNDE

Chemical Characterization of Individual Particles by Electron Probe X-Ray Microanalysis and Electron Energy-Loss Spectrometry

Proefschrift voorgelegd tot het behalen van de graad van doctor in de wetenschappen aan de Universitaire Instelling Antwerpen te verdedigen door Chris Xhoffer.

Promotor : Prof. Dr. R. Van Grieken

Antwerpen, 1993

Dankwoord

Bij de voltooiïng van dit proefschrift wens ik in de eerste plaats mijn promotor Prof. Dr. R. Van Grieken te bedanken voor zijn permanente begeleiding en konstruktieve raadgevingen.

Prof. Dr. W. Jacob ben ik erkentelijk voor de vele praktische raadgevingen en morele steun.

Ik wens Prof. Dr. J.A.C. Broekaert (Universität Dortmund, Dortmund, FRG) te danken voor zijn welwillendheid en gastvrijheid op het ISAS en voor zijn verhelderende discussies aangaande nebulisatieëffecten in ICP's.

Mijn verblijf in Arizona, USA, dat met tussenkomst van het Nationaal Fonds voor Wetenschappelijk Onderzoek (NFWO) tot stand kon komen, heeft op alle fronten mijn horizonten verruimd. Hiervoor ben ik in het bijzonder Prof. Dr. P.R. Buseck dankbaar.

Verder dank ik alle personen van het departement geneeskunde groep elektronenmikroskopie voor hun hulpzaamheid en aangename tussendoortjes, Jan Van Puymbroeck voor de interessante discussies, Walter Dorrine voor de vele interessante conversaties en wetenschappelijke opdrachten en alle collega's van het departement scheikunde voor de aangename werksfeer.

Het Instituut tot Aanmoediging van het Wetenschappelijk Onderzoek in Nijverheid en Landbouw (IWONL) ben ik erkentelijk voor de financiële steun die ik gedurende drie jaar heb genoten.

Tenslotte wil ik graag mijn verloofde Ann Deweer bedanken voor haar begrip en de niet aflatende aanmoediging gedurende de laatste moeilijke maanden.

Antwerpen, maart 1993

Table of Contents

Chapter 1: Microanalytical techniques and applications to individual environmental particle analysis

Chapter 2: Chemical characterization and source apportionment of individual aerosol particles over the North Sea and English Channel using multivariate techniques

Chapter 3: Characterization of individual particles in the North Sea surface microlayer and underlying seawater: comparison with atmospheric particles

CHAPTER 1

Microanalytical techniques and applications to individual environmental particle analysis

1.1 Introduction

Individual particle characterization is nowadays one of the more challenging aspects of microbeam analysis. Several microanalysis beam techniques have been developed which can advantageously be applied to particulate environmental samples. Such microanalyses can reveal whether a specific element or compound is uniformly distributed over all the particles of a population or whether it is a component of only a specific group of particles. Sometimes even the element lateral and depth distribution within a particle can be inferred. In this way it becomes more straightforward to assign particles to specific sources, while more refined information about source mechanisms and heterogeneous surface reactions can often be derived. The combination of results from sensitive and specific analytical techniques as electron probe X-ray microanalysis (EPXMA), secondary electron microscopy (SEM), laser microprobe mass spectrometry (LAMMS), secondary ion mass spectrometry (SIMS), electron energy-loss spectrometry (EELS) and (scanning) transmission electron microscpy [(S)TEM], available at the Micro and Trace Analysis Centre (MiTAC), are necessary to study and learn as much as possible about aerosols. We shall give a brief overview of these techniques and their recent instrumental applications in coastal, marine, urban and forestal environments. More attention will be given in the context of characterizing and apportioning elemental concentrations to their respective sources and of elucidating formation mechanisms and chemical transformation reactions of environmentally important particle types.

Some aspects of micro- and surface- analytical techniques for environmental studies as well as microanalysis applied to individual environmental particles have previously been reviewed by Grasserbauer (1978 and 1983). Table 1.1 gives an overview of the main analytical features of some micro- and surface- analytical beam techniques for the characterization and analysis of environmental particles.

1.2 Microanalytical techniques present at MiTAC

1.2.1 Electron microprobe analysis

The term "electron microscope" is generally used to describe the conventional transmission instrument that uses an electron beam for image formation. Since the development in the early 1960's of newer types of electron microscope instruments, where no transmission signals are involved, this classification is somewhat superseded and the term "electron probes" seems more convenient to use. The most important types of electron probe instruments used for environmental studies can be classified as follows:

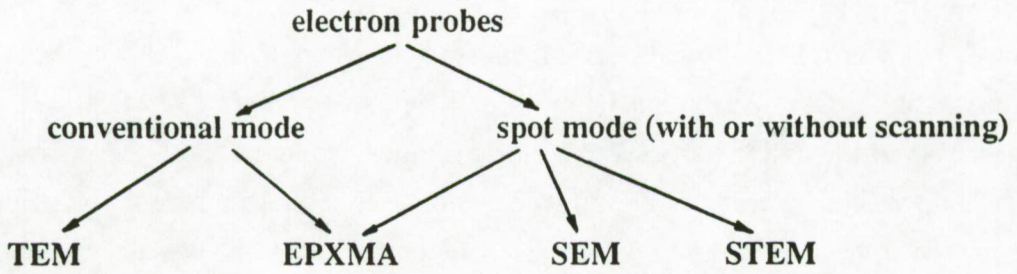

We shall limit the discussion to a brief description of EPXMA and SEM/EDX since these two techniques are well developed for automated individual particle characterization. All these instruments use an electron beam to excite various signals. By means of coils, the exciting electron beam can be focused to a 10 nm diameter probe. Both EPXMA and SEM/EDX instruments have one or more X-ray spectrometer attachments for the measurements of X-ray photons emitted as a result of the interaction of the electron beam with the specimen atoms. The emitted X-ray photons can be detected by wavelength- or energy-dispersive spectrometers (WDX and EDX, respectively).

Table 1.1: Comparison of some microanalysis techniques and their characteristics.

	EPXMA SEM/EXD	micro-PIXE	LAMMS	SIMS	EELS	FTIR	micro-RAMAN	XPS
Source	Electron	Protons	Photons	Ions	Electrons	Photons	Photons	Photons
Detection	Photons	Photons	Ions	Ions	Electrons	Photons	Photons	Electrons
Elemental coverage (Z)	EDX: 11–92	EDX: 11–92	1–92	1–92	3–92	Func. groups	Func. groups	3–92
In-depth resolution (μm)	0.5–5	100	>1	10^{-3}	0.01–0.1	>10	10^{-3}	5.10^{-4}
Lateral resolution (μm)	0.1–5	5–10	1	<1	<0.01	5–10	<10	10
Detection limit (ppm)	1000	10	10	1	1000	10–30	>1000	1000
Quantization	Yes	Yes	Difficult	Difficult	Difficult	Yes	Yes	Difficult
Molecular information	Yes (WDX)	Yes (WDX)	Sometimes	Sometimes	Yes	Yes	Yes	Yes
Element mapping	Yes	Yes	No	Yes	Yes	Yes	Yes	Yes
Destructive	No	No	Yes	Yes	No	No	No	No

Note: Some of the values in this table can vary with the elements present in the sample, the sample itself, instrumental set-up and the goal of the analysis.

Abbreviations: SEM/EDX: scanning electron microscopy/energy dispersive X-ray analysis; EPXMA: electron probe microanalysis; micro-PIXE: micro-proton induced X-ray microanalysis; LAMMS: laser microprobe mass spectrometry; SIMS: secondary ion mass spectrometry; EELS: electron energy loss spectroscopy; FTIR: Fourier transform infrared spectroscopy; XPS: X-ray photo-electron spectroscopy.

Figure 1.1 shows a schematic drawing of an electron microprobe. Similar to PIXE analysis (section 1.2.2), the detected signals are transformed to electronic pulses and, after amplification, stored in a multichannel device according to the corresponding wavelength or energy. The result is a spectrum of intensity versus wavelength or energy. Characteristic X-rays are superimposed on a Bremsstrahlung continuum which is rather intense as compared to e.g. PIXE. This background is a result of non-characteristic emissions from incident electrons interacting with the electrostatic field of the atomic nuclei and inner electron shells. In general, the variety of signals that are available in the EPXMA can rapidly provide information about composition and surface topography in small areas of the specimen. One of these signals is derived from backscattered electrons and it gives origin to two types of images: a topographical image which shows the roughness of the sample and a compositional image which is a visualization of the atomic number variation with location in the sample. On the other hand, secondary electrons are mostly used for secondary electron imaging and electron micrographs. Both the backscattered and secondary electron signals can therefore be used for morphology studies.

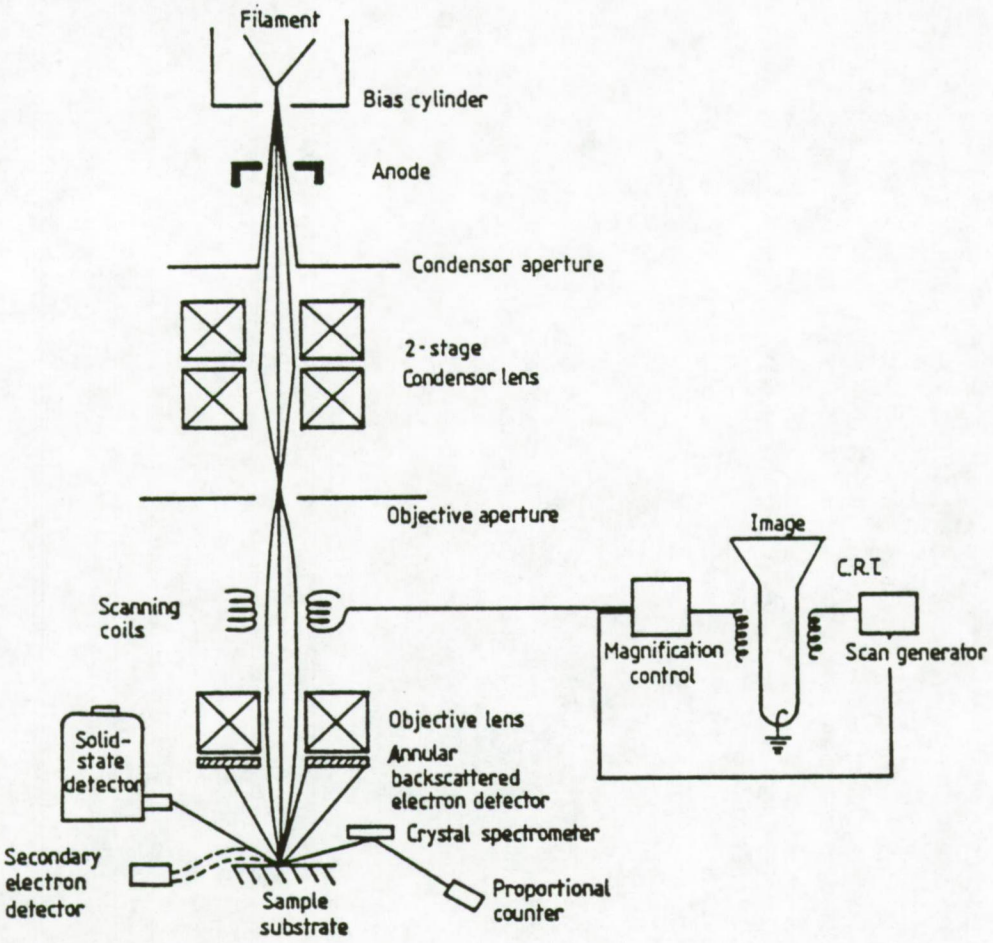

Figure 1.1: Schematic drawing of an EPMA instrument.

The theory for EPXMA and SEM/EDX analysis is described in detail in textbooks by e.g. Goldstein and Yakowitz (1987), Holt et al. (1974) and Reed (1975). In fact, there is no longer a sharp distinction between the two electron microprobe techniques EPXMA and SEM/EDX. SEM was originally used for high resolution imaging rather than for chemical analysis. EPXMA was primarily developed for achieving quantitative elemental information rather than for imaging purposes. This difference is more a matter of instrumental set-up and practical arrangement of the detectors. Both techniques are now converging to some extent for the purpose of chemical and morphological studies.

To study particulate samples by individual particle analysis requires the measurements of a large population set in order to obtain statistically meaningful data. At the University of Antwerp, a JEOL Superprobe JXA-733 electron probe X-ray microanalyzer is automated with a Tracor Northern TN-2000 system and controlled by an LSI 11/23 minicomputer. The following methodology is generally used for the automated particle recognition and characterization (PRC). An electron beam is raster scanned over a preset sample area by means of a digital beam control. A particle is detected when the electron backscattered signal of the closed particle contour points exceeds a preset threshold value. The area, perimeter and equivalent diameter (diameter of a circle which corresponds with the measured particle area) are calculated. An X-ray spectrum can be accumulated at the center of the particle or while performing cross scans over the particle. Thus the PRC program is set up in three sequential steps: localizing, sizing and chemical characterization, after which the beam scans for the next particle. Typical working conditions are a beam current of 1 nA at an acceleration voltage of 20 to 25 keV. X-ray spectra are accumulated for about 20 seconds in the energy-dispersive (EDX) mode using a Si(Li) detector. All the data can be stored on magnetic tape or floppy disc for off-line processing. Automated EPXMA is a very efficient method for analyzing many individual particles within a short time. For example, 500 particles can be multi-element analyzed in less than 2.5 hours under optimized working conditions. The limiting time factors for such automated method are the time to search for a particle and the time to analyze it. For such analysis, a relative accuracy of about 5 % can be obtained. The relative detection limit of EPXMA using EDX analysis is about 0.1 %. However, it is not straightforward to interpret the huge amount of information available from EPXMA measurements. Therefore, multivariate clustering procedures are used to classify each particle according to a most representative particle type. Most often hierarchical and non-hierarchical clustering procedures are used occationally in combination with principal component analysis (PCA). The purpose of the PCA method is to represent the variation present in the data in such a way that, without losing significant information, the dimensionality is reduced. The particles are

thus classified according to their matrix composition by multivariate methods resulting in the assessment of the abundances for the different particle types that can be correlated with their source of emission or their formation mechanism. General information about these classification procedures can be found in the textbook of Massart and Kaufman (1983). So, individual particle analysis partitioning of the bulk chemical data can provide supplementary and complementary information. This type of analysis can be employed in a number of environmental studies dealing with source characterization and apportionment, particle transport and deposition, or with reaction mechanisms such as sulfatation and condensation. Combined with multivariate techniques and/or clustering analysis, this technique constitutes a powerful method for discriminating different particle types originating from the same source. Lee et al. (1986) pointed out that, so far, only a limited number of studies have been published on the use of automated EPXMA in the field of environmental research.

1.2.2 Particle-induced X-ray emission

Ion beams collimated to micrometer size can become a very useful tool for the study of individual particle analysis. In the Scanning Proton Microprobe (SPM) analysis, a well focused beam of high energy protons is scanned over the sample. A variety of signals that can be collected and processed is used to obtain unique information on the composition of the sample. One of the major advantages of this technique is the excellent detection limit, of the order of 1 to 10 ppm, depending on the SPM design. Quantification is relatively easy to perform, with an accuracy of 10 to 20 % (Watt and Grime, 1987; Vis, 1985). The proton beam with an energy from 1 to 3 MeV is finely focused in the sample by means of magnetic quadrupoles and/or electrostatic lenses. The high energy proton beam is obtained with cyclotrons or with nuclear electrostatic accelerators like Van de Graaffs. The proton beam is focused to diameters of 0.5 to 10 μm, with currents of about 100 pA. A scanning system controls the beam positioning, and a computer system collects data from several detectors and beam information. The proton microprobe instrument is very alike to the electron microprobe. The only difference lies in the nature of the microbeam. The latter uses an electron beam whereas the former uses a proton beam.

Most SPM instruments provide routinely a spatial resolution of 0.5 to 10 μm. As the proton beam generally goes through the sample and is collected in a Faraday cup, quantification is very easy and matrix effects are not significant. An accuracy of 10 to 20 percent is obtained for absolute analysis, and detection limits down to 10 ppm.

For aerosol particle analysis it is necessary to limit the proton beam current under 100 pA in order to avoid specimen damage. As with LAMMS and EPXMA, the sample is analyzed in a vacuum chamber, so possibly some of the organic components are lost. There are several processes occurring during the interaction of the proton beam with the sample. When the generated X-rays are measured in Particle Induced X-Ray emission (PIXE) elements heavier than sodium can be detected; PIXE has been reviewed in depth by Johansson and Campbell (1988).

Backscattered particles provide information on light elements like carbon, nitrogen and oxygen through the "Rutherford Back Scattering" (RBS) analysis (Finstad and Chu, 1988). In RBS the elastic back scattering of protons is used to obtain quantitative analysis of light elements like carbon, nitrogen and oxygen. The sensitivity is not so good as in PIXE, but then these elements occur generally in higher concentrations in aerosol particles; hence this is not a limitation for this application. A semiconductor surface barrier detector is often used to detect the back-scattered particles, and the energy spectra are analyzed by computer codes. It is also possible to make elemental maps of C, N and O in real time, simultaneously with the trace element elemental maps. This has shown to be very useful to measure the stoichiometry of compounds in atmospheric aerosol particles (Artaxo et al., 1990). Frequently, PIXE and RBS analysis are done simultaneously, allowing the determination of carbon, nitrogen and oxygen together with 10 to 15 trace elements heavier than sodium.

The proton beam also generates gamma rays from nuclear reactions, allowing to measure fluorine, sodium and other elements by Particle Induced Gamma Emission or PIGE (Bird, 1989). In PIGE, a Ge(Li) detector is used to collect the prompt gamma rays produced in nuclear reactions due to the interaction between the proton beam and the sample. This technique is suitable to measure Li, B, F, Na, Mg, Al and Si in particles. PIGE can be used simultaneously with PIXE and RBS, with a judicious choice of the proton beam energy (Boni et al., 1988).

The SPM is a recent technique, and most of the applications are in biology, archaeology, geology and material sciences. Artaxo et al. (1990) showed the feasibility of a combined approach of EPXMA, LAMMA and SPM analysis of individual aerosol particles. By exploring the advantages and disadvantages of each particular technique, it is possible to obtain a wealth of information for individual aerosol particles.

1.2.3 Laser microprobe mass spectrometry

Laser microprobe mass spectrometry (LAMMS) is based on the mass spectrometric analysis of ions, formed by the interaction of the sample with a high power density pulsed laser beam. Soon after their development in the early sixties, lasers were applied in mass spectrometry. Originally, LAMMS was developed for analysis of biological samples, with high lateral resolution and extreme sensitivity. Nowadays, various instrumental set-ups have been developed for different analytical purposes. Figure 1.2 shows a schematic drawing of a typical LAMMS instrument.

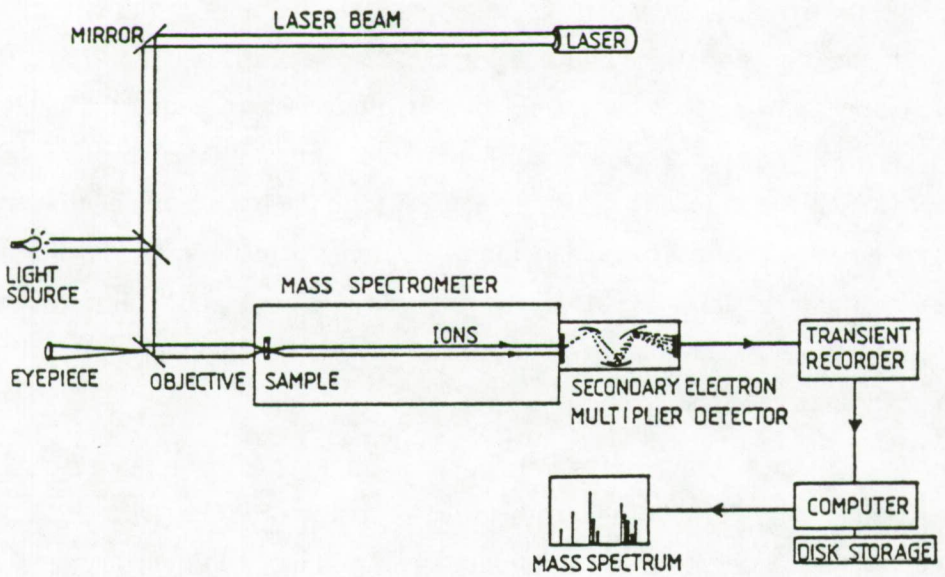

Figure 1.2: Schematic drawing of a LAMMS instrument.

Van Vaeck and Gijbels (1989) published an overview of LAMMS techniques. Some of the instruments that have been constructed, have also been commercialized; e.g. the LIMA-2A of Cambridge Mass Spectrometry, Cambridge, UK and the LAMMA-1000 and LAMMA-500 of Leybold Heraus, Cologne, Germany. In the latter instrument, a Nd-YAG laser generates very short and intense light pulses for vaporization and ionization of a microvolume of the sample. The power density is 10^{-7} to 10^{-11} W.cm^{-2} for a 1 μm laser focus and can be reduced to 2 % of its initial value by a 25 step attenuating filter system. This is especially interesting for particle surface analysis. Depending on the spectrum polarity chosen, positive or negative ions which are formed by laser irradiation of the selected sample area are accelerated by a potential of 3000 V

into a field-free drift region of the time-of-flight (TOF) mass spectrometer. The time-of-flight needed by an ion to traverse this region is related to its mass-over-charge ratio (Cotter, 1989). The signal is then fed into a 32 kbyte memory transient recorder and digitized. Spectra are stored in a personal computer for off-line data handling. Software packages are available for data processing and include a baseline correction algorithm, a peak integration routine and spectrum averaging facilities. The commercial instruments differ in this geometry for ion collection from the specimen. Sometimes, other mass spectrometers are used in LAMMS, e.g. the single focusing magnetic sector instrument of the laser probe mass spectrograph (LPMS) and the double focusing Mattauch-Herzog type set-up of a scanning laser mass spectrometer (SLMS). A detailed description of these mass spectrometers can be found in the literature (Davis and Frearson, 1987). Various review articles on several aspects of laser microprobe mass spectrometry are available in the literature: early developments are discussed by Conzemius and Capellen (1980); laser desorption by Cotter (1984); applications in medicine, biology and environmental research by Verbueken et al. (1985). Recently, Kaufmann et al. (1989) evaluated achievements, shortcomings and promises of LAMMS, especially in biomedical research. Just as for microprobe analysis, manual interpretation and classification of several hundreds of individual particle spectra is certainly the time limiting step in the analysis procedure. To speed up things, one searches for computer aided methods. Different approaches have been used: pattern recognition techniques (Fletcher and Currie, 1989), artificial intelligence (Harrington et al., 1989) and library search (Wouters, 1991). Generally the LAMMS-technique has various interesting features: it can detect all elements, and, compared to other microchemical techniques, detection limits are quite good. It can give indications concerning stoichiometry or compound determination, and information about several organic compounds of environmental importance. Disadvantages are the facts that the technique is destructive and rather unreproducible and that the theoretical aspects of ion formation and behaviour in the system are not yet elucidated.

1.2.4 Secondary ion mass spectrometry

Secondary ion mass spectrometry (SIMS) is based on the bombardment of a sample surface by primary ions (Ar^+, F^-, O^-, etc.) or molecules generated in a duoplasmatron (energies in the keV range). Only a small fraction (typically 0.01-1%) of the sputtered atoms are charged. These secondary ions are attracted to a mass spectrometer where the separation according to their mass/charge ratio takes place. The separated positive or negative secondary ions are collected as mass spectra, as in-depth profiles or line-scans, or as distribution images of the sputtered surface.

A mass spectrum can range from hydrogen to an m/z ratio of several hundreds. The mass spectrometer is based on electric/magnetic deflection fields or on the quadrupole/time-of-flight principle; the latter being cheaper, but less satisfactory with respect to mass resolution and transmission. Figure 1.3 represents the principle of SIMS schematically.

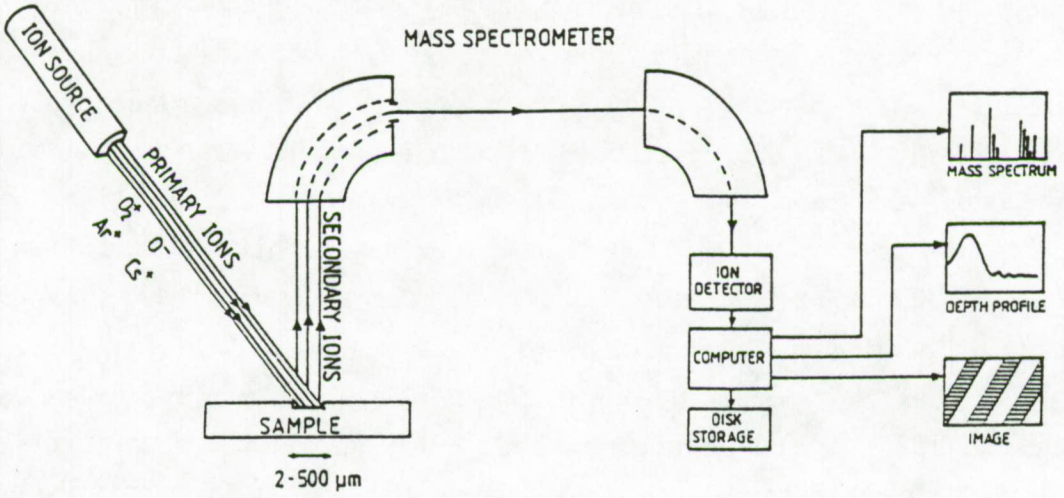

Figure 1.3: schematic drawing of a SIMS instrument.

Lodding (1988) distinguishes 3 classes of SIMS instrumentation: (a) non imaging probes (static SIMS), used for depth profiling on laterally homogeneous specimens or for surface analysis, (b) imaging ion microprobes (dynamic SIMS), which use a narrow (<10 µm) beam of primary ions at energies of 5-20 keV, and allow imaging and microscopy by rastering the beam over the sample surface, and (c) direct imaging microscope microanalyzers, which use wide (5-300 µm) primary beams. Method (b) is best suited for determination of depth profiles, since the sputter rate is highest. SIMS offers special capabilities for particle analysis. Heterogeneities in the composition in single particles are frequently observed from site to site. The distribution of constituents with depth in a particle is another microstructural feature of interest. SIMS is capable of obtaining signals from a depth of about 1-2 nm and this information originates from the surface of the sample. SIMS can also be used as a microanalysis technique with a minimum sampling volume of 0.01 μm^3 (Goldstein and Yakowitz, 1987). The capabilities of SIMS for detection of all elements, compound detection, isotope ratio measurements, depth profiling and ion imaging of specific constituents have been described (Newbury, 1980) with special reference to particle studies. Depth profiling can be successfully applied to individual particles; however, irregular topography of particles can degrade the depth resolution. Ion specific images of elemental or molecular

constituents can be obtained in the ion microscope or ion microprobe (Morrison and Slodzian, 1975). The limiting lateral resolution is about 0.5 μm for the ion microscope and about 1 μm for the scanning ion microprobe.

The absolute detection limit for SIMS analysis is about 10^{-15} g for most elements and chemical compounds, and for anions down to 10^{-18} g (Benninghoven and Storp, 1973). For more detailed information, the reader is referred to the literature (Klaus, 1986). When molecular information of particles is needed, both LAMMS and SIMS can be used since they exhibit qualitatively the same positive ions. A comparative study of these two microtechniques was performed in inorganic sodium sulfoxy salts (Mariën and De Pauw, 1985).

1.2.5 Other microanalytical techniques

Many other microanalytical techniques are known and some of them are well developed and suited for single particle analysis. Among these, Fourier Transform Infrared Spectroscopy (FTIR), Micro Raman Spectroscopy, Auger Electron Spectroscopy (AES) and X-ray Photoelectron Spectroscopy (XPS) all have proven their success. However, a detailed discussion of these techniques would be too tedious and goes beyond the scope of this chapter. Nevertheless, some applications discussed in the next paragraphs refer to their specific advantages as they are necessary for the better understanding of environmental particle behaviour.

For more information about these techniques with applications on single particle analysis, the reader is best refered to the references cited below.

Small et al. (1988) and Gordon et al. (1988) reported on the use of FT-IR spectroscopy to study atmospheric pollutants and characterize organic substances in aerosols. The scope and limitations of single particle analysis by Raman microprobe spectroscopy is demonstrated by Etz and Blaha (1980). Also Purcell and Etz (1982) and Etz and Roscasco (1976 and 1977) demonstrated a new spectrograph with a multichannel optical detector for the Raman characterization of microparticles and applications to the identification of airborne particulates. Cox III and Linton (1986) already discussed extensively the aspects of environmental applications of XPS involving airborne particle chemistry. Also a brief review of X-ray photoelectron spectroscopy for the characterization of surface regions of particulate pollutants from the atmosphere is given elsewhere (Powell, 1980). A brief discussion of applications of Auger electron spectroscopy (AES) and X-ray photoelectron spectroscopy (XPS) to single particle analysis is given by Powel (1978).

1.3 Applications

1.3.1 Marine aerosols

The investigation of the aerosol composition over different oceans and seas is important for several reasons: particles from remote regions can serve as a marine background aerosol, while transport, transfer and wet and dry deposition of aerosol pollutants from continental sources to the marine environment can be assessed. In studies of the marine aerosol, Na and Cl are the most frequently used reference materials (Duce and Hoffman, 1976). Their presence in the atmosphere can unambiguously be related to the ocean.The marine aerosol composition has been studied by impactor sampling at coastal sites, well away from major land areas or by sampling at coastal sites under on-shore wind conditions, and in laboratories under simulated conditions (Otten et al., 1986).

1.3.1.1 North Sea

The North Sea is an important sink for dry and wet deposition of atmospheric particulate matter from the surrounding industrialized pollution sources (Table 1.2).

Table 1.2: Total input (ton.year^{-1}) and relative contribution (%) of trace elements through different sources into the North Sea (source: Otten, 1991).

	Cd	Cu	Pb	Zn	References
Total (ton.year^{-1})	281	4510	6900	26100	Otten, 1991
Rivers	19	34	14	31	PARCOM, 1989
Discharges	6	6	2	5	PARCOM, 1989
Dumping	9	29	35	34	STWG, 1987
Atmosphere	66	31	49	30	Otten, 1991

Laser microprobe mass spectrometry (LAMMS) and automated electron probe X-ray microananalysis (EPXMA) have been used for the characterization of individual North Sea aerosols (Bruynseels et al., 1988). With the aid of EPXMA, about 2,500 particles, sampled from a research vessel, were sized, chemically analyzed and classified. Sea salt constituted the most abundant particle type when the collected air masses originated from over the Atlantic Ocean and traveled toward the continent. Contrarily, in air masses that spent longer residence times over the continent, high concentrations of aluminosilicate particles (mostly spherical flyash particles), carbonaceous particles, $CaSO_4$ and spherical iron oxides were observed.

LAMMS was applied to a number of representative particles from the different particle types in order to elaborate trace element contents and surface layer composition. Applying low energy laser shots to the spherical flyash particles revealed typical mass spectra that were interpreted as fingerprints for the desorption of polynuclear aromatic hydrocarbons (PAH). The most typical marine aerosol particles are of course seasalt particles, formed by the bubble bursting mechanism. Spectra of "pure" seasalt are dominated by Na, K, and typical Na/K/Cl cluster ions. Often, seasalt particles are found to have been transformed to some extent; in this case, nitrate and sulfate coatings are readily detectable (Bruynseels and Van Grieken, 1985). Also Allegrini and Mattongo (1978) proved with XPS the existence of various nitrogen and sulfur species on particle surfaces.

Another advantage of LAMMS in aerosol research is its ability to detect ammonium compounds, which are very interesting from an environmental point of view. Otten et al. (1986) found the relative abundances of ammonium-rich particles in the North Sea aerosol to increase dramatically under the influence of polluted airmasses.

Continentally derived aerosols are often found in the marine environment. By use of EPXMA, it was found that high number concentrations of aluminosilicates present as internal mixture with sea salt aerosols are more likely to be the result of coagulation of sea salt and silicate particles within clouds, including droplet coalescence (Andreae et al., 1986) rather than resuspension of silicate particles from the sea surface as a result of bubble bursting processes. The fine aerosol mode contains higher concentrations of S, K, V, Ni, Cu and Zn.

1.3.1.2 Remote ocean areas

The atmospheric aerosol composition over remote ocean areas, such as the Atlantic Ocean, has been investigated fairly intensively, either from island-based sites or from research vessels.

Aerosols collected over the Eastern Equatorial Pacific from a sailboat (from Panama to Tahiti) were analyzed both by bulk-PIXE (Maenhaut et al., 1983) and single particle EPXMA techniques (Xhoffer, 1987). Beside the major sea salt aerosols, a substantial crustal component and fine Cu and Zn, resulting from continental sources, were characterized. Long-range transport from natural high-temperature sources such as volcanoes or emission from fuel combustion on the American continent, or enrichment at the sea surface are possible sources for the Cu and Zn concentrations found. Excess fine S sometimes reached levels similar to those reported for other remote regions. Excess fine K and partly fine S showed a tendency to exhibit higher values for samples collected near harbors, suggesting local island derived sources such as biomass burning and fossil fuel burning.

EPXMA of more than 5,000 individual particles, combined with cluster techniques, provided a classification of all particles on the basis of their chemical composition. The most abundant particle type was rich in S (45% of all particles) and this in the absence of other detectable elements. Morphological inspection of these particles allowed to differentiate between two groups, namely one group of S-rich particles in the sub-micrometer range that are unstable under the electron beam and are most probably $(NH_4)_2SO_4$, and one S-rich group in the micrometer range (mean particle diameter of 2 μm) showing more spherical contours. The latter group is much less affected by electron irradiation. The crustal component and also Cu and Zn are more abundant in those samples collected near the American continent in accordance to PIXE analysis. The mean diameter for the Cu- and Zn-rich particles is about 0.7 μm. An important fraction of particles only yielded characteristic Ca and P X-rays; their mean diameter varied between 0.4 and 0.8 μm. Their abundance shows a slight tendency to increase as the sample location approaches the continent.

Aerosols collected from an aircraft in remote continental and marine regions at altitudes ranging from the boundary sea-air interface to the troposphere were analyzed with SEM/EDX and PIXE (Patterson et al., 1980). The continental aerosol population consisted of crustal particles with $r > 0.5$ μm and sulfate aerosols with $r < 0.5$ μm. No qualitative differences were noted as a function of altitude. Contrarily, Pacific marine measurements show large variations between the boundary layer and the troposphere. A decrease of the crustal component was observed from the North towards the South.

The detection of methanesulfonate, a biogenic airborne organic compound, above the Sargasso Sea and the Bahamas area (Kolaitis et al., 1989) constitutes an excellent illustration of the occasional "organic successes" of the LAMMS technique.

1.3.2 Remote continental aerosols

The aerosol composition of extremely remote locations has always been a subject of interest. Indeed, due to the growing industrialization and the long-range transport of pollutants (e.g. linked to high-stack technology), it has become increasingly difficult to define the composition of baseline natural aerosols in the absence of any pollution. Several remote locations, most of the time located in the Southern hemisphere, have already been the subject of an extensive study.

1.3.2.1 Antarctica

The Antarctic continent is probably the most convenient place on earth to study the composition of background aerosols because it is the most distant area from the world's predominant pollution sources and local anthropogenic contributions are negligible. Single particle X-ray analyses of Antarctic aerosol samples from different locations have revealed the following particle types: sulfur-rich particles (which may be formed by gas to particle conversion), seasalt particles (formed by the bursting of gas bubbles that arise through wave action), aluminosilicates (earth crustal dust or particles originating from local sources like volcanoes, geysers, or other surface/ocean-floor disruptions), and particles whose X-ray spectra contain mostly Fe peaks (long-range transported anthropogenic or maybe meteoric dust particles) (Parungo et al., 1981; Shaw, 1983; Ito, 1985; Bodhaine and Murphy, 1980; Bodhaine et al., 1986). Naturally, their relative concentrations vary with sampling site, season and meteorological conditions. Especially in summer, sulfate particles tend to dominate the Antarctic aerosol by number and also by mass (Shaw, 1983; Cunninghan and Zoller, 1981). This sulfate should predominantly exist in the form of H_2SO_4, $(NH_4)HSO_4$, $(NH_4)_2SO_4$ or a mixture, possibly including more complex species as was also revealed by Raman microprobe measurements on identical particles (Etz and Blaha, 1980). Ito (1985) and Bigg (1980) detected H_2SO_4 and $(NH_4)_2SO_4$ particles. Hierarchical and non-hierarchical cluster analyses were performed on individual coastal Antarctic aerosols using EPXMA (Storms, 1988). The results show a domination of marine components in both the fine and the coarse mode fractions. Only a minor crustal component was found and thus crustal weathering processes must be far less important than the strength of the marine source.

LAMMS of similar aerosol particles (Wouters et al., 1990) revealed the presence of salts derived from methane sulfonic acid (MSA). MSA is a reaction product of the photo-oxidation of dimethylsulfide (DMS), which originates from the metabolism of certain marine algae and decay processes of dead krill. This compound contributes significantly to the global sulfur cycle.

Various metallic particles as Fe-rich and Zn-rich particles both containing Pb were only observed by LAMMS because of the higher sensitivity compared to EPXMA. Parungo et al. (1981) stated that the Fe-Pb-containing particles could be meteoritic dust. Also intense K-peaks associated with much less intense but nevertheless obvious Pb-isotope patterns were detected in some particles. They could originate from biogenic emissions. According to their size (< 1 μm), however, long range transport does not seem so obvious.

1.3.2.2 Alaska

Sheridan and Musselman (1985) performed LAMMS and EPXMA on particles sampled during flights over the Alaskan Arctic. Virtually all sub-micrometer particles yielded spectra that highly resembled those of a ammonium sulfate standard. Because the likelihood of finding appreciable amounts of ammonium vapor in the winter Arctic atmosphere is small, they concluded that those particles were collected as sulfuric acid and gradually transformed in the laboratory. K-rich particles in this aerosol were tentatively attributed to wood smoke.

1.3.2.3 Bolivia

Surkyn et al. (1983) performed LAMMS on aerosol particles from the uplands of central Bolivia. The sampling station was located at 5230 m above sea level. The immediate surroundings are totally unhabitated, and the ground over a wide area is stony, partly snow-covered year-round and without vegetation. Particles from this site were soil derived aluminosilicates and/or Ca-rich particles and, in the smallest size fraction, ammonium sulfates. Occasionally, K- and C-rich particles were detected; most probably they resulted from forest burning.

EPXMA and LAMMA in combination with particle classification routines were discussed by Raeymaekers (1986). Silicates, a group in which quartz and aluminosilicates are classified, originate from the suspension of soil dust. Modified silicates were present and are characterized by a silicate nucleus on which sulfates, phosphates and chlorides are deposited due to atmospheric processes. Some samples contained high relative weight fractions of silicates with equal atomic fractions of K and Cl, suggesting the presence of KCl on the particles. No significant sources of Cl exist in the vicinity of the sampling area except volcanic emissions. Shaw (1983) suggests that volcanic activity can explain the high Cl concentrations and its correlation with Si. Most

probably, Cl enters the environment in a gaseous form, as supposed by Adams et al. (1983) who found also a strong correlation between these two elements.

Sulfate particles only constitute a minor weight fraction among the present groups. LAMMS results showed that the negative mass spectra of these particles closely correspond to those obtained for $(NH_4)_2SO_4$ standards (Surkyn et al.,1983). The consistent presence of Pb in the LAMMS spectra of the fine particulate sulfate suggests that the element has a gaseous precursor. Other atmospherically enriched elements (As, Cu, Zn,...) were not detected in the same particles probably as a result of inferior detection sensitivity.

Bigg (1980) analyzed individual particles from Cape Grim (Tasmania), Mauna Loa Observatory (Hawaii) and Point Barrow (Alaska), using an electron microscope, and performed some chemical tests on them. This approach turned out to be very effective. The great majority of those particles were found to be composed of sulfuric acid or its reaction products with ammonia. The Barrow and Mauna Loa particles were predominantly sulfuric acid, while the South Pole and Cape Grim particles were predominantly ammoniumsulfate. The latter aerosol was also analyzed with LAMMS (Surkyn et al., 1983), and was found to contain seasalt-derived and exceptionally crust-derived particles.

1.3.3 Transect from marine to industrial environment

The LAMMS-technique has been applied to a set of aerosol samples collected on a Brazilian transect from a beach site toward and through a heavily polluted industrialized area (Bruynseels et al., 1985). The aim was to find aswers to the questions concerning sources, transport processes and physico-chemical changes of airborne particulate matter.

The LAMMS spectra of nearly all particles could be classified to one of six representative particle types namely seasalt, transformed seasalt, Ca-rich, crustal components, organic N-rich and various components.

A specific advantage of the LAMMS technique over other microananalytical techniques was demonstrated by applying low laser energy desorption shots on seasalt particles. It was proven that a significant fraction of these particles are coated with a layer of $NaNO_3$ devoid of chloride. These chemical transformation reactions can be the result of differential crystallization of liquid seawater containing nitrate as a result of a heterogeneous reaction between HNO_3 vapour and the particles (Harrison and Sturges, 1984). Only a minor fraction of the seasalt particles are found to be rich in $NaNO_3$ in the samples taken at the beach location. Inland, the NaCl-$NaNO_3$ particles

become predominant in the industrial area; pure seasalt particles are not observed at all. This drastic abundance difference of $NaNO_3$-rich particles on the transect gives direct indication for a very fast and efficient gas-to-particle conversion mechanism.

An other typical transect particle type yielded positive mass peaks corresponding to organic N-compounds such as amines. These particles are observed in the smallest size-range and their relative abundance increases from the seaside station towards the industrial area. Amines can be released into the atmosphere by decomposition of proteins of biogenic origin, by the combustion of polyamides or they can be emitted by the local amine-producing industry.

1.3.4 Biogenic aerosols

It has already been hypothesized that the forest is a major source of aerosols of both the fine and coarse fractions (Bigg and Turvey, 1978). Plant leaves can be responsible for a large number of biogenic aerosol emission processes: large particles can be released by mechanical abrasion of the plant leaves as a result of wind action (Beauford et al., 1977), biological activity of leaf surface microorganisms can result in the production of airborne particles and windblown pollen, and during crop plant transpiration, migration of Ca^{2+}, SO_4^{2-}, Cl^-, K^+, Mg^{2+} and Na^+ into the atmosphere can occur (Nemeruyk, 1970). The forest is also a source of sulfates (specially during the rainy season), ammonium and nitrates (Delmas et al., 1986). Despite the relatively vast area of tropical forests, only a few comprehensive studies on the composition and origin of aerosols in the tropical forest have been published (Artaxo and Orsini, 1986; Maenhaut and Akilimali, 1987; Artaxo et al., 1988). On a 4 year sampling strategy, the Amazon Boundary Layer Experiment refers to a long-term study of the chemistry of the atmospheric boundary layer supported within the Global Tropospheric Experiment (GTE) of the NASA Tropospheric Chemistry Program (Storms, 1988; Bruynseels, 1987; Wouters, 1991; Artaxo et al., 1988).

Morphological and elemental EPXMA data of all sampling locations were treated by hierarchical cluster analysis. Careful examination of the obtained particle types showed two main particle groups namely, aerosols rich in Al, Si, Ti and Fe denoted as mineral dust and one group containing aerosols emitted by plants. The morphological structure of the latter particles were diversified and some particles were clearly pollen grains, fungi, algae and plant fragments. Biogenic emission accounts for almost 80% of the total number of particles. The most frequently observed particles by EPXMA are those containing high P, S and K concentrations. There is also a significant contribution of Cl among the different particle types. Sodium is present together with S, Cl and K, and is detected in 8% of the particles. Most of the particle types have a large

contribution of low-Z elements (C, H, N, O); this can be deduced from the high spectral background present in the corresponding X-ray spectra. These particles are assumed to be generated by vegetation.

The most important contribution in the fine mode aerosol is made by the particle type containing mainly S, K, Ca and P. These aerosol particles originate from biogenic emissions and were released by the vegetation; indeed, their composition agreed with the one expected for plant material. This large group may be subdivided in more specific particle types, each probably originating from a different biogenic source or process. The most abundant element is sulfur which is present in a considerably large amount in almost all particle types related to the vegetation. Some low abundance particle types were present in the fine mode aerosol which are more difficult to identify namely: Zn-S-, Na-S-, Mn- and Cl-rich particle types. They are all believed to originate from vegetation.

LAMMS spectra of Amazon Basin aerosols are very complex due to the presence of different organic compounds, fragmented to various extents: sulfate salts of amines, methane sulfonate and fragmentation patterns of hydrocarbons, terpenes and phospholipids have been identified up to now (Bruynseels et al., 1987; Artaxo et al., 1988). Part of this organic material was found to be associated with inorganic salt mixtures consisting of plant nutrients, which points to a plant-transpiration origin. The conjugated base of methane sulfonic acid (MSA) was frequently detected in biogenic aerosols, especially among the smallest ones. Until recently, this species was believed to originate exclusively from the photochemical oxidation of organic sulfur products as dimethyl sulfide (DMS) and methyl sulfide (MeSH) that are emitted by oceanic and continental ecosystems (Andreae et al., 1986; Lovelock et al., 1972).

The metal-rich group contains predominantly Cr/Fe/Pb-rich, Cu-rich and Ti-rich particles. Beauford et al. (1977) showed that plants are capable of emitting heavy elements as Zn and Pb. But then, roughly 60% of these particles show no peaks other than the metal(oxide) related ones and there is no reason to assume that heavy metals should be emitted separately from the biologically important elements as e.g. Mg, Ca, K and Na. Micro-PIXE and RBS were used simultaneously on Amazon Basin aerosol particles (Artaxo et al; 1988). It was easy to measure elements like Rb, Zn and Mn with concentrations below 10 ppm.

1.3.5 Urban aerosols

The composition of an urban aerosol will of course largely depend on its geographical location, the activities performed locally and the industries surrounding the sampling site. Still, some trends can be defined. Soil dust particles are usually abundant.

Other particle types often found are sulfates ($CaSO_4$, fine and coarse sulfur-rich particles), auto exhausts (Pb-halides and sulfate derivatives) and different anthropogenic particles derived from various sources such as oil burning processes (S, V, Ni), abrasion processes (Fe-, Cr-oxides), and emissions of incinerators (Zn-, Pb-, Cu-, Zn- and Sb-rich particles) (Van Borm et al., 1989). The principal source of particulate Pb in the urban atmosphere is the combustion of leaded petrol. Automated EPXMA and LAMMS studies were performed on more than 15,000 individual Pb-containing particles sampled near the city of Antwerp, Belgium (Van Borm et al., 1990). The results indicated that partial conversion of Pb-halide containing particles into Pb-sulfates often occurs by the reaction with ammonium sulfate present in the urban atmosphere. The ammonium sulfate can also be present as a coating on the Pb-containing particles. Keyser et al. (1978) have reported elemental distributions as a function of the sputter depth by SIMS from large (10 μm) automobile exhaust particles. Enrichments of Pb and Br and, less obvious, of S at the particle surfaces were found.

A comprehensive study of particulate material in the 0.1 to 30 μm size range in the urban aerosol of Phoenix, Arizona, was conducted (Post and Buseck, 1985). More than 8000 individual particles were analyzed by analytical scanning electron microscope. The coarse particle fraction (>1 μm) is mainly crustal material i.e. clays, quartz, feldspar, calcite etc.. A minority of biological material and S-compounds and Pb-salts from automobiles were observed as well. The submicron aerosol fraction comprises S-containing particles (60 to 80%) presumably present as $(NH_4)_2SO_4$. Some of these particles contain various amounts of elements as Zn, Pb, Cu, Ca, Na and K.

More than 50 pairs of aerosol samples collected at the Santiago (Chile) environment were studied by EPXMA and LAMMS (Rojas et al., 1990; Kolaitis, 1988). The most characteristic particle clusters recognized are soil dust, (transformed) seasalt, S-rich, aluminosilicates, metal-rich, gypsum, Si-Fe-rich and particles derived from biomass burning. Only the two former particle types are produced by natural sources. The others are all generated by anthropogenic activities. The particles associated with seaspray, sulfate, metallurgical emissions and wood-burning processes have sub-μm diameters, whereas those related to the Earth's crust range from 1-16 μm diameter. In addition, an organic fraction (8%) was noticed and morphological inspection indicated that some of these particles refer to biological material. The results of EPXMA pointed

toward the presence of a marine aerosol forming part of the Santiago de Chile atmospheric particulate matter. In fact, Prèndez and Ortiz (1984) reported that the city of Santiago had non-marine impact mainly due to its topographical configuration and geographical location. This assumption was based on enrichment factor calculations performed on total suspended matter elemental concentrations. Hence, another microananalytical technique, namely LAMMS, was invoked for confirming marine influences. Indeed, among the particles in the size range of 0.25 to 0.5 μm, positive ion LAMMS spectra were mainly characterized by Na and Na-derived molecular fragments. Also S-enrichment was present in most of the spectra pertaining to seasalt derived aerosol particles. LAMMS confirmed the presence of particles as sulfates and nitrates and, in many cases, the aerosol was uniquely composed of carbon series. With relatively low frequency, also phosphates formed part of the LAMMS spectra.

1.3.6 Volcanic and stratospheric aerosols

Some research efforts have been focused on natural aerosols released by other pathways. Analyses by SEM combined with XPS of volcanic ash particles have been reported by several authors (Fruchter et al., 1980; Wightman, 1982; Gooding et al., 1983). Major elements detected by SEM/EDX were Al, Ca, K, Si; minor ones were Fe, Mg and Ti. Volcanic eruptions are proven to be responsible for a fraction of terrestial particles released directly into the stratosphere (Rampino and Self, 1984). Particles present in the stratosphere can also be derived from sulfuric acid aerosols, sapphires and meteorites (Brownlee, 1980). They contain Al metal, Al_2O_3 spheres and Al-prime particles. The submicron regime is dominated by sulfate aerosols of terrestrial origin (Cadle and Grams, 1975). Relatively high concentrations of sulfur are emitted during volcanic eruptions and the presence of thin sulfate gels on the surface of ash particles is probably the result of processes within stratospheric clouds (Mackinnon et al., 1984).

1.3.7 Industrial and workplace aerosols

Industrial aerosol research is often concerned with the quality of the working environment. As toxic effects are often correlated with specific particles, shapes, sizes or element distributions, microananalysis is a very powerful tool to point out the dangerous parameters. The superiority of microananalysis over bulk analysis techniques in this field is clearly demonstrated in the analysis of coal mine dust. The predominant role of quartz in the induction of "coal mine workers disease" (pneumoconiosis) is widely accepted but there are still unambiguities about the existence of

additional and/or modulating factors determining the degree of toxicity. Since coal mine dust is known to be a heterogeneous mixture, the use of single particle analysis seemed appropriate in this respect. Barths et al. (1987) investigated airborne dust from 11 European coal mines. Correlating LAMMS results with toxicity data, they could confirm the role of quartz as a specific toxic agent for German, but not for French coal samples. Cluster analysis of the element distribution patterns revealed factors which clearly modulate the quartz related toxicity and also factors with their own toxic potency. They seem to be mine dependent, or at least area dependent. The cytotoxicity of different silica dusts was found to be primarily determined by the incidence of silicon-dominated particles. The latter turned out to be a better cytotoxic parameter than the quartz content as determined by bulk analysis. Their results support the idea that some fraction of the quartz is toxicologically ineffective.

Different asbestos types, which are known to promote fibrosis and/or cancer, can be distinguished on the base of their LAMMS spectra (De Waele et al., 1982). LAMMS and SIMS were also applied for the analysis of organic impurities at the surface of asbestos fibers (De Waele et al., 1983; Van Espen et al., 1983). The absorption behaviour of different asbestos varieties for various organics were studied by LAMMS (De Waele et al., 1983b and 1983c) and EELS (Xhoffer et al., 1991). Moreover, LAMMS revealed preferential leaching of elements in e.g. biological liquids. These results are of importance in the sense that, next to fiber geometry, chemical properties and reactivities also determine the carcinogenic effect.

In an attempt to identify Ni-compounds emanating from pollution sources, Musselman et al. (1985) managed to distinguish different (standard) Ni-species on the base of their LAMMS-spectra. They developed a characterization algorithm using LAMMS and SEM. Characterizing different compounds in airborne particles, however, turned out to be less straightforward, which is due to the complexity of the environmental aerosol.

Gondouin and Muller (1986) and Poitevin et al. (1989) used LAMMS to infer the oxidation state of chromium in dust particles formed during stainless steel machining and soldering operations. Their stoichiometric information, which is important from a toxicological point of view, was based on relative cluster ion intensities in the LAMMS spectra. Michaud (1991), who analyzed Cr-containing particles from pigmentation, soldering and plating industries, showed that these ratios are extremely dependent on instrumental fluctuations, so standards should be analyzed on a regular basis. The anthropogenic Cr-particles appeared most of the time in the hexavalent (i.e. the most harmful) oxidation state. It should however be stressed that, in general, obtaining stoichiometric results with LAMMS is by no means straightforward. Cox et al. (1985) used XPS for the investigation of ferrochrome smelter dust particles. They showed that surface-detectable

Cr(VI) can be removed by aqueous leaching and the remaining particle surface residue contains only insoluble Cr_2O_3.

Fly ash is a much investigated type of industrial aerosol. This name covers a variety of particles. They are emitted to the atmosphere by combustors mostly used for the generation of electric power. In 1968, the global fly ash emission to the environment was estimated at 4×10^7 ton (Seinfeld, 1975). Knowledge of the bulk composition of fly ash is often insufficient because of the important internal composition heterogeneity within a particle population. Consequently, the impact and behaviour differs largely from one particle to another and may be extremely complex. The characteristics of fly ash particles furthermore depend on the mineral matter used, the thermal behaviour of the coal in the furnace, melting and decomposition temperatures of the mineral matter and possible chemical reactions and heterogeneous assemblages of the different emission products during their cooling in the atmosphere (Ramsden and Shibaoka, 1982). Several workers have used SEM and/or EPXMA to determine the morphological and chemical characteristics of fly ash particles (Bonafede and Kiss, 1973; Baker et al., 1975; Jan de Zeeuw and Abresch, 1976; Chiu, 1978; Gibbon, 1979; Carpenter et al., 1980; Lichtman and Mroczkowski, 1985). Energy dispersive X-ray analysis in the electron microscope provides semiquantitative element analysis of individual particles (Middleman and Geller, 1976; Small and Zoller, 1977; Fisher et al., 1978; Parungo et al., 1978; Hayes et al., 1978; Capron et al., 1979; Kaufherr and Lichtman, 1984). The main elements present in both the micron and submicron particles are Si, Al, K, Fe, Ti, Mg and S. Ca, P, Na, Cl and Ni are minor constituents (Kaufherr and Lichtman, 1984). Campbell et al. (1978) used ion sputtering in combination of XPS to monitor the concentration and speciation of various elements in fly ash as a function of sputter depth. The concentrations of Ca, Na, C, O and S were found to decrease with depth, whereas the concentrations of matrix elements as Al, Fe and Si increased with depth. Recorded SIMS depth profile studies of coal fly ash particles ($d > 4\ \mu m$) showed a significant surface enrichment of lead (von Rosenstiel et al., 1981). Similar studies (Linton et al., 1975; Linton et al., 1977) indicated strong surface enrichments of Pb and Tl; this implies that coal fly ash may have a more deleterious environmental impact than is apparent solely on the basis of conventional bulk analysis. Cox et al. (1987) investigated particles from a coal-fired power plant with a digital imaging system interfaced to an ion microscope. The setup they used permitted the simultaneous acquisition of spatially resolved mass spectral data for a number of single particles. These authors found substantial differences in the relative concentrations and/or depth profiles of the elements Ba, Pb, Si, Th, Tl and U from particle to particle. Pb, Tl and U were generally concentrated on the particle surfaces. The major part of fly ash particles have a characteristic spherical geometry although irregularly shaped particles are

observed as well (Capron et al., 1979; Xhoffer, 1987). One should differentiate between two fly ash types according the material (oil or coal) used for the operation of a power plant. Differences between oil fly ash and coal flyash were reported by several authors (Xhoffer, 1987; Wagman, 1976; Denoyer et al., 1982; Mamane et al., 1986; Raeymaekers, 1987). Oil fly ash particles vary in morphology from nearly rounded spheres to lacey or spongy lumps, which indicate a long exposure history to heat and oxidants (McCrone and Delly, 1973). These spongy structures easily break down to smaller aggregates. Over 90 % of the mass fraction occurs in the fine fraction. Oil combustion particles contain considerably more sulfur and substantial amounts of V and Ni. Coal fly ash predominantly consists of smooth mineral spheres and contain less cenospheres. Almost 90% of the mass fraction occurs in the coarse fraction. Mamane et al. (1986) have made extensive measurements on suspended particulate material from oil- and coal-fired power plants using a Raman microprobe. They found the existence of V_2O_5 as a principal component in the oil ash particles but not in the coal derived particles. LAMMS of fly ash particles in some occasions leads to the detection of PAH's (Denoyer et al., 1982; Vis et al., 1983) have analyzed fly ash particles with the SPM system of the Free University of Amsterdam. A beam size of 7 by 10 μm was used with a current of 20-40 pA. It was possible to measure trace elements like Se, V, Cr, Ti and Cu, and to obtain concentration profiles for large particles. The analysis was complemented by tube excited X-ray fluorescence for bulk trace element measurements.

PAH's were also detected using LAMMS on soot particles from an experimental oil-shale retort (Mauney and Adams, 1984). SIMS analysis of single oil-soot particles ($d \geq 1.5$ μm) showed that they are characterized by high levels of O, V, C, Na, Ca and K (McHugh and Stevens, 1972). Secondary ion micrographs of these elements provided information about their distributions throughout the particle.

Lang et al. (1988) studied individual dust particles (ranging from 10 to 50 μm) from an office/lab environment using infrared and Raman spectroscopy. Raman spectra were obtained on dust specimens if the infrared spectra did not provide enough information to permit suitable characterization of the sample. Many of the dust particles identified could be linked to a paper product as the source.

1.3.8 Sediments, suspension and estuarine/riverine particles

Suspended particulate matter from estuarine and marine environments is being investigated extensively in order to assess sedimentation processes, the interactions between sediments and the water column, and the physico-chemical reactions that particles undergo. Most of the analytical

techniques used for this study, such as instrumental neutron activation analysis, atomic absorption spectrometry and X-ray diffraction, provide information on the bulk composition or mineralogy of the samples. Alternatively, only few beam techniques for individual analysis of estuarine particles are invoked.

SEM/EDX were successfully applied (Dehairs et al., 1980; Jedwab, 1980; Skei and Melson, 1982; Sundby et al., 1984). These studies had in common that the particles were searched and analyzed manually for their chemical and morphological characteristics. The first results of automated EPXMA of marine suspended particulate matter was reported (Bishop and Biskaye, 1982). They applied this technique to individual particles from the nepheloid layer in the Atlantic Ocean, and classified the analyzed particles on the basis of their Si/Al ratio. A part of the data was also described by Lambert et al. (1984).

Later, various aquatic (estuarine and marine) environments were studied, all by using EPXMA. Suspended matter particles from the Scheldt river estuary (Belgium, the Netherlands) have also been studied with LAMMS (Bernard et al., 1986; Wouters et al., 1988; Bernard et al., 1989).

For all estuarine systems, EPXMA made it possible to evaluate the effect of mixing material from different origin and to separate the mixing process from other processes such as deposition and remobilization. The results on the Ems estuary (in Germany and the Netherlands) elucidated that the mixing with marine material occurs in the fresh water tidal area and that the suspended matter of marine origin is transported upstream the tidal area, across the salt wedge (Bernard et al., 1986). The same approach proved to be equally successful when applied on the sediment fraction of the Elbe estuary (Germany), for which the findings were in agreement with those of the Ems river (Wilken, 1993). For the Garonne and Rhône river (France), no evidence was found for a net flux of marine suspended particulate matter into the estuaries; this is a consequence of the different nature of these estuaries (Eisma et al., 1985; Eisma et al., 1991).

For the Nile river (Egypt), no marine intrusion and thus no mixing process had to be taken into account; still significant relative abundance variations were observed for both the sediment and the suspended particulate matter. Information was gained on the impact of the Aswan Dam: the behaviour of the particles in this area and their further course along the Sohag area downstreams (Araújo et al., 1993).

For the Magela Creek river system (Australia) an advanced approach was achieved by analyzing both the suspension (> 1 μm) and colloidal (1 to 0.1 μm) particles whereas most previous work was concentrated on the larger sized suspended particulate matter (generally > 0.45 μm). The significance of these results lies in the fact that recent studies recognize an increasing importance

of the role of this colloidal fraction for certain aquatic environments (Hart et al., 1991). The inorganic mineral composition proved also to serve as an equally good tracer for the origin of suspended particulate matter of non fluvial estuarine environments. The abundance variations of the particle types correlated with hydrographical/hydrochemical and bulk data, provided information about geochemical and physical processes that influence the levels and distribution patterns of certain particle types throughout the Baltic Sea and the transient area to the North Sea (Bernard et al., 1989). A better insight in the sources and lateral/depth dispersal of suspended matter in Makasar Strait and Flores Sea and around the Sumbawa Island (Indonesia) was satisfactorily accomplished by EPXMA. It was found possible to differentiate between particles of terrestrial volcanic and biogenic origin of the sediment (Eisma et al., 1989; Eisma et al., 1993).

Manual examinations by electron microprobe were found to be very valuable for recovery particle associations, e.g. $BaSO_4$ formation in recently dead siliceous plankton (Bishop, 1988) and distinguishing different structures e.g. for manganese (Middelburg et al., 1989) and species e.g. for pyrite (Luther et al., 1980). The Hamburg SPM group has measured trace elements in particles from river sediments (Grossmann et al., 1985). Using a 2 Mev proton beam of 2.3 by 3.0 micrometer and beam currents of 0.3 to 3 nA, detection limits were about 10 ppm. It was possible to detect Si, S, K, Ca, Ti, V, Cr, Mn, Fe, Ni, Cu, Zn, As, Br, Rb, Sr, Zr, and Pb. Using different absorbers, the SPM analysis can be optimized for a certain range of elements, further increasing the sensitivity for heavier elements.

1.4 Conclusions

Conventional studies of environmental systems are based on bulk sampling procedures in order to determine average concentrations. Such information is very important for environmental control purposes, but sometimes does not provide information about the identities and amounts of pollutants present in the microscopically small regions that constitute environmental interfaces.

Individual particle analysis has been proven extremely valuable as a complement of the bulk methods. Information concerning origin, formation, transport, reactivity, transformation reactions and impact on the environment that would have been very difficult, if not impossible to get with bulk analysis techniques, has been obtained.

Microananalysis techniques have their own specific problems that are often related to the extreme small sizes of the samples:

(1) Quantitative analysis is extremely troublesome because of the uncertainty in defining the precise analytical interaction volume and the difficulties encountered when preparing suitable standards on that level.

(2) In order to get statistically relevant information, huge numbers of particles need to be analyzed. This makes the analyses very time-consuming. Therefore, much effort has been invested in automation and computerization. In this respect, EPXMA is certainly the most advanced.

Moreover, each technique has its own specific constraints, related to its principle (sample-beam interaction, experimental set-up, ...). As a consequence, they can complement each other with respect to lateral resolution, detection limits, detectable elements etc.. Hence, the characterization procedure that uses several single particle analysis techniques (and preferably also a bulk method) will of course give the best results. Each of the above discussed instruments is however very expensive, so interlaboratory cooperation will most of the time be necessary.

1.5 References

Adams F., Van Espen P., Maenhaut W.; Aerosol composition at Chacaltaya, Bolivia, as determined by size-fractionated sampling, *Atmos. Environ.*, 17, 1521, 1983

Allegrini I., Mattogno G.; Analysis of environmental particulate matter by means of photoelectron spectroscopy, *Sci. Tot. Environ.*, 9, 227, 1978

Andreae M.O., Charlson R.J., Bruynseels F., Storms H., Van Grieken R., Maenhaut W.; Internal mixture of sea salt, silicates and excess sulphate in marine aerosols, *Science*, 232, 1620, 1986

Araújo F., Komy Z., Van Put A., Van Grieken R.; Elemental characterization of sediments, water and groundwater in the Nile river Basin (Central Egypt): a preliminairy study, *Sci. Tot. Environ.*, 1993

Artaxo P., C. Orsini. "Emission of aerosol by plants revealed by three receptor models" in *Aerosols: Formation and Reactivity*, Ed. G. Israel, Pergamon Journals Ltd. London, 148, 1986

Artaxo P., Storms H., Bruynseels F., Van Grieken R., Maenhaut W.; Composition and sources of aerosols from the Amazon Basin, *J. Geophys. Res.*, 93, 1605, 1988

Artaxo P., Van Grieken R., Watt F., Jaksic M.; The microanalysis of individual aerosol particles by electron, proton and laser microprobe, *Proc. of the Second World Congress on Particle Technology*, Society of Powder Technology, Tokyo, Japan, 421, 1990

Baker J.E., Evans C.A., Loh A., Natusch D.F.S.; Microscope investigations of coal fly ash particles; *Proc. Annu. Conf., Microbeam Analyt. Soc.* 10, 33A, 1975

Barths G., Schmidtz G, Kaufmann R., Bruch J., Tourmann J.; *Colloque INSERM*, 1987

Beauford W., Barber J., Barringer A.; Release of particles containing metals from vegetation into the atmosphere, *Science*, 195, 571, 1977

Bernard P, Van Grieken R., Eisma D.; Classification of estuarine particles using automated electron microprobe analysis and multivariate techniques, *Environ. Sci. Technol.*, 20, 467, 1986

Bernard P, Van Grieken R., Brügmann L.; Geochemical composition of suspended matter in the Baltic Sea: 1. Results of individual particle characterization by automated electron microprobe, *Mar. Chem.*, 26, 155, 1989

Benninghoven A., Storp S.; Study of silicon-oxygen interaction with statical method of secondary ion mass spectroscopy (SIMS), *Appl. Phys. L.*, 22, 170-171, 1973

Bigg E.K.; Comparison of aerosol at baseline atmospheric monitoring stations; *J. Appl. Met.*, 19, 521, 1980

Bigg E.K., Turvey D.E.; Sources of atmospheric particles over Australia, *Atmos. Environ.*, 12, 1643, 1978

Bird J.R.; "*Ion Beams for Material Analysis*" Ed. Williams, J.S., Academic Press Australia, Marrickville (1989)

Bishop J.K.B.; The barite-opal-organic carbon association in oceanic particulate matter, *Nature*, 332, 341, 1988

Bishop J.K.B., Biskaye P.E.; Chemical characterization of individual particles from the nepheloid layer in the Atlantic Ocean, *Earth and Planet. Sci. Lett.*, 58, 265, 1982

Bodhaine B.A., Deluisi J.J., Harris J.M.; Aerosol measurements at the South Pole, *Tellus*, 38B, 223, 1986

Bodhaine B.A., Murphy M.E.; Calibration of an automatic condensation nuclei counter at the South Pole, *J. Aerosol Sci.*, 11, 305, 1980

Bonafede G., Kiss L.T.; Study of ash deposits from brown coal fired boilers with the aid of scanning and transmission electron microscopy, *Am. Soc. Mech. Engng.*, 73-WA/CD-7, 1973

Boni C., Cereda E., Braga-Marcazzan G.M., De Tomasi V.; Prompt gamma-remission excitation-functions for PIGE analysis of Li, B, F, Mg, Al, Si and P in thin samples, *Nucl. Instrum. Meth. Phys. Res.*, B35, 80, 1988

Brownlee D.E.; Terrestrial and extraterrestrial pollution in the stratosphere, *Microbeam Anal.*, 199, 1980

Bruynseels F., Van Grieken R.; Direct detection of sulphate and nitrate layers on sampled marine aerosols by laser microprobe mass analysis, *Atmos. Environ.*, 19, 1969, 1985

Bruynseels F.; Application of laser microprobe mass analysis in aerosol research, Ph.D. Thesis, University of Antwerp (UIA), Belgium, 1987

Bruynseels F., Artaxo P., Storms H., Van Grieken R., LAMMA study of aerosol samples collected in the Amazon Basin, *Microbeam Anal.*, 356, 1987

Bruynseels F., Storms H., Van Grieken R., Van der Auwera L.; Characterization of North Sea aerosols by individual particle analysis", *Atmos. Environ.* 22, 2593, 1988

Cadle R.D., Grams G.W.; Stratospheric aerosols and their optical properties, *Rev. Geophys. Space Physics* 13, 475, 1975

Campbell J.A., Smith R.D., Davis L.E.; Application of X-ray photoelectron spectroscopy to the study of fly ash, *Appl. Spectrosc.*, 32, 316, 1978

Capron R., Haymann P., Pellerin F.; Preliminary quantitative analysis of combustion products by electron microscopy in environmental monitoring, *C.R. Acad. Sci.*, C 289, 313, 1979

Carpenter R.L., Clark R.D., Su Yin Fong; Fly ash from electrostatic precipitators and characterization of large spheres, *J. Air Pollut. Control Ass.*, 30, 679, 1980

Chiu A.S.; Characterization of submicron fly ash in cyclone boilers, Ph.D. Thesis, Department of Chemical Engeneering, New Hampshire University, Durham, 1978

Conzemius R., Capellen J.; A review of applications to solids of laser ion source in mass spectrometry, *Int. J. Mass Spectrom. Ion Phys.*, 34, 197, 1980

Cotter R.; Laser and mass spectrometry, *Anal. Chem.*, 56, 485A, 1984

Cotter R.; Time of flight mass spectrometry: an increasing role in the life sciences, *Biomed. Environm. Mass Spectrom.*, 18, 513, 1989

Cox III X.B., Linton R.W.; Particle Analysis by X-ray Photoelectron Spectroscopy, in "*Physical and Chemical Characterization of Individual Airborne Particles*", Ed. K.R. Spurny, J. Wiley and Sons, New York, chapter 18, 1986

Cox III X.B., Linton R.W., Butler F.E.; Determination of chromium speciation in environmental particles. Multitechnique study of ferrochrome smelter dust, *Environ. Sci. Technol.*, 19, 345, 1985

Cox III X.B., Bryan S.R., Linton R.W.; Microchemical characterization of trace elemental distributions within individual coal combustion particles using secondary ion mass spectrometry and digital imaging, *Anal. Chem.*, 59, 2018, 1987

Cunningham W., Zoller W.; The chemical composition of remote aerosols, *J. Aerosol Sci.*, 12, 367, 1981

Davis R., Frearson M.; *Mass Spectrometry*; Eds. F.E. Prichard, J. Wiley and Sons, London, Chichester,New York, Brisbane, Signapore, 1987

Dehairs F., Chesselet R., Jedwab J.; Discrete suspended particles of barite and barium cycle in the open ocean, *Earth Planet. Sci. Lett.*, 49, 528, 1980

Delmas R., Clairac B., Cros B., Cachier H., Servant J.; Chemical composition of atmospheric aerosols in an equatorial forest area, *2nd. Int. Symp. on Biosphere-Atmosphere Exchanges*, Mainz FRG, March 16, 1986

Denoyer E., Mauney T., Natusch D.F.S., Adams F.; Laser microprobe mass analysis of coal and oil fly ash particles, *Microbeam Anal.*, 191, 1982

De Waele J., Van Espen P., Vansant E., Adams F.; Study of asbestos by laser microprobe mass analysis, Ed. K.F.J. Heinrich, *Microbeam Anal.*, 371, 1982

De Waele J., Vansant E., Van Espen P., Adams F.; Laser microprobe mass analysis of asbestos fiber surfaces for organic compounds, *Anal. Chem.*, 55, 671, 1983

De Waele J., Vansant E., Adams F.; Laser microprobe mass analysis of N,N-dimethylaniline and catalytic oxidation products adsorbed on asbestos fiber surfaces, *Microchim. Acta* [Wien], 367, 1983b

De Waele J., Verhaert I., Vansant E., Adams F.; Laser microprobe mass analysis (LAMMA) and adsorption study of alifatic alkylammonium ions and alkylamines on asbestos fibre surfaces, *Surf. and Interface Anal.*, 5, 186, 1983c

Duce R.A., Hoffman E.J.; Chemical fractionation at the air/sea interface, *Annu. Rev. Earth Planet. Sci.*, 3, 187, 1976

Eisma D., Bernard P., Boon J., Van Grieken R., Kalf J., Mook W.; Loss of particulate organic matter in estuaries as exemplified by the Ems and the Gironde estuaries, *Mitt. Eol. Palaentol. Inst. Univ. Hamburg*, 58, 1985

Eisma D., Kalf J., Karmini M., Mook W., Van Put A., Bernard P., Van Grieken R.; Dispersal of suspended matter in Makasar Strait and the Flores Basin, *Neth. J. of Sea Res.*, 24, 383, 1989

Eisma D., Bernard P., Cadee G., Ittekkot V., Kalf J., Laane R;, Martin J., Mook W., Van Put A., Schumacher T.; Suspended matter particle size in some West European estuaries, *Neth. J. of Sea Res.*, 28, 193-220, 1991

Eisma D., Van Put A., Van Grieken R.; Distribution and composition of suspended particulate matter around Sumbawa island, Indonesia, *Neth. J. of Sea Res.*, 1993

Etz E. and Rosasco G., Application of a new micro-raman spectrometer to the identification of airborne particulates; *Proc. 5th Int. Conf. Raman Spectrosc.*, Eds. Schmid E., Brandmieller J., Kiefer W., Hans Ferdinand Schulz Verlag Freiburg, Germany, 776, 1976

Etz E., Rosasco G.; Identification of individual microparticles with a new micro-Raman spectrometer, *NBS Spec. Publ.* (US), vol 464, National Bureau of Standards, Gaithersburg, M.D., 343, 1977

Etz E., Blaha J.; in "Characterization of Particles", *Proc. of the Particle Analysis Session of the 13th Int. Conf. of the Microbeam Analysis Society*, Ed. K. Heinrich, Ann Arbor, Michigan, June 22, 153, 1980

Finstad T.G., Chu W.K.; Ion Beam Techniques, in "*Analytical Techniques for Thin Films*", Eds. Tu, K.N., Rosemberg, R., Academic Press, Boston, 1988

Fisher G.L., Prentice B.A., Silberman D., Ondov J.M.; Physical and morphological studies of size-classified coal fly ash, *Environ. Sci. Technol.*, 12, 447, 1978

Fletcher R., Currie L.; Utility of the laser microprobe for source identification of carbonaceous particulate material, Ed. P.E. Russell, *Microbeam Anal.*, 303, 1989

Fruchter J.S.,Robertson D.E., Evans J.C., Olsen K.B., Lepel E.A., Laul J.C., Abel K.H., Sanders R.W., Jackson P.O., Wagman M.S., Perkins R.W., Van Tuyl H.H., Beauchamp R.H., Shade J.W., Daniel J.L., Erikson R.L., Sehmel G.A., Lee R.N., Robinson A.V., Mass O.R., Briant J.K., Cannon W.C.; Mount St. Helen ash from the 18 May 1980 eruption: Chemical, physical, mineralogical and biological properties, *Science*, 209, 1116, 1980

Gibbon D.L.; Microcharacterization of fly ash and analogs: the role of SEM and TEM, *Scanning Electron Microscopy*/1979/I, 501, SEM Inc., AMF O'Hare, Illinois, 1979

Goldstein J.I., Yakowitz H.; *Practical Scanning Electron Microscopy*, Plenum Press, New York, 1987

Gonduin S., Muller J.; In situ identification of chromium oxidation states by LAMMA, *Proc. of the 3rd International Laser Microprobe Mass Spectrometry Workshop*, Belgium, Antwerp 26-27 August, 1986

Gooding J.L.; Clanton, U.S.; Gabel E.M., Warren J.L.; El Chichón volcanic ash in the stratoshere: Particle abundances and size distributions after the 1982 eruption, *Geophys. Res. Lett.* 10, 1033, 1983

Gordon R., Trivedi N., Singh B.; Characterization of aerosol organics by diffuse reflectance fourier transform infrared spectroscopy. *Environ. Sci. and Technol.*, 22, 672, 1988

Grasserbauer M.; The Present State of Local Analysis: Analysis of Individual Small Particles, *Microchim. Acta* (Wien), 329, 1978

Grasserbauer M.; Micro and surface analysis for environmental studies, *Microchim. Acta* (Wien), III, 415, 1983

Grossmann, D., Kersten, M., Niecke, M., Puskeppel, A.; Determination of trace elements in membrane filter samples of suspended matter by the Hamburg proton microprobe, *SCOPE/UNEP* Sonderband Heft 58, 619, 1985

Harrington P., Street T., Voorhees K., Radicati di Brozolo F., Odom R.W.; Rule-building expert system for classification of mass spectra, *Anal. Chem.*, 61, 715, 1989

Harrison R.H., Sturges W.T.; Fysicochemical speciation and transformation reactions of particulate nitrogen and sulphur compounds, *Atmos. Environ.*, 18, 1829, 1984

Hart B., Douglas G., Beckett R., Van Put A., Van Grieken R.; Characterization of SPM in the Magela Creek system-northern Australia, submitted to *Environ. Sci. and Technol.*, 1991

Hayes T.L., Pawley J.B., Fisher G.L.; Effect of chemical variability of individual fly ash particles on cell exposure, *Scanning Electron Microscopy*/1978/I, 239, SEM Inc., AMF O'Hare, Illinois, 1978

Holt D., Muir M.D., Grant P.R., Boswarva I.M.; *Quantitative Scanning Electron Microscopy*, Academic Press, London, 1974

Ito T.; Study of background aerosols in the Antartic troposphere, *J. Atm. Chemistry*, 3, 69, 1985

Jan de Zeeuw H., Abresch R.V.; Cenospheres from dry fly ash; *Proc. 4th Int. Ash Utilization Symp.*, St. Louis, ERDA, Morgantown, WV, 386, 1976

Jedwab J.; Rare anthropogenic and natural particles suspended in deep ocean waters, *Earth Planet. Sci. Lett.*, 49, 551, 1980

Johansson S.A.E., Campbell J.L.; *PIXE - A Novel Technique for Elemental Analysis*, John Wiley, New York, 1988

Kaufherr N., Lichtman D.; Comparison of micron and submicron fly ash particles using scanning electron microscopy and X-ray elemental analysis, *Environ. Sci. Technol.*, 18, 544, 1984

Kaufmann R., Richmann P., Tourmann J., Schnatz H.; LAMMS in biomedical research: Achievements, shortcomings, promises; *Microbeam anal.*, 35, 1989

Keyser T.R., Natusch D.F.S., Evans Jr. C.A., Linton R.W.; Characterizing the surfaces of environmental particles, *Environ. Sci. and Tech.* 12, 768, 1978

Klaus N.; Aerosol analysis bu secondary ion mass spectrometry, in "*Physical and Chemical Characterization of Individual Particles*", Eds. K.R. Spurney, J. Wiley and Sons, New York, 1986

Kolaitis L.; Applications of laser ionization/desorption in mass spectrometry, Ph.D. Thesis, University of Antwerp (UIA), Belgium, 1988

Kolaitis L., Bruynseels F., Van Grieken R., Andreae M.; Determination of methanesulphonic acid and non-sea-salt sulfate in single marine aerosol particles, *Env. Sci. Technol.*, 23, 236, 1989

Lambert C.E., Bishop J.K.B., Biscaye P.E., Chesselet R.; Particulate aluminium, iron and manganese chemistry in deep Atlantic Boundary layer, *Earth and Planet. Sci. Lett.*, 70, 237, 1984

Lang P., Katon J., Bonanno A.; Identification of dust particles by molecular microscopy, *App. Spectrosc.*, 42, 313, 1988

Lee R.J., Walker J.S., McCarthy J.J.; Evolution of automated electron microscopy, *Microbeam Anal.*, 485, 1986

Lichtman D., Mroczkowski S.; Scanning electron microscopy and energy-dispersive X-ray spectroscopy analysis of submicrometer coal fly ash particles, *Environ. Sci. Technol.*, 19, 274, 1985

Linton R.W., Loh A., Natusch D., Williams P.; Surface predominance of trace elements in airborne particles, *Science*, 191, 853, 1975

Linton R.W., Williams P., Evans C.A., Natusch D.F.S.; Characterization of surface predominance of toxic elements in airborne particles by ion microprobe mass spectrometry and Auger electron spectrometry, *Anal. Chem.*, 49, 1514, 1977

Lodding A.; Secondary ion mass spectrometry, in "*Inorganic Mass Spectrometry*" Eds. Adams F., Gijbels R. and Van Grieken R., J. Wiley and Sons, New York, 1988

Lovelock J.E., R.J. Maggs, R.A. Rasmussen; Atmospheric dimethyl sulfide and the natural sulphur cycle, *Nature*, 237, 452, 1972

Luther G., Meyerson A., Krajewski J., Heres R.; Metal sulfides in estuarine sediments, *J. Sedim. Petrol.*, 50, 1117, 1980

Mackinnon I.D.R., Gooding J.L., McKay D.S., Clanton U.S.; The El Chichón stratospheric cloud: solid particulates and settling rates, *J. Volcanol. Geotherm. Res.*, 23, 125, 1984

Maenhaut W., Raemdonck H., Selen A., Van Grieken R., Winchester J.W.; Characterization of atmospheric aerosol over the Eastern Equatorial Pacific, *J. Geophys. Res.*, 88, 5353, 1983

Maenhaut W., Akilimali K.; Study of atmospheric aerosol composition in equatorial Africa using PIXE as analytical technique, *Nucl. Instrum. Methods*, B 22, 254, 1987

Mamane Y., Miller J.L., Dzubay T.G.; Characterization of individual fly ash particles emitted from coal- and oil-fired power plants, *Atmos. Environ.* 20, 2125, 1986

Marien J., De Pauw E.; On the identification of sulphur oxidation state in inorganic sodium sulphoxy salts by laser mass analysis and secondary ion mass spectrometry, *Anal. Chem.*, 57, 361, 1985

Massart D.L., L. Kaufman; *The Interpretation of Analytical Data by the Use of Cluster Analysis*, Wiley and Sons: New York, 1983

Mauney T., Adams F.; Laser microprobe mass spectrometry of environmental soot particles, *Sci. Tot. Environ.*, 36, 215, 1984

McCrone W.C., Delly J.G.; Eds., The Particle Atlas, Edition two: An encyclopedia for small particle identification, Vol III, *The Electron Microscope Atlas*; Ann Arbor Sci. Publishers Inc., Michigan, 1973

McHugh J., Stevens F.; Elemental analysis of single micrometersize airborne particulates by ion microprobe mass spectrometry, *Anal. Chem.*, 44, 2187, 1972

Michaud D.; Personal communications, 1991

Middelburg J., De Lange G., Van der Sloot H., Van Emburg P., Sophiah S.; Particulate manganese and iron framboids in Vau Bay, Halmahera (Eastern Indonesia), *Mar. Chem.*, 23, 353, 1989

Middleman L.M., Geller J.D.; Trace element analysis using X-ray excitation with an energy dispersive spectrometer on scanning electron microscope, *Scanning Electron Microscopy*/1976/, 171, IITRI, Chicago, Illinois, 1976

Morrison G., Slodzian, G.; The ion microscope opens new vistas in many fields of science by its ability to provide spatially resolved mass analysis of solid surfaces, *Anal. Chem.*, 47, 932A, 1975

Musselman I., Linton R., Simons D.; The use of laser microprobe mass analysis for nickel speciation in individual particles of micrometer size, *Microbeam Anal.*, 337, 1985

Nemeruyk G.E.; Migration of salts into the atmosphere during transpiration, *Sov. Plant Physiol.*, Engl. Transl., 17, 560, 1970

Newbury D.E.; Secondary ion mass spectrometry for the analysis of single particles; in "*Characterization of particles*", NBS special publication 533, Proc. of the Particle Analysis Session of the 13th Annual Conference of the Microbeam Analysis Society held at Ann Arbor, Michigan, June 22, 1978, Ed. K.F.J. Heinrich, 139, 1980

Otten P., Bruynseels F., Van Grieken R.; Nitric acid interaction with marine aerosols sampled by impaction, *Bull. Soc. Chim. Belg.*, 95, 447, 1986

PARCOM, Secretariat of the Paris Commission: Report on land-based inputs of contaminants to waters of the Paris Convention in 1987, *PARCOM 11/6/1-E*, 1989

Parungo F., Ackerman E., Proulx H., Pueschel R.; Nucleation properties of fly ash in coal-fired-power-plant plume, *Atmos. Environ.* 12, 929, 1978

Parungo F., Bodhaine B., Bortnak J.; Seasonal variation in Antarctic aerosol, *J. Aerosol Sci.*, 12, 491, 1981

Patterson E.M., Kiang C.S., Delany A.C., Artburg A.F., Leslie A.C.D., Huebert B.J.; Global measurements of aerosols in remote continental and marine regions: Concentrations, size distributions and optical properties, *J. Geophys. Res.*, 8, 7361, 1980

Poitevin E., Muller J., Klein F., Dechelette O.; Application de la détermination des dégres d'oxydation du chrome à l'hygiène industrielle par microsonde à impact laser, *Analysis*, 17, 47, 1989

Post J.E., Buseck P.R.; Characterization of individual particles in the Phoenix urban aerosol using electron-beam instruments, *Environ. Sci. Technol.*, 18, 35, 1985

Powel C.J.; Applications of Auger electron spectroscopy and X-ray photoelectron spectroscopy to the characterization of pollutant particles; National Bureau of Standards Special Publications 533; *Special Session on Particle Analysis, 13th Annual of the Microbeam Ananlysis Society*, Ann. Arbor, MI, June 22, 131-137, 1978

Powell C.J.; in "*Characterization of Particles*", Proc. of the Particle Analysis Session of the 13th Int. Conf. of Microbeam Analysis Society, Ann Arbor, Michigan, June 22, Ed. K. Heinrich, 131, 1980

Prèndez M., Ortiz J.; Elemental composition of airborne particulate matter from Santiago City, Chile, *J. Air Pollut. Control Ass.*, 34, 54, 1984

Purcell F., Etz E.; A new spectrograph with a multichannel optical detector for the Raman characterization of microparticles, *Microbeam Anal.*, 17, 301, 1982

STWG: Scientific and Technological Working Group of the Department of the Environment of the European Community, "Quality status of the North Sea", *Second International Conference on the Protection of the North Sea*, London, September, 1987

Raeymaekers B.; Characterization of particles by automated electron probe microanalysis, Ph.D. Thesis, University of Antwerp (UIA), Belgium, 1986

Rampino M.R., Self S.; The atmospheric effects of El Chichón, *Sci. Am.*, 250; 48, 1984

Ramsden A.R., Shibaoka M.; Characterization and analysis of individual fly ash particles from coal-fired power stations by combination of optical microscopy, electron microscopy and quantitative electron microbrobe analysis, *Atmos. Environ.* 16, 2191, 1982

Reed S.J.B.; *Electron Microprobe Analysis*, Cambridge University Press, Cambridge, 1975

Rojas C.M., P. Artaxo, Van Grieken R.; Aerosols in Santiago de Chile: A study using receptor modelling with X-ray fluorescence and single particle analysis, *Atmos. Environ.*, 2, 227, 1990

Seinfeld J.H.; *Air Pollution: Physical and Chemical Fundamentals*, McGraw-Hill, New York, 1975

Shaw G.E.; X-ray spectrometry of polar aerosols; *Atmos. Environ.*, 17, 329, 1983

Sheridan P.J., Musselman I.H.; Characterization of aircraft-collected particles present in the Arctic aerosol, Alaskan Arctic Spring 1983, *Atmos. Environ.*, 19, 2159, 1985

Skei J.M., Melson S.; Seasonal and vertical variations in the chemical composition of suspended particulate matter in an oxygen-deficient fjord, *Est. Coast. Shelf Sci.*, 14, 61, 1982

Small J.A., Zoller W.H.; Single-particle analysis of ash from the Dickerson coal-fired power plant, *Natl. Bur. Stand. Monogr.* 464, 651, 1977

Small G., Kroutil R., Ditillo J., Loerop W.; Detection of atmospheric pollutants by direct analysis of passive Fourier transform interferograms, *Anal. Chem.* 60, 264, 1988

Storms H.; Quantification of automated electron probe X-ray analysis and application in aerosol research; Ph.D. Thesis, University of Antwerp (UIA), 233, 1988

Sundby B.N., Silverberg N., Chesselet R.; Pathways of manganese in an open estuarine system, *Geochim. Cosmochim. Acta*, 45; 293, 1984

Surkyn P., De Waele J., Adams F.; Laser microprobe mass analysis for source identification of air particulate matter, *Int. J. Environ. Anal. Chem.*, 13, 257, 1983

Van Borm W., Adams F., Maenhaut W.; Characterization of individual particles in the Antwerp aerosol, *Atmos. Environ.*, 23, 1139, 1989

Van Borm W., Wouters L., Van Grieken R., Adams F.; Lead particles in an urban atmosphere: An individual particle approach, *Sci. Tot. Environ.*, 90, 55, 1990

Van Espen P., De Waele J., Vansant E., Adams F.; Study of asbestos using SIMS and LAMMA, *Int. J. of Mass Spectrom. Ion Phys.*, 46, 515, 1983

Van Vaeck L., Gijbels R.; Overview of laser microprobe mass spectrometry Techniques, *Microbeam Anal.*, XVII-XXV, 35, 1989

Verbueken A.H., Bruynseels F.J., Van Grieken R.E.; Laser microprobe mass analysis: a review of applications in the life sciences, *Biomed. Mass Spectrom.*, 12, 438, 1985

Vis R.D.; *The Proton Microprobe: Applications in the Biomedical Field*, CRC Press, Chemical Rubber Company, Boca Raton, 1985

Vis, R.D., Bos, A.J.J., Valkovic, V., Verheul, H.; The analysis of fly ash particles with a proton microbeam, *IEEE Trans. Nuclear Sci.*, Vol. NS-30, 2, 1236, 1983

von Rosenstiel A.P., Gay A.J., Van Duin P.J.; Mikromorphologische und Microchemische Untersuchungen von Flugasche, *Beitr. Elektronenmikroskop. Direktabb. Oberfl.*, 14, 153, 1981

Wagman J.; Chemical composition of atmospheric aerosol pollutants by high resolution X-ray fluorescence spectrometry, *Colloid and Interface Sci.*, vol II, Aerosols, Emulsions and Surfactants, Academic Press Inc., New York - San Francisco - London, 1976

Watt F., Grime G.W.; *Principles and Applications of High-energy Ion Microbeans*, Adam Hilger, Bristol, 1987

Wightman J.P.; XPS analysis of Mount St. Helens ash, *Colloids and Surfaces*, 4, 401, 1982

Wilken J.; Submitted to *Sci. Tot. Environ.*, 1993

Wouters L.; Laser microprobe mass analysis of environmental particles, Ph.D. Thesis, University of Antwerp, 1991

Wouters L., Bernard P., Van Grieken R.; Characterization of individual estuarine and marine particles by LAMMA and EPXMA, *Intern. J. Environ. Anal. Chem.*, 34, 17, 1988

Wouters L., Artaxo P., Van Grieken R., LAMMA of individual Antarctic aerosol particles, *Intern. J. Environm. Anal. Chem.*, 38, 427, 1990

Xhoffer C.; Electronenprobe microanalyse van vliegas en partikels uit het marine milieu, Master of Science Thesis, University of Antwerp, 1987

Xhoffer C., Berghmans P., Muir I.; Jacob W., Van Grieken R., Adams F.; A Method for the characterization of surface modified asbestos fibres by electron energy loss spectroscopy, *J. Microsc.*, 162, Pt 1, 179, 1991T

CHAPTER 2

Chemical characterization and source apportionment of individual aerosol particles over the North Sea and the English Channel using multivariate techniques.

2.1 Introduction

Since the North Sea is surrounded by the Western and Northern parts of the European continent and by Great Britain, it undergoes strong influences of industrial, agricultural and domestic activities. On a long term, accumulation into the North Sea could change the chemical environment. Therefore attempts are made to estimate the impact of the surrounding anthropogenic activities on the North Sea. The man-made pollutants can reach the North Sea by several pathways including river transport, direct discharges by pipelines, dumping activities and atmospheric transport. The North Sea aerosol is a mixture of many components, some derived from the sea itself and some having descended from aloft.

Because of internal heterogeneity of the aerosol samples (i.e. the chemical diversity of the particles as a consequence of their different production mechanisms), individual particle analysis can advantageously be applied for the source identification of various atmospheric pollution processes. The relative percentage abundance of the specific particle types can be a measure for the source strength. Besides source apportionment, microananalysis can also be useful for the investigation of the behavior of particles during transport (e.g. gas-to-particle conversion, coagulation processes, etc.). A reduced sampling time and the small amount of material needed for individual microananalysis can be advantages in the study of different dynamic processes.

2.2 Samples and sample preparation

A total of 51 aerosol samples were collected over the North Sea and English Channel during various cruises in a time range of 4 years (1984-1987) aboard the R/V "BELGICA". Atmospheric aerosols were sampled on 47 mm diameter Nuclepore filters with a pore-size of 0.4 μm. The filtration units are provided with a hat-type inlet to avoid the collection of large droplets and rain. The whole is mounted in the mast on the foredeck of the ship, 6 m above deck, 11 m above the sea surface and facing 0.5 m upwind from the mast itself. When the relative wind direction to the ship is unfavorable, or not within +45 to -45 degrees, the power supply of the pump is cut off in order to avoid contamination by the vessel. Figure 2.1 shows different tracks for the various cruises.

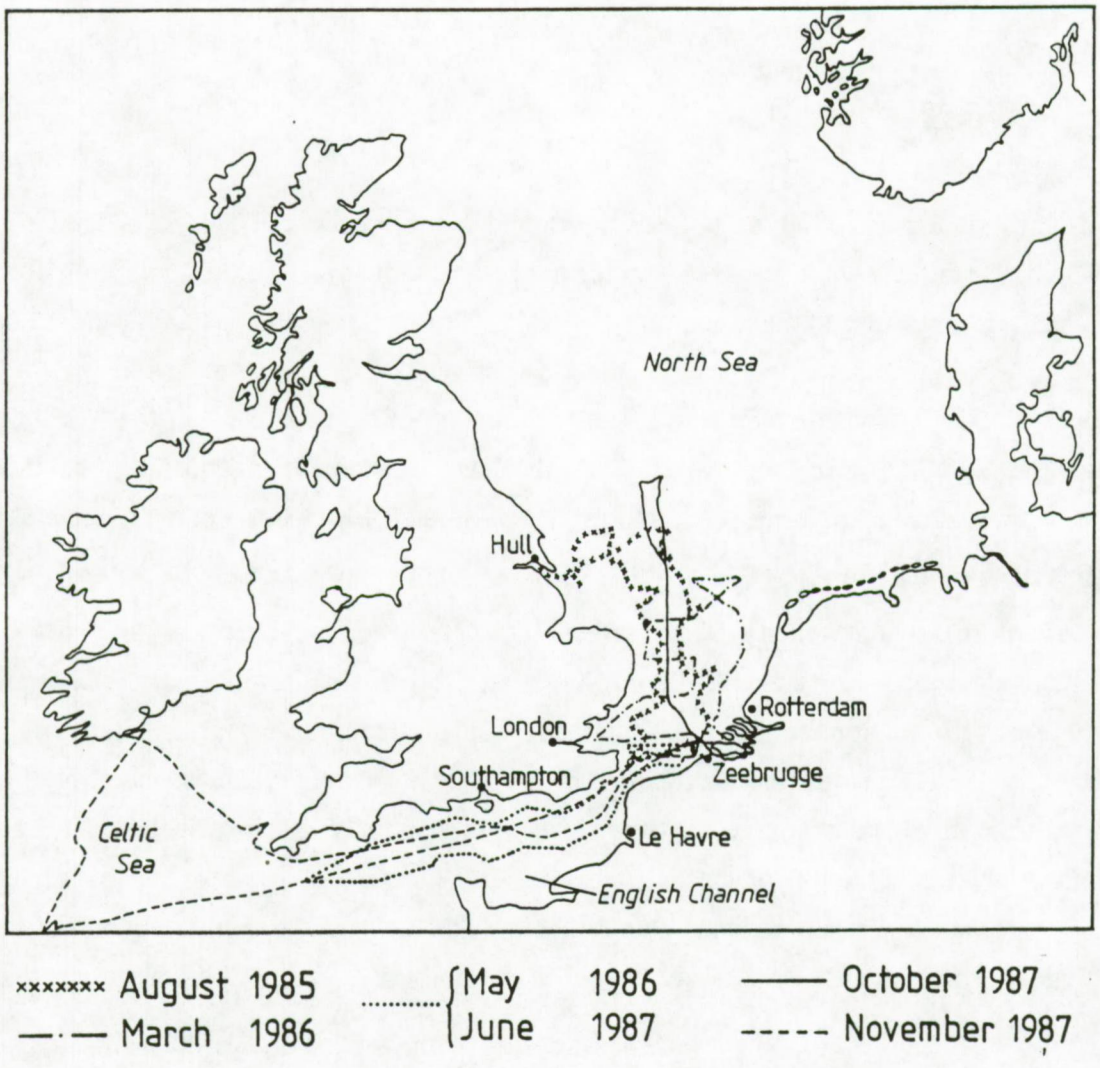

Figure 2.1: Different sampling routes on the North Sea, English Channel and Celtic Sea.

Comparison of the particle sizes for samples simultaneously collected with and without the hat-type inlet, showed no differences in size range below 15 μm (Otten, 1986). Depending on weather conditions and sampling area, the sampling time was 4 - 8 hours in order to collect 5 - 10 m^3 of air. For sampling sites near coastal regions, smaller sampling volumes are needed compared to "off-shore" locations. On the contrary, higher sampling volumes are necessary during or after rain events because of reduced particle number concentration in the air by "rain-out" effects. To reduce chemical changes as well as compositional and morphological transformations of the atmospheric aerosol, each filter was immediately put between Petri-dishes and stored in a refrigerator. A part of the Nuclepore filter was mounted on a plastic ring that fits into the electron microprobe sample holder. All samples were coated with a thin carbon layer of approximately 40 nm to improve electrical conductivity.

2.3 Methodology

For each aerosol sample, about 500 particles in a size range from 0.2 μm to 15 μm were automatically analyzed with a JEOL JXA-733 Superprobe. X-ray spectra were accumulated for 15 seconds with a beam current of 1 nA and an acceleration voltage of 20 kV. This whole operation takes less than 3 hours per sample and yields a huge data set. To reduce the data, two hierarchical and one non-hierarchical cluster analysis were applied for each sampling campaign (Bernard et al., 1986). First a hierarchical cluster analysis performed on the elemental composition data of 500 particles resulted in an average composition data-set. For this, every particle i is presented in a N-dimensional space as an object vector with coordinates according its N-elemental composition. Here N is the number of variables and equals the number of different elements detected in one sample. The method starts from m objects (m = 500 particles) that are to be classified, and at each step the two most similar objects (particles) or already formed clusters are merged into a single cluster. The similarity between two pair of objects was derived from the Euclidian distance coefficient between the objects. The Ward's method (error sum of squares method) was used for the calculation of the distances between newly formed clusters and the remaining objects and/or clusters. So, the more close two objects or clusters are, the more similar they are. A second hierarchical clustering was performed on the average composition data of the samples and resulted in a set of training vectors (centroids) that are representative for that sampling campaign. Finally, a nearest centroid sorting (non-hierarchical cluster analysis) is used to classify all particles from one campaign according their distance from the centroids of the clusters. The method of Forgy (1965) minimizes the sum of squares of the distances to the

centroids for a fixed number of clusters. This procedure results in an average composition data-set for each North Sea sample according the centroids of the corresponding campaign.

The whole particle classification procedure involves thus a series of cluster analysis and is followed by a principal component analysis (PCA) (Figure 2.2).

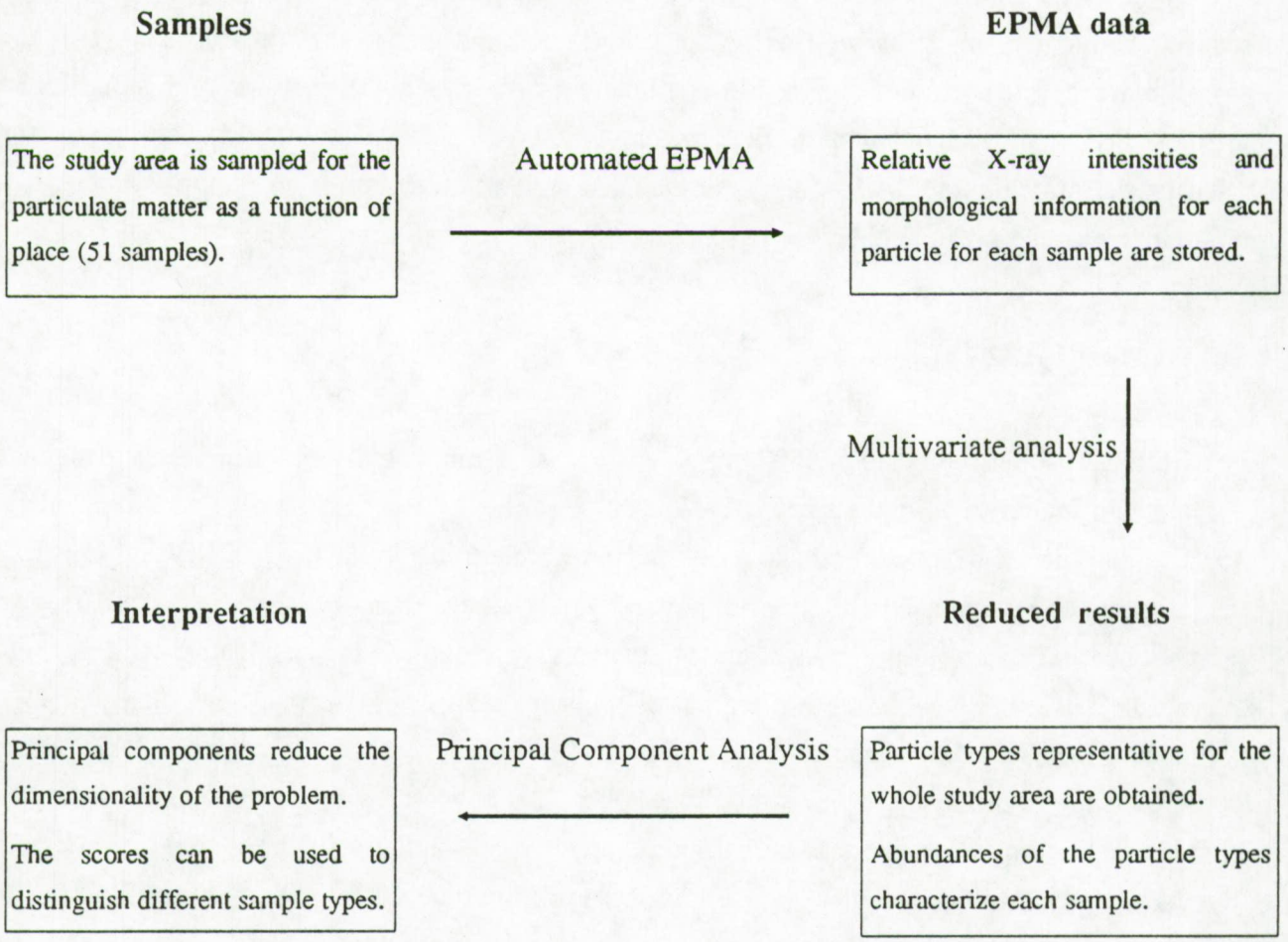

Figure 2.2: Schematic representation of the particle classification procedure.

The purpose of the PCA method is to represent the variations present in the data in such a way that, without losing significant information, the dimensionality is reduced. To achieve this, new variables (components) are constructed, according to a linear combination of the original variables, in such a way that the newly formed principal components are uncorrelated and that they are constructed with decreasing degree of importance. The principal components obtained in this way represent the linear independent variance present in the data of original variables. By

studying the first principal components, the most important sources for the variance in the data are examined. General information about the PCA technique can be found elsewhere (Massart and Kaufman, 1983). Several papers discuss expert systems to sort out individual particle data (Bernard et al., 1986; Shattuck et al., 1985; Hopke, 1985; Saucy et al., 1987; Kim et al., 1987).

The accuracy for the X-ray measurements is close to 1% for abundant elements. The reliability (2 σ values) of the relative abundances of the particle types can be calculated from binomial statistics and is between 2 and 5 % absolute when 500 particles are measured. It has been shown (Van Borm and Adams, 1988) that the variability on the composition of the clusters is almost entirely due to the variation in the particle's composition and is therefore a reliable measure for the heterogeneity of the clusters. The accuracy of particle sizing depends mainly on 2 different factors nl.: (a) threshold setting of the backscattered image signal and (b) the magnification used. Accuracies within 20 % are obtained (Raeymaekers, 1987). The reproducibility for particle sizing using the backscattered electron image is within 6% for the mean diameter.

2.4 Results and discussion

Conventional X-ray microananalysis makes it possible to detect elements from $Z \geq 11$. The measured X-ray output-data consists of relative peak intensities obtained by a Fast Filter Algorithm (FFA), nl. a symmetrical convolution function by the Hardeman transformation (Op de Beeck and Hoste, 1975). The relative % X-ray intensity expresses the ratio of the net X-ray intensity of that element to the total net X-ray intensities collected from that particle. This information is important for chemical intercomparison of particles and can thus be used for the assignment of particles to various particle types. The hierarchical clustering procedure applied to the elemental composition of more than 25,000 particles collected from different parts over the North Sea, the English Channel and the Celtic Sea, resulted in the identification of 9 major relevant particle types. Some low abundance particle types were encountered; although their abundance cannot be determined with high accuracy, their occurrence in the aerosol can be important with regard to the deposition and source apportionment of some specific trace elements. The characteristics of these minor particle types will be discussed separately. Table 2.1 gives an overview of the 9 major particle types with the range of the average composition of the groups for each sampling campaign. This data gives an idea on the criteria by which a particle was assigned to a specific particle type by hierarchical cluster analysis. Note that the relative X-ray intensity of Na in NaCl is much lower than that of Cl. Indeed, Na has much lower sensitivity due to physical effects and because the absorption effects of the X-ray signal by the detector window are more

important for Na than for Cl. Typical relative % X-ray ratio's of $1/12 \leq Na/Cl \leq 1/8$ are observed.

Relative abundances or particle number concentrations (expressed in percent) of each particle type for every individual sample are given in Table 2.2. The standard deviations on the relative abundances are given by binomial statistics. For the individual EPXMA-measurements, where a total of 500 particles were analyzed, the standard deviations are between 1-5 % on a 95 % confidence interval.

Table 2.1: Range for the particle identification bases on the mean percent abundance for each cluster group

Particle type	Criterium: based on relative X-ray intensities		
Seasalt	Cl > 75%	7% < Na < 10%	
Aged seasalt	24% < S < 44%	38% < Cl < 60%	
Sulphur-rich	S > 71%		
Calcium sulphate	23% < Ca < 45%	46% < S < 60%	
Calcium-rich	12% < Ca < 90%	5% < P < 58%	S < 16%
Aluminosilicates	17% < Al < 30%	50% < Si < 62%	4% < Fe < 8%
Quartz	88% < Si < 91%		
Titanium-rich	72% < Ti < 82%		
Iron-rich	72% < Fe < 91%		

The number concentration of particles present in a m^3 of marine air can be derived from the number of particles analyzed and multiplying these with the ratio of the filter area to the analyzed area. Table 2.3 tabulates the range of number concentrations of particles between 0.2 and 15 μm above the North Sea calculated for the 51 samples analyzed. Accuracies were estimated to be about 10 % as based on uncertainties in analyzed filter area and sampled air volume. The findings of these data are in good agreement with aircraft measurements performed over the North Sea at sea level (Rojas et al., 1989). There is clearly a tendency of increasing particle number concentration as the sampled air masses originate from over the continent.

Table 2.2: Relative percent abundances of nine particle types for 51 North Sea samples

Date	Seasalt	Aged ss	S-rich	CaSO4	Ca-rich	Al-silic	Si-rich	Ti	Fe
	0	2	19	0	20	47	4	0	8
Dec 84	63	10	4	0	9	3	0	0	10
	33	7	7	0	7	36	4	0	5
	0	0	35	0	15	12	2	0	36
	77	0	2	11	0	6	4	0	1
	26	0	3	9	1	50	5	1	6
Aug 85	8	0	2	8	0	71	8	0	3
	0	0	5	5	0	74	7	1	7
	0	0	33	21	0	6	9	1	30
	0	0	11	48	2	14	8	0	18
	0	0	61	0	0	18	10	0	12
	0	0	32	4	0	42	11	0	11
Mar 86	0	0	67	3	0	14	5	0	11
	0	0	61	3	0	21	8	0	7
	1	0	24	12	0	27	8	0	29
	18	0	53	5	10	5	5	1	5
	20	20	35	3	10	6	3	0	3
	60	27	0	3	2	7	0	0	0
	52	40	0	2	5	1	1	0	0
	68	17	3	2	9	0	0	0	0
	84	8	4	1	3	0	0	0	0
	91	6	2	0	1	0	0	0	0
May 86	77	4	4	5	7	2	2	0	1
	94	5	0	0	1	0	0	0	0
	91	9	0	0	1	0	0	0	0
	83	14	0	0	2	1	1	0	0
	90	4	0	2	2	2	1	0	0
	77	12	1	2	5	3	0	0	0
	56	26	7	4	8	0	0	0	1
	11	11	32	18	7	18	2	0	1
	2	0	38	9	1	32	5	5	8
	0	0	13	82	0	4	1	0	0
	0	0	69	17	0	6	2	2	4
	0	0	12	5	0	59	21	1	3
	0	0	19	72	0	4	4	0	0
Jun 87	0	0	2	94	0	2	0	0	1
	1	0	33	50	0	9	7	0	1
	0	0	21	68	0	3	7	0	1
	0	0	4	84	0	10	2	0	0
	0	0	85	6	0	3	6	0	0
	0	0	32	13	0	36	17	0	2
	3	2	21	37	0	30	0	0	7
Oct 87	2	36	8	8	0	46	0	0	1
	1	42	6	3	0	47	0	0	1
	1	4	41	14	0	39	0	0	0
	0	1	43	17	0	24	0	4	10
	0	1	38	9	0	11	0	37	4
Nov 87	1	0	60	19	0	8	0	9	3
	0	0	50	13	0	24	0	8	5
	0	0	56	8	0	6	0	27	2
	0	0	35	20	0	22	0	19	4
<diam> (μm)	0.8	0.7	0.7	0.8	0.8	1.3	1.3	1.0	0.8

Table 2.3: Particle number concentrations (m^{-3}) observed for three types of air masses

Type of air masses	Range	Mean
Marine	$(7.9 \pm 0.2)\ 10^3$ to $(6.9 \pm 0.7)\ 10^4$	$(3.9 \pm 0.4)\ 10^4$
Mixed	$(2.9 \pm 0.3)\ 10^4$ to $(4.7 \pm 0.7)\ 10^5$	$(2.5 \pm 0.5)\ 10^5$
Continental	$(8.7 \pm 0.9)\ 10^5$ to $(2.9 \pm 0.6)\ 10^6$	$(1.9 \pm 0.7)\ 10^6$

Knowing the total number concentrations of aerosol particles above the North Sea, the % abundance of each particle type, the assumed density for each particle class, and the mean equivalent spherical diameter of each particle belonging to that particle class, one can calculate the mass concentrations for each particle type. However, the accuracy for mass concentrations is worse than 60 % and is highly dependent on the accuracy for the diameter determination. The nature, source and relative abundance variations for each particle type will subsequently be discussed in more detail.

2.4.1 Different Particle Types

2.4.1.1 Sea salt particles.

A particle type is defined as sea salt (ss) when the average content of Cl exceeds 75 % in relative X-ray intensity. No other element, except Na, is of any significance. It is postulated that the total contribution of freshly generated NaCl present in the marine atmosphere is attributed to a marine source. The main process for the generation of fresh seasalt into the atmosphere is the breaking of waves. This process is more effective as the wind speed increases (Blanchard, 1983).

Very large variations in number concentrations for ss aerosols are found ranging from 0 up to 94 % of the total number fraction. High seasalt abundances were found in the August campaign of 1985 when samples were taken under stormy SW winds: whitecap formation and sea spray induced by wind action, are predominantly responsible for the ejection of ss into the atmosphere. The anthropogenic particle fraction is not necessarily low but is totally suppressed by the domination of ss. Contrarily, for the cruise of May 1986, the air mass trajectory went through the Channel, via the South Coast of England until the influence of the Atlantic Ocean was clearly observed. Nearing more westerly regions is reflected by an increase in ss concentrations. Back

trajectories of the sampled air evolved from far over the Atlantic Ocean without continental interferences. No anthropogenically derived particulate matter was detected.

2.4.1.2 Transformed or aged seasalt particles.

This particle type is rich in S and Cl. Also mixtures of $NaNO_3$, Na_2SO_4 and NaCl are possible (Bruynseels et al., 1988). These S- and Cl-rich particles are identified as aged seasalt (aged ss). They are formed by the conversion of NaCl into Na_2SO_4 by SO_2, implying the release of HCl in the marine atmosphere. These results are consistent with the findings of other authors (Hitchcock et al., 1980; Clegg and Brimblecombe, 1985).

The contribution of S enrichment in seasalt aerosols is more pronounced in the samples for which an important anthropogenic influence on the marine atmosphere is expected. The mixing of air masses is always observed on passing from continental conditions toward more marine ones or vice versa. This is clearly observed for the campaign of May 1986. The corresponding back trajectory (Figure 2.3) shows originally marine air travelling over the Southern part of England.

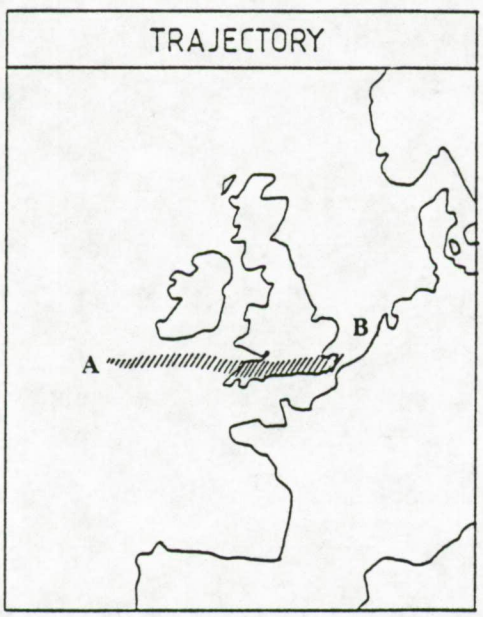

Figure 2.3: Air mass back trajectory for aerosols collected during the May 1986 campaign. The shaded area corresponds to ca. 36-h back trajectories calculated for a height of 10 m above the Nort Sea. The air masses have traveled from point A toward B.

2.4.1.3 Sulfur-rich particles.

In general, the S-concentration is greater than 70 % for this particle type, and no associations with Ca are present. Studies on particulate S present in urban sites showed that numerous secondary reactions can take place (Harrison and Sturges, 1984; Van Borm et al., 1989). Industrial SO_2-gas emissions are oxidized in homogeneous or heterogeneous reactions and form SO_4^{2-}. Anthropogenic emissions like combustion of fossil fuel constitute the main source for the SO_4^{2-} release into the atmosphere. Often NH_4^+ is present in continental aerosols in concentrations high enough for partial or complete neutralization of H_2SO_4 acid with the formation of various ammonium salts as $(NH_4)_2SO_4$, $(NH_4)HSO_4$ and $(NH_4)_3H(SO_4)_2$ (Charlson et al., 1978). Similar particles were found in the Phoenix urban aerosol (Post and Buseck, 1984) where the only detectable element was S. Here, several of these Phoenix S-bearing particles were detected indicating that the cores are soot. It was also observed (Mamane and Noll, 1985) that biological particles (composed of light elements, such as H, C, O and N) with their complex morphology and wet surfaces provide an attractive nucleating surface for SO_2 absorption and conversion to sulfate. In analogy for the North Sea aerosol, probably S-rich compounds have condensed onto or reacted with existing carbonaceous particles that have acted as condensation nuclei. The shape of the spectrum with its very high background is typical for organic and biological material although carbon X-rays cannot readily be detected with conventional EDX analysis (Mamane and Noll, 1985). However, X-ray spectra can distinguish between carbonaceous particles and e.g. crustal particles, whereas morphology studies often differentiate botanical particles from soot (Dzubay and Mamane, 1989). Signals from organic particulate matter can exceed the backscattered electron image threshold above the Nuclepore filter necessary for the localization of particles. The image signals from the filter backing material are normally completely suppressed by this threshold setting. So, if a localized and detected particle is composed almost entirely of lighter elements than Na, the organic nature can be ascertained from the relatively noisy background in its collected X-ray spectrum (Mamane et al., 1986). However, one must keep in mind that the total X-ray counts are still much lower than what is observed for e.g. mineral particles.

Carbonaceous particles enriched in $(NH_4)HSO_4$ and $(NH_4)_2SO_4$ or mixtures at their surface are present over the North Sea as was also inferred from LAMMS results (Bruynseels et al., 1988). Most of these S-rich particles have a diameter in the sub-micrometer range. This might be an indication that they are formed by gas-to-particle conversion processes. Combustion processes are almost exclusively responsible for the high pollution gaseous sulfur compounds, although a smaller fraction can have a marine origin as is the case for dimethylsulfoxide (DMSO) and

derived compounds. For the most westerly located sampling place of the May 1986 campaign, where only pure marine conditions were encountered, low concentrations of marine S-bearing compounds were detected.

The S-rich particulate matter is the most important particle type encountered in the sampling campaigns of March 1985 and November 1987. In March 1985, the atmosphere above the North Sea had been influenced by a long period of easterly wind and at the time of sampling the sea surface was smooth and the visibility strongly reduced due to a persistent fog. The particle concentration was very high, because of the presence of an inversion layer. The 36 hour air-mass back trajectories (Figure 2.4) show a steady supply of continental air travelling over West-Germany, The Netherlands and Belgium. For the November 1987 cruise, no fog and inversion conditions were observed. All filters have collected air masses originating from above Eastern European countries. Comparable S concentrations were found in the June 1987 campaign, although the air masses had long residence times above the South of England. Consequently high S emissions must be related to industrial and automotive sources from all over Europe.

Figure 2.4: Air mass back-trajectory for aerosols collected during the March 1986 campaign.

2.4.1.4 Calcium sulfate particles

Both Ca and S are present in the same particles with their elemental composition ranges given in Table I. These particles are very often found in both marine and continental aerosols. They are identified as $CaSO_4$. Some possible marine formation mechanisms are postulated (Andreae et al., 1986) e.g.:

(1) $CaSO_4$ can be produced by fractional crystallization of marine aerosols, a process that is especially efficient with high relative humidity. Possibly breakup of the $CaSO_4$ crystal from the seasalt aerosol particle takes place either by impaction on the filter or during its atmospheric residence.

(2) $CaSO_4$ could result from the aerosol interaction between marine or airborne $CaCO_3$ with atmospheric SO_2 or H_2SO_4 e.g. within clouds.

The abundance of $CaSO_4$ particles under purely marine conditions (May 1986) does not vary proportionally with seasalt. Furthermore, in the samples with highest $CaSO_4$ contributions, NaCl is virtually absent. Actually much higher abundances are present in the samples influenced by the continent (June 1987). The March 1986 and June 1987 campaigns are both characterized by high S-rich and Ca-rich particle number concentrations. For the reaction of particles with SO_2 and/or SO_4^{2-}, particles need to have the appropriate surface chemistry (to this aspect calcite scores better than clay minerals and much better than silicates) and long suspension times in the air (Mamane and Noll, 1985). Such sampling conditions: high humidity, persistent fog and an inversion layer, were observed for the March 1986 sampling campaign favouring such transformation reactions. It is however not evident that in the June 1987 campaign, acid transformation reactions between $CaCO_3$ (may partly be derived from the cliffs of Dover) and SO_2 or SO_4^{2-} components are dominant for the formation of $CaSO_4$ particles. If such reactions would have taken place, it implies that all $CaCO_3$ particles had been fully transformed. Indeed, in the June samples with exceptionally high number concentrations of $CaSO_4$, the Ca-rich ($CaCO_3$) particle type, which is the obvious precursor for $CaSO_4$, has not been observed at all. This means that $CaSO_4$ is predominantly emitted by anthropogenic sources such as combustion processes and by eolian transport from the continent to the North Sea. $CaSO_4$ has also been found in the fly-ash particles collected from coal power plants (Parungo et al., 1979). It is remarkable that all $CaSO_4$-rich filters were influenced by continental air-masses travelling over the South of England (June 1987 and October 1987) (Figure 2.5).

Figure 2.5: Air mass back-trajectory for aerosols collected during the October 1987 campaign.

In some particular samples, the relative intensity of S is much higher than what is normally measured for $CaSO_4$. Hence this particle type can partly be identified as $CaSO_4$ enriched with S, in the form of e.g. $(NH_4)_2SO_4$. The formation of $CaSO_4.(NH_4)_2SO_4$ aerosols can be explained by the coagulation of $CaSO_4$ particles with sub-micrometer sulfate aerosols (Harrison and Sturges, 1984). These results were confirmed by LAMMA measurements (Bruynseels et al., 1988).

2.4.1.5 Calcium-rich particles

For the Ca-rich particle type, we can only postulate that they are mainly characterized as $CaCO_3$ although C and O cannot be detected by our method.

All Ca-rich aerosols that contain less than 16 % S are classified in this group. They can originate both from the marine environment and from continental sources.

As seawater evaporates, various dissolved salts begin to crystallize out sequentially. First calcite ($CaCO_3$) and dolomite [$CaMg(CO_3)_2$] precipitate, then gypsum ($CaSO_4.aq$) followed by halite (NaCl) and finally the Mg-salts (Borchert, 1965). If this crystallization effect takes place in an aerosol droplet, $CaSO_4$ as well as other salts (e.g. the remaining residues) would be detected on the filter. Only Ca-rich particles, $CaSO_4$ and NaCl were identified. Mg was detected in low

abundances, never as the major cation in individual particles. Mg is mostly associated with Ca-rich or Ca-S-rich particles. Probably also the mixed salt [$CaMg(CO_3)_2$] can undergo further reaction with gaseous S-rich components. A small fraction of Ca-rich particles show up to 15 % of S in the relative X-ray spectrum but are not classified into the $CaSO_4$ group according to the creteria of Table 2.1. This can be an indication for the initiation of Ca-S-rich particle formation from $CaCO_3$ and/or derived components with atmospheric SO_2 or H_2SO_4. The highest abundances for Ca-rich particles are found during the December 1984 campaign where no marine influences are present. On the other hand, minor Ca contributions are observed in May 1986. According to the obtained data set, Ca-rich particles above the North Sea cannot unambiguously be apportioned to one source type.

2.4.1.6 Aluminosilicate-rich particles

These particles are characterized by the presence of Al, Si, S, K, Ca and Fe as major elements and Ti, Cr, Mn, Ni and Zn as minor ones. This mineral type of particles finds it origin on the continent. X-ray spectra cannot distinguish whether these particles are soil dust or fly-ash derived. Only morphology can sometimes differentiate their source. The soil dust particles have variable shapes and diameters ranging from sub-micrometer to about 5 μm. However, sometimes 40 % or more of all alumino-silicates have a smooth and nearly perfect spherical shape. This is especially true for the November 1987 cruise when the sampled air-masses are influenced by Eastern European emissions (Figure 2.6). Hence these particles must be fly-ash derived. They are formed during high-temperature combustion processes of fossil fuel and obtain their typical shape after solidification of the molten material. Smaller fly-ash contributions are also observed during air mass trajectories over England and Western Europe. In about 5 % of all aluminosilicates, a rather high S-concentration was present in the aerosol during the March 1986 campaign. Because meteorological conditions favoured high continental influences over marine ones, anthropogenic S from SO_2-emissions is very likely to be responsible for secondary reactions. H_2SO_4 derived from SO_2-emissions can have long residence times during calm weather conditions at high relative humidities. During long fog periods, high humidity and inversion layer conditions, mineral particles that were initially hydrophobic, can most probably be wetted with acidified water droplets and are left behind as possible cloud condensation nuclei (CCN) for further reactions (Andreae et al., 1986). These CCN can in an initial state be composed of an aluminosilicate nucleus covered by a S-rich surface coating. But also further transformation or

element specific extraction processes are possible. Such reactions are responsible for further break down of silicate mineral particles forming silicon-rich clusters.

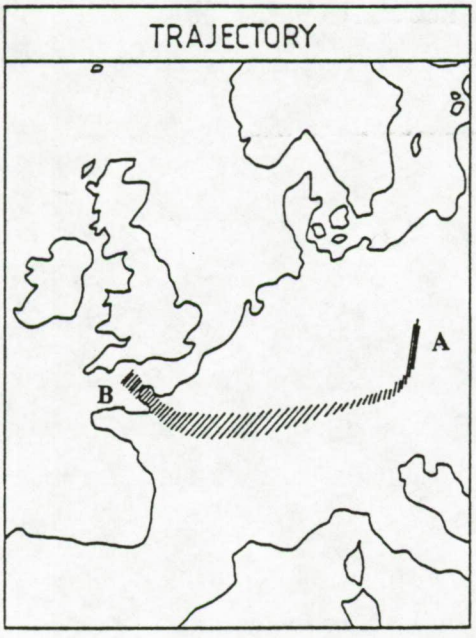

Figure 2.6: Air mass back-trajectory for aerosols collected during the November 1987 campaign.

2.4.1.7 Silicon-rich particles.

In the Si-rich group, the Si-K X-rays constitute more than 88 % of the characteristic X-ray spectrum. These mineral quartz particles are irregularly shaped. They can be derived from soil dust and therefore are often found in the presence of aluminosilicates. Another fraction of the quartz particles are emitted during the combustion of coal in power plants (Husain, 1986; Xhoffer, 1987). Most of the Si-rich particles are present in the size range below 1 μm. The fact that these particles, just as the Fe-rich particles, are found in the smallest size range could strengthen the hypothesis that they are formed during combustion processes.

2.4.1.8 Titanium-rich particles

For some North Sea samples (November 1987), rather high abundances of Ti-rich particles were observed. The mean relative X-ray intensity for Ti ranges between 65% and 85%.

The mean diameter of the Ti-rich particles is 1.0 μm and the shape factor of 3 deviates far from 1

for spherical particles. The main source for Ti-release into the atmosphere are pigment spray, but also minor pollution processes and sources such as soil dispesion, asphalt production and coal fired boilers and power plants are known (Hopke, 1985). Sometimes chromium is detected in this particle group beside some contributions of Si, Zn, Pb and Ba.

2.4.1.9 Iron-rich particles

The samples taken near the continents show high contributions of Fe-rich particles. Within this cluster, 3 different Fe-rich particle types are recognized. The first sub-group consists of pure iron oxide. Most of these particles are spherical, but irregularly shaped particles are found as well. They are mainly produced by ferrous metallurgy processes. The second sub-group are Fe-Zn-Mn rich particles. Within this group, the abundances for Zn and Mn are much more pronounced. They are derived from ferrous manganese furnace processes. Very often S is associated with Fe-rich particles: the Fe-S-rich particles constitute the third sub-group. These particles, probably pyrite and iron sulfate, can be formed by reaction between iron oxide and sulfuric acid, during their release in ferrous metallurgy related combustion processes.

2.4.1.10 Minor particle type

Rare particles are also interesting because they can sometimes be apportioned unambiguously to one specific source.

Characteristic X-ray spectra showed that some S-bearing aerosols have P and Cl as detectable elements. Also a very high X-ray background is often observed originating from an organic matrix. Organic phosphorus is primarily formed through biological activities. Bubble bursting can cause enrichments of P in the sea salt aerosol particles by fractionation out of the sea surface microlayer (Graham et al., 1979). When these P-rich particles mix with anthropogenic air masses, the S components can also react with these sea salt particles forming aged sea salt enriched in P. The major sources for particulate P in marine aerosols of New Zealand (Chen et al., 1985) are soil particles containing both naturally occurring and fertilizer derived P, as well as sea salt particles and industrial emissions. Na, Al and V were associated with P as indicators or markers for respectively a marine source, a crustal weathering source and an anthropogenic pollution source (e.g. burning of biological material). For the North Sea samples, no association between P and Al or V was detected and hence these particles probably have a marine origin.

Alternatively, the presence of P is often associated with Ca. These particles are classified into the Ca-rich group, although their % abundance of relative X-ray intensities from Ca and P are respectively 13 % and 55 %. This particulate matter can be fertilizer derived or is a residual from biological material (e.g. pollen) and can be transported over the North Sea by wind action. Ca and P rich particles were also found in aerosol samples taken above the equatorial Pacific Ocean where only marine influences were expected (Xhoffer, 1987). The relative X-ray intensities of 60 % for Ca and 30 % compared to what we found here for P, suggest indeed an other, still unidentified source.

For some samples, higher abundances of heavier elements like Pb and Br together with Cl were detected. These Pb-rich particles are originating from automobile exhaust emissions. Pb is added to the petrol together with ethylene dihalide compounds (Br, Cl). Pb/Cl/Br compounds can be identified as $2PbBrCl.NH_4Cl$ (Post and Buseck, 1985). The emitted Pb-halides can readily be converted to Pb-sulfates by reaction with SO_2, H_2SO_4 or $(NH_4)_2SO_4$ with the loss of HBr (Sturges and Harrison, 1986). However none of the transformed Pb-halide particles were observed in spite of the very high S-concentrations present in the sampled air masses.

2.4.2 Principal component analysis

To study variations in the abundance data set, Principal Component Analysis (PCA) was applied using a software package, the so-called "Data Processing Program (DPP)" (Van Espen, 1984). We used the relative % abundances of 9 particle types (9 variables) for 51 North Sea samples from Table 2.2 as input data for the PCA. The covariance matrix was used for the calculation of the principal components. The first three principal components explain 91% of the total variance present in the original data set. The loadings of the first three principal components, listed in Table 2.4, are plotted in Figure 2.7a, while the scores are represented in Figure 2.7b.

Three main clusters are recognized. The first group with a high score on the first principal component contains 14 samples with high abundances of sea salt and aged sea salt. A second cluster of 8 samples is separated by the second principal component. The samples in this cluster are characterized by high $CaSO_4$ abundances. Because of the low negative score on the first principal component, the emission of $CaSO_4$ particles has to be related to continental anthropogenic sources. The third cluster of 29 samples is elongated in the direction of the first and third principal components. The third component is related to high sulfur and aluminosilicate abundance variations.

Table 2.4: Cumulative eigenvalues and loadings for the first three principal components derived from the covariance matrix for two PCA performed on the North Sea data.

	Principal components					
	For all samples (51)			For the third cluster (29)		
	1	2	3	1	2	3
Cum. Percentage	54	75	91	61	80	88
Variables	Loadings					
Seasalt	0.99	0.01	-0.09			
Aged seasalt	0.42	-0.10	0.22			
Marine Fraction (MF)				-0.50	0.86	-0.10
Sulfur	-0.66	-0.40	-0.62	0.97	-0.04	-0.21
$CaSO_4$	-0.41	0.91	-0.01	0.25	-0.13	0.06
Ca-rich	0.24	-0.19	0.00	-0.08	0.29	0.39
Aluminosilicates	-0.42	-0.39	0.80	-0.90	-0.37	-0.22
Quartz	-0.39	-0.18	0.26	-0.21	-0.46	0.01
Ti-rich	-0.23	-0.14	-0.23	0.29	-0.06	0.02
Fe-rich	-0.33	-0.21	0.00	0.11	-0.22	0.90

To validate the robustness of these identified clusters, a hierarchical cluster analysis (Ward's method, unstandardized variables) was performed on the data. By studying the result at a three cluster level, exactly the same clusters were found. The third group, however, cannot be attributed unambiguously to a specific source. Therefore further separation within this group is necessary to differentiate marine influences from continental ones. A second PCA was applied on these 29 samples. To enhance the difference between marine and continental aerosols, a new variable, the marine fraction (%) was introduced replacing the ss and aged ss variables. The marine fraction was defined as:

$$\text{marine fraction (\%)} = \frac{\langle \text{ss + aged ss} \rangle}{\langle \text{ss + aged ss} \rangle_{\text{marine cluster}}} \times 100 \qquad (1.1)$$

ss and aged ss represents the abundance of respectively the ss and aged ss particle type for each sample, and $\langle$ ss + aged ss$\rangle_{\text{marine cluster}}$ is the mean of the sum of the seasalt and aged seasalt particle type abundances for the marine cluster. The calculated value for the latter was 89%.

(a)

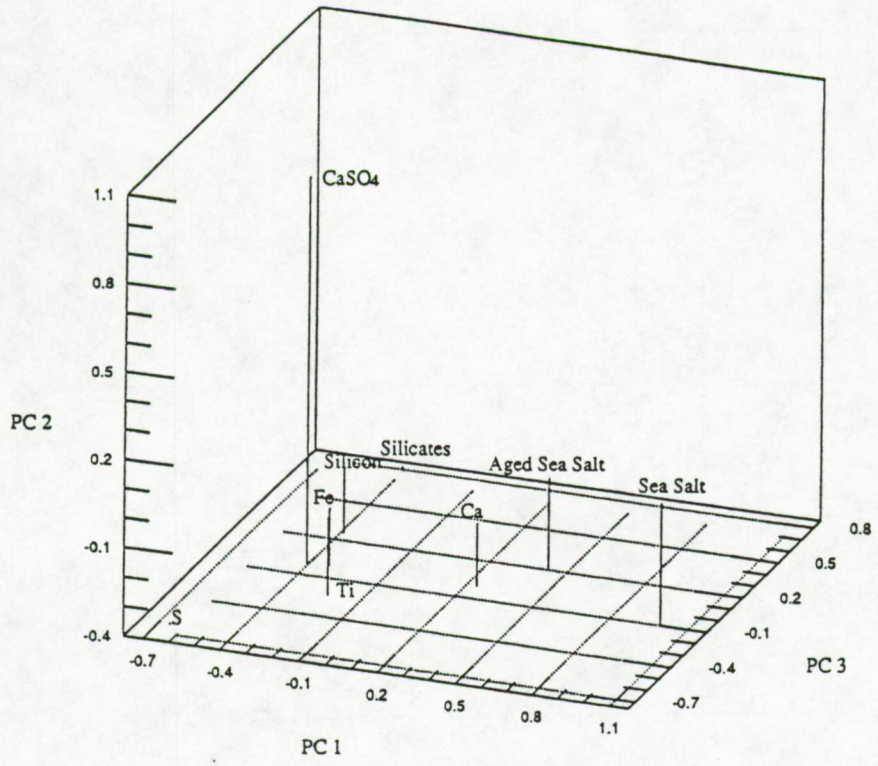

(b)

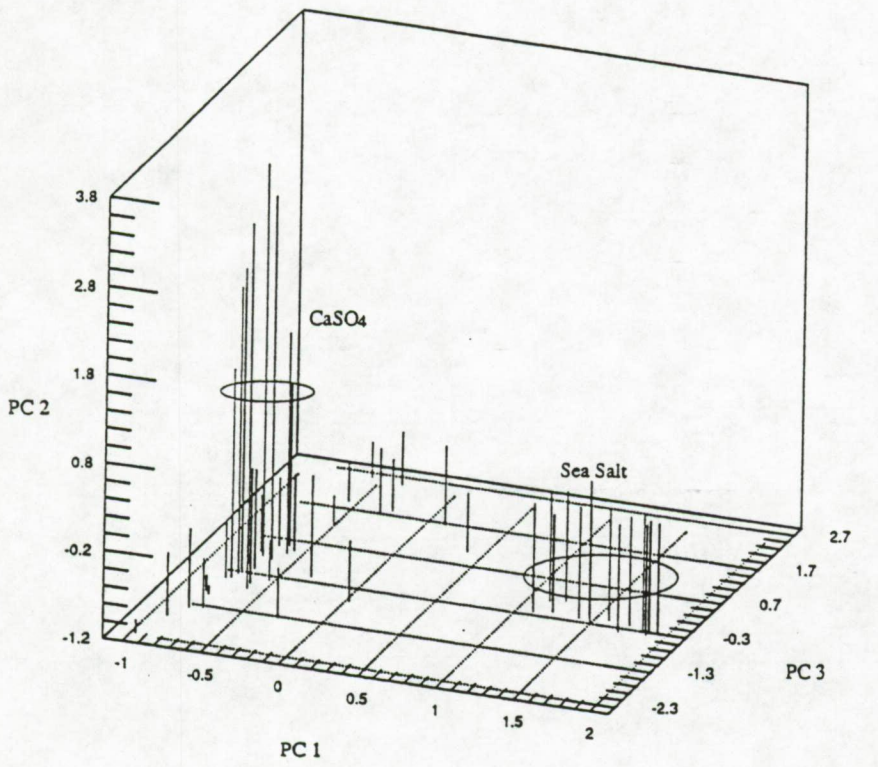

Figure 2.7: (a) Loadings of the first three principal components (51 samples) obtained by PCA of EPMA of the North Sea aerosol results. (b) Component scores of the first three principal components (51 samples), obtained by PCA of EPXMA of the North Sea aerosol results.

(a)

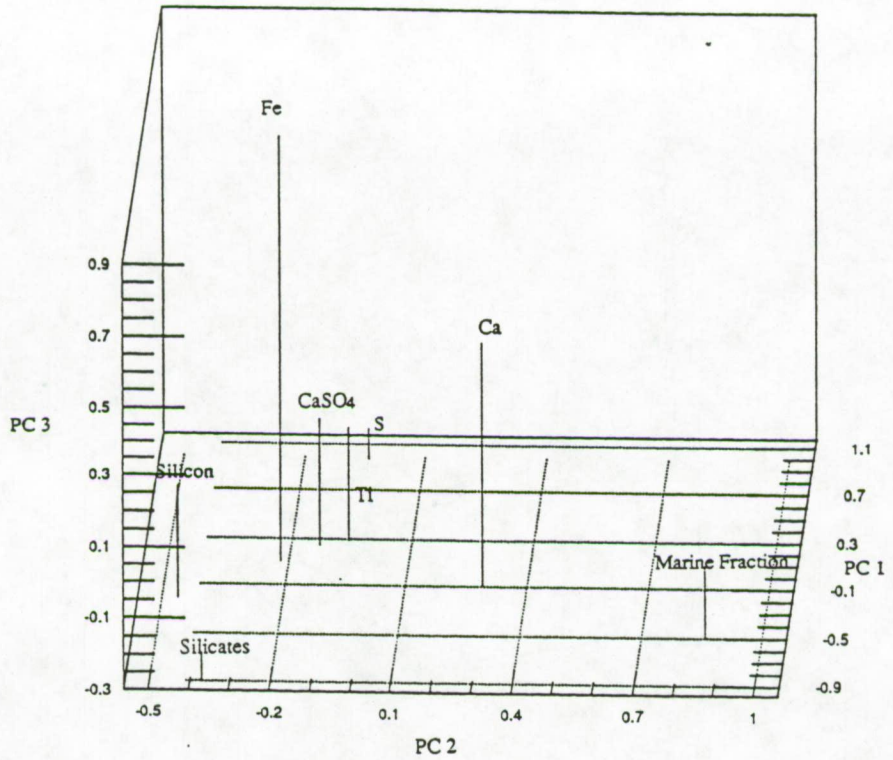

(b)

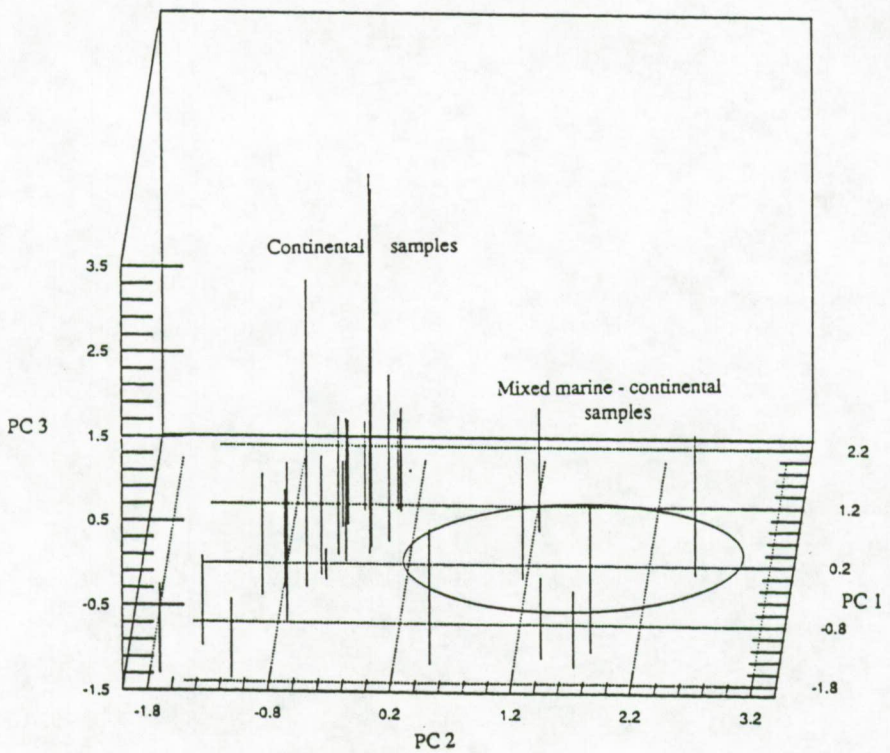

Figure 2.8: (a) Loadings of the first three principal components obtained by a second PCA on the third cluster (29 samples) resulting from the first PCA. (b) Component scores of the first three principal components, obtained by a second PCA on the third cluster (29 samples) resulting from the first PCA.

The loadings of the first three principal components, listed in Table 2.3, are plotted in Figure 2.8a and the scores are represented in Figure 2.8b. This figure shows two distinct clusters. One of them with high score on the second principal component, consists of seven samples, and all have a high marine fraction (mean marine fraction of 37%). This means that these analyzed particles originate from mixed marine-continental air masses. The other identified cluster contains nearly 100% continent-derived particles (22 samples), e.g. mean marine fraction of 1%. Variations in this group are mainly due to a different silicate/sulfur ratio. Principal component 1 describes this and even a negative linear relationship between the silicate and sulfur is present (r=-0.82) (Figure 2.9).

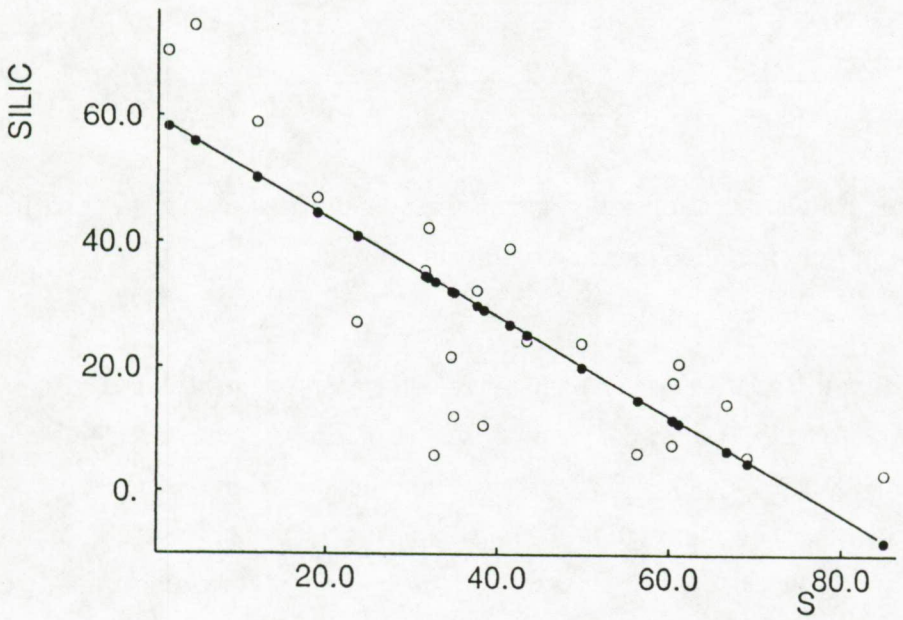

Figure 2.9: Negative linear relationship between the silicate fraction and the sulfur fraction of North Sea aerosols present in continental samples.

The determination of the silicate/sulfur ratio reflects the contribution ratio of their respective emission sources. The mixing ratio combined with bulk trace metal analysis can probably be used to determine the trace metal content of the distinct emission sources. Besides the relative importance of the silicate and sulfur particulate sources, iron particulate source contributions are superimposed (principal component 3). In the mixed marine-continental group, the same dependency on the silicate/sulfur ratio is found (Figure 2.10).

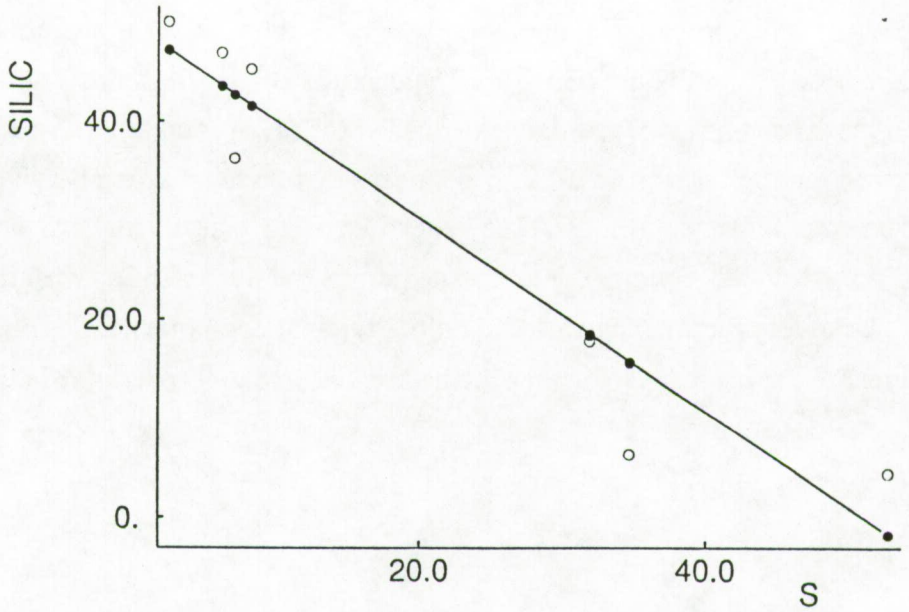

Figure 2.10: Negative linear relationship between the silicate fraction and the sulfur fraction of North Sea aerosols present in mixed marine-continental samples.

Table 2.5 summarizes the relative particle abundances for each of the 4 cluster groups as well as the mean abundance for all particles analyzed. Also the marine fraction is calculated and listed. Note that the marine fraction obtained for the mixed continental/marine sample group has a value of 37%, whereas the mean marine fraction for all samples is 33%. This suggests that the mean of all samples taken during the six campaigns are also representative for mixed sampling conditions.

Table 2.5: Mean relative percent abundance of each particle type calculated for the four clusters that were formed by principal component analysis.

Type	Number	Seasalt	Aged ss	S-rich	$CaSO_4$	Ca-rich	Al-silic	Si-rich	Ti	Fe	M.F.
Marine	14	76	13	2	2	4	2	1		1	100
$CaSO_4$	8	1		16	67		9	4		4	1
Mixed	7	16	17	21	7	5	30	3		3	37
S/Silic	22	1		41	9	2	27	6	5	9	1
Mean	51	23	6	23	16	3	18	4	2	5	33

2.5 Conclusions

The aerosol concentrations near sea-level vary greatly depending on proximity to natural and man-made sources. From the data set resulting from 25,000 individual particle analyses of 51 North Sea aerosol samples, four different aerosol groups could be differentiated on the basis of their composition. These groups were apportioned according to distinct particle emission sources.

More than 21 % of all particles detected above the North Sea and surrounding waters represent seasalt particles. Within this group, the marine contribution for S-rich, $CaSO_4$ and Ca-rich particles was estimated to be 0.5%, 0.6% and 1.1%, respectively. Anthropogenic derived S-rich particles and aluminosilicates represent 21% and 16% respectively of the aerosol composition, whereas industrial derived $CaSO_4$ contributes for almost 15% of all particles analyzed. About 13% of all North Sea particles are a mixture of particles from both marine/natural and continental/anthropogenic emission sources. For all other particle types detected, their contribution is less than 5% of the total North Sea aerosol and they are derived from various emission sources.

2.6 References

Andreae M.O., Charlson R.J., Bruynseels F., Storms H., Van Grieken R., Maenhaut W.; Internal mixture of sea salt, silicates and excess sulfate in marine aerosols, *Science*, 232, 1620-1623, 1986

Bernard P., Van Grieken R., Eisma D.; Classification of estuarine particles using automated electron microprobe analysis and multivariate techniques, *Environ. Sci. and Technol.*, 20, 467-473, 1986

Blanchard D.C.; "*Air-Sea Exchange of Gasses and Particles*", eds. Liss P.S., Slinn W.G.N, Riedel D.; Publishing Company, Dordrecht, 407, 1983

Borchert B.; "*Chemical Oceanography*" eds. G. Skirrow and J.P. Riley, vol. 2, Academic Press, London, 1965

Bruynseels F., Storms H., Van Grieken R., Van der Auwera L.; Characterization of North Sea aerosols by individual particle analysis, *Atmosph. Environ.*, 22, 2593-2602, 1988

Charlson R.J., Covert D.S., Larson T.V., Waggoner A.P.; Chemical properties of tropospheric sulfur aerosols, *Atmos. Environ.*, 12, 39-53, 1978

Chen L., Arimoto R., Duce R.A.; The source and forms of phosphorous in marine aerosol particles and rain from northern New-Zealand, *Atmos. Environ.*, 19, 779-787, 1985

Clegg S.L., Brimblecombe P.; Potential degassing of hydrogen chloride from acidified sodium chloride droplets, *Atmos. Environ.*, 19, 465-470, 1985

Dzubay T.G., Mamane Y.; Use of electron microscopy data in receptor models for PM-10, *Atmos. Environ.*, 23, 467-476, 1989

Forgy E.W.; Cluster analysis of multivariate data-efficiency vs interpretability of classifications, *Biometrics*, 21, 768, 1965

Graham W., Piotrowicz S.R., Duce R.A.; The sea as a source of atmospheric phosphorous, *Mar. Chem.*, 7, 325-324, 1979

Harrison R.H., Sturges W.T.; Physico-chemical speciation and transformation reactions of particulate atmospheric nitrogen and sulphur compounds, *Atmos. Environ.*, 18, 1829-1833, 1984

Hitchcock D.R., Spiller L.L., Willson W.E.; Sulfuric acid aerosols and HCl release in coastal atmospheres: Evidence of rapid formation of sulfuric acid particulates, *Atmos. Environ.*, 14, 165-182, 1980

Hopke P.K.; "*Receptor Modelling in Environmental Chemistry*"; John Wiley and Sons, N.Y./ Chichester/ Brisbane/ Toronto/ Singapore, 1985

Husain L.; Chemical elements as tracers of pollutant transport to a rural area; in "*Toxic Metals in the Atmosphere*"; Eds. Nriagu J.O., Davidson C.L., Advances in Environmental Science and Technology, 17, John Wiley and Sons, New York, 1986

Kim D.S., Hopke P.K., Massart D.L.; Multivariate analysis of CCSEM auto emission data, *Sci. Tot. Environ.*, 59, 141-155, 1987

Mamane Y., Noll K.E.; Characterization of large particles at rural site in the Eastern United States: Mass distribution and individual particle analysis, *Atmos. Environ.*, 19, 611-622, 1985

Mamane Y., Miller J.L., Dzubay T.G.; Characterization of individual fly ash particles emitted from coal- and oil-fired power plants, *Atmos. Environ.*, 20, 2125-2135, 1986

Massart D.L., Kaufman L.; "*The Interpretation of Analytical Data by the Use of Cluster Analysis*", Wiley: New York, 1983

Op de Beeck J.P., Hoste J.; Gamma-ray spectrometry data-collection and -reduction by single computing systems, *Atomic Energy Review*, 13, 743-805, 1975

Otten Ph.; Private communications, 1986.

Parungo F., Ackerman E., Proulx H., Pueschel R.; A study of plume aerosols from a coal-fired power plant by electron microscopy and X-ray energy spectrometry, in "*Electron Microscopy and X-Ray Applications to Environment and Occupational Health Analysis*", Eds Russel P.A., Hutchings A.E., Ann Arbor Science, Ann Arbor, Michigan, 1979

Post J.E., Buseck P.R.; Characterization of individual particles in the Phoenix urban aerosol using electron beam instruments, *Environ. Sci. Technol.*, 18, 35-42, 1984

Post J.E., Buseck P.R.; Quantitative energy dispersive analysis of lead halide particles from the Phoenix urbam aerosol, *Environ. Sci. Technol.*, 19, 682-685, 1985

Raeymaekers B.; Characterization of particles by automated electron probe microanalysis, Ph. D. Thesis, University of Antwerp (UIA), 1987

Rojas C.M., Otten P., Van Grieken R.; Penetration of atmospheric aerosols during collection in cellulose filters, studied by secondary ion mass spectrometry, *J. Aerosol Sci.*, 20, 569-574, 1989

Saucy D.A., Anderson J.R., Buseck P.R.; Cluster analysis applied to atmospheric aerosol samples of the Norwegian Artic, *Atmos. Environ.*, 21, 1649-1657, 1987

Shattuck T.W., Germani M.S., Buseck P.R.; Cluster analysis of chemical compositions of individual atmospheric particle data, in "*ACS Simposium Series 292*", eds. Breen J.J. and Robinson P.E, American Chemical Society, Washington, D.C., 118-129, 1985

Sturges W.T., Harrison R.M.; Bromine in marine aerosols and the origin, nature and quality of natural atmospheric bromine, *Atmos. Environ.*, 20, 1485-1496, 1986

Van Borm W., Adams F.; Cluster analysis of electron microprobe analysis data of individual particles for source apportionment of air particulate matter, *Atmos. Environ.*, 22, 2297-2307, 1988

Van Borm W., Adams F., Maenhaut W.; Characterization of individual particles in the Antwerp aerosol, *Atmos. Environ.*, 32, 1139-1151, 1989

Van Espen P.; A program for the processing of analytical data (DPP), *Anal. Chim. Acta*, 165, 31-49, 1984

Xhoffer C.; Elektronenprobemicroanalyse van vliegas en partikels uit het marine milieu, M.Sc. Thesis, University of Antwerp (UIA), 1987

CHAPTER 3

Characterization of individual particles in the North Sea surface microlayer and underlying seawater: comparison with atmospheric particles

3.1 Introduction

The sea surface microlayer is the channel of communication for material transfer between the atmosphere and the ocean. It is well known that the surface microlayer of the ocean has unique chemical, physical and biological properties quite different from those of the water underneath, most of which are still poorly understood (Södegren, 1977). Important processes for material transport from the sea body to the microlayer comprise diffusion, convection, upwelling and rising of bubbles (Garrett, 1970; Liss, 1975; Wallace and Duce, 1975). Dispersion of the microlayer material into the bulk water mainly occurs by sinking of particles and dissolution of water soluble molecules. Processes like bubble bursting (Blanchard, 1964) and the generation of aerosols by wind action are responsible for the upward transport into the atmosphere. Additional material transfer into the microlayer results from wet and dry atmospheric deposition processes. Figure 3.1 illustrates some of the routes of entry and removal of material to and from the sea surface, and also the internal transformations of such material whithin the microlayer. Most of the pathways and processes shown apply equally to both natural and anthropogenic materials.

Many pollutants (chlorinated hydrocarbons, petroleum hydrocarbons) may be concentrated and stabilized in the microlayer. These can, just as organic acids, proteinaceous material and other surface-active organic substances, provide complexing sites for many heavy metals (Pb, Fe, Ni, etc.) and thus be responsible for the concentration of these metals at the water surface. High concentrations of metals (Wallace and Duce, 1975; Barker and Zietlin, 1972; Piotrowicz et al., 1972; Duce et al., 1972) and other trace substances are thought to be associated with particulate

matter and surface active organic material and foams (Szekielda et al., 1972; Simoneit and Mazurek, 1985; Mopper and Zika, 1987).

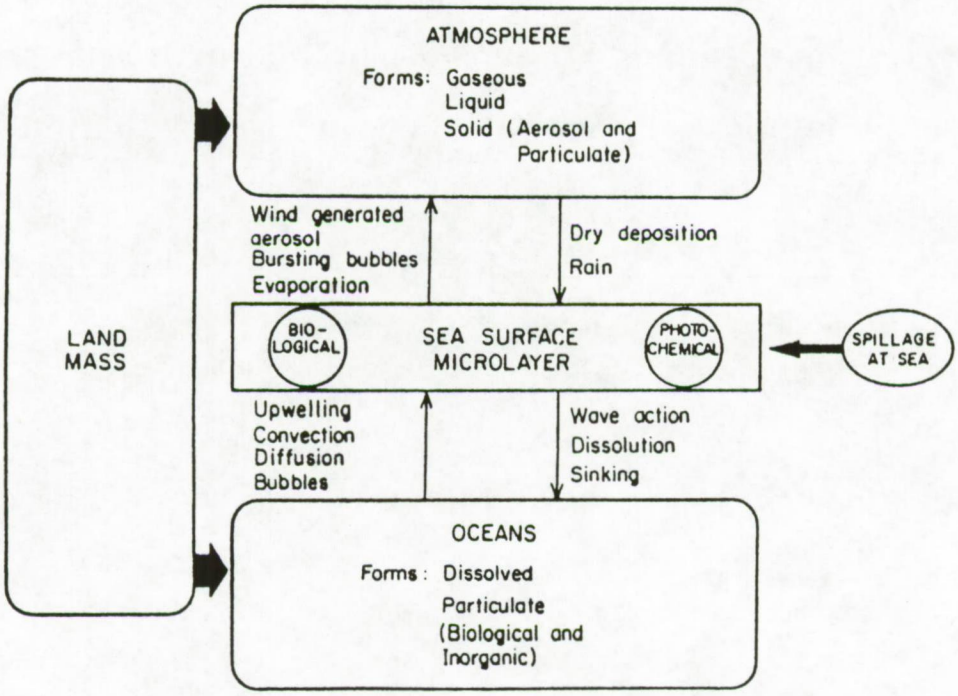

Figure 3.1: Sources and sinks of natural and man-made materials for the sea surface microlayer, including internal processes within the layer (Garrett, 1970).

Ideally, the microlayer thickness should only comprise the uppermost atomic water layer. Practically, it corresponds more or less to a thickness between 0.1 μm and 3 μm as defined by MacIntyre (1974) which is near the extreme limit of non-turbulent kinetics with no wind. But much of the thickness of collection depends on the surface sampling device (Liss, 1975).

Most of the previous microlayer research has been performed on chemical composition determination of the organic components or on distribution differences of heavy metal concentrations throughout the water column. The techniques are thus dealing with bulk analytical determinations.

In this work we present data obtained by automated electron microprobe x-ray analysis (EPXMA) and laser microprobe mass analysis (LAMMS) in order to complement measurements made by traditional bulk analysis methods.

3.2 Samples and sample preparation

Different sea-surface microlayer and bulk seawater samples were collected during 3 cruises in the Southern bight of the North Sea under very calm weather conditions. Figure 3.2 shows the followed trajectories and the respective sampling locations.

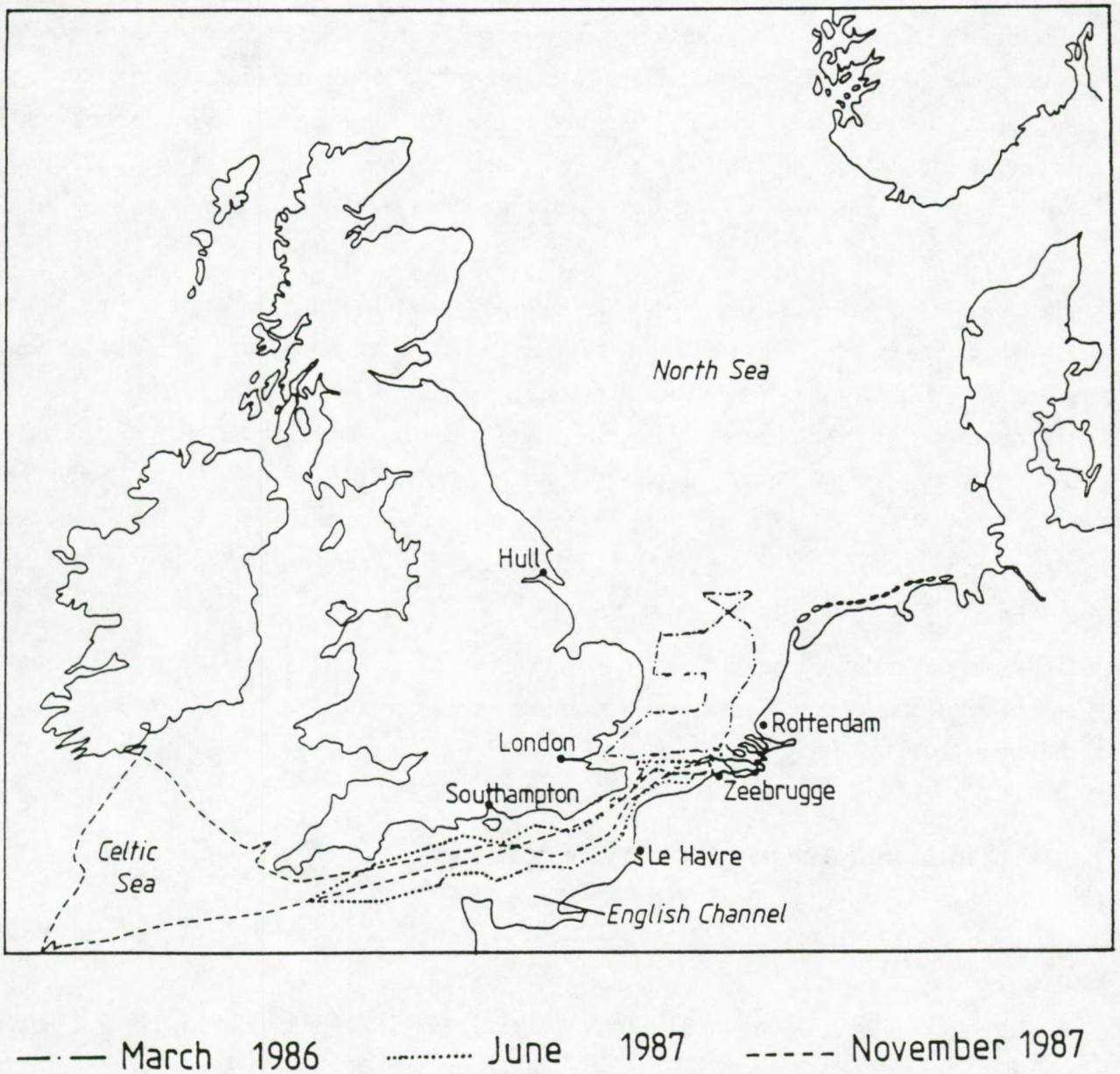

Figure 3.2: Location af sampling sites during different campaigns on the North Sea, English Channel and Irish Sea.

The sea surface microlayer samples were collected using the Garrett screen technique (Garrett, 1967). The sampler consists of a nylon window screen with openings of 400 by 400 μm and a fabric thickness of 440 μm stretched in a plexyglass frame. To avoid contamination from the research vessel (smoke stacks, corrosion products, dirt and dust particles, etc...), an uncontaminated sampling zone several hundred meters upstream was reached by a small rubber boat. Approximately 100 ml of surface water was collected, representing a waterfilm of about 100 μm. The sample was then transferred from the collecting screen to prewashed polyethylene bottles. After collection, the whole volume was immediately pressure filtered in a clean bench through 0.4 μm pore-size Nuclepore filters (diameter 2.5 mm) using a 50 ml syringe connected to a suitable filter holder. The loaded filters were flushed two times with 10 ml de-ionized "Milli Q" water for removal of freshly crystallized sea salt particles and air dried prior to deep freeze storage in petri dishes.

For LAMMS, the samples were prepared as follows: after collection, filtration and washing over a Nuclepore filter, particulate matter was resuspended by ultrasonic agitation in a clean test tube containing Milli-Q-water. Finally a drop of suspension was deposited on a thin foil of Formvar supported by 300 mesh electron microscope (EM) grids. Prior to LAMMS, the presence of the major elements composing the particles was checked by EPXMA. However, as the grids could not be carbon coated, EPXMA could not be performed in optimum conditions. Finally, the loaded grid was mounted in the LAMMS sample chamber where for every sample 100 to 150 particles were randomly selected for analysis.

Bulk seawater was collected at the same location as the microlayer samples using a Niskin bottle at 1 m below the surface. The bulk water samples were treated and analyzed in the same way as described above.

3.3 Results and discussion

3.3.1 EPXMA results.

A multivariate classification procedure was applied on the elemental composition of five pairs of samples, each pair consisting of a microlayer sample and an underlying bulk seawater sample.

As indicated by Table 3.1, seven representative particle types could be discerned and separated on the basis of the percent abundances of more than 13 elements by applying cluster algorithms. The standard deviations of the relative abundances can be calculated by binomial statistics. For a

total of 500 particles analyzed in each sample, the standard deviations range between 1 and 5 percent on a 2σ criterion. In addition to the automated EPXMA described in the instrumentation section, each filter was screened visually in the secondary electron mode and sometimes in the backscattered mode in order to obtain an idea about typical particle morphologies. LAMMS was applied in an attempt to obtain more information about trace element composition, organic composition and surface characteristics. The different particle types will be discussed in more detail below.

Table 3.1: Relative percent abundances for the North Sea microlayer (ML) and bulk (B) seawater samples after hierarchical and non-hierarchical clustering

Cruise	March '86		March 1986		November 1987		June 1987		June 1987	
Particle type	ML1	B1	ML2	B2	ML3	B3	ML4	B4	ML5	B5
Al, Si, K, Fe	17	34	23	29	47	66	38	50	7.0	19
Si	19	31	32	21	27	26	26	20	21	24
Organic	46	27	38	24	18	2.0	2.4	1.0	43	5.2
Ca	10	2.2	0.4	9.0	2.2	0.4	19	18	13	34
Ca, Al, Si	3.3	0.6	0.2	8.8	1.6	2.2	6.4	6.8	2.4	14
Fe	4.0	4.0	0.6	2.8	2.0	2.0	6.4	3.0	10	2.0
Ti	0.8	1.2	2.0	0.8	1.8	1.6	1.4	1.4	1.6	0.8

3.3.1.1 Aluminosilicates.

The aluminosilicate particle type is characterized by high relative elemental X-ray intensities of Al, Si, K and Fe and lower, though frequent contributions of Ti, Mn and Cr. For all samples, the number concentrations of the aluminosilicate fraction is higher in the bulk sea water than in the microlayer. A size distribution for this particle type is presented in Figure 3.3 and it shows a maximum number of particles at a diameter of 0.8 μm. The cut-off at the lower side of the particle size distributions is mainly a consequence of two factors, namely: (a) the magnification used during the particle analysis, higher magnifications allowing smaller particles to be detected and (b) the setting of the cut-off for the backscattered threshold intensity criterion. No differences in size distributions were observed between the microlayer and bulk water aluminosilicates. The

aluminosilicates can be subdivided into two particle fractions namely those enriched in Fe and those depleted or poor in Fe. Van Put (1991) observed the same particle types in an estuarine environment and assigned them to the respective sources of Fe-smectite and/or chlorite and to an illite clay mineral. Clay minerals are known to act as an adsorbent for trace metals and as a transport medium for riverine suspensions into the estuaries and ocean systems (Koppelman and Dillard, 1975). Various marine clay minerals like kaolinite, illite and chlorite absorb iron and chromium species from solution (Blackmore, 1973; Fordham, 1973; Goldberg, 1978).

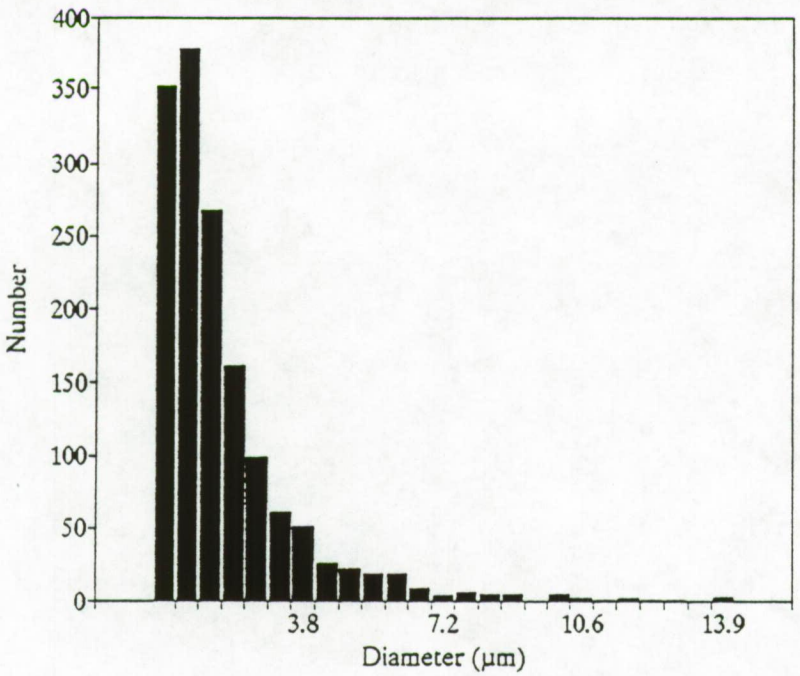

Figure 3.3: Particle size distribution for all aluminosilicate particles present in the North Sea surface microlayer and underlying bulk water.

In some of the microlayer and bulk sea water samples, smooth and nearly spherical aluminosilicate particles were observed (Figure 3.4). These typical round shaped aerosols are often observed after high temperature combustion processes or might be formed during gas-to-particle conversion processes. These particles could be identified as fly-ash and they maintain their structural integrity in an aquatic environment for extended periods of time (Duedall et al., 1981). It is not possible to distinguish fly-ash from e.g. soil dust on the basis of the relative X-ray intensities because their elemental compositions are very alike. Sometimes the distinction can be made by morphology studies as was done here. Visual inspection in the secondary electron mode revealed that fly-ash is more often found in the microlayer.

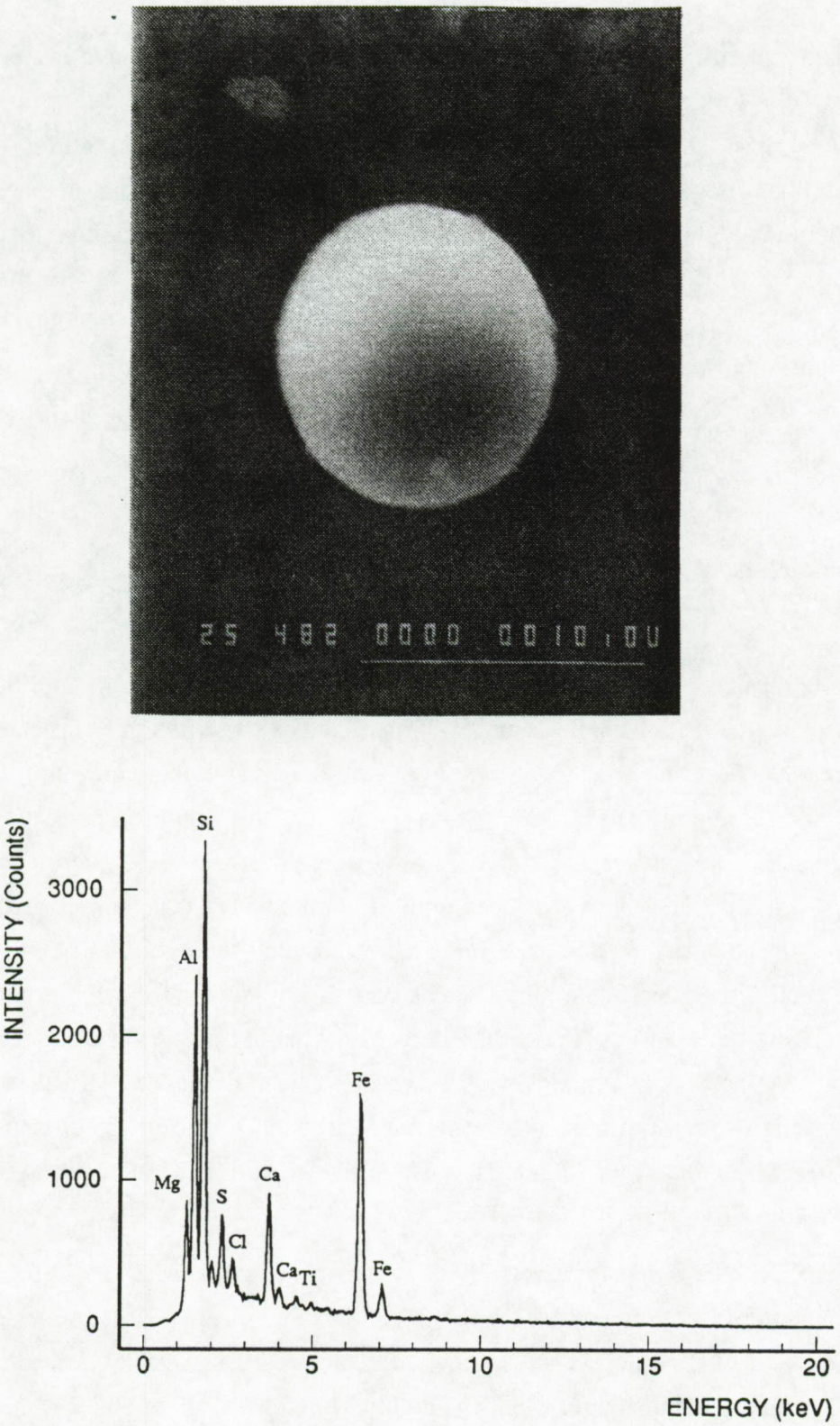

Figure 3.4: Secondary electron micrograph and X-ray spectrum of a fly-ash particle found in the surface microlayer of the North Sea.

The hollow and accordingly relatively low density structures probably have low sinking rates once they reach the water phase after atmospheric deposition. Especially during the November 1987 sampling cruise, the samples ML3 and B3 showed higher contributions of spherical aluminosilicate particles. The same observations were found for North Sea aerosols that were sampled at 11 m above the sea surface during the same cruise discribed in chapter 2. Here, the number concentration of spherical aluminosilicates (fly-ash) was much higher than normally observed. The 36 hour air mass back-trajectories of the November 1987 campaign show that the air masses had long residence times above Eastern European countries. Therefore, even middle-to-long distance anthropogenic emission sources can be responsible for the input of particulate material into the North Sea surface microlayer and bulk water.

3.3.1.2 Silicon-rich particles.

For this particle cluster, the mean relative Si-K X-ray intensity ranges from about 72% for the ML3 sample to about 99% for the B1 sample. All particles belonging to this class are denoted as Si-rich. Whereas the first March 1986 bulk sample is enriched in number concentration of Si-rich particles compared to the microlayer, the reverse is true for the second March 1986 sample. For the other samples, no significant differences were observed between microlayer and bulk samples. The Si-rich particle number concentration in bulk and microlayer water is comparable for all samples (it accounts for about 20 to 30% of the total particulate fraction). During the March 1986 and June 1987 sampling campaigns also higher Si-rich particle number concentrations were detected in continentally derived air masses above the sea surface (chapter 2). On the contrary, no Si-rich particles were observed at all in the lower North Sea atmosphere while we found high concentrations in the water phase for the November 1987 cruise. So, there cannot be a direct correlation between the presence of Si-rich particles in the atmospheric and the aquatic phase of the North Sea.

It is known that Si can be removed effectively by organisms (Broecker, 1971). In fact a great part of the phytoplankton in the sea consists of diatoms having a siliceous structure (Parsons, 1963; Riley and Chester, 1971; Kido., 1974). Figure 3.5 represents a secondary electron image of a Si-rich particle observed in the microlayer. The highly symmetrical shape and the holes present in the structure suggest it to be a siliceous frustule from a diatom. They usually appear as flat structures with a regular array of holes. Figure 3.6 shows an other Si-rich particle identified as a sponge spicules (McCrone and Delly, 1973).

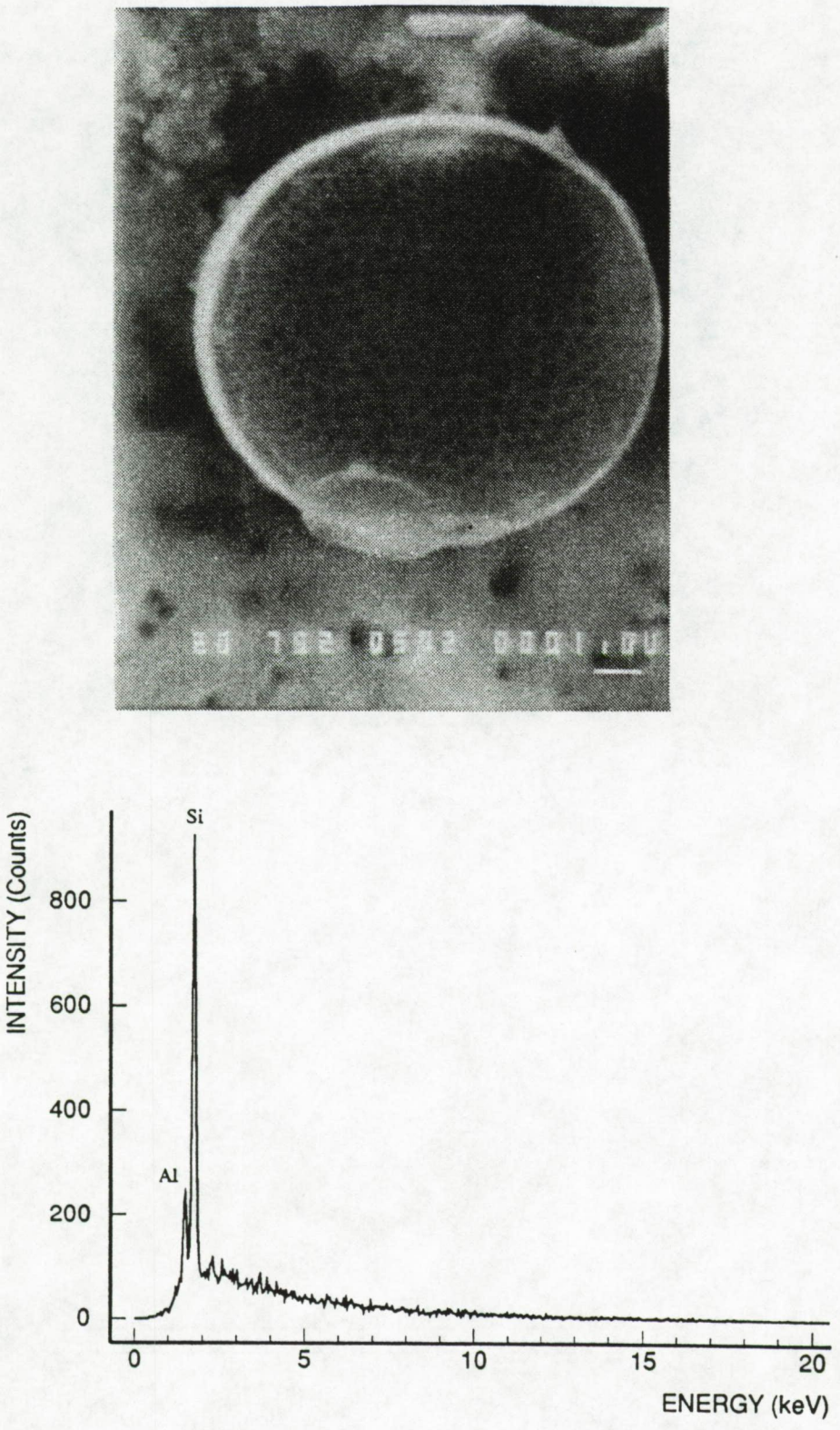

Figure 3.5: Secondary electron micrograph and X-ray spectrum of a diatom observed in the surface microlayer of the North Sea.

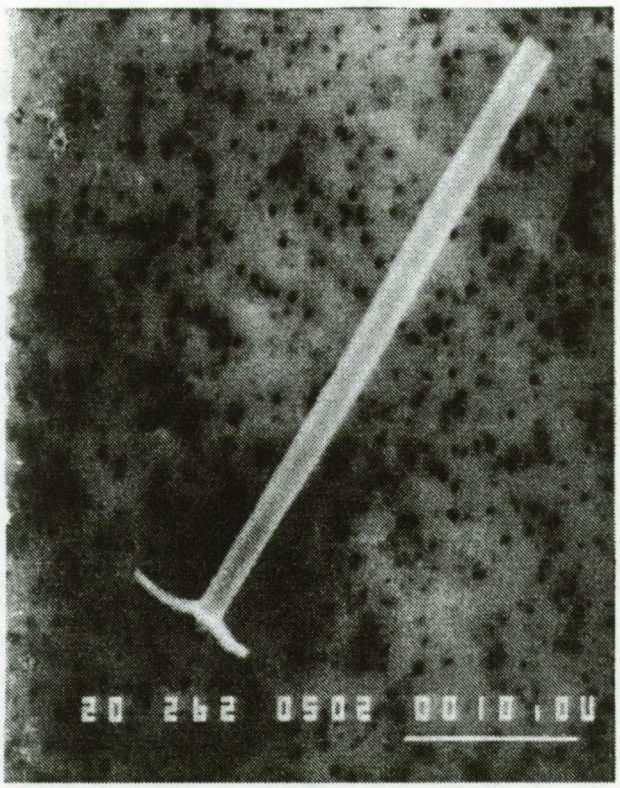

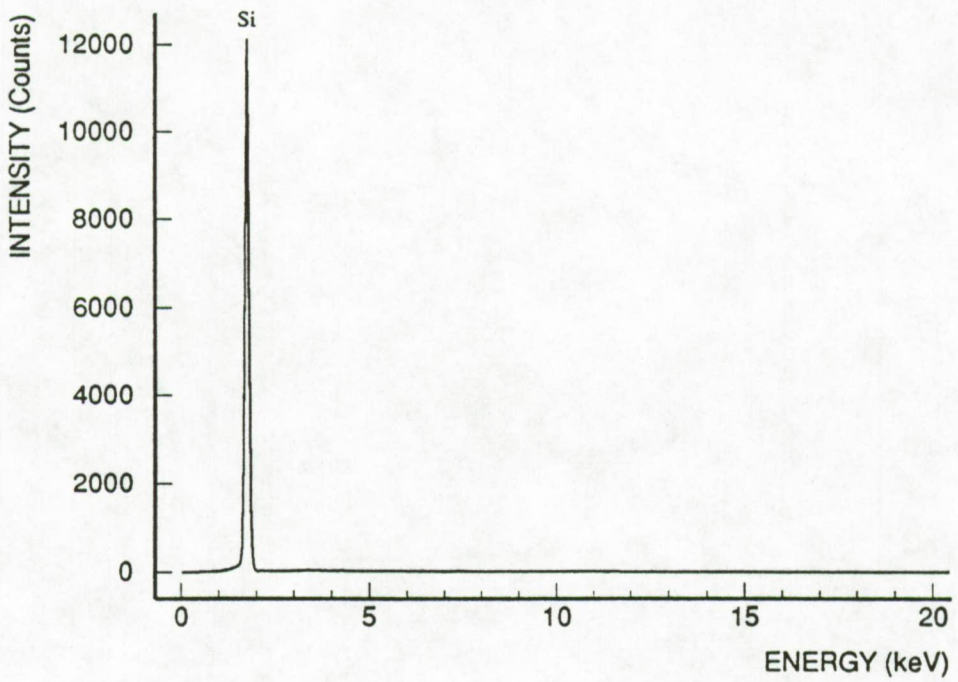

Figure 3.6: Secondary electron micrograph and X-ray spectrum of a skeletal fragment from a sponge present in the surface microlayer of the North Sea.

These are skeletal fragments of sponges and exist in thousands of shapes. Sometimes elements as Ca, Cl, S, K and even Fe are associated with them. Both the diatoms and the sponges were observed throughout the whole water column. In general, the concentration of dissolved silicate is low at the surface water due to uptake by organic activity and increases with depth where regeneration occurs because of decomposition of organisms in the deeper layer (Kido, 1974). The concentration gradient between surface water and deeper water layers becomes more marked as biological activity increases (Wollast, 1974). There are also other factors controlling the Si-content in the sea water like e.g. interactions of Si with clay minerals carried into the oceans by streams (Mackenzie and Garrels, 1965; Mackenzie et al., 1967). The properties of the surface layer of sediments generally differ considerably from those of the deeper layers, and may strongly affect the mass transport across the water sediment interface (Vanderborght et al., 1977). Mass balance estimations have shown that biological uptake of dissolved silica is an order of magnitude higher than that supplied by rivers and submarine activities (Wollast, 1974). Biological activity in the sea water generates an extremely high chemical mobility of silica. The quasi-closed cycle of uptake of dissolved silica by silica-secreting microplankton is essentially maintained by the rapid dissolution of debris of silicified skeletons during settling. The riverine input and the release of dissolved silica from interstitial waters play only a minor role in the distribution of dissolved silica in the ocean.

3.3.1.3 Ca-rich particles.

The relative abundance of this particle type varies from 0.2% up to 35%. Some contradictory results are observed for the Ca-rich particle distribution between the microlayer and the underlying bulk water. For the first March 1986 sample, a higher microlayer abundance is observed, whereas for the second March 1986 and second June 1987 samples, a more pronounced enrichment is observed in the bulk water. No significant differences were noticed for ML3-B3 and ML4-B4.

Since no other elements beside Ca are detected, this particle type is identified as $CaCO_3$. The equilibrium of $CaCO_3$ in the marine environment is very complex because there exist two polymorph crystalline structures, namely: calcite and aragonite. Both substances are found in oceans, though calcite is the most important. Aragonite is sometimes formed during precipitation processes, especially from organisms. Secreted skeletal $CaCO_3$ can be either calcite or aragonite; if calcite, it can have a high or low magnesium content depending on the organism involved and/or the environmental conditions (Horne, 1969). Figure 3.7 shows a picture of a foraminifera

particle as compared to a particle atlas (McCrone and Delly, 1973). These are $CaCO_3$ skeletons but of animals rather than plants and calcium is by far the most intense X-ray signal in the spectrum. Many shapes and surfaces may be encountered.

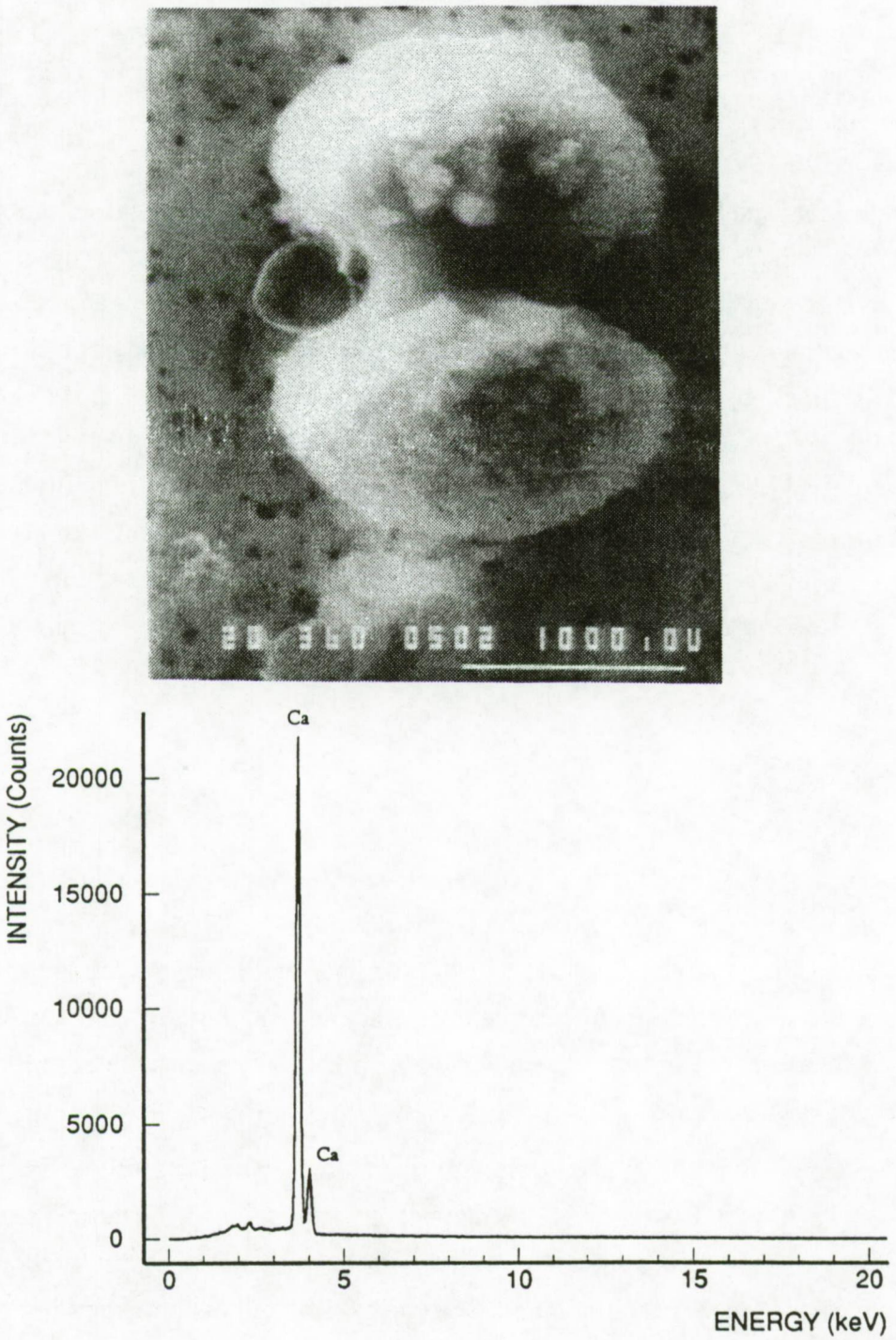

Figure 3.7: Secondary electron micrograph and X-ray spectrum of a foraminifora particle found in the surface microlayer of the North Sea.

Mg was detected in only very few particles (1 to 10% of the Ca-rich fraction). This might be the result of the high detection limit inherent of the applied FFA (fast filter algorithm). Elements with very low atomic number such as Mg are not very efficiently deconvoluted by this spectrum deconvolution technique (Bernard, 1989). The particle size distribution plot (Figure 3.8) shows a regularly decreasing shape and might indicate one major source.

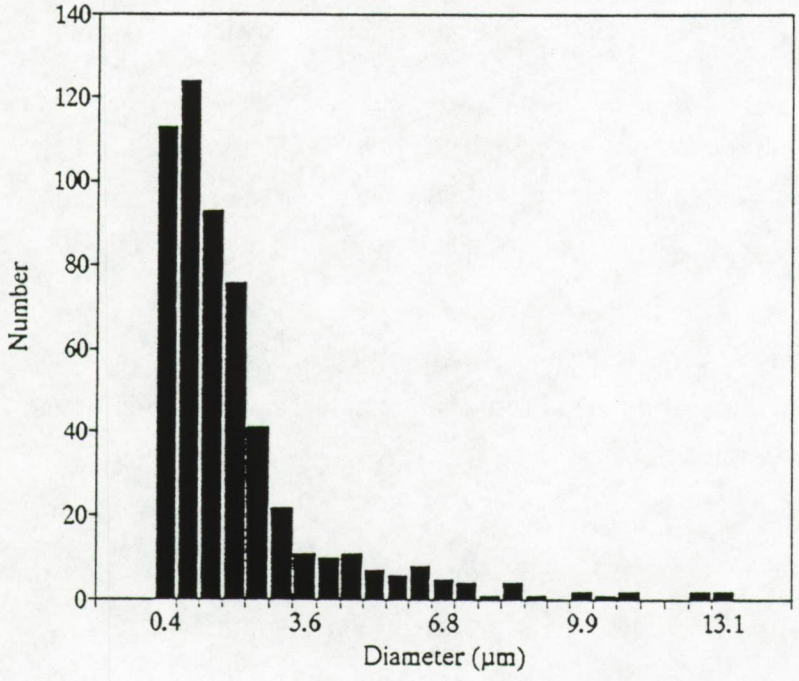

Figure 3.8: Particle size distribution for all calcium-rich particles present in the North Sea surface microlayer and underlying bulk water.

Resuspension of a Ca-rich particle fraction into the marine atmosphere could occur during sea spray processes. Reactions with atmospherically S-rich species like SO_2, H_2SO_4 or dimethyl sulfoxide (DMSO) might take place with the formation of $CaSO_4$ (Andreae et al., 1986). This transformation process can be important for the atmospheric $CaSO_4$ contribution in remote areas, but will totally be suppressed by anthropogenic $CaSO_4$ emissions sources in near-continental regions like the North Sea. During the March 1986, June 1987 and November 1987 sampling campaigns, sea spray production was an unimportant process as was reflected by the absence of NaCl in the corresponding atmospheric samples. The absence of particulate $CaSO_4$ in the North Sea water samples can be explained by its high solubility in water.

3.3.1.4 Calcium-aluminosilicate-rich particles.

This particle type comprises aluminosilicates that are enriched in their Ca-content. The relative abundances for this particle type are quite low. Except for the first microlayer-bulk water couple, comparable or somewhat higher concentrations are observed in the bulk water. The origin of these particles is not well known. Several Ca-containing minerals are present in natural waters like e.g. anorthite ($CaAl_2Si_2O_8$), zeolites, pseudo-zeolites, clay minerals and epidotes (Michard et al., 1986; Veldeman, 1991).

Comparable element compositions were observed in brown-coal fly-ash samples (Xhoffer, 1987). But since this particle type was totally absent in air masses collected above the North Sea, atmospheric transport processes can be excluded, ruling out the possibility that this particle type might be fly-ash derived.

A size distribution of this particle type is shown in Figure 3.9. The somewhat irregular shape of the distribution could suggest different sources or might be a reflection of the various minerals encountered in the water phase.

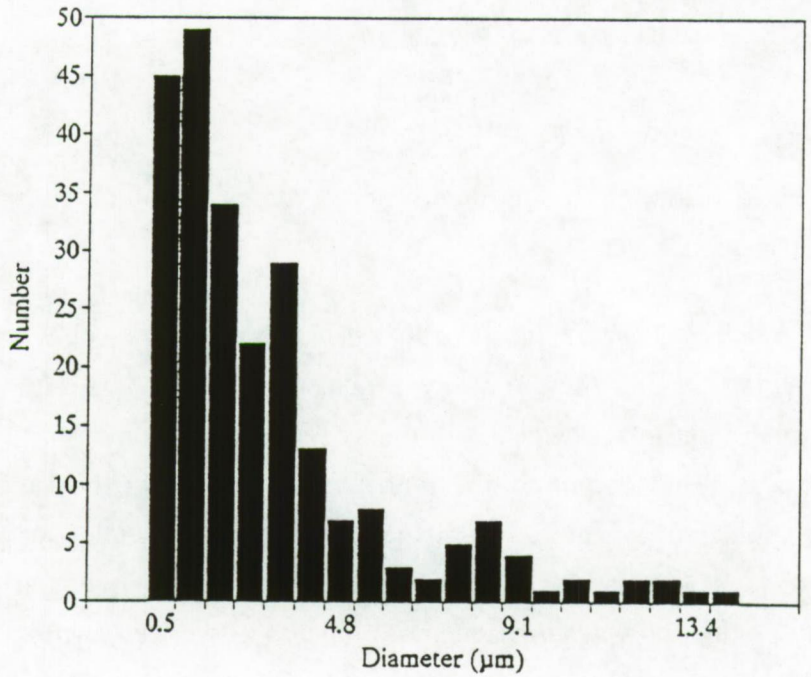

Figure 3.9: Particle size distribution for all calcium-aluminosilicate-rich particles present in the North Sea surface microlayer and underlying bulk water.

3.3.1.5 Organic particles.

Under conventional EPXMA measurements, elements lighter than Na cannot be readily detected and thus C, N and O signals are not to be interpreted from X-ray spectrum analysis. However, one can sometimes distinguish the inorganic fraction from the organic fraction since the latter exhibits a relative noisy background in its collected spectrum (Mamane et al., 1986; Post and Buseck, 1984). Backscattered electron signals from organic particulate matter can sometimes exceed the image threshold of the Nuclepore filter. At least some of the organic particular residue will then be localized, sized and analyzed showing no interpretable X-ray peaks in the spectrum. Probably only the thicker or more dense organic particles like e.g. biological material and microorganisms will give rise to sufficient backscattered signals.

From the EPXMA, it can be seen that organic material makes up an important part of the total particulate material in the microlayer. For four couples of samples a clear difference in organic contribution can be observed in favour of the microlayer. In one case (ML4-B4), the relative abundances are too small to observe any significant difference. Because of the lipophylic properties of the organic material, one expects the organic contribution to be more pronounced in the microlayer as is also seen from this data.

It was sometimes observed that organic material was incorporating other particles like sea salt, $CaCO_3$ and aluminosilicates (Figure 3.10). It was not possible to deduce whether these particles exist in the water phase or whether they are combined during the filter preparation process.

Note that the organic fraction observed in these samples only reflects a part of the total organic particular material present in the water phase since an appreciable fraction will escape detection by this technique.

3.3.1.6 Fe-rich particles

The major particles classified in this cluster have Fe as only detectable element and thus must be iron-oxide, -hydroxide or -carbonate. The particle abundance concentrations are too low to observe any significant differences between the microlayer and the underlying bulk sea water. Except for the June 1987 campaign, somewhat more abundant Fe-rich particles seem to be detected in favour of the microlayer.

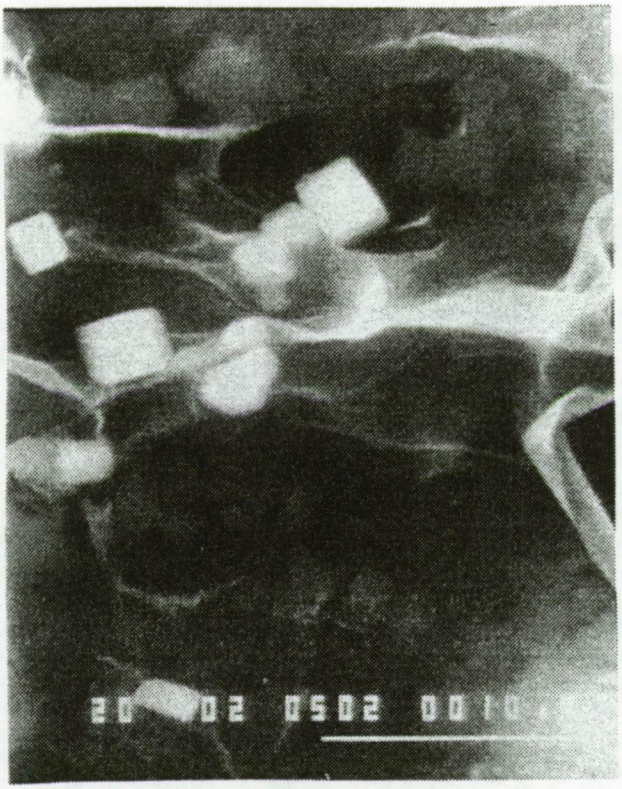

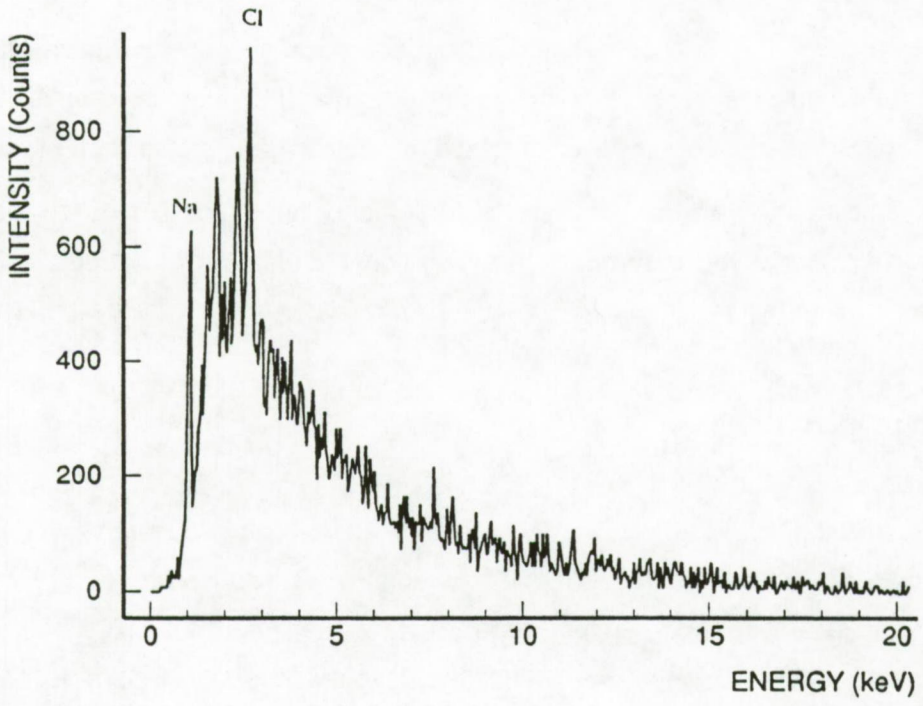

Figure 3.10: Secondary electron micrograph and X-ray spectrum of an organic particle enclosing various salt particles.

Their contribution for the June 1987 campaign is not in accordance to the sampled air-masses above the North Sea since low number concentrations occurred in the corresponding air masses. In most of the marine sediments, an anoxic sulfate-rich environment can be encountered due to (a) the high initial SO_4^{2-} concentrations in the water and /or (b) organic sediments with large benthic populations. Various Fe-S-rich phases can exist like pyrite, marcasite (FeS_2) and organic matter. In oxic environments as encountered in the coastal North Sea surface waters, hematite (Fe_2O_3) and goethite (FeOOH) form the major representers. Pyrite framboids can be formed through concentration of Fe-hydroxides and organic matter by biogenic activity like e.g. by diatoms (Degens and Buck, 1986).

The mean Fe-rich particle diameter in the water phase is 1.4 μm and is almost the double of the observed diameter of Fe-oxide particles in the air. The mean shape of this particle type is 1.9 and is expressed by the shape factor (SHF) and calculated as SHF=(perimeter)^2/4π x area. It deviates strongly from sphericity (SHF=1). However, the origin of these Fe-rich particles in the microlayer cannot be ascertained to one specific source on the basis of this data.

3.3.1.7 Ti-rich particles

Titanium-rich particles were observed both in the microlayer and in the bulk sea water of the North Sea. Their relative number concentrations are again low (2% or less). The relative abundances correspond very well to the atmospheric North Sea concentrations of Ti-rich particles (chapter 2). Also the mean particle diameter (1.1 μm) and shape factor (1.5) for this group are in accordance to the atmospheric fraction. These particles are thus more likely to be derived from continental pollution sources such as e.g. paint spray, soil dispersion and asphalt production. However, riverine input into the North Sea may not be excluded. Both Bernard (1989) and Van Put (1991) found the presence of Ti-rich particles (probably rutile) in respectively the Scheldt and Elbe estuaries.

3.3.1.8 Miscellaneous particle types.

Occasionally, particles containing elements like Cu, Zn, Co, Cr, Ba, Pb and Ni were detected. Among them, Cu, Zn and Cr are the metals that were most frequently recognized. Figure 3.11 shows a secondary electron image of a very large chromium oxide particle with a $CaCO_3$ particle sticking to its surface.

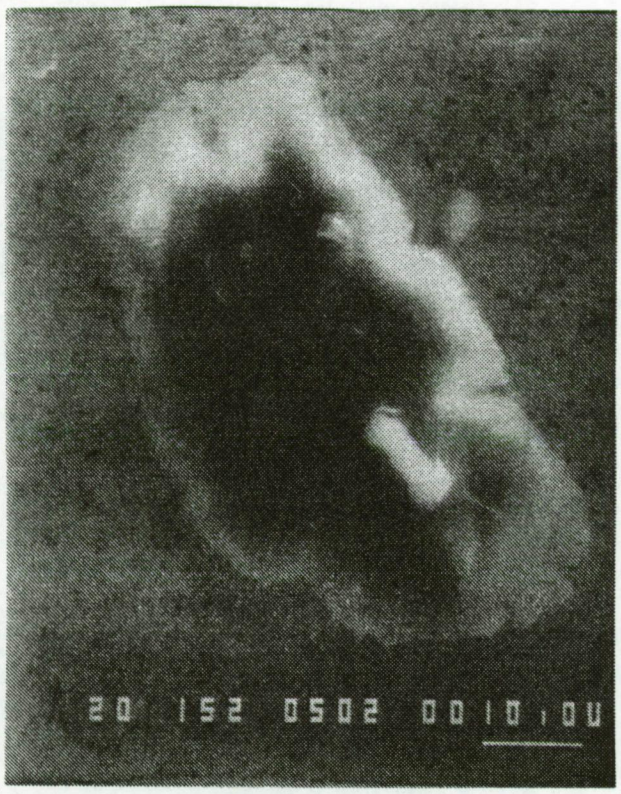

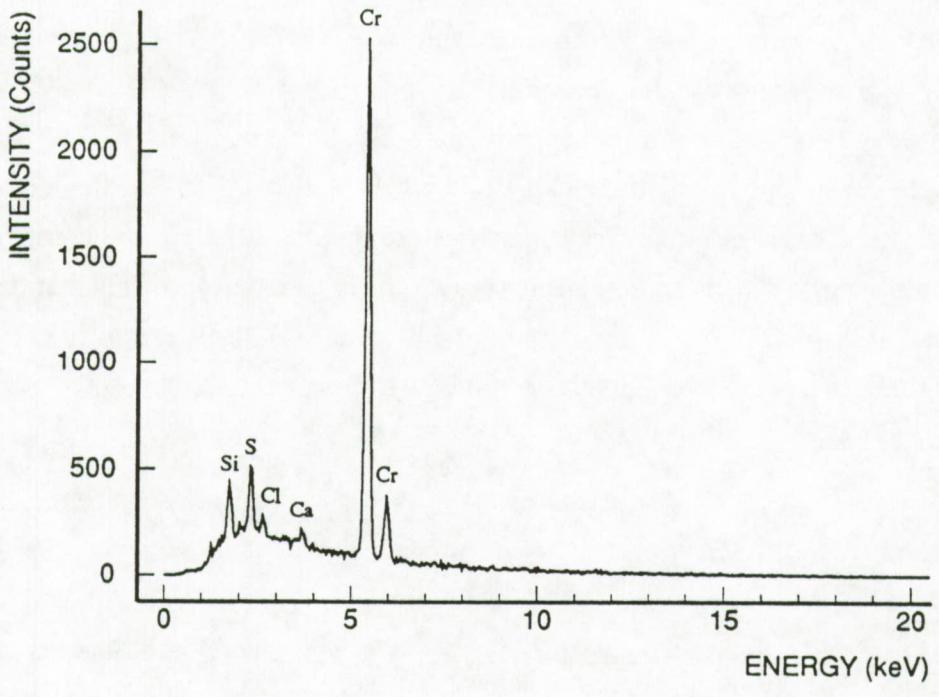

Figure 3.11: Secondary electron micrograph and X-ray spectrum of a chromium-rich particle with a $CaCO_3$ particle sticking to its surface.

Most of the metal-rich particle types have low number concentrations and their abundance cannot be determined with high accuracy. This is the result of the abundance variations of the more abundant particle types, influencing relatively the abundance of these metal-rich particles. Nevertheless, their occurrence as individual particles can sometimes be used as indicator for source apportionment because of their specificity. Most of these metal-rich particles were clustered together with the organic fraction. Sometimes relatively low X-ray counts were observed and the sum of the X-ray intensities did not always add to 100% because of unidentified peaks. This might indicate an association of these metals with particles of organic origin.

Hood (1967) reported great variation of both kinds and amounts of Cu, Mn and Zn in the water column from the Gulf of Mexico, with Cu and Zn mostly associated with the particulate fraction and Mn in solution. Much of the Zn, substantial amounts of Cu and small amounts of Mn were nondialyzable, that is, firmly bound to organic complexes. There is also indirect evidence of an organic-bound fraction of elements such as Mn and Zn (Rona et al., 1962), Fe (Laevastu and Thompson, 1958) and Cu (Slowey et al., 1967). It is known that some fungicides with chlorinated hydrocarbons can have metal components as copper (sulfate, naphthenate) and zinc (as sulfite or oxide) (Merlini, 1971).

Copper is a trace metal and microlayer enrichment factors of 10^3-10^4 times are found relative to bulk sea water (Szekielda et al., 1972; Cattel and Scott, 1978). The concentration of dissolved Cu in surface waters of the coastal North Sea (average ~ 200 ng/l) is twice as high as those in remote open oceans (average ~ 100 ng/l) (Kremling, 1983).

Hunter (1980) performed studies on the North Sea and found that both Fe and Mn were strongly depleted in the microlayer. He suggested that the phase bearing these two trace metals, consisted of river derived terrigenous material present on large particles. From comparing residence times of both atmospheric deposition and flotation, he deduced that bubble flotation formed the major process for the enrichment of most trace metals in the microlayer.

Surface ocean concentrations of Pb have dramatically increased as a consequence of the deposition of man introduced lead from the atmosphere. Contents of Pb in surface waters of the Northern hemisphere today easily reaches 0.07 µg of Pb per kg of seawater compared with estimated prehistoric values of 0.01 to 0.02 µg/kg (Chow and Patterson, 1966). About 49% of the total Pb-quantity (3390 ton.yr^{-1}) reaches the North Sea by atmospheric input routes and the other 51% by dumping activities (2400 ton.yr^{-1}), rivers (970 ton.yr^{-1}) and discharges (144 ton.yr^{-1}) (Otten, 1991).

3.3.1.9 Conditional selection of particle types.

The multivariate classification procedure as mentioned above, can be applied when there is no previous knowledge on the chemical composition of the samples. The hierarchical classification of particles into a certain number of characteristic groups implies that indeed every particle will be added or pushed into just one group although there is only a marginal similarity. No completely satisfactory statistical test exists for determining the minimum number of significant clusters. So, more often a rather biased method, the so called cut-off-threshold method is applied on the connection diagram that results from the hierarchical cluster routine. To avoid these problems and in order to check the results of the final clustering, we also performed a classification procedure on objects or particles into characteristic groups based on selection rules. Table 3.2 shows the criteria used for a particle to be selected into one particle type. The values in this table also refer to relative percent X-ray intensities that are normalized to the total net X-ray intensities of all elements collected from that particle. The same selection conditions were applied on each microlayer and bulk sea water sample. The constraints for these selection rules can be made more or less severe. However, overlap of the different groups must be avoided.

Table 3.2: Relative X-ray intensities used as criteria for the conditioned selection of the particles in different particle types.

Particle type	Criteria: based on relative X-ray intensities		
1 Aluminosilicates	Al + Si + K + Fe > 90	and	15 < Si < 85
2 Si-rich	Si > 85	and	Al < 5
3 Ca-rich	Ca > 70		
4 Ca-rich aluminosilicates	Ca + Si + Al + K + Fe > 90	and	15 < Ca < 70
5 Fe-rich	Fe + Mn + S + Cl + Cr + Zn + Cu > 90	and	Fe > 50
6 Ti-rich	Ti + Si + Fe + Mn + Cr + Zn + Cu > 90	and	Ti > 50
7 Si-S-rich	Si + S > 75		
8 Al-rich	Al > 50	and	Si < 15
9 S-rich	S > 75		

The choice of the values for the selection rules can be deduced from measurement of standards or from the data obtained from reference samples. The selection criteria used in this work, were derived from the mean relative X-ray intensities of several characteristic particle types found in riverine suspensions and in air masses above the North Sea during either pure marine or continental sampling conditions. The relative intensities and therefore the chemical composition of the specific particle types like aluminosilicates, Si-rich, Ca-rich, Fe-rich and Ti-rich particles agree within less than 10 % for these two different environments. Particle types 8 (Al-rich) and, 7 (Si-S-rich) and 9 (S-rich) were selected using severe conditions derived from atmospheric measurements.

The particle types, as defined by the selection rules, act as a replacement for the hierarchically obtained centroids. Since they are the same for all samples, no further classification routines are necessary.

The relative percentage abundances after such conditional selectioning for each particle type in each sample is given in Table 3.3. The obtained dataset shows good agreement with those obtained by the clustering technique (Table 3.1). No significant differences were observed. The good comparison gives an indication that most of the particles are classified according to the proper training vectors what implies that these training vectors are well formed and separated in space and all 10 samples show high similarity in chemical composition for the clusters i.e. the same particle types are observed in both layers of the water column. There is also good agreement in chemical composition and elemental abundances for particles detected in the water phase of the North Sea compared to those determined in the North Sea atmosphere or in estuarine and riverine suspensions. Thus, our assumption for using these selection criteria is valid.

Closer inspection of the samples shows that, beside quartz, the Si-rich particle type is composed of different subclasses of particles with elemental composition of: Si+Cl, Si+Cl+S, Si+S+Ca and Si+Cl+Ca. Considering the presence of Cl, S and Ca, they are probably related to or derived from a marine or biological environment.

Significant amounts of Si, P, S, Mn and Cr can be present in the Fe-rich particles. This cluster can be sub-divided into five different Fe-rich particle types namely: Fe-oxide/hydroxide/carbonate, and particles rich in Fe-Si, Fe-Cr, Fe-S-P and Fe-Mn. Most of them are believed to have an authigenic character (Van Put, 1991; Bernard, 1989). The sometimes higher Si-contents of these particles could indicate that aluminosilicates act as condensation nuclei for the precipitation of iron. Eventually coprecipitation and/or adsorption of Mn-oxides/hydroxides and of Mn(II) occurs (Ingri and Ponter, 1986). The association of P with

Fe is namely due to adsorption of P onto the Fe-oxides or hydroxides (Williams et al., 1976; Filipek and Owen, 1981). The Fe-oxides, Fe-Mn and Fe-Cr-rich particles were also found in a continentally derived North Sea atmosphere and assigned to industrial sources. Fe-oxide and Fe-Cr rich particles are both released into the atmosphere by ferrous metallurgy processes.

Other elements detected in single particles were V, Co, Mn and Ni. They are associated to an organic fraction as they occur in crude oils as nonvolatile porphyrins (Johannesson, 1955).

The rest group found in Table 3.3 results from the remaining particles that could not be classified in one of the other clusters and comprise particle types like aluminosilicates, Si-rich and Ca-rich particles. However they have element abundances that do not fulfill the proper selection rules.

Table 3.3: Relative percent abundances for the North Sea microlayer and bulk seawater after conditioned selection.

Cruise	March 1986		March 1986		November 1987		June 1987		June 1987	
Particle type	ML1	B1	ML2	B2	ML3	B3	ML4	B4	ML5	B5
Al, Si, Fe	14	32	21	21	47	65	34	45	6.2	16
Si	17	29	25	19	24	20	20	17	13	21
Ca	10	2.0	0.4	8	2.0	0.4	19	18	13	35
Ca, Si	3.5	0.8	0.4	10	1.6	0.4	6.0	8.6	2.2	15
Fe	3.5	2.4	2.0	1.6	1.0	0.4	4.4	1.6	10	1.6
Ti	1.0	1.2	2.0	0.8	1.4	1.6	1.2	1.4	1.4	0.8
Si, S	0.3	0.2	-	1.4	0.4	0.2	-	-	-	-
Al	1.0	0.6	1.2	2.8	1.2	-	0.4	-	-	0.8
S	0.3	-	0.4	0.8	0.4	-	0.2	-	-	0.2
Organic	42	24	34	22	15	1.4	2.0	0.8	36	4.4
M^{n+} (*)	2.4	1.6	2.2	1.6	1.4	1.0	0.4	0.2	3.0	0.4
Rest(**)	6.0	6.2	11	11	4.4	9.0	,12	7.2	15	4.4

(*) % abundance of particles that contain various metal elements (different from Fe and Ti).

(**) % abundance of particles that was not classified in either of the above selected groups.

3.3.1.10 Principal Component Analysis (PCA).

The variations of the characteristic particle types among the various samples can be studied applying principal component analysis (PCA). The relative percent abundances of Table 3.3 were taken as input data for a Data Processing Program (DPP) (Van Espen, 1984). The covariance matrix was used for the calculation of the principal components. The first two principal components explain more than 94% of the total variance in the data (Table 3.4).

Table 3.4: Cumulative eigenvalues and loadings for the first two principal components derived from the covariance matrix performed on the North Sea microlayer and bulk water data.

	Principal Components	
	1	2
Cumulative %	69	94
Aluminosilicates	0.93	-0.34
Silicon-rich	0.10	-0.39
Calcium-rich	0.06	0.97
Ca-rich aluminosilic.	0.11	0.89
Iron-rich	-0.54	0.19
Titanium-rich	0.12	-0.61
Silicon-Sulfur-rich	-0.15	-0.12
Aluminium-rich	-0.37	-0.02
Sulfur-rich	-0.33	0.01
Organic	-0.93	-0.34
Metal-rich	-0.82	-0.47

The loadings of the first two principal components are plotted in Figure 3.12a while the scores are represented in Figure 3.12b.

a)

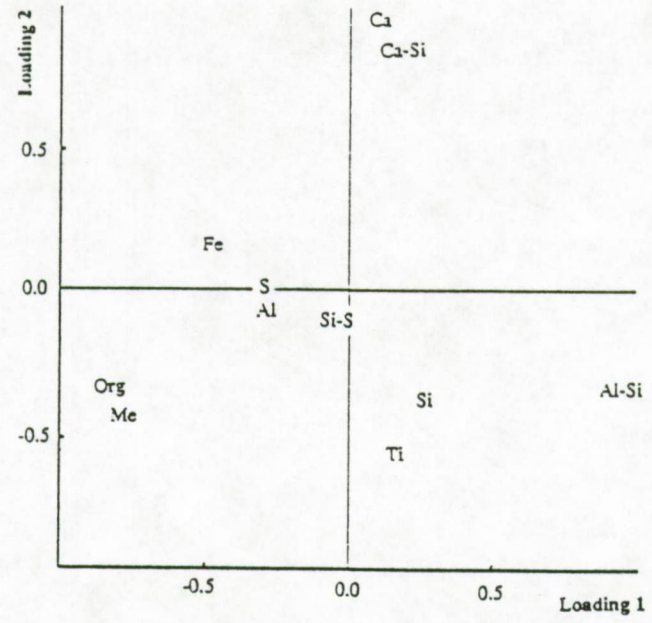

(b)

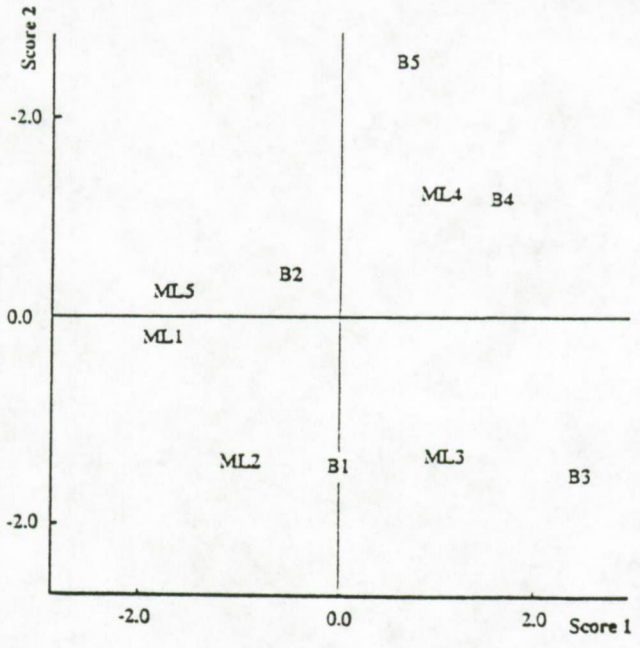

Figure 3.12: (a) Loadings of the first two principal components obtained by PCA of EPXMA of North Sea microlayer and bulk water results. (b) Component scores of the first two principal components obtained from the same data set. Particle types: Org = organic; Me = metal-rich; Fe = Fe-rich; Ti = Ti-rich; S = S-rich; Al = Al-rich; Si = Si-rich; Ca-Si = Ca-rich aluminosilicate; Al-Si = aluminosilicate.

The first principal component elaborates the difference between the aluminosilicates and the organic and metal-rich particles. This can be seen from the high negative correlation between these particle types. Indeed, a two dimensional plot (Figure 3.13a) of the aluminosilicates versus the organic component shows a negative linear relationship (r = -0.74). Contrarilly, Figure 3.13b shows the very good correlation between the organic fraction and the metal rich particles (r = 0.94). The second component has high positive loadings on both the Ca-rich and Ca-Si-rich particle types (Figure 3.13c). The good linear correlation between these two particle types (r = 0.80) might indicate that these particle types can be apportioned to the same source.

When the results were studied on a three-cluster-level using the results of Table 3.3 as input data, the dendrogram as seen in Figure 3.14 shows that one cluster is composed of the sample ML3 together with B3, one cluster of sample ML4 with B4 and B5; and one cluster of ML1, B1, ML2, B2 and ML5. Except for the ML5-B5 pair that is separated in different cluster groups, each microlayer and corresponding bulk water sample are found in the same group. This means that the bulk and corresponding microlayer samples show more resemblance to each other than there is between the various microlayer and bulk water samples taken during the different cruises.

3.3.2 LAMMS Results.

As mentioned previously, the LAMMS technique has not only better detection limits for most of the elements, but is also able to detect elements such as C, N and O.

About 150 particles of each sample were randomly analyzed by LAMMS. Five major particle types could be discerned from these results as shown in Table 3.5; the relative % abundance of each group is based on the EPXMA data. The given particle type abundances should be considered as a slightly biased rough estimate of the actual situation since particles were sometimes subjectively selected on the base of their appearance. No significant differences between microlayer and bulk water samples were observed. Group 1 is the most abundant and reveals the presence of aluminosilicate ions. Negative mode LAMMS spectra revealed that phosphates and less frequently nitrates are found to be present on a large fraction of the aluminosilicate particles. Graham et al. (1979) already suggested that the sea surface microlayer is a major source for organic phosphorus in the ejected drops. Mopper and Zika (1987) interpreted the low molecular weight fragment ions of nitrogen as organic-N-compounds such as dissolved free amino acids and primary amines.

(a)

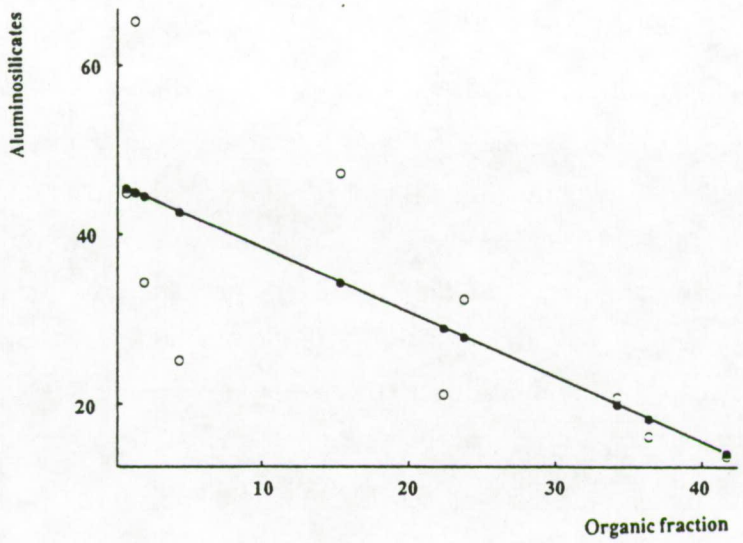

(b)

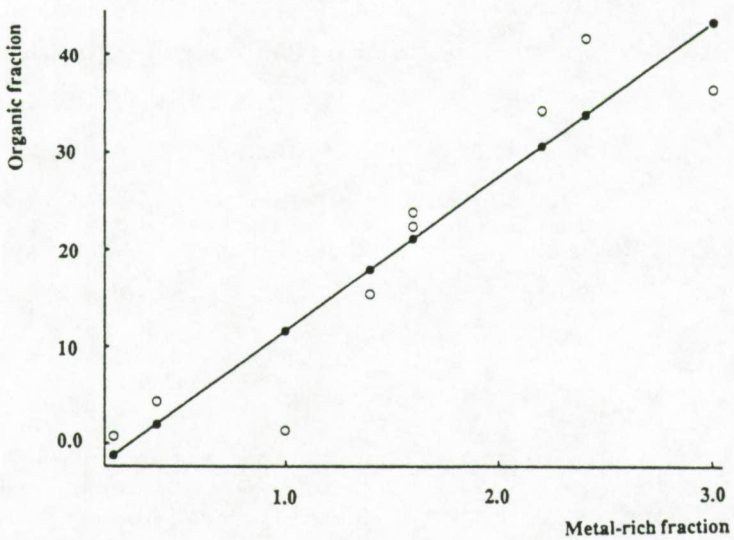

(c)

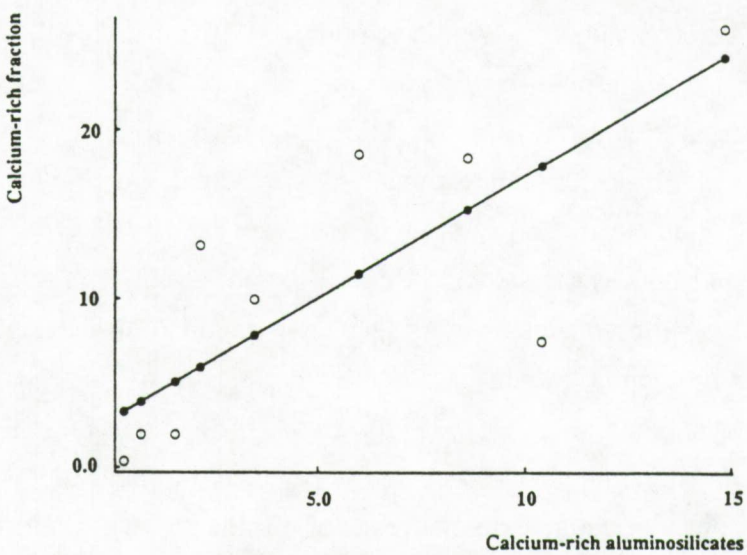

Figure 3.13: Two-dimentional correlation plot of (a) aluminosilicate fraction versus organic particulate fraction, (b) organic fraction versus metal-rich fraction, (c) Ca-rich fraction versus Ca-rich aluminosilicate fraction

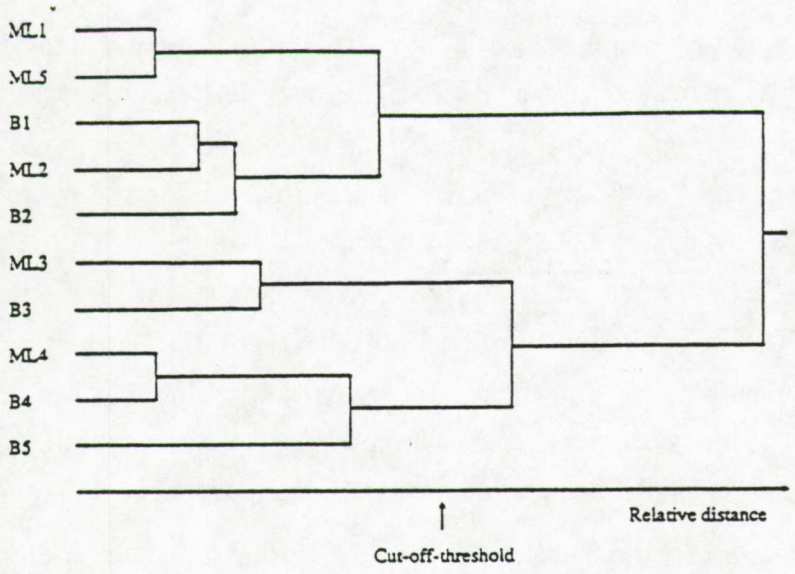

Figure 3.14: Dendogram representation after hierarchical clustering performed on the microlayer and bulk water samples of the North Sea showing the cut-off-threshold for a three-cluster level.

Table 3.5: Abundances of particle types observed in the microlayer and bulk seawater of the North Sea as obtained by LAMMS analysis.

	Mass peaks observed	% abundance
Group 1	Al^+, Si^+, SiO^+	46
	$SiAlO_4^-$, $SiAlO_5^-$, $Si_2AlO_6^-$	
	Cl^-, NO_2^-, NO_3^-	
	PO_2^-, PO_3^-, $H_2PO_4^-$	
Group 2	C_n^+ (n = 1-10)	19
	C_n^-, CNO^-, $HCNO^-$, $HCOO^-$	
Group 3	Si^+, SiO^+, $HSiO^+$, Si_2O^+, $Si_2O_2^+$	26
	SiO_2^-, SiO_3^-	
Group 4	$(CaO)_n^+$, $(CaO)_nH^+$	5
Group 5	Fe^+, FeO^+, Fe_2O^+	4
	$(CuCN)X^-$ (X=CN or Cl)	
	$(CuCl_n)Cl^-$	
	Ti^+, TiO^+	

These authors suggest that high molecular weight organic nitrogen compounds are degraded by chemical processes (in the atmosphere or in the light intensive upper seawater layer) to low molecular weight species, e.g. primary amines and ammonium. Group 2 and 3 classify respectively the organic and Si-rich particles. Also here, phosphates and sometimes nitrates were recognized in negative mode spectra. The detailed composition of the organic material present in the surface microlayer is still unclear. Beside C_n^+-clusters, negative mode fragments of as C_n^-, CNO^-, $HCNO^-$ and $HCOO^-$ could be identified. These have however little or no decisive value for compound determination. They appeared in many particles. The LAMMS spectra are most likely a superposition of many different organic compounds and because of the fragmentation of long chain hydrocarbons, a detailed structural interpretation of the spectra was not possible.

Positive LAMMS spectra of Ca-rich particles (group 4) often reveal the presence of Sr. This result is more or less expected since calcite is known to accommodate Sr in its structure. The metal-rich cluster (group 4) is mainly characterized by Fe and Ti. Especially the Fe-rich phase seemed to contain the highest relative amounts of trace elements like Pb (Figure 3.15a) and Ba. Barium was also found to be associated with aluminosilicates (Figure 3.15b).

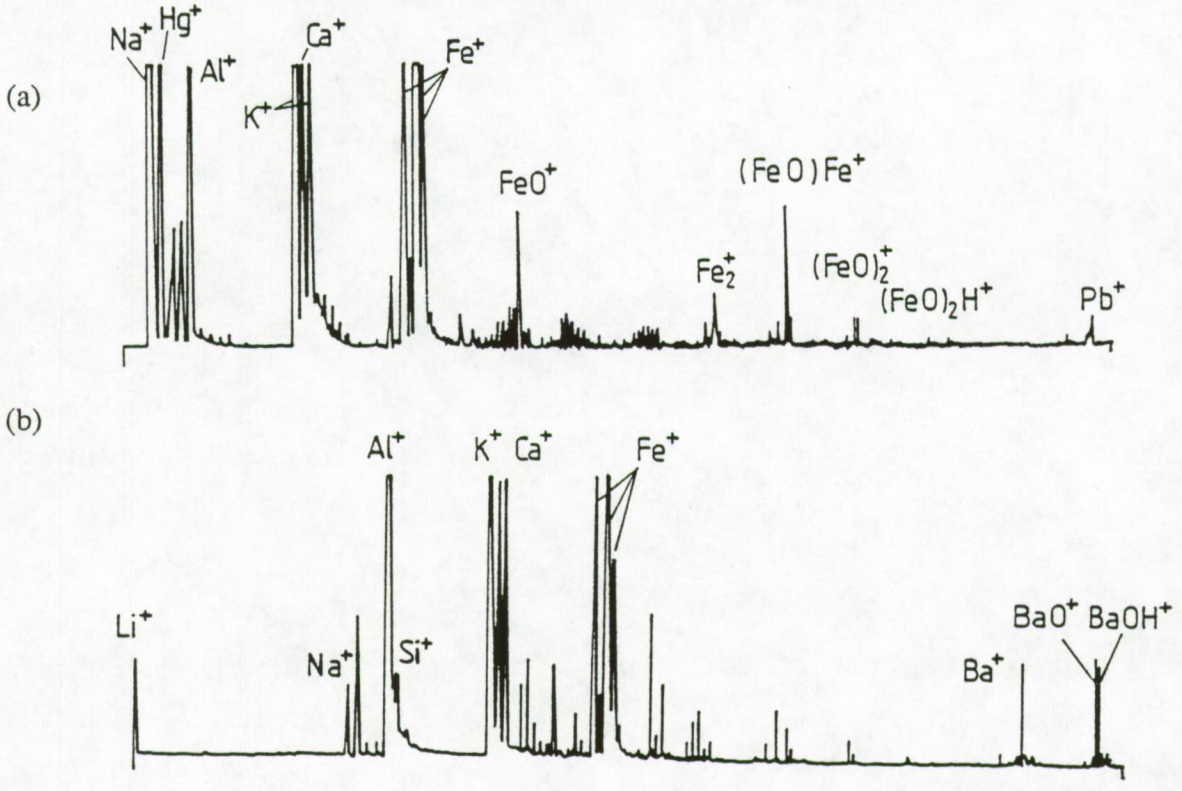

Figure 3.15: LAMMA spectra of (a) an Fe-rich particle present in the water of the North Sea containing relative small amounts of the trace element Pb and (b) an aluminosilicate particle showing associations with Ba mass fragments.

Also some very surprising particle types were observed within this group, namely: mixed particles including Cu clusters with Cl and/or CN/CNO. Indeed, Cu as well as Al, Ti, Mn, Fe, V, Zn, Ni, Pb, Cr and Cd could be scavenged by bubbles and transported to the air/sea interface (Wallace and Duce, 1975). More likely, copper can undergo fractionation in the sea surface microlayer leading to salts having enhanced concentrations relative to bulk sea water and according to Chester and Murphy (1986). Positive mode LAMMS spectra revealed the presence of such elements (Kolaitis, 1988).

3.4 Conclusions

Most of the analyzed particles in the microlayer and underlying bulk water could be chemically characterized and classified into specific particle types. It is not always evident to assign them to one specific source (marine or continental). Source apportionment is even made more difficult because there is hardly any distinction possible between some major particle types observed in either the aquatic or atmospheric environment of the North Sea. On the contrary, chemical data from the atmospheric and riverine/estuarine environment can be used for selection criteria in the particle classification procedure.

During the collection of microlayer samples, the sea surface has to be very calm, which is not always the case in the North Sea. This might explain the low variation observed between the microlayer samples and the corresponding bulk water samples and is probably due to mixing of the water layers.

An important part of the oceanic source of particulate matter is characterized by detritus (dead organisms) like biogenic skeletons of diatoms, foraminifera, but also coccoliths, phytoplankton with minor amounts of bacteria, yeasts and fungi are found. The organic particulate matter was more abundantly observed in the microlayer than in the underlying bulk water and showed very good correlation with the metal-rich fraction.

Aluminosilicates form the major particulate fraction (about 30% of the total number concentration) classified in the North Sea water samples. We observed a relative enrichment for the bulk water compared to the microlayer. Most of these aluminosilicates are clay minerals that can partly originate from coastal sources due to marine erosion. Among the aluminosilicates, fly ash particles were recognized in the sea surface microlayer.

Silicon rich particles represent about 20 to 30% of the total particle concentration. This particle type mainly contains resuspension material and detrital quartz but also biogenic features rich in

silicon. Manual search for morphological information states the presence of diatom skeletons and fragments from sponges. There seems to be no preference for one of the analyzed water layers. Atmospheric deposition processes do not contribute for the total Si-fraction in the water phase.

Si-rich and Ca-rich particulate material present in the North Sea can originate from various sources like e.g. suspended matter that contains the same minerals as the sediment, by transmutation of some mineral substances such as silica and $CaCO_3$ which dissolve and are precipitated by organisms, or from continental aerosol (both natural or anthropogenic) deposition processes.

The Ca-rich aluminosilicates must have an aquatic (marine or riverine) origin since no chemical analogues were observed in air masses above the North Sea.

The relative abundances for the Fe-rich, Ti-rich and metal-rich particle types are rather too low to observe any significant difference between the microlayer and bulk water. It seems that the Fe-rich particle number concentration does not correspond well with the atmospheric number concentrations, whereas good similarity is found for the Ti-rich marine and atmospheric fraction. The metal-rich fraction showed very good correlation with the organic particulate fraction.

3.5 References

Andreae M.O., Charlson R.J., Bruynseels F., Storms H., Van Grieken R., Maenhaut W.; Internal mixture of sea salt, silicates and excess sulphate in marine aerosols, *Science*, 232, 1620-1623, 1986

Barker D.R., Zietlin H.; Metal-ion concentrations in sea-surface microlayer and size-separated aerosols sampled in Hawaii, *J. Geophys. Res.*, 77, 5076-5086, 1977

Bernard P.; Automated electron probe X-ray microanalysis combined with multivariate analysis for application in marine research, Ph.D. Thesis, University of Antwerp (UIA), Belgium, 1989

Blackmore A.V.; Aggregation of clay by products of iron 3 hydrolysis, *Aust. J. of Soil. Res.*, 11, 75, 1973

Blanchard D.C.; Sea-to-air transport of surface active material, *Science*, 146, 396-397 (1964)

Broecker W.S.; *Quaternary Res.*, 1, 188-207, 1971

Cattel F.C.R., Scott W.D.; Copper in aerosol particles produced by the ocean, *Science*, 202, 429-430, 1978

Chester R., Murphy K.J.T.; Oceanic sources of copper to the Atlantic aerosol, *Sci. Tot. Environ.*, 49, 325-338, 1986

Chow T.J., Patterson C.C.; Concentration profiles of barium and lead in Atlantic waters of Bermuda, *Earth and Planetary Science Letters*, 1, 397-400, 1966

Degens E., Buck B.; Smear-sliding around Sumbawa, *Cruise SO 45-B report*; Lembar-Sumbawa Bear-Surabaya, 1986

Duce R.A., Quinn J.G., Olney C.E., Piotrowiez S.R., Ray B.J., Wade T.L.; Enrichment of heavy metals and organic compounds in surface microlayer of Narragansett-Bay, Rhode-Island, *Science*, 176, 161, 1972

Duedall I.W., Roethel F.J., Seligman J.D., O'Conners H.B., Parker J.H., Woodhead P.M.J., Dayal R., Chezar B., Roberts B.K., Mullen H.; Stabilized power plant scrubber sludge and fly ash in the marine environment, in "Marine Science 12": *Ocean Dumping of Industrial Wastes*; Ketchum B.H., Kester D.R., Park P.K., Eds.; Plenum Press, New York and London, 315-346, 1981

Filipek L.H., Owen R.H.; Diagenetic controls of phosphorus in outer continental shelf sediments from the Gulf of Mexico, *Chem. Geol.*, 33, 181-204, 1981

Fordham A.W.; Location of Fe-55, Sr-85 and I-125 sorbed by kaolinite and dickite particles, *Clays and Clay Minerals*, 21, 175, 1973

Garrett W.D.; Organic chemical composition of ocean surface, *Deep-Sea Res.*, 14, 221, 1967

Garrett W.D.; *Organic Matter in Natural Waters*; Hood D.W., Ed.; 469-477, 1970

Goldberg E.D.; Biogeochemistry of estuarine sediments, *Proc. Workshop in Melreux/Belgium Nov. 29-Dec.* 3, 1976 UNESCO Press, Paris, 1978

Graham W.F., Piotrowicz S.R., Duce R.A.; Sea as a source of atmospheric phosphorus, *Marine Chem.*, 7, 325, 1979

Hood D.W.; Chemistry of the Oceans: Sometrace metal-organic oxidations and chemical parameter differences in top one meter of surface, *Environ. Sci. Tech.*, 1, 303-305, 1967

Horne R.A.; "*Marine Chemistry*"; Wiley and Sons, New York-London-Sydney-Toronto, 253, 1969

Hunter K.A.; Processes affecting particulate trace metals in the sea surface microlayer *Mar. Chem.*, 9, 49-70, 1980

Ingri J., Ponter C.; Iron and manganese layering in recent sediments in the Gulf of Bothnia, *Chem. Geology.*, 56, 105-116, 1986

Johannesson J.K.; The identification of fuel oil polluting coastal waters, *Analyst*, 80, 840-841, 1955

Kido K.; Latitudinal distribution and origin of particulate silica in the surface water of the North Pacific, *Mar. Chem.*, 2, 277-285, 1974

Kolaitis L.; Applications of laser ionization/desorption in mass spectrometry, Ph.D. Thesis, University of Antwerp (UIA), Belgium, 1988

Koppelman M.H., Dillard J.C.; An ESCA study of sorbed metal ions on clay minerals, in "Marine Chemistry in Coastal Environment"; Church T.M., Ed.; *ACS Symposium Series 18*, American Chemical Society Washington, D.C., 186, 1975

Kremling K.; Trace metal fronts in European shelf waters, *Nature*, 303, 225-227, 1983

Laevastu T., Thompson T.G.; Soluble Fe in Coastal waters, *J. Marine Res.*, 16, 192, 1958

Liss P.S.; Chemistry of the sea surface microlayer, in "*Chemical Oceanography*", Part 2, 2-nd edition; Riley J., Skirrow G., Eds.; Academic Press: London-New York-San Francisco, 193-243, 1975

Mackenzie F.T., Garrels R.M.; Silicates-reactivity with sea water, *Science*, 150, 57-58, 1965

Mackenzie F.T., Garrels R.M., Bricker O.P., Bickley F.; Silica in sea water - control by silica minerals, *Science*, 155, 1404-1405, 1967

Mamane Y., Miller J., Dzubay T.G.; Characterization of individual fly-ash particles emitted from coal- and oil-fired power plants, *Atmos. Environ.*, 20, 2125-2135, 1986

McCrone W.C., Delly J.G.; The Particle Atlas, Edition two: An encyclopedia of techniques for small particle identification, Vol III, "*The electron microscopy atlas*", Ann Arbor Science Publishers Inc., Michigan, 1973

Merlini M.; Heavy metal contamination, in "*Impingement of Man on the Oceans*"; Hood D.W., Ed.; John Wiley & Sons, Inc. New York,-London-Sydney-Toronto, 461-486, 1971

Michard G., Sanjuan B., Criaud A., Fouillac C., Pentcheva E.N., Petrov P.S., Alexieva R.; *Geochem. J.*, 20, 159-171, 1986

Mopper K., Zika R.G.; Free amino-acids in marine rains - evidence for oxydation and potential role in nitrogen cycling, *Nature*, 325, 246, 1987

Otten P.; Transformation, concentrations and deposition of North Sea aerosols, Ph.D. Dissertation, University of Antwerp (UIA), Belgium, 1991

Parsons T.R.; Suspended organic matter in sea water, *Progr. Oceanogr.*, 1, 203-243, 1963

Piotrowicz S.R., Ray B., Hoffman G.L., Duce R.A.; Trace metal enrichment in the sea surface microlayer, *J. Geophys. Res.*, 77, 5243-5254, 1977

Post J.E., Buseck P.R.; Characterization of individual particles in the Phoenix urbam aerosol using electron beam instruments, *Environm. Sci. Technol.*, 18, 35-42, 1984

Riley J., Chester R.; "*Introduction to Marine Chemistry*"; Riley J., Chester R., Eds.; Academic Press, London, New York, 1971

Rona E., Hood D.W., Muse L., Buglio B.; Activation analysis of Mn and Zn in seawater, *Limnol. Oceanogr.*, 7, 201-206, 1962

Simoneit B.R.T., Mazurek M.A.; *CRC Critical Reviews in Environmental Control*, 11, 219, 1985

Slowey J.F., Jeffrey L.M., Hood D.W.; Evidence for organic complexed Cu in seawater, *Nature*, 214, 377-378, 1967

Södegren A.; The significance of surface microlayers in evaluation of persistent pollutants with aquatic model ecosystems in "*Aquatic Pollutants Transformation and Biological Effects*"; Hutzinger O., Van Lelyveld L.H., Zoeteman B.J.C., Eds.; Pregamon Press, Oxford, New York, Toronto, Sydney, Paris, Frankfurt, 1977

Szekielda K-H., Kupfermann S.L., Klemas V., Polis D.F.; Element enrichment in organic films associated with aquatic frontal systems, *J. Geophys. Res.*, 77, 5278-5282, 1972

Vanderborght J.-P., Wollast R., Billen R.; Kinetic models od diagenesis in disturbed sediments, Part 1: Mass transfer properties of silica diagenesis, *Mar. Chem.*, 22, 787-793, 1977

Van Espen P.; A program for the processing of analytical data (DPP), *Anal. Chim. Acta*, 165, 31-49, 1984

Van Put A.; Geochemical and morphological characterization of individual particles from the aqueous environment by EPXMA, Ph.D. Thesis, University of Antwerp (UIA), Belgium, 1991

Veldeman E.; Geochemical characterization of hydrothermal systems in a granitic environment, Ph.D. Thesis, University of Antwerp (UIA), Belgium, 249, 1991

Wallace G.T., Duce R.A.; Concentration of particulate trace metals and particulate organic carbon in marine surface waters by a bubble flotation mechanism, *Mar. Chem.*, 3, 157-181, 1975

Williams J.D.H., Jacquet J.M., Thomas R.L.; Forms of phosphorous in surfacial sediments of Lake Erie, *J. Fisheries Research Board of Canada*, 33, 413-429, 1976

Wollast R.; in "*In the sea: ideas and observations on progress in the study of the seas*"; Goldberg E.D., Ed.; J. Wiley & Sons, New York, London, Sydney, Toronto, 359-393, 1974

Xhoffer C.; Elektronenprobe microanalyze van vliegas en partikels uit het marine milieu, M.Sc. Thesis, University of Antwerp (UIA), Belgium, 1987

Xhoffer C., Bernard P., Van Grieken R., Van der Auwera L.; Chemical characterization and source apportionment of individual particles over the North Sea and the English Channel using multivariate techniques, *Environ. Sci. Technol.* 25, 1470-1478, 1991

CHAPTER 4

Principles and Practice of Electron Energy Loss Spectroscopy

4.1 Introduction

As demonstrated in chapter I, electron-beam instruments such as scanning electron microscopes (SEM), (scanning) transmission electron microscopes [(S)TEM] and especially electron probe X-ray microanalyzers (EPXMA) have proven their success in various fields like physics, biology, medicine and chemistry for quite some time. However each of these techniques is either limited by resolution, by detection possibilities (high detection limits or low-Z elemental detection), or by a lack of qualitative and/or quantitative information. From a theoretical point of view, electron energy-loss spectroscopy (EELS) does not show these shortcomings, but practically, analyses are not always as rosy as often presented.

EELS is best compared with EPMA to which it is complementary. The advantages and disadvantages of both techniques are discussed later in this chapter.

Apparatus for EELS has recently become commercially available and until now very few publications have dealt with individual particle analysis (Wolf, 1988; Katrinak et al., 1992; Maynard and Brown, 1992).

Most of the recent work concerning EELS in electron microscopy is related to instrumental developments and physical applications. The aim of this part of the thesis is to attempt to present in a pedagogical manner the subject of EELS and single particle analysis.

In this chapter we will discuss the main aspects of EELS in a more theoretical way as it is of importance for microanalysis studies. By combining electron spectroscopy and transmission electron microscopy, the analytical power of EELS is coupled with the ability to select, image and obtain diffraction patterns from small areas.

The following chapters will demonstrate the use of EELS within various domains of individual particle analysis pointing out some specific analytical and chemical information that can be obtained.

4.2 The electron energy-loss spectrum

Electron energy-loss spectroscopy (EELS) studies the energy distribution of electrons after they have been transmitted through a very thin sample. As the electrons of the beam (initial energy of E_0) interact with electrons of the atoms present in the sample, they can loose an amount of energy ΔE characteristic for these atoms. The initial electrons will leave the sample with reduced energy (E_0-ΔE). Thus the electron energy-loss spectrum represents the graphical display of the energy lost (ΔE) by the scattered electrons as a function of their corresponding intensity. Accordingly, EELS detects directly the electron beam interaction with the atoms, which in turn, produces inner shell ionizations, rather than the subsequent decay of this ionization to produce an X-ray photon. The principle of EELS is thus based on the theory of electron-solid interactions. We will see how the various interactions can be related to the properties of the specimen by examining the features of a typical energy-loss spectrum (Figure 4.1).

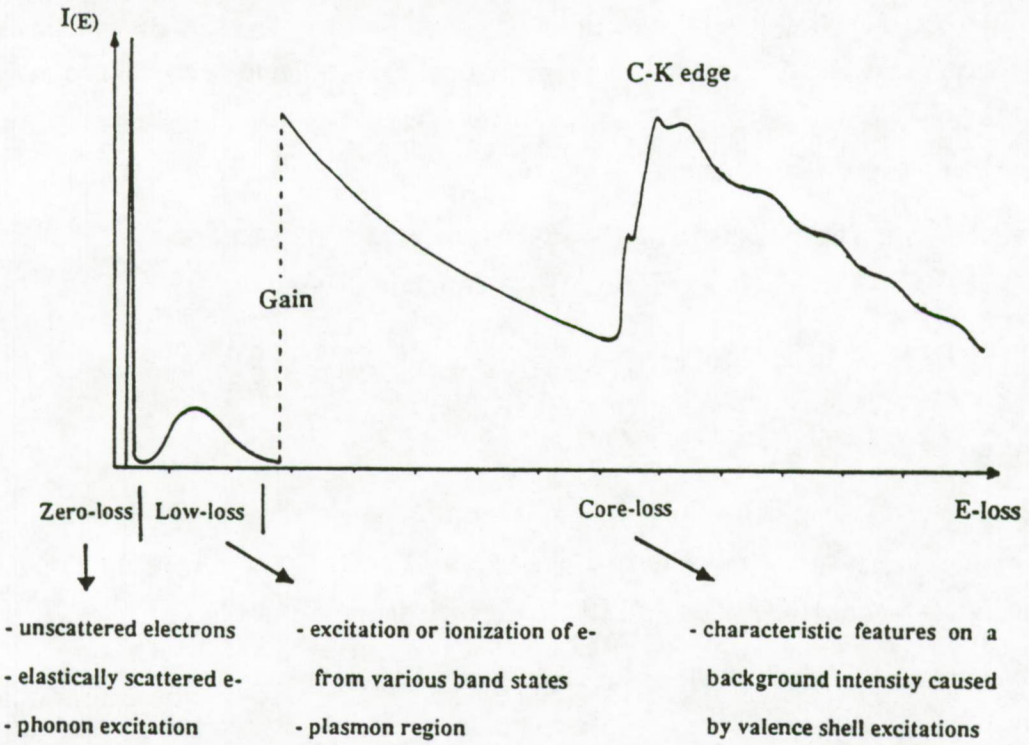

Figure 4.1: Typical electron energy-loss spectrum recorded from a thin carbon foil showing the different features and the physical processes that have given rise to them.

4.2.1 Zero-loss peak

The zero-loss peak is by far the most intense feature of the spectrum and so it demands some attention even though it is of limited use for microanalysis. The definition of "zero-loss" needs to be qualified because the peak has a definite width. There are two reasons for this. First, any spectrometer has a definite energy resolution typically in the range of 1 - 5 eV. Second, the incident beam of electrons has an energy spread in the range of 1.5 ev for a thermionic tungsten filament. With this proviso, the zero-loss peak contains three groups of electrons that can be classified to electrons that have not lost any significant amount of energy namely:

- Those that are unscattered, having passed trough the sample without being involved in any interaction and thus carrying no significant information. The angular distribution represents typically a cone of 10^{-3} rads.
- Elastically scattered electrons which have been deflected by the nuclear charge of an atom. This event is mainly caused by Coulomb interactions. Electrons can be scattered over a high angle by the electric field of the atomic nuclei present in the material.
- Phonon excitation. Phonons are thermal vibrations of the atoms in the sample and, although present in all materials, they are most significant in crystals. In transmission electron microscopy, these vibrations are generated as a result of the conversion of kinetic energy from the electron beam into heat in the specimen. The energy loss associated with phonon scattering is small, typically 0.1 eV or less. Hence, these losses are indistinguishable from the components of the zero-loss peak.

The angular distribution of the transmitted zero-loss electrons is comparable to that of the incident electron beam (~1-5 mrad). Although the microanalytical information carried by the zero-loss peak is small, its importance should not be underestimated. It provides the energy reference for the spectrum, gives a measure of the resolution and accuracy of spectrometer adjustment and provides the normalization factor required for quantitative microanalytical calculations.

4.2.2 Low-loss region

The low-loss region can conveniently be denoted as the portion of the spectrum extending from the edge of the zero-loss peak out to about 50 eV. The signal intensity of the plasmon region is normally about 5% to 15% that of the zero-loss peak. The plasmon energy losses are due to direct

electrostatic interactions in which atomic valence or conduction electrons are excited. These inelastic scattering processes from outer-shell electrons may involve many atoms of the solid giving rise to a peak, or in some cases, to a series of peaks. The best known of these events is the "Plasmon" excitation, a collective effect also known as plasma resonance (an oscillation of the valence-electron density). Plasmon excitations occur in metals and in alloys that have a large number of valence electrons free enough to participate in such a collective oscillation.

The lowest energy losses (below 15 eV) come from excitations of electrons in molecular orbitals. Each molecular type has a characteristic spectrum in this range which, although too complex to be interpreted directly, can be used as a "fingerprint" (Hainfeld and Isaacson, 1978). For example, the graphitic form of carbon shows a peak at 6 eV that is absent in amorphous carbon. Above 15 eV, the spectrum shows structures which are mostly due to valence shell excitations. There is often a broad peak observed in biological sections that is centered around 20 eV. Isaacson (1972) suggested these electron excitations to come from π-π^* transitions.

It is worth noting that plasmon excitations provide a convenient way to assess, directly from the EELS spectrum, whether or not the sample is thin enough for good microanalysis, since the thickness should be significantly less than the mean free path of plasmon scattering (λ_p). The theory is based on the probability that plasmon excitation obeys Poisson's law as we will see later in paragraph 8 of this chapter.

4.2.3 Core losses

At energy losses above 50 eV, the tail of the plasmon peak, the transmission electron intensity decreases according to some fairly high power of energy loss, making it convenient to use a logarithmic scale for the recorded intensity. The background in this region is mostly due to valence excitations and plasmon losses. Superimposed on the background are the so called characteristic, or "core-loss" edges, which are the visible evidence that an atom has been ionized. These inner-shell "ionization edges" are the result of interaction processes between the incident electrons and the inner shell electrons of the atoms. As sufficient energy is transferred from the electron to the atom, the ionization threshold (e.g. K-shell ionization requiring an energy E_k) is reached giving rise to well defined transition from a core atomic level towards a vacant electronic state above the Fermi level. The result is a characteristic edge at an energy-loss coordinate corresponding approximately to the binding energy of the specific atomic shell. Since atomic binding energies depend on the atomic number of the scattering atom, the ionization edges

present in an energy-loss spectrum indicate which elements occur within the specimen. The threshold energies for inner-shell ionizations occur at slightly higher energies than the corresponding X-ray emission energies. The lower energy of emitted X-rays is because some energy is redistributed during the process of repopulating the inner-shell electron state.

Because of the complexity of the background intensity, it is impossible to calculate its contribution to the total spectrum from first principles. It has however been found experimentally (Egerton, 1975; Maher, 1979; Joy, 1979) that the intensity of the background is of the form:

$$I = A.E^{-R} \tag{4.1}$$

where I is the measured intensity, E is the energy loss and A and R are parameters depending on the acceptance angle β of the spectrometer. R varies between 2 and 6 (Liu and Brown, 1987). The angular distribution of the background is fairly broadly forward peaked, so that for small collection angles β, the intensity is low. Just as for X-ray spectroscopy, the characteristic absorption edges are of major importance for the microanalytical approach of EELS. The rapid increase in the spectrum intensity at the edge makes it fairly easy to distinguish among the elements. However, the gradual decrease in intensity following the edge means that there is commonly significant overlap from the trailing tail arising from the excitation of inner-shell electrons of one element to the edge of another element. Such overlaps greatly complicate quantization and consequently limit the sensitivity and accuracy of chemical analysis using EELS.

EELS can observe edges of all elements from Li to U. They have at least one edge in the energy loss range of 0 to 2000 eV that can be used for analysis.

One complication in energy loss spectra is the variation in edge shapes that can be observed. For EELS analysis at small angles, the dipole selection rules hold approximately and many aspects of the edge shape can be understood from application of these rules. Remembering the quantum numbers necessary to distinguish atomic electrons, the nomenclature of the EELS edges can be given according to Table 4.1. For chemical analysis using electron energy losses, low Z elements from Li to Si can be identified by the K-onset features. These edges are always cusp shaped and retain their "sawtooth" shape for different values of E_0 and β. For the determination of elements from Mg up to As, it is better to go over to L edges. These peaks show more rounded profiles for Na to Cl.

Table 4.1: Nomenclature for EELS edges.

Quantum numbers			EELS edge
n	l	j	
1	0	1/2	K
2	0	1/2	L_1
2	1	1/2	L_2
2	1	3/2	L_3
3	0	1/2	M_1
3	1	1/2	M_2
3	1	3/2	M_3
3	2	3/2	M_4
3	2	5/2	M_5
.	.	.	.

n = main quantum number n=1, 2, 3,...

l = orbital quantum number l = n-1,...0

j = total angular quantum number $j = l \pm 1$

s = electron spin quantum number s = 1/2

The maximum in their edge intensity is not at threshold but delayed by about 10-15 eV. This is because for 2p (L_{23}) excitations, the allowed final states have d or s character as the selection rule states that Δl, the change in angular momentum, is equal to ± 1. As an electron is ejected to the continuum, an additional term $l(l+1)/r^2$ appears in the effective atomic potential of the radial Schrödinger equation, also called the centrifugal barrier and causes shifts towards higher energy losses. This effect can be seen in Figure 4.2 where a net Si-L_{23} edge is presented. At threshold the intensity mainly comes from the p - s transitions. Superimposed on the 2p edge is the much smaller 2s edge (L_1) which has a much lower transition probability. As the Si-$L_{2,3}$ edge becomes very weak, the maximum of the peak at about 110 eV loss becomes the only visible evidence of the presence of Si.

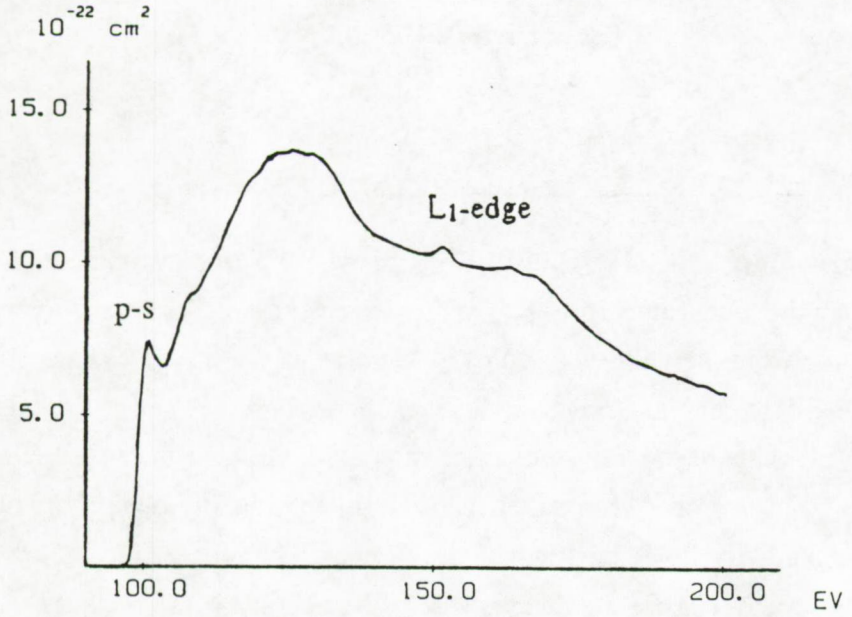

Figure 4.2: Experimental Si-L_{23} edge shape obtained from a SiC particle.

For the fourth-period elements (K, Ca and Sc), d states become bound or transitions to the d like states just above threshold are strongly favoured. This will result in quite distinctive L-peaks at threshold that are often called "white lines". In fact the correct quantum number to use when analyzing inner shell edges is j which is given by $j = l \pm s$. The atomic levels are $2p^{2/3}$ (L_3) and $2p^{1/2}$ (L_2) and the energy difference is called the spin orbit splitting. Consequently two threshold peaks can be observed, whose separation can vary between 8 and 20 eV for the transition elements.

For fifth-period elements, it is generally advisable to look for the very strong M edges that are particularly useful for rare earth elements (Ahn and Krivanek, 1983). Edges arise from excitations of 3d electrons and appear with the intensity maximum delayed by 50 to 100 eV beyond the threshold. Small bumps arising from 3p excitations (M_{23} edges) are often seen on the tail of the edge.

4.2.4 Edge Fine Structures

More often, characteristic absorption edge region contain more analytical information than simply the identification of the element composition. Sometimes valence states and local

environments of atomic species can be obtained. These properties can be determined from EELS spectra by using the techniques of EXELFS and ELNES.

4.2.4.1 EXELFS

Extended energy-loss fine structure (EXELFS) is a weak periodic modulation caused by interference between the outgoing electromagnetic wave emitted from the ionized atom and components reflected from neighboring atoms (Leapman et al., 1981). This fluctuation or fine-structure in the EELS edge extends over several hundreds of eV above the edge onset and contains information about the bonding environment of the atom in question. EXELFS has a great potential, but significant problems arise because of the relatively low number of counts plus the even lower intensities of the fluctuations. These effects combine to produce poor counting statistics. So EXELFS are rarely observed.

4.2.4.2 ELNES

Just around the edge energy E_k there is often a "pre-ionization fine structure" observed. The form is a function of the density of occupied bound states into which the ionized electron can be placed. These structures, also known as energy loss near edge fine structures (ELNES), vary depending on the chemical and crystallographic state of the atom. For example quite marked changes are observed in the shape of a carbon edge for graphite, diamond and silicon carbide (Egerton and Whelan, 1974). ELNES modulations are stronger than those of EXELFS, but they are more difficult to interpret. They can however be used qualitatively to determine the atomic coordination of the elements in a sample. By calibrating the form of the ELNES with samples of the same elements in known coordination, the coordination of the same elements in poorly known samples can be specified (Taft and Zhu, 1982).

4.2.5 Multiple scattering

Multiple scattering can significantly change the appearance of energy loss spectra. As the specimen gets thicker the first thing that is noticed is the appearance of multiple plasmon peaks. Then the jump ratio for low lying inner shell edges will deteriorate with energy. Multiple scattering can be minimized by using a higher accelerating voltage (Jouffrey, 1984). It is also

possible to process spectra mathematically to recover the single scattering profile (Johnson and Spence, 1974). This process is often called deconvolution and should not be confused with the deconvolution of overlapping X-ray peaks. In theory it should only apply if all inelastically scattered electrons are collected but in practice the restrictions may be less severe. An example of single scattering profile recovery is given in Figure 4.3 for a spectrum collected from a $(NH_4)_2SO_4$ particle.

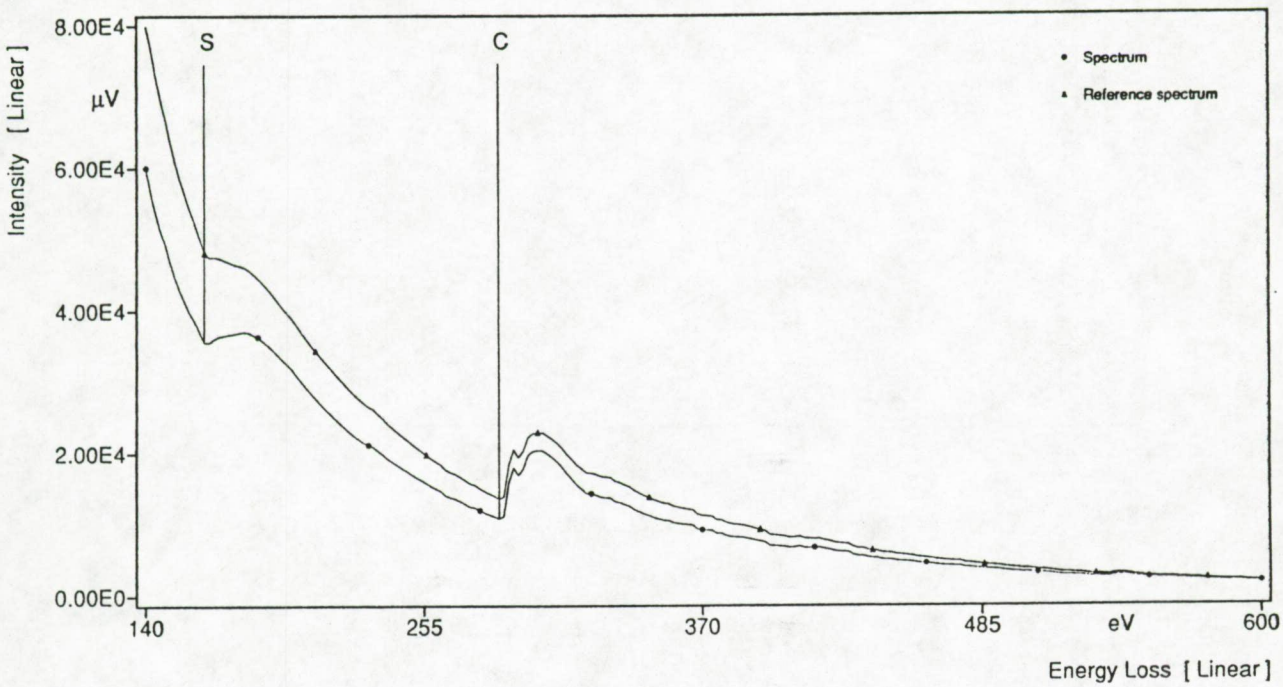

Figure 4.3: Logarithmic single scattering recovery (deconvolution) for the sulfur edge of a $(NH_4)_2SO_4$ particle. The triangles represent the original spectrum and the points represent the recovered deconvoluted spectrum.

Deconvolution generally improves the signal-to-background ratio (jump ratio) and sharpens the fine-structure in the spectrum, although it can also introduce artifacts. However, deconvolution does not improve the signal-to-noise and so it is preferable to use specimens thin enough to be free of plural scattering.

4.3 Quantitative EELS analysis

One of the important applications of energy loss spectroscopy is quantitative analysis, particularly of light elements. Figure 4.4 shows parameters that are to be selected prior to spectrum processing for quantitative purposes.

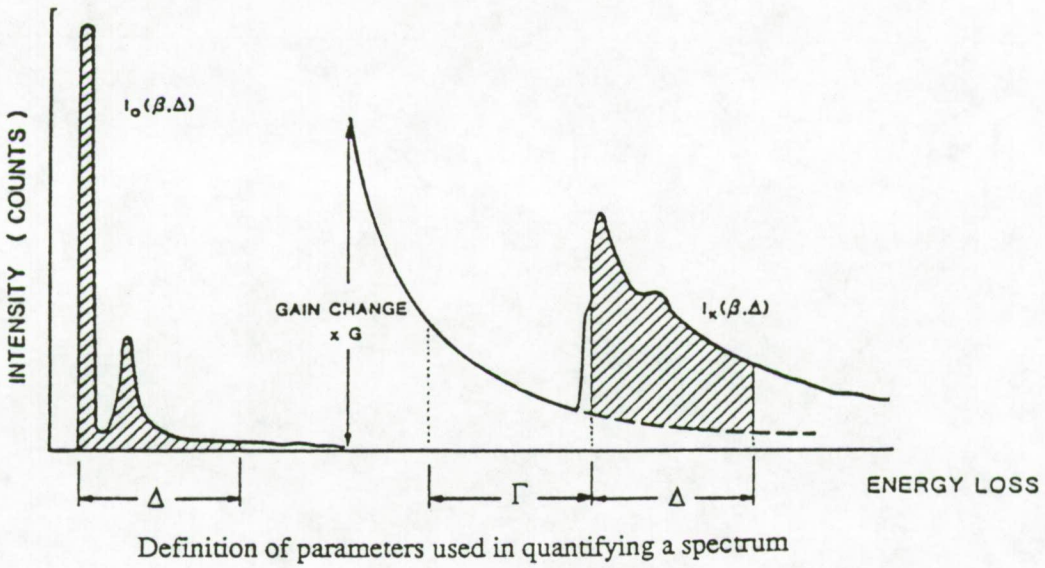

Figure 4.4: Definitions of parameters used in quantifying a spectrum.

Here, Γ and Δ represent respectively the fitting and extrapolation region. Both of these parameters have to be chosen with care since they are of most importance for the determination of the final statistics in quantitative analysis.

Quantitative analysis is simply the conversion of the measured number of inner-shell excitation events to an atomic concentration. From a recorded EELS spectrum, one can get the elemental concentration (N) of a particular element, expressed as the number of atoms per area, using the equation:

$$N = \frac{I_k(\beta,\Delta)}{I_0(\beta,\Delta)\ \sigma_k(\beta,\Delta)\ G} \qquad (4.2)$$

where $I_0(\beta,\Delta)$ represents the integrated intensity from the zero-loss and low-loss region and $I_k(\beta,\Delta)$ is the area above the background and beyond the k-shell ionization edge (k = K, L, M...) as integrated for an energy window equal to Δ and a scattering angle less than β. $\sigma_k(\beta,\Delta)$ is the corresponding partial cross section for inelastic scattering from a particular shell of an element, and G accounts for the gain change of the detector between low- and high-energy regions of the spectrum. Although this expression is an approximation, it has been found to be very satisfactory in use (Egerton, 1978). The net integrated energy intensities are determined from the experiment while the hydrogenic "SIGMAK2" and modified hydrogenic "SIGMAL2" cross sections are used for the calculation of the partial cross sections of, respectively, the K- and L-edges (Egerton, 1986).

In general, an absolute measure of N is less useful than the relative number of atoms of each constituent. The ratio N^x/N^y for two elements X and Y in the same particle, giving rise to the characteristic edges, can then be calculated from the relation:

$$\frac{N^x}{N^y} = \frac{I^x(\beta,\Delta)\ \sigma^y(\beta,\Delta)}{I^y(\beta,\Delta)\ \sigma^x(\beta,\Delta)\ G'} \qquad (4.3)$$

where G' refers to the gain change between the regions of the two elements of interest. Note that equation (4.3) can be used for elements of different edge-types.

One has to be aware that changing the fitting-window region (Γ) by even one channel, might change the values of both A and R, and this will lead to statistical error in the calculation of the peak integral. The region over which the background fit is performed should be chosen with care. If the fitting region is too wide, A and R may not be constant and the fit will be poor. As a practical guide, the width of the background fitting region (Γ) should not exceed ~ 30% of E_k. This means that for a C-K edge at 300 eV a Γ of less than 100 eV should be selected. Although some authors proposed different "goodness of fit" criteria (Trebbia and Manoubi, 1989; Unser et al., 1987), the quality of the fit should in any case be visually judged by superimposing the computed background fit over the experimental spectrum (Joy, 1986). The integration window (Δ) must be large enough to cover all fine structures in the cross section calculations but, in order to fulfill the power law, it should not be too large. A Δ is best to be less than or equal to the region over which the background fit (Γ) is performed (Joy, 1986). The extrapolated fit must not intersect the spectrum. If a proper fit cannot be achieved, it is usually a sign that the spectrum is corrupted by one or more artifacts (Joy and Maher, 1980). A good check on the reliability of a

quantitative EELS analysis is to apply equation (4.1) for several different energy windows. This often shows those cases where the procedure is failing because of multiple scattering. Nowadays a power law fit can be used that is searched by minimizing the χ^2 parameter between the model curve and the exponential data for each of the edges (Van Puymbroeck, 1992).

The net edge integral (I_k) is calculated by integrating the total edge intensity (I_t) over the preset energy window (Δ) and subtracting the extrapolated background (I_b) values for the corresponding channels within Δ. The standard deviation of the characteristic edge signal is based on the error propagation and calculated as proposed by Van Puymbroeck (1992). Only statistical errors are taken into account rather than errors of the measurement itself (incorrectly measured values for the electron-collection angle, β, or lens aberration errors) and errors in the inelastic cross sections used. Statistical errors can occur in the measurement of the characteristic edge intensity (I_k) arising from the limited number of core-loss electrons included within the integration window Δ (Egerton, 1984). However, this error is normally small in comparison with extrapolation errors inherent in the background fitting procedure. The extrapolation error is partly statistical, being related to the number of electrons recorded within the background fitting region and related to the range of the extrapolation (Egerton, 1984; Rez, 1983).

The method generally used for the calculation of the partial cross section relies on the "hydrogenic" atomic model (Inokuti, 1971), which treats an atom of atomic number Z as if it were a hydrogen atom possessing a nuclear charge of Z, with a binding energy equal to that of the K- (or L-) shell of the real atom. Two short computer programs "SIGMAK2" for K-shell and "SIGMAL2" for L-shell ionizations have been developed by Egerton (1986) and used throughout this work for cross section calculations.

For serial recording, a detector gain change is introduced to expand the dynamic range if the characteristic features are separated by an energy increment of more than 300 eV. For quantization, one needs to determine this gain factor, G, accurately. This determination can be done by calculating the amplification ratio from the intensities between overlapping channels for the two connecting regions (Van Puymbroeck, 1992).

4.4 Instrumentation

In 1986, the first dedicated EELS instrument derived from a conventional TEM became available from ZEISS. This instrument, the ZEISS EM 902 uses a magnetic-prism spectrometer of the Henry-Castaign-Ottensmeyer type that is integrated in the optical column and positioned between

the imaging lenses. Owing to the dispersive properties of the prism and the characteristics of a lens, the energy filter has a dual operation mode. On the one hand, electrons of different energies can be dispersed in a plane that contains the electron energy loss spectrum (spectrum mode). On the other hand, within the same prism geometry, there exists an image plane that can be projected to form a real image (image mode). An aperture or slit can be selected so that the final image is an energy selected (or filtered) image. Figure 4.5 gives a schematic representation of the ZEISS EM902. The energy loss spectra of the ZEISS EM902 is sequentially collected by scanning the energy-loss spectrum over a small slit. The acceleration voltage is limited to 80 keV. The intensity of the transmitted electron-loss signal is converted into a voltage and integrated by a PREMA 4000 digital voltmeter. The digital read-out is transferred to, stored, and displayed on an IBM compatible personal computer (PC/AT) acting as a multichannel analyzer (Van Puymbroeck et al., 1989). Typical acquisition times are in the order of 10 minutes for an energy span of 400 eV and a 3 times 1 second acquisition per channel in steps of 2 eV. Recording times can be reduced at the expense of the statistical validity of the obtained data. If the spectrometer is operated in image mode, the energy filtered image can be deflected into a silicon intensified vidicon camera. The intensity of the electronic signal per image pixel can be transferred, stored and processed by an image processing system. This procedure is important for obtaining element specific images (ESI) as it enables to picture element maps. The methodology of ESI will be discussed separately in the next chapter. The whole EELS and ESI environment is schematically presented in Figure 4.6.

4.5 Preparation of the specimen support

Very small particles to be examined by electron microscopy are not self supporting and must always be mounted on a thin membrane supported by a grid. Before any particulate material can be examined, grids have to be coated with suitable substrata or support films. These may either be a plain plastic such as collodion or polyvinyl formaldehyde (Formvar); a plastic film coated with evaporated carbon; or a plain carbon film. The plain carbon film is the most preferred for high resolution work since it is tough and withstands the electron beam. It also conducts the electricity more efficiently and hence reduces specimen drift due to the charge effects and conducts heat from the specimen to the copper grid bars. The preparation of grids filmed with plastic is reasonably simple, but the preparation of good thin plain carbon films is a tedious, time-consuming and somewhat irreproducible procedure. Here, the carbon evaporation procedure was used for the preparation of very thin and plain carbon foils, unless otherwise specified.

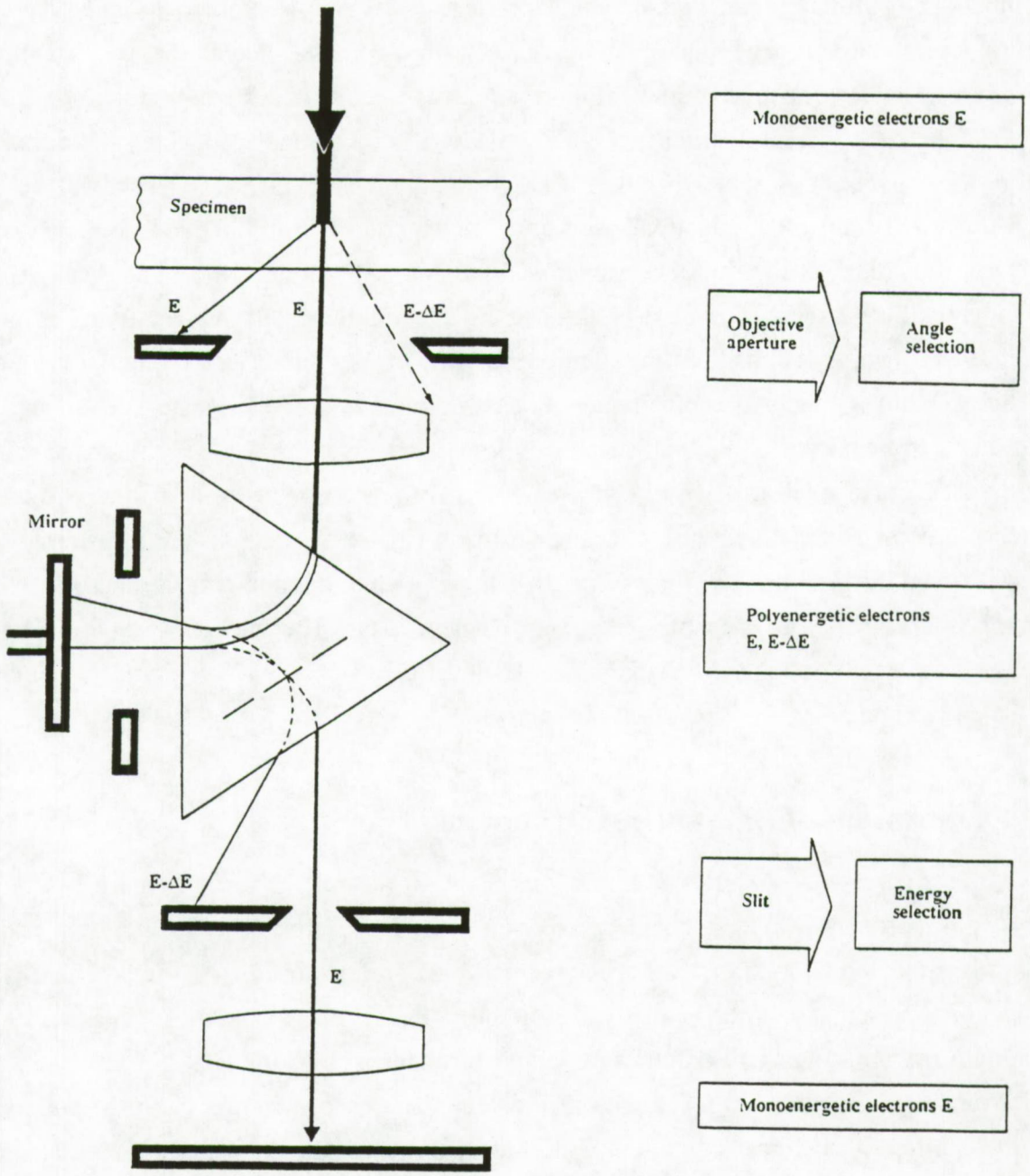

Figure 4.5: Beam path of the ZEISS EM902 transmission electron microscope with an integrated image electron energy spectrometer.

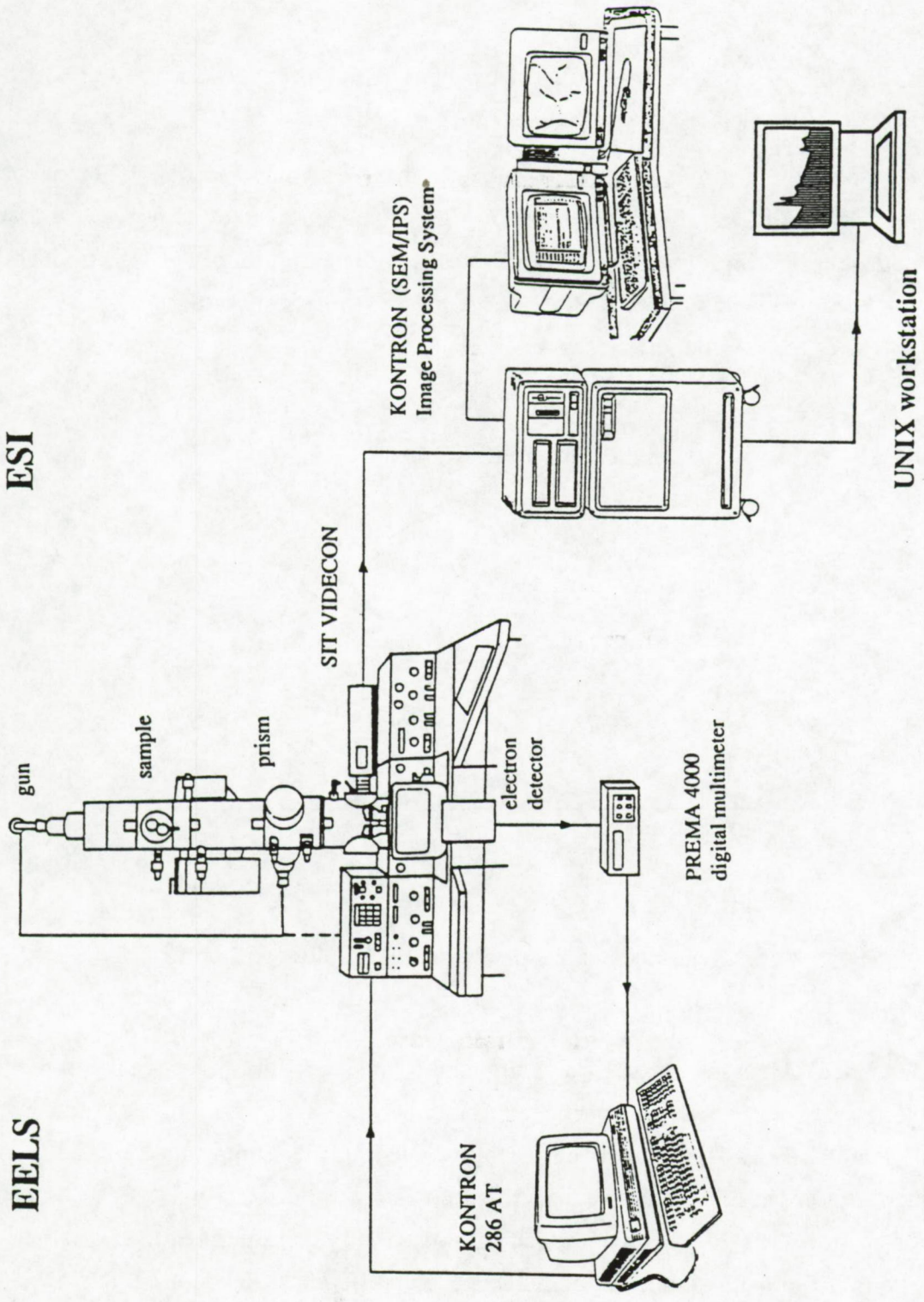

Figure 4.6: View of the ZEISS EM902 within a computer controlled environment.

4.6 Instrument optimization

The quality of the EELS spectra is affected by many parameters. To achieve the best possible quantitative analysis, each of these parameters must be optimized.

Figure 4.7 gives the definition of the parameters that determine the quality of an observed energy-loss edge. "S" is the characteristic edge signal measured above the extrapolated background intensity "B". The ratio (S+B)/B is called the jump ratio and is a measure of the visibility of the edge. The ratio $S/(S+B)^{0.5}$ is a measure of the signal-to-noise ratio or statistical validity, of the edge.

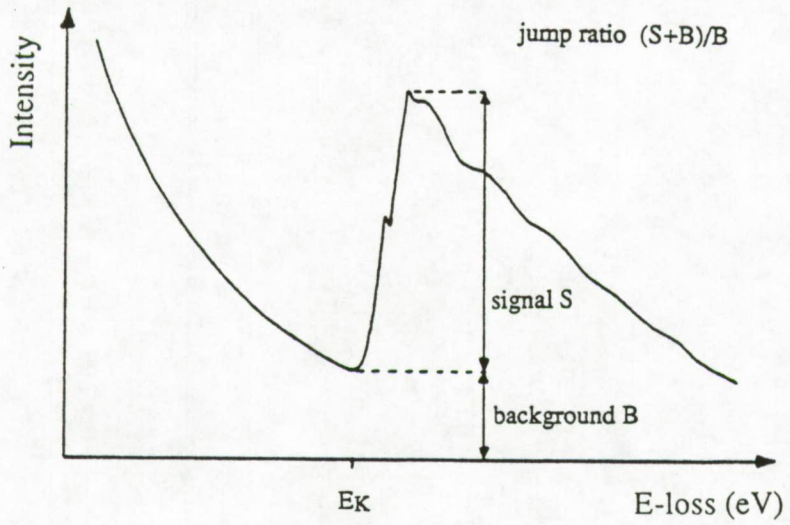

Figure 4.7: Presentation of parameters that determine the quality of an edge.

The dependence of parameters as the illumination angle (α), the objective aperture (β), the selector (entrance) aperture of the spectrometer and the slit (exit aperture of the spectrometer) on the quality of the EELS-spectra was tested by calculating the "jump ratio" of C-K ionization edges in spectra of very thin carbon foils. All spectra were collected between 250 and 350 eV in steps of 0.5 eV for the same channel acquisition time. During the experiment, all parameters were kept constant to eliminate as much as possible eventual differences in counting statistics.

4.6.1 Energy resolution

The energy resolution of a spectrum (ΔE) is deduced from the full width at half maximum (FWHM) of the zero-loss peak and is dictated by the spread of the electron gun and the aberrations of the spectrometer. Better energy resolution can be achieved with smaller spectrometer entrance apertures, but this comes at the expense of a lower counting rate. For a tungsten filament, energy resolutions of 1.4 to 2.0 are possible. For a LaB_6 electron source and a cold field emission gun, energy resolutions of respectively 1.1 and 0.3 have been achieved (Batson, 1986).

4.6.2 Condenser aperture

The choice of the condenser aperture selects the illumination angle α. Table 4.2 shows the results for the measurements of the jump ratio, signal-to-noise ratio and obtained energy resolution for the 3 possible condenser apertures.

Table 4.2: Jump ratio, signal-to-noise ratio and energy resolution calculated from carbon energy loss spectra collected for different condenser apertures.

Diam. aperture (μm)	α (mrad)	J=(S+B)/B	$S/(S+B)^{0.5}$	ΔE
400	2.5	12.2	117	2.3
200	1.2	13.0	122	2.3
100	0.6	15.0	135	2.2

The use of the third aperture gives the best jump ratio, what corresponds to a nearly parallel incident electron beam. However, smaller illumination angles result in a strong reduction of the final transmission intensity and can only be compensated by using higher electron doses. The choice of the condenser aperture has no influence on the energy resolution of the spectra.

4.6.3 Objective aperture

As the objective bore normally used for analysis corresponds to about 60 to 90 mrad, which is much greater than the width of the energy distribution (5-15 mrad for losses of interest), this means that practically all inelastically scattered electrons are collected. The spectrometer acceptance angle is limited by the size of the objective aperture at high magnifications (magnifications below 12.000 times). This angle is important for the calculation of the scattering cross section σ. The objective aperture is thus of most importance, since it controls the two important parameters "S" and "B". The results are shown in Table 4.3.

Table 4.3: Jump ratio, signal-to-noise ratio and energy resolution calculated from carbon energy loss spectra collected for different objective apertures.

Diam. aperture (μm)	β (mrad)	J=(S+B)/B	$S/(S+B)^{0.5}$	ΔE
180	35	10.0	162	2.1
90	17	10.4	133	1.8
60	11	10.4	127	1.6
30	6	11.0	129	1.5

The jump ratio reaches a maximum for the smallest diaphragm. When selecting smaller values of β, both S and B are small, so the signal-to-noise ratio is bad, but the jump ratio is high. For higher values of β, both S and B will rise and, because the characteristic edge rises faster than the background, an improved signal-to-noise ratio is obtained. Although not observed here, for large values of β, S will reach a saturation value and the signal-to-noise ratio will consequently show a maximum at some intermediate value of β (Joy and Maher, 1978). Medium collection angles of 10-20 mrad are a good compromise. Using smaller objective apertures increases the energy resolution as more elastically and inelastically scattered electrons are excluded from detection. Thus, the best choice of β corresponds to the largest value consistent with maintaining the desired energy resolution.

4.6.4 Spectrometer acceptance angle

The spectrometer acceptance angle is the angle that the electron beam forms when it enters the detector opening. It is defined by the detector opening or the spectrometer diaphragm at low magnifications and by the size of the objective aperture image at high magnifications. In spectrum mode, the magnified diffraction (rear focal plane of the objective lens) is imaged in the energy-dispersive plane (EDP) and then in the final image plane (FIP), so that a diffraction length can be indicated for the energy-dispersive and final-image planes. Table 4.4 lists the diffraction lengths and the corresponding magnifications in the energy-dispersive and final-image planes.

Table 4.4: Listing of the different diffraction lengths for the energy-dispersive and final-image planes as well as the diameter of the 60 µm objective aperture in the final-image plane, all corresponding to the various magnifications.

Magnification	Diffraction length in EDP (mm)	Diffraction length in FIP (mm)	Diameter of the obj. aperture in FIP (µm)
3000	2.2	5601	12.3
4400	1.3	312	6.9
7000	0.7	176	3.9
12.000	0.42	103	2.3
20.000	0.25	61.8	1.4
30.000	0.16	40.3	0.9
50.000	0.10	25.4	0.6
85.000	0.059	15.0	0.3
140.000	0.034	8.5	0.2
250.000	0.021	5.2	0.1
400.000	0.012	3.1	0.07

At M=3000, the diameter of the 60 μm aperture image in the FIP is 12.3 mm. The slit width (in the EDP) must be open as far as 48 μm (energy width of 26 eV) if it is not to be the limiting factor for the acceptance angle. Only 1/4 of the electron beam through the aperture reaches the detector because the opening of the electron detector is only 3mm wide. This fact must be considered for quantitative analysis. The conditions are much better at a magnification of 30.000 times. The diameter of the objective aperture in the EDP is 3.5 μm so that a slit of approximately 2 eV does not limit the aperture. The diameter of the object lens aperture in the final image is 0.9 mm which is much less than the 3 mm detector opening.

4.6.5 Selector aperture

Three different diaphragms are interchangeable at the entrance of the spectrometer. These diaphragms determine the acceptance angle of the spectrometer at magnifications below 12.000 times or when the spectrometer is conjugated with the diffraction image (focal plane of the objective lens). This aperture also selects the area of the sample to be analyzed. Measurements of S, B and ΔE were performed at a magnification of 30.000 times with a condenser and objective diaphragm of respectively 200 and 90 μm (Table 4.5).

Table 4.5: Jump ratio, signal-to-noise ratio and energy resolution calculated from carbon energy loss spectra collected for different selector apertures.

Diam. aperture (μm)	β (mrad)	J=(S+B)/B	$S/(S+B)^{0.5}$	ΔE
400	1.000	8.5	108	1.9
200	0.500	7.2	97	1.7
50	0.125	4.9	64	1.6

As smaller diaphragms are selected, the jump ratio and the signal-to-noise ratio decreases but the energy resolution increases.

4.6.6 Selector slit

This diaphragm is positioned at the energy dispersive plane of the spectrometer. The slit width is continuously variable and selects the energy specific electrons to be detected. Its width is measured by scanning the spectrometer caustic figure across the slit and reading the energy increment associated to its displacement. The results (Table 4.6) show that for larger slit widths more characteristic signal reaches the detector and positively influences the jump ratio and signal-to-noise ratio. Energy resolution gets worse and a best compromise between detectability and energy resolution should be made. A useful compromise is achieved by decrease of the slit width until the height of the zero loss peak is reduced by a factor of about two.

Table 4.6: Jump ratio, signal-to-noise ratio and energy resolution calculated from carbon energy loss spectra collected for different slit widths.

Slit width (eV)	J=(S+B)/B	$S/(S+B)^{0.5}$	ΔE
0.5	10.5	66	1.6
1.0	11.2	105	1.6
2.0	11.6	149	2.2
3.0	11.9	192	3.6
4.0	11.2	222	4.8

After withdrawing of the slit from the electron path, the electron detector measures an energy resolution of approximately 6 eV as given by the 3 mm opening of the final-image screen.

4.6.7 Magnification

Besides the objective lens, the pre-spectrometer system consists of 3 intermediate lenses that focus the transmitted signal into the spectrometer. Due to the use of the pre-spectrometer lenses, the physical acceptance angle of the spectrometer is decreased to β/M with M the intermediate magnification at the filter entrance image plane. The results of the jump ratio and the signal-to-noise ratio are shown in Table 4.7.

Table 4.7: Jump ratio, signal-to-noise ratio and energy resolution calculated from carbon energy loss spectra collected for different magnifications.

Magnification	J=(S+B)/B	$S/(S+B)^{0.5}$	ΔE
3000	14.0	194	2.6
7000	13.6	187	2.2
20.000	12.6	148	1.9
30.000	12.3	129	1.6
50.000	10.1	109	1.5
85.000	4.0	80.0	1.6

The visibility and also the signal to noise ratio of a peak decreases as the magnification increases. At higher magnifications, insufficient transmission signal reaches the detector and the signal needs to be amplified introducing more noise in the spectrum. If energy resolution is desired, one needs to work at magnifications of at least 20.000 times.

4.6.8 Magnification calibration

The calibration of the different magnifications was done by recording the transmission signals of a Pd shadowed carbon replica calibration grid (LADD Inc.) and measuring the gratings on respectively the photographic plates, the Ibas TV monitor and the video printouts.

Table 4.8 lists the magnification measured for the different recording devices, the value of a one cm scale bar and the diameter of circular analyzed area when the 60 μm aperture is used. The standard deviations are all within 5% of the measured values as limited by the measuring device used.

The number of pixels in a image determines the resolution. A typical high quality CRT present on the IBAS system has a spacing of 0.31mm and is adequate for displaying 512 x 512 pixel images. The actual pixel resolution can be calculated as follows:

$$R\ (\mu m/pixel) = \frac{L\ (cm)\ 10^4}{N\ (pixels)\ M} \qquad (4.4)$$

where R is the pixel resolution, L is the length of the CRT screen digitized by the imaging system, M is the actual magnification displayed on the CRT and N is the number of pixels available (512).

Table 4.8: Detremination of the magnification (M), the actual display for a one centimeter scale bar display and the analyzed area of a 60 μm selector aperture for the different recording devices.

ZEISS	Photographic plate		IBAS TV-screen		Video printout		d_{area} (μm)
Magnif.	real M	1 cm (μm)	real M	1 cm (μm)	real M	1 cm (μm)	
3000	7285	1.37	14897	0.67	9000	1.11	2.21
7000	15958	0.63	31418	0.32	18609	0.54	1.06
12000	29540	0.34	55800	0.18	33120	0.30	0.59
20000	51158	0.19	97200	0.10	57780	0.17	0.33
30000	69000	0.14	124200	0.08	75600	0.13	0.26
50000	116058	0.03	218018	0.03	133920	0.03	0.10

4.7 Relative thickness determination of an amorphous carbon foil

It is well established that EELS can provide at least an approximate value of thickness from specimens by straightforward investigation of an EELS-spectrum. The probability, P(m), of an electron exciting "m" plasmons and so losing m times a specific plasmon energy (E_{pl}), can be derived from Poisson statistics:

$$P(m) = (1/m!)\,(t/\lambda_p)^m \exp(-t/\lambda_p) \qquad (4.5)$$

where t is the sample thickness and λ_p is the plasmon mean free path. Thus, the ratio of the probabilities P(0) and P(1), of exciting no plasmons and one plasmon is:

$$P(1)/P(0) = t/\lambda_p \qquad (4.6)$$

This is just the ratio of the intensity of the first plasmon peak to the zero-loss peak. The ratio t/λ_p of a material can be given by (Joy et al., 1979; Leapman et al., 1984):

$$\frac{t}{\lambda_p} = \ln \frac{I_t}{I_0} \tag{4.7}$$

I_t and I_0 are the respective areas of the first plasmon peak and no-loss peak (zero-loss peak). They are relatively easy determined from the spectrum itself and thus provide an accurate method of either determining relative changes in thickness or of estimating the absolute thickness of the specimen if λ_p is known (Jouffrey, 1978). For the evaluation of t/λ_p, the parameters ε, δ and ϕ are to be defined as in Figure 4.8. The lower limit ($-\varepsilon$) of the zero-loss region is taken where the intensity drops to zero. The separation point δ between the zero-loss and the first plasmon peak is generally taken at the first minimum. The choice of the upper limit ϕ corresponds to an energy-loss at which the intensity reaches again low values. The linear relationship between t/λ_p and ln(It/I0) is accurate within 10% in an interval $0.2 < t/\lambda_p < 5$ (Hosoï et al., 1981; Leapman et al., 1984b). In practice, an edge of a freshly prepared carbon foil is collected on a 100 mesh Cu-grid. Because of the wide mesh and small ruptures present in the foil, regions of multiple C-layers will be observed (Figure 4.9). Since the carbon foil is very homogeneous in thickness over several hundreds of micrometers (the spread between individual readings was less than 7%.), multiple foldings will give rise to a proportionally increasing thickness. From these different thicknesses, EELS spectra were collected under the same conditions. Here, ε, δ and ϕ correspond respectively to 5, 14 and 100 eV. The results of the obtained t/λ_p values versus the relative thickness are plotted in Figure 4.10.

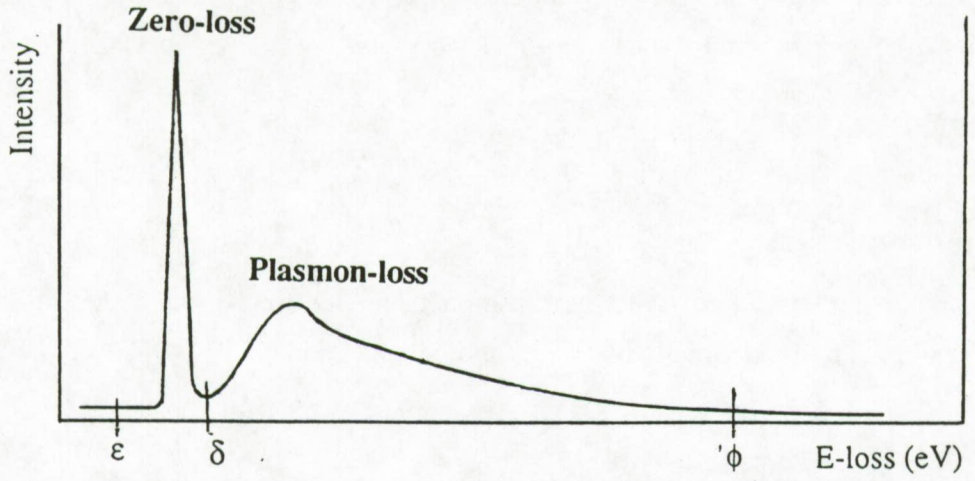

Figure 4.8: Definitions of parameters used for the thickness determination.

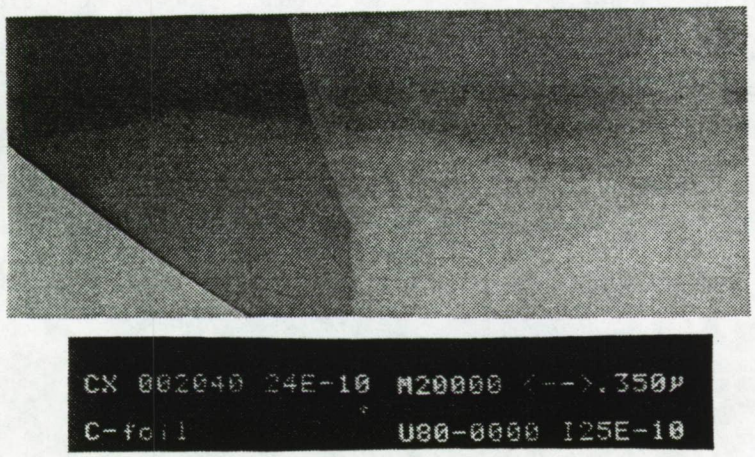

Figure 4.19: Zero-loss filtered image of a multiplicative folding in a carbon foil.

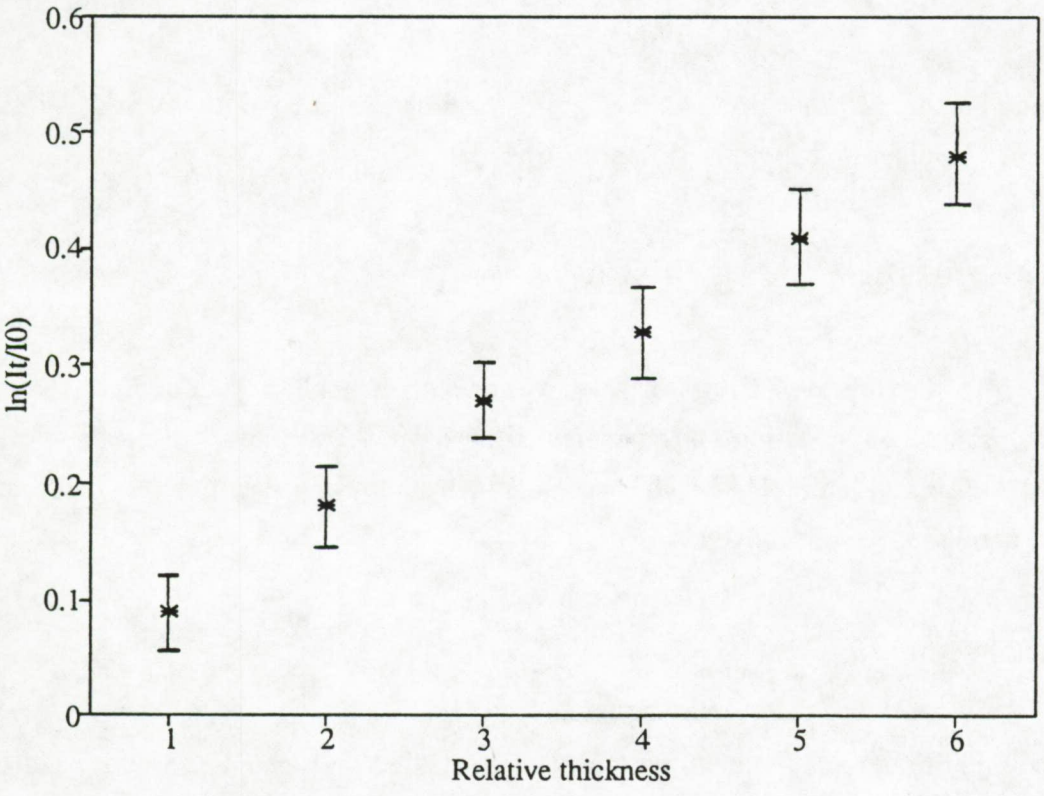

Figure 4.11: Plot of the t/λ_p values versus the relative thickness of a carbon foil.

Knowing the value of λ_p, the absolute thickness t of the carbon foil can be determined. Several theoretical approaches for the calculation of λ_p were discussed by Van Puymbroeck (1992). Jouffrey (1978) calculated λ_p values for different acceleration voltages. A good approximation of λ_p for plasmon scattering in a carbon foil at 80 keV and a collection angle of 11 mrad corresponds to 95 nm. This is close to the value of 96 nm as calculated by an experimentally derived expression (Malis et al., 1988):

$$\lambda_p = \frac{106F\,(E_0/\bar{E})}{\ln[2\beta\,(E_0/\bar{E})]} \tag{4.8}$$

λ_p is in nm where E_0 is the energy of the incident electrons (keV), β is in mrad, $\bar{E}$ is a parameterized function of the atomic number, and F is a relativistic correction factor:

$$F = \frac{1 + (E_0/1022)}{[1 + (E_0/511)]^2} \tag{4.9}$$

$$\bar{E} = 7.6\,Z^{0.36} \tag{4.10}$$

The absolute thickness of the carbon foil is therefore estimated to be 9 nm. According to Egerton (1988), λ_p can be determined within 20% of its true value.

4.8 Features of the EELS technique

Microanalysis deals with the analysis of small volumes and should not be confused with trace element analysis, which by definition is the analysis of low concentrations irrespective of the size of the sample. Therefore, terms like spatial resolution, accuracy and sensitivity of EELS are best understood in relation to microanalysis.

4.8.1 Spatial resolution

Spatial resolution refers to a scale on the specimen over which one can detect either a change in the relative intensity of a characteristic peak in the EELS spectrum, or a contrast modification in an image which can be unambiguously related to a chemical composition variation.

When spatial resolution is conserned, one has to distinguish between lateral resolution and depth resolution. Lateral resolution of the ZEISS EM902 depends mostly on lens aberrations in the image mode. There are no appreciable beam spreading effects for EELS since the electrons scattered at high angles are excluded by the entrance aperture. Depth resolution depends on the penetration of the primary beam in the sample and thus also on the section thickness.

Since EELS studies the primary beam effect after passage through a very thin sample, a lateral and depth resolution of respectively below 1 and 5 nm are obtainable in spectrum mode. Figure 4.11 shows a plot of the depth resolution versus the lateral resolution for various microanalytical techniques. For energy-loss imaging, resolutions below 5 nm are normal although resolutions of better than 2 nm have been produced.

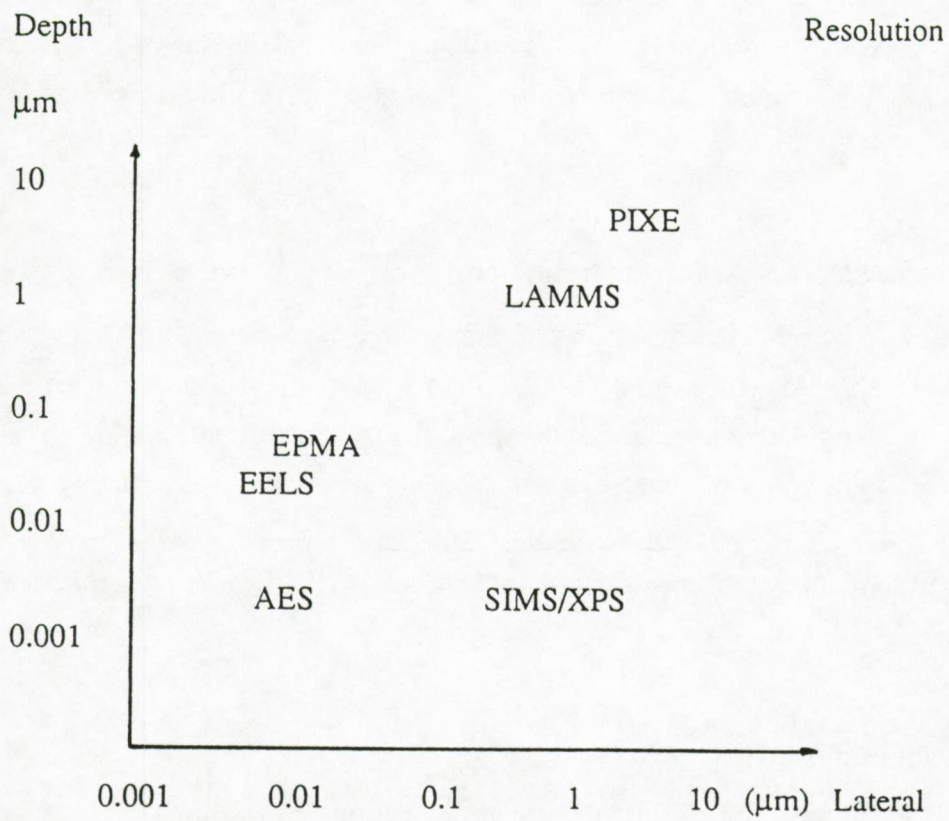

Figure 4.11: Lateral and depth resolution of some analytical techniques (source: Roomans et al., 1988).

4.8.2 Accuracy

A test for any quantitation method is that a calculated N value agrees, in absolute terms, with an independently determined value. This is not a pre-requisite for a microanalytical technique since it are atomic ratios that are most often required.

EELS has been used to identify quantities of less than 10^{-20} g and concentrations of less than 100 ppm of elements such as phosphorus and calcium in an organic matrix (Ottensmeyer, 1986; Shuman and Somlyo, 1987). However, the accuracy of quantitative analysis is often no better than 20%. The main sources of error are background subtraction, inner shell cross section determination, lens aberration errors and radiation damage.

4.8.2.1 Background subtraction

The pre-edge background is usually taken to be a power law (see equation 4.1). Particularly for lower-energy edges, deviations from this exponential behavior are observed and alternative fitting functions and procedures can be used to reduce systematic errors (Egerton, 1986; Van Puymbroeck, 1992).

4.8.2.2 Inner-shell cross section determination

The accuracy of absolute quantization is clearly dependent on the accuracy with which the inner-shell cross section (σ) in formula 4.2 is known. Likewise, the accuracy of elemental ratios will depend on the relative accuracy of the inner-shell cross sections. K-shell cross sections can be calculated rapidly (on-line) by use of a hydrogenic approximation, probably with an accuracy of around 10%. L- and M-shell cross sections require some empirical correction factors based on photoabsorption data or on experimental data (Egerton 1986) and accuracies below 20% are obtainable.

4.8.2.3 Lens-aberrations

Spherical and chromatic aberrations of any electron lenses between the specimen and spectrometer can cause a loss of energy resolution, spatial resolution and collection efficiency, all of which could lead to analysis errors.

4.8.2.4 Radiation damage

The electron beam used for microanalysis can cause both structural damage and chemical change (mass loss) within the analyzed region, leading to errors in elemental ratios. Parallel recording devices can greatly increase the signal-collection efficiency and reduce the electron exposure time. The use of a liquid-nitrogen stage may reduce the radiation sensitivity.

4.8.3 Sensitivity and minimal detectable concentration

It is not easy to express the sensitivity of EELS analysis in terms of absolute values. Much is dependent on the type of sample, the element investigated and the spatial resolution. Instead of discussing sensitivity and minimal concentration, it is better to refer to the minimal amount of element that can be detected. As for EELS at very high spatial resolution, the term "concentration" becomes more difficult to define. It has been the subject of much discussion.

When considering the sensitivity of EELS, much is dependent on the integrated count and peak-to-background value. EELS microanalysis performed using sequential data storage, fares badly. The recording time per channel equals the total recording time (τ) divided by the number of channels (C). Also the maximum jump ratio for trace elements may be less than unity. Therefore, it is better to use the term "minimal detectable mass" (MDM). It can be shown (Joy and Maher, 1980) that N, the minimal number of atoms of element A detectable in the matrix is

$$N = \frac{[(\sigma_b + \sigma_m)\, M]^{0.5}}{\sigma_A\, (J\tau)^{0.5}} \qquad (4.11)$$

where:

σ_A, σ_b and σ_m = partial cross sections for the edge, background and matrix respectively

J = incident current density (el/cm^2)

M = number of atoms of matrix in the analyzed volume

τ = dwell time (seconds/channel)

Under normal experimental conditions for the ZEISS EM902, the MDM corresponds to 10^3 to 10^5 atoms of the element of interest, which is in the order of a few atomic percent of that element in the matrix. According to Colliex (1986), even a lower minimal mass fraction (0.5%) is

sufficient for obtaining an EELS signal for element detection. EELS microanalysis is therefore not a trace detection technique, but it does offer very high absolute sensitivity.

4.9 Comparison between EPXMA/SEM-EDX and EELS/ESI

As a method of elemental microanalysis, EELS/ESI is most directly comparable with energy dispersive X-ray spectroscopy (EPXMA or SEM-EDX), particularly if the latter uses a windowless detector.

With the sole exception of hydrogen and helium, all elements can be analyzed with EELS/ESI, whereas EDXS with a standard (windowed) Si-Li detector is limited to elements with $Z \geq 11$. This can be extended using windowless Si-Li detectors, but only to $Z \geq 5$.

In general, EDX analysis is restricted to elemental information. EELS on the other hand cannot only give elemental information but can also be used to obtain information on chemical and physical properties by the use of e.g. EXELFS and ELNES.

4.9.1 EELS-spectra

The ionizations observed in EELS are at first stage similar to the ones of EDXS.

The EELS signal I_{EELS} from an ionization edge is:

$$I_{EELS} = I_0 \, . \, N \, . \, \sigma(\beta,\Delta) \tag{4.12}$$

where I_0 is the incident beam intensity, N is the number of atoms per unit area participating in the scattering event observed and $\sigma(\beta,\Delta)$ is the appropriate cross-section for the edge and the angle accepted by the spectrometer.

The X-ray signal I_{EDXS} detected in an EDXS measurement under the same conditions would be:

$$I_{EDXS} = I_0 \, . \, N \, . \, \sigma_{x\text{-}ray} \, . \, \omega \, . \, F \tag{4.13}$$

where $\sigma_{x\text{-}ray}$ is the X-ray ionization cross section, ω is the fluorescent yield and F is the collection efficiency of the detector.

Although EELS ionization cross sections are much smaller than those of EDXS, the counts/channel for elemental analysis using comparable incident beam currents are typically a factor of 10^4 greater than for EDXS because inner shell scattering is concentrated into a narrow angular range. The characteristic features in EELS are edges rather than peaks, the core-loss intensity being spread out over an extended energy range. Therefore, EELS edges have a lower visibility than corresponding peaks in the EDX spectrum. The signal/background in EELS spectra is thus lower by a factor of 10^2 resulting in lower jump ratio of the edges.

Quantitative EDX analysis requires standards and elaborate but well-known correction procedures (i.e. ZAF method). However, for light element analysis, extensive absorption corrections may be necessary (Chen et al., 1984). Although quantization with EELS is standardless and the correction procedures are less complex, results are considerably less accurate (accuracies are about 10 to 20% relative).

The inaccuracies in EELS quantization can also be attributed to inadequacies in the atomic models used to calculate these cross sections.

Background subtraction is more difficult for EELS than for EDXS. In EDX spectra, the background varies relatively slowly and predictably. The narrowness of the EDX peaks means that the interpolation required to calculate the background under the peak is not mathematically strenuous. It is generally much more difficult to subtract properly the background in EELS core edge images (Shuman and Somlyo, 1987) than in EDXS (Fiori et al., 1988). For EELS background fitting is an extrapolation rather than interpolation procedure and hence is more prone to error.

With respect to X-ray microanalysis, EELS shows high sensitivity. This enhancement is related to two factors. Firstly, ionization in an electron energy-loss process is a primary effect, whereas X-ray emission is a secondary effect and only one of several mechanisms of de-excitation. A result is that EDXS is less efficient because only a small fraction (the fluorescence yield) of the relaxation event results in the production of an X-ray. The factor ω in equation (4.13) is close to unity for heavy elements but decreases rapidly for lighter elements. Compared with X-ray microanalysis or Auger spectroscopy, EELS is free of fluorescence phenomena. The second factor responsible for a better sensitivity of EELS is the much higher collection efficiency F with values in the range of 0.5-1 while this is ~ 10^{-3} for the efficiency in X-ray microanalysis. The differences in efficiencies mean that the counting time per energy channel can be shorter for EELS than for EDXS. On the contrary, in the EELS case, the performance actually decreases for heavier elements because of the poor signal-noise ratios at high energy losses.

The only physical process which could affect resolution is delocalization, i.e., a fast incident electron can ionize an atom at a certain distance. This delocalization effect is estimated to be no more than a few nanometers (Bourdillon et al., 1981) and is typically less than 1 nm for an energy loss of 285 eV (K edge of C). The resolution of EELS is a factor of about ten better in resolution when compared to X-ray microanalysis. This high spatial resolution is necessary for analyzing very small features as e.g. sub-micrometer particles.

Peak overlap occurs and potentially presents serious problems in both EELS and EDX. The EDX detector has an energy resolution in the range of 100-150 eV. The narrow and well-defined character of EDX peaks gives X-ray analysis a considerable advantage when resolving peak overlaps. In EELS, the long trailing tails after the edges means that, with rare exceptions, element interferences present a more severe problem. In the case of low Z-element detection with a standardless detector, the situation may be the reverse.

4.9.2 ESI-images

The spatial resolution attainable with ESI, for inner shell excitations, is considerably better than in X-ray maps. A spatial resolution of 0.3-0.5 nm has been reported for 150 eV energy-loss images displaying the distribution of phosphorus in 30-nm sections of leukaemia virus (Adamson-Sharpe and Ottensmeyer, 1981). A minimum spatial resolution of about 10-20 nm and a minimum detectable mass of 5.10^{-19} g of iron (Z=26) can be achieved for EDXS (Shuman and Somlyo, 1976; Somlyo et al., 1979). These values are limited by the signal/noise ratios in the case of small electron beam diameters with their low probe currents, and by the counting statistics of the X-ray process. For elements of lower atomic number such as Ca, S, P, O, N or C, the X-ray strength decreases due to the lower fluorescent yield and the poor detector efficiency, resulting in a deterioration in minimum detectable mass.

The potential advantages and disadvantages of EELS/ESI over EDXS are summarized in Table 4.9.

Table 4.9: Comparison of EELS/ESI with windowless EDXS of a STEM specimen.

Advantages of EELS	Disadvantages of EELS
Higher core-loss signal	Higher background
Higher ultimate spatial resolution	Very thin specimen needed
Absolute stardardless quantization	Higher quantization errors
Structural information available	More operator intensive

Advantages of ESI	Disadvantages of ESI
High counts/pixel	Background subtraction
Fast method	Slow processing
Resolution	Large storage

4.10 References

Adamson-Sharpe K.M. , Ottensmeyer F.P.; Spatial resolution and detection sensitivity in microanalysis by electron energy-loss selected imaging, *J. Microsc.*, 122, 309-314, 1981

Ahn C.C., Krivanek O.L.; "*EELS Atlas*", Center of Solid State Science, Arizona State University, Tempe, AZ, and Gatan Inc., Pleasanton, CA, 1983

Batson P.E.; High energy resolution electron spectrometer for 1nm spatial analysis, *Rev. Sci. Inst.*, 57, 43-48, 1986

Bourdillon A.J., Self P.G., Stobbs W.M.; Crystallographic orientation effects in energy dispersive X-ray analysis, *Philos. Mag.*, [Part] A 44, 1335-1350, 1981

Chen Z., Cochrane R., Loretto M.H.; Microanalysis of extracted precipitates from extracted steels, in "*Analytical Electron Microscopy*" Eds Williams D.B., Joy D.C., San Francisco Press, San Francisco, 243-246, 1984

Colliex C.; "*Electron Energy Loss Spectroscopy Analysis and Imaging of Biological Specimens*", Ann NY Acad. Sci. 483, 311, 1986

Egerton R.F.; Inelastic scattering of 80 keV electrons in amorphous carbon, *Phil. Mag.*, 31, 199-215, 1975

Egerton R.F.; Formulas for light element micro analysis by electron energy loss spectrometry, *Ultramicroscopy*, 3, 243-251, 1978

Egerton R.F., Whelan M.J.; Electron energy loss spectra of diamond, graphite and amorphous carbon, *J. Electron. Spectr. Rel. Phen.*, 3, 232-236, 1974

Egerton R.F.; Principles and practice of quantitative electron energy-loss spectroscopy, *Microbeam Analysis*, Ed. K.F.J. Heinrich, San Francisco Press Inc., San Francisco, 43-53, 1982

Egerton R.F.; Quantitative microanalysis by electron energy loss spectroscopy: The current status, *Scanning Electron Microscopy /1984/II* Ed. A.M.F. O'Hare, 505-512, 1984

Egerton R.F.; *Electron Energy Loss Spectroscopy in the Electron Microscope* Plenum Press, New York and London, 1986

Fiori C.E., Leapman R.D., Swyt C.R., Andrews S.B.; Quantitative X-ray mapping of biological cryosections, *Ultramicroscopy*, 24, 237-249, 1988

Hainfeld J. and M. Isaacson; Use of electron energy-loss spectroscopy for studying membrane architecture - preliminary report, *Ultramicroscopy*, 3, 87-95, 1978

Hosoï J., Oikawa T., Inoue M., Kokubo Y., Hama K.; Measurement of partial specific thickness (net thickness) of critical-point-dried cultured fibroblast by energy analysis, *Ultramicroscopy*, 7, 147-154, 1981

Johnson D.W., Spence J.C.H.; Determination of single scattering probability distribution from plural scattering data, *J. Phys.*, D7, 771-780, 1974

Jouffrey B.; Electron energy losses with special reference to high voltage electron microscopy, in "*Short Wavelength Microscopy*", Ed. D.F. Parsons, New York Acad. Sciences, New York, 29-46, 1978

Jouffrey B.; in "*Electron Beam Interactions with Solids*", Eds. Kyser D.F., Heibrig M., Newbury D.E., Shimizu R., SEM Inc., Chicago, 235, 1984

Jouffrey B., Kihn B.Y., Perez J.Ph., Sevely J., Zanchi G.; On chemical analysis of thin films by energy loss spectroscopy, in "*Electron Microscopy*" 1978/III State of the Art, Ed. J.M. Stugess, Microscopical Society of Canada, Toronto, 292, 1978

Joy D.C.; Quantitative microanalysis using EELS, in "*Principles of Analytical Electron Spectroscopy*" Ed. D.C. Joy, D. Romig, J.I. Goldstein, Plenum Press, New York - London, 1986

Joy D.C., Maher D.M.; Choise of operating parameters for microanalysis by electron energy-loss spectroscopy, *Ultramicroscopy*, 3, 69-74, 1978

Joy D.C., Maher D.M.; *Scanning Electron Microscopy 1980*, Ed. O. Johari, SEM Inc., Chicago, I., 25, 1980

Joy D.C., Maher D.M.; Electron energy-loss spectroscopy detectable limits for elemental analysis, *Ultramicroscopy*, 5, 333-342, 1980

Joy D.C.; Basic principles of electron energy loss spectroscopy, in "*Introduction to Analytical Electron Microscopy*", Ed. J.J. Hren, J.I. Goldstein and D.C. Joy, Plenum Press, New York, 223, 1979

Joy D.C., Egerton R.F., Maher D.M.; Progress in the quantization of electron energy-loss spectra; in "*Scanning Electron Microscopy*" SEM Inc., AMF O'Hare, Chicago, Il., part 2, 817-826, 1979

Joy D.C.; *Principles of Analytical Electron Microscopy*, Eds. D.C. Joy, A.D. Romig and J.I. Goldstein, Plenum Press, New York, 277-299, 1986

Katrinak K., Rez P., Buseck P.R.; Structural variations in individual carbonaceous particles from the urban aerosol, *Environ. Sci. Technol.*, 26, 1967-1976, 1992

Leapman R.D., Grunes P.L., Fejes P.L., Silox J.; *EXAFS Spectroscopy*, Eds. B. Teo, D.C. Joy, Plenum Press New York, 217, 1981

Leapman R.D., Fiori C.E., Swyt C.R.; Mass thickness determination by electron energy-loss for quantitative X-ray microanalysis in biology, *J. Microsc.*, 133, 239-253, 1984

Leapman R.D., Fiori C.E., Swyt C.R.; Mass thickness determination by inelastic scattering in microanalysis of organic samples; in "*Analytical Electron Microscopy*", Ed. D.B. Williams and D.C. Joy, San Francisco Press, San Francisco, 83-88, 1984b

Liu D.R., Brown L.M.; Influence of some practical factors on background extrapolation in EELS quantization, *J. Microscopy*, 147, 37-49, 1987

Malis T., Cheng S.C., Egerton R.F.; EELS log-ratio technique for specimen-thickness measurement in the TEM, *J. Electron Microsc. Techn.*, 8, 193-200, 1988

Maynard A.D., Brown L.M.; Electron energy loss spectroscopy of ultrafine aerosol particles in scanning transmission electron microscopy, *J. Aerosol Sci.*, 23, S433-S436, 1992

Ottensmeyer F.P.; Elemental mapping by electron energy filtration in biology: limits and limitations, *Electron Microscopy*, Proc. 11th Int. Cong., Kyoto, 1986

Rez P.; *Microbeam Analysis*, Ed. R. Gooley; San Francisco Press, San Francisco, CA., 153-155, 1983

Roomans G.M., Wroblewski J., Wroblewski R.; Elemental analysis of biological specimens; *Scanning Microscopy*, 2, 937-946, 1988

Shuman H., Somlyo A.P.; Electron-probe X-ray analysis of single ferritin molecules, *Proc. Nat. Acad. Sci.*, Philadelphia P.A., USA 73, 1193, 1976

Shuman H., Somlyo A.P.; Electron energy loss analysis of near-trace element concentrations of calcium, *Ultramicroscopy*, 21-32, 23, 1987

Somlyo A.P., Somlyo A.V., Shuman H.; Electron probe analysis of muscle and X-ray mapping of biological specimens with a field emission gun, *Scanning Electron Microscopy*, 2, 711, 1979

Taft J., Zhu J.; Electron energy-loss near edge structure (ELNES), a potential technique in the studies of local atomic arrangements, *Ultramicroscopy*, 9, 349-354, 1982

Trebbia P.; Unbiased method for signal estimation in electron energy loss spectroscopy, concentration measurements and detection limits in quantitative microanalysis: methods and programs, *Ultramicroscopy*, 24, 399-408, 1988

Unser M., Ellis J.R., Pun T., Eden M.; Optimal background estimation in EELS, *J. Microscopy*, 145, 245-256, 1987

Van Puymbroeck J., Van Espen P. and Jacob W.; Acquisition of electron energy-loss spectra; *Micron and Microscopica Acta*, 20, No 2, 155-156, 1989

Van Puymbroeck J.; Electron energy-loss spectrometry: Development of methodology and software for the acquisition and processing of spectra, PhD. thesis, University of Antwerp, UIA, 64, 1992

Wolf B.; Elektronen-Energie-Verlust Spektroskopische Untersuchungen an Luftfiltern zur Bewertung der Luftqualität, *Z. Naturforsch.*, 43c, 155, 1988

Zaluzec N., McConville R., Sandborg A.; A comparison of KEDS and EELS with the use of conventional beryllium window and windowless Si(Li) detectors, in "*Analytical Electron Microscopy*" Eds Williams D.B., Joy D.C., San Francisco Press, San Francisco, CA., 348-352, 1984

CHAPTER 5

Zero-loss imaging and element specific imaging (ESI)

5.1 Introduction

Electron energy-loss analysis provides a tool which has the spatial resolution close to that of the microscope itself if the concentration of the chosen element on which elemental analysis and mapping is perfomed, is sufficiently high. This resolution potential is at the same time responsible for the high sensitivity of detection of a very small number of highly localized atoms. In spite of this, the resolution observed in electron micrographs of samples mainly composed of low-Z elements is generally not better than about 3 nm. The loss in resolution has basically two causes: insufficient intrinsic contrast of the specimen and chromatic aberration of the microscope. An approach for reducing the deleterious effects of electron energy loss and chromatic aberration on images is the use of an energy filter to narrow the energy spread of electrons that are used to form the image. This chapter will highlight the imaging possibilities of the ZEISS EM902.

5.2 Imaging possibilities with an energy filter

Transmitted electrons bearing information about the specimen in the form of angular deviation and velocity loss, can be separated into undeviated primary electrons and inelastically scattered electrons. The undeviated electrons are those which pass into the image-forming lenses of the conventional TEM; this image is therefore the conventional or "bright-field" image. Whithout an energy filter, most of the inelastically electrons pass through the objective aperture. The failure of the lens system to focus these energy-loss electrons correctly leads to chromatic error in the image resulting in a deterioration of the image quality. Using an energy filter and appropriate apertures, inelastic electrons can be removed from the bright field image thus promoting contrast and resolution in the pure elastic image by eliminating chromatic aberrations and reducing the

background from plasmon scattering events. The physical theory behind contrast in the electron spectroscopic imaging mode of a TEM by zero-loss filtering is discussed elsewhere (Reimer and Ross-Messemer, 1989).

The inelastic signal is composed of electrons which have been subtracted from the bright-field signal and therefore form an image of reversed contrast resembling the "dark-field" image. Depending on the specificity of electron interaction with the specimen, the energy distribution of the inelastically scattered electrons can also bear elemental information in the final image as will be discussed later in this chapter. As an example, Figures 5.1a and 5.1b show a zero-loss filtered and plasmon filtered image of aerosol particles collected on a carbon foil, respectively.

The most frequently used imaging modes of the ZEISS EM902 with integrated energy filter are:

1) Global image: With open slit or withdrawing the slit results in no energy selection: the image contrast is comparable with conventional TEM.

2) ESI, $\Delta E = 0$ eV: Elastic image with slit as energy window and $\Delta E = 0$; inelastic electrons are removed and the image contrast is enhanced (zero-loss imaging).

3) ESI, $\Delta E > 0$ eV: Inelastic image with slit as energy window and $\Delta E > 0$; high resolution spectroscopic imaging (energy-loss imaging).

(a) (b)

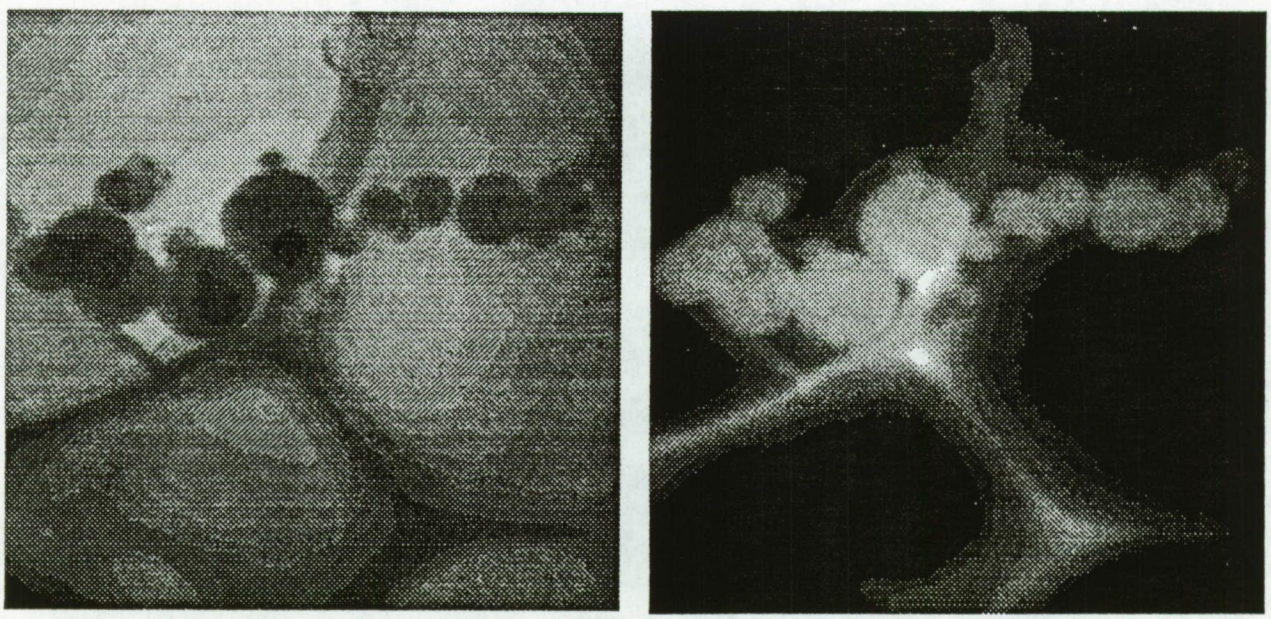

Figure 5.1: (a) Zero-loss filtered image ($\Delta E = 0$ eV) and (b) plasmon-loss filtered image ($\Delta E = 60$ eV) of aerosol particles from urban Phoenix (magnification of 20,000 times).

Thus, electron spectroscopic imaging using an energy filter of the prism-mirror-prism type, generally provides normal electron micrographs, elastic bright field images and inelastic images with any selected energy band in the electron energy-loss spectrum of the specimen.

5.3 Image recording

In some cases it is insufficient to observe the transmitted electrons on the fluorescent screen of a microscope or to record on a photographic emulsion. To process a series of images in a fast and efficient way, a record with a camera that uses a on-line TV-adapter is useful. The energy filtered images of the ZEISS EM902 are projected onto a transmission phosphor and acquired with a silicon intensified TV camera. The integration of a parallel image recording device as a SIT Vidicon camera extended with an efficient computer system, provides the simultaneous acquisition and processing of images. A general overview of the computer controlled EELS environment was already picturized in Figure 4.8.

The general characteristics of the SIT Vidicon tube include two-dimensional image fidelity, a linear response over a wide dynamic range, a low geometrical distortion, simplicity of operation and high reliability (Talmi, 1975; Olesik and Walters, 1983; Michiels, 1990). Its high sensitivity allows real-time observations of energy filtered images. The channel-to-channel and pixel-to-pixel response signal of the Vidicon camera is in the form of a voltage, a so-called "analog" signal. This signal can be digitized by dividing the range from full black (zero signal) to peak white (maximum signal) into a number of grey levels. The resulting digital image can then be processed by a programmed computer. In this way, multiple television frames can be stored and processed.

Prior to the recording of images, the dynamic range of the camera needs to be adapted to the signal intensity at the specific energy-losses. Using a pre-defined color lookup table, the brightest feature of the most intense image and the darkest feature in the least intense image are displayed on-line in colors corresponding with grey values of white and black, respectively (Nys, 1992).

5.4 Zero-loss imaging for particle sizing

The detection of a particle using a SIT Vidicon camera and an image processing system, is based on the intensity of an electron image. The quality of the feature detection depends mainly on the image contrast between sample substrate (the supporting foil or the embedding medium) and the

object of interest (particles). Therefore, energy filtration in bright field images can be very well applied for the detection, characterization and size classification of sub-micrometer and even sub-nanometer particles. The use of an energy filter is here advantaged since an appreciable gain in contrast can be obtained (Trinick and Berriman, 1987).

On-line electron images containing particles on amorphous substrate often need to be enhanced by digital processing in order to facilitate the differentiation of the particles from the background. In this study, enhancement is carried out with an IBAS image processor (Kontron) after digitizing the transmission images to 512 x 512 pixels of 8 bits by a SIT Vidicon camera. The following 2 processing steps are applied: (a) shading correction and (b) thresholding.

Shading correction is used to reduce the effect of a non-uniform illumination, which is frequently obtained when a TV camera is used as digitizer for conventional TEM images. Two different approaches for shading can be applied. The first can be applied when the projected area of the particles is low compared to the total imaged area. Then the original image (512 x 512) pixels can be divided in regions of e.g. 32 x 32 pixels. Assuming a uniform distribution on the support, the local mean pixel grey value is calculated for each 32 x 32 pixel field. These mean values are set for every pixel in the corresponding sub-field and the result is a mean background image that can be subtracted from the original one. The second approach for shading correction (not used in this work) can be performed by introduction of a reference image (without signal), which is subtracted from the original non-uniform image. For both approaches, a contrast enhancement can be achieved by linearly stretching the grey level histogram over its full dynamic range.

Sometimes a noise reduction by median filtering might be useful for feature recognition. However this mathematical intervention on the image always results in a loss of contour definition of the particles (Soria et al., 1988) and this is not acceptable if particle sizing is of interest.

Thresholding is a very important step to obtain credible results as it is dependent of the contrast between the characteristic and non-characteristic features. The best contrast is obtained for the selection of the smallest energy selecting slit. As a consequence, this limits the total area that can be investigated at once. As a good compromise, a selector aperture of 400 μm and an energy window of 10 eV are very well suited. The cut-off threshold is interactively selected. All image pixels containing an intensity below this threshold are scaled to black and those above are scalled to white. The result is that inadequate regions in the final image are rejected leaving behind only the isolated intensity features.

A macro was written to semi-automatically characterize particles with only a small amount of interactive support (editing). The macro is started by the selection of the first image field containing the particles to be analyzed. After processing the first field, the image system is automatically switched to on-line TV mode and a second field of the sample can manually be selected and subsequently processed. The macro terminates by interaction of the operator when sufficient particles are sized. The manual field selection is by far the most time limiting factor. The speed of particle characterization also depends on the loading of the supporting grids and the working magnification used. Under ideal conditions, more than 100 particles can be analyzed within 5 minutes. The resolution by which the particles can be analyzed, is mostly dependent on the magnification, as this determines the pixel resolution of the TV screen.

Three different monodisperse Latex particle suspensions (NBS, Washington, DC) with certified diameter (in μm) of 0.269 ± 0.007 (reference number 1691), 4.821 ± 0.019 (166) and 9.475 ± 0.018 (167) were used as a reference material for testing the sizing capabilities of the ZEISS EM902 in combination with a TV camera and image processing system. The samples were prepared by taking 25 μl of a standard suspension. The whole quantity was transferred into a small test tube and diluted with Milli-Q water to 500 μl. The tube was treated ultrasonically for about 30 minutes. A drop of the suspension was then transferred by a seringe to a carbon coated electron microscope grid and dried to air.

The data collection for more than 100 Latex 0.269 μm spheres recorded without energy-filtering or inducing the filter in the zero-loss mode and plasmon-loss mode, consists of 4 measurements per particle namely the minimum, the maximum and the circular particle diameter as well as the projected area of the particle. From these parameters, the shape factor [Shf = (perimeter)2/(4 Π area)] and the aspect ratio (AR = Dmax/Dmin) can be calculated. Particles that are sticking together were retained from analysis. The results for the particle sizing are presented in Table 5.1. The conversion of the parameters obtained in number of pixels to their values in μm is based on the instumental magnification calibration as explained in chapter 4.

No significant differences are observed when sizing parameters are determined for different mapping modes. However, in case of no filtering, slightly lower parameters are obtained. This can be explained when comparing the contrast (measured by grey values) across the interface of the supporting foil and the Latex sphere as recorded for different operation modes of the energy filter (Figure 5.2).

Table 5.1: Determination of morphological parameters of 0.269 μm standard Latex spheres by a semi-automated image analysis using different filter imaging modes. A magnification of 20,000 times was used. The values between brackets are the corresponding standard deviations.

Filtering mode	Area (μm2)	Dmax (μm)	Dmin (μm)	Dcircle (μm)	Shf	AR
no filtering	0.05	0.27	0.24	0.25	1.08	1.13
	(0.02)	(0.04)	(0.03)	(0.03)	(0.04)	(0.04)
zero-loss	0.06	0.28	0.26	0.26	1.05	1.09
	(0.02)	(0.02)	(0.02)	(0.02)	(0.03)	(0.03)
plasmon (30 eV)	0.06	0.28	0.26	0.27	1.05	1.10
	(0.02)	(0.02)	(0.02)	(0.02)	(0.03)	(0.03)

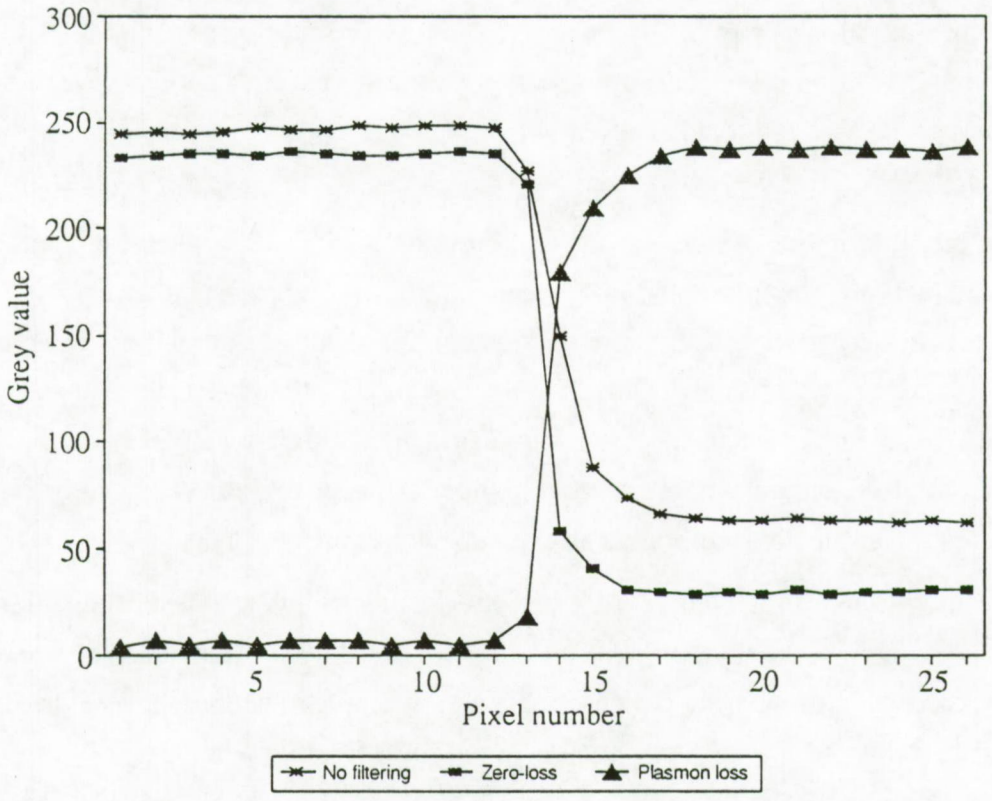

Figure 5.2: Contrast across a Latex particle and the supporting foil as determined for different filtering modes.

It can be seen that for the same experimental conditions and appropriate diaphragms, a decrease in contrast is observed when the sizing is performed whithout the use of the energy filter. This contrast reduction when the energy filter is absent, results in a lower change between maximum and minimum grey level value. Also the jump measured across the interface is not sharply defined. So much of the measured parameters will depend on the threshold setting of the background. For plasmon imaging, a new camera setting was introduced because of the lower and inversed signal collected.

As another test, three different Latex spheres were characterized for their morphology parameters using zero-loss filtering. The results of more than 100 particles in each class are shown in Table 5.2.

Table 5.2: Morphological parameters of 3 different Latex spheres standard as determined by a semi-automated image analysis using zero-loss filtering. The values between brackets are the corresponding standard deviations.

Manufacturer Size (μm)	Magnif.	Area (μm2)	Dmax (μm)	Dmin (μm)	Dcircle (μm)	Shf	AR
0.269	20000	0.06	0.28	0.26	0.26	1.05	1.09
(0.007)		(0.02)	(0.02)	(0.02)	(0.02)	(0.03)	(0.03)
4.821	7000	17.8	4.91	4.63	4.76	1.12	1.06
(0.019)		(0.4)	(0.05)	(0.05)	(0.05)	(0.06)	(0.04)
9.475	3000	70.3	9.81	9.10	9.46	1.13	1.08
(0.018)		(0.3)	(0.02)	(0.04)	(0.02)	(0.05)	(0.05)

The obtained results in Table 5.1 and 5.2 show systematically lower values as compared with the reference particle sizes given by the manufacturer. This can be explained by the shrinking process of Latex particles within the first few minutes of exposure to the electron beam (Cermola and Schreil, 1987).

5.5 Element specific imaging (ESI)

The major application of transmission electron microscopy with integrated energy filter, resides in elemental mapping using inner-shell edges. Absorption core edges can, in suitable circumstances, localize an element with a resolution of down to 1 nm. But generally, elemental imaging does not requires an ultimate energy resolution as for most spectral purposes. Thus, the energy window Δ can be set to larger values (e.g. 10 eV) and a larger acceptance angle can be selected, both allowing an increase in collected signal. Because of the goog spatial resolution of the system, the resultant picture looks similar to a regular image rather than to the familiar X-ray "dot" map.

In analogy to spectrum processing, only the image signal which is above the background represents the characteristic elemental signal. During the history of ESI, background subtraction evolved in different stages.

5.5.1 Two-image method

The simplest method for background subtraction is to take an image just below the edge and an image at the ionization edge and subtract the former from the latter (Henkelman and Ottensmeyer, 1974; Ottensmeyer and Andrew, 1980). The disadvantage of this procedure lies in the assumption that energy dependence in the spectrum is independent of thickness, density or composition of the matrix. This may not necessarily be the case for complex specimens. If background subtraction is not properly carried out, since the signal is typically 1/100 or 1/1000 of the inelastic intensity, the major features of such an image are given by mass-thickness variation. Hence considerable care is needed to avoid that a possible analytical map becomes simply a morphological image. It is for this reason that the simple subtraction of two images, one before and one after the edge, is a method fraught with danger (Rez and Ahn, 1982; Leapman et al., 1984).

5.5.2 Three-image method

In analogy to spectrum processing, the background can be approximated by an inverse-power law ($I = A\ E^{-R}$). There does not exist an a priori satisfactory calculation of the involved (A,R) parameters in given experimental conditions and for a well determined specimen. The constants

A and R may vary from pixel to pixel as they are sensitive to the factors (foil thickness, orientation and density changes, collection acceptance,...) which are responsible for the contrast observed in the electron microscope. Consequently, these constants are semi-empirical parameters pertaining to each pixel and they must be determined experimentally. To compensate for background variations, it is necessary to model, fit and strip the background contribution at each pixel of the image.

There are three independent variables which must be obtained for each corresponding pixel in the image: A, R for the background and the signal S after the edge. Therefore, at least three independent measurements must be performed, that is, three energy images have to be acquired for the energies E1 and E2 before the edge, and E3 after it (Figure 5.3).

For every corresponding pixel position in the two pre-edge images, the intensities I1 and I2 at the energy losses E1 and E2 can then be approximated as:

$$I_1 = A.E_1^{-R} \text{ and } I_2 = A.E_2^{-R} \qquad (5.1)$$

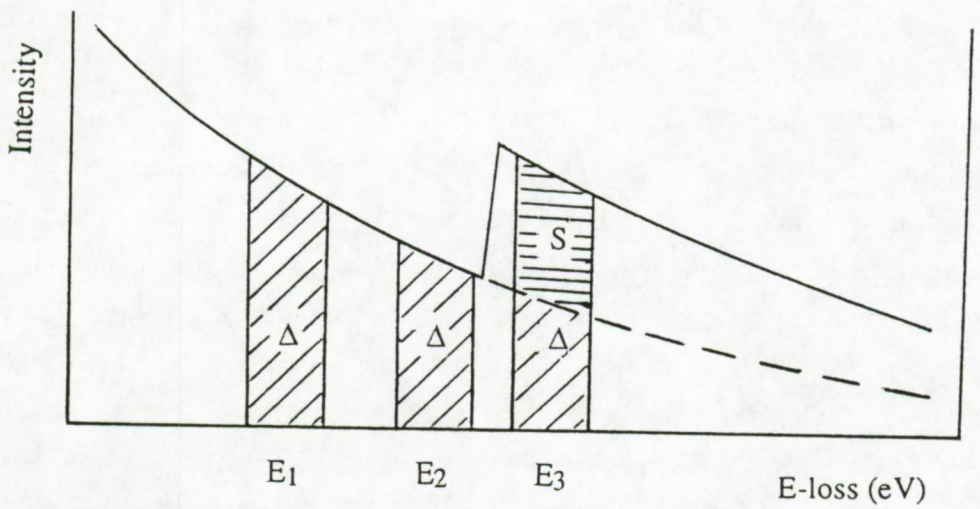

Figure 5.3: Scheme of a typical EELS spectrum defining the net-characteristic core loss signal (S), the three selected energies E1, E2, E3 and, in dashed curve, the extrapolated background.

After a logarithmic transformation, the parameters A and R can be computed according to the expressions:

$$R = \frac{\log I_1/I_2}{\log E_2/E_1} \tag{5.2}$$

$$A = I_1 E_1^{R} = I_2 E_2^{R} \tag{5.3}$$

For each pixel, the background image can be calculated and subtracted from the third recorded image at an energy position E3 resulting in the net-image intensity:

$$S = I_3 - A.E_3^{-R} \tag{5.4}$$

Using the three-image procedure, we thus obtain chemical maps which do not exhibit "false-positive" features, i.e., intensity regions where the analyzed element is absent. The elimination of thickness effects is clearly demonstrated in the following experiment. A small irregular BN-particle showing local dense structures and supported by a thin carbon-supporting film is imaged for the carbon distribution of the support. The zero-loss filtered image and the net-carbon distribution are shown in Figure 5.4. If artefacts derived from thickness variations occur in the net-elemental carbon distribution, enhanced pixel intensities (false-positive) should be observed at the position of the BN particle. However, the maximum C-specific intensity underneath the BN particle never exceeds the values of the carbon foil. On the contrary, even lower carbon characteristic pixel values are observed. This reduction of local intensity is the result of insufficient transmission intensity that reaches the detector as the thickness increases. At this level, we can ascertain that the obtained element specific image discriminates chemical information from thickness effects. Now, the question remains how to evaluate the power law background extrapolation procedure in imaging mode. The validity of the image processing has been checked for a set of "ghost' images from and around a hypothetical edge which does not exist (e.g. for an energy loss position of the third image just below the characteristic edge). ESI was performed on three images taken below the characteristic C-onset of an organosilane treated chrysotile asbestos fiber at energies of respectively 265 eV, 270 eV and 275 eV. The result is shown in Figure 5.5a. Ideally, no net signal should be present. Only a few pixels with a maximum grey level of 4 representing noise as a result of non-characteristic artefacts, the extrapolation procedure and camera artefacts. The result of ESI with pre-edge images taken at 265 and 270 and one C-edge image at 290 eV losss, is presented in Figure 5.5b.

(a) (b)

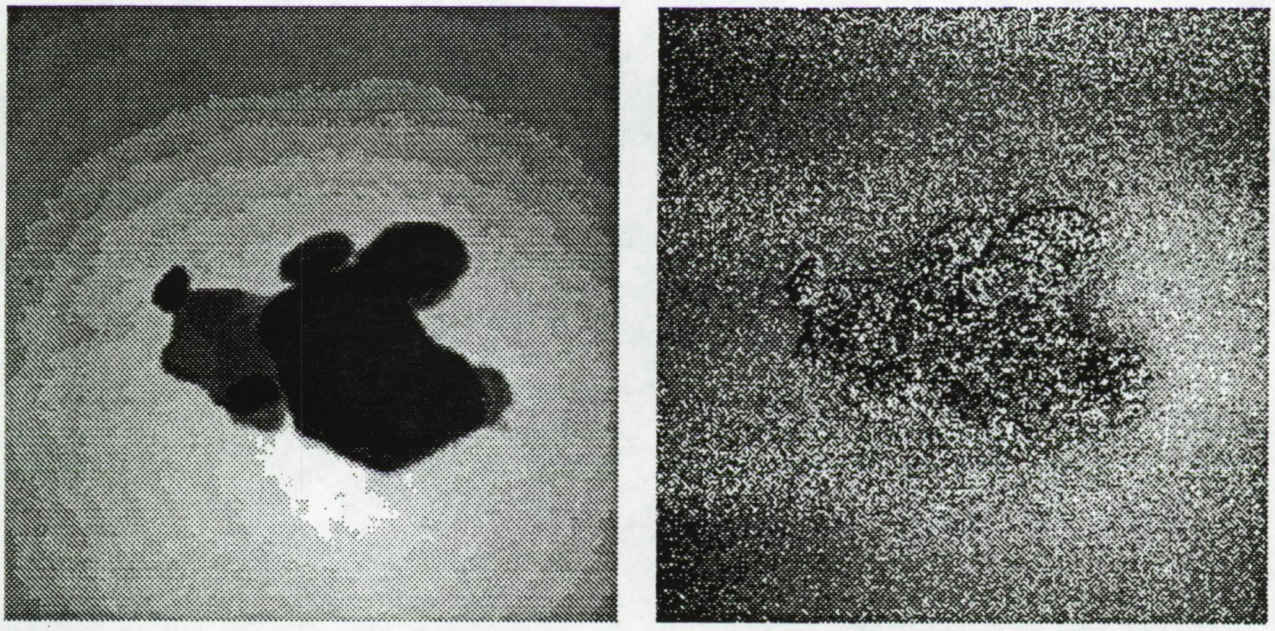

Figure 5.4: (a) Digitized zero-loss filtered image of an amorphous carbon film supporting an irregular BN particle showing local density variations, (b) net-elemental distribution of carbon as obtained by the three-image ESI method.

(a) (b)

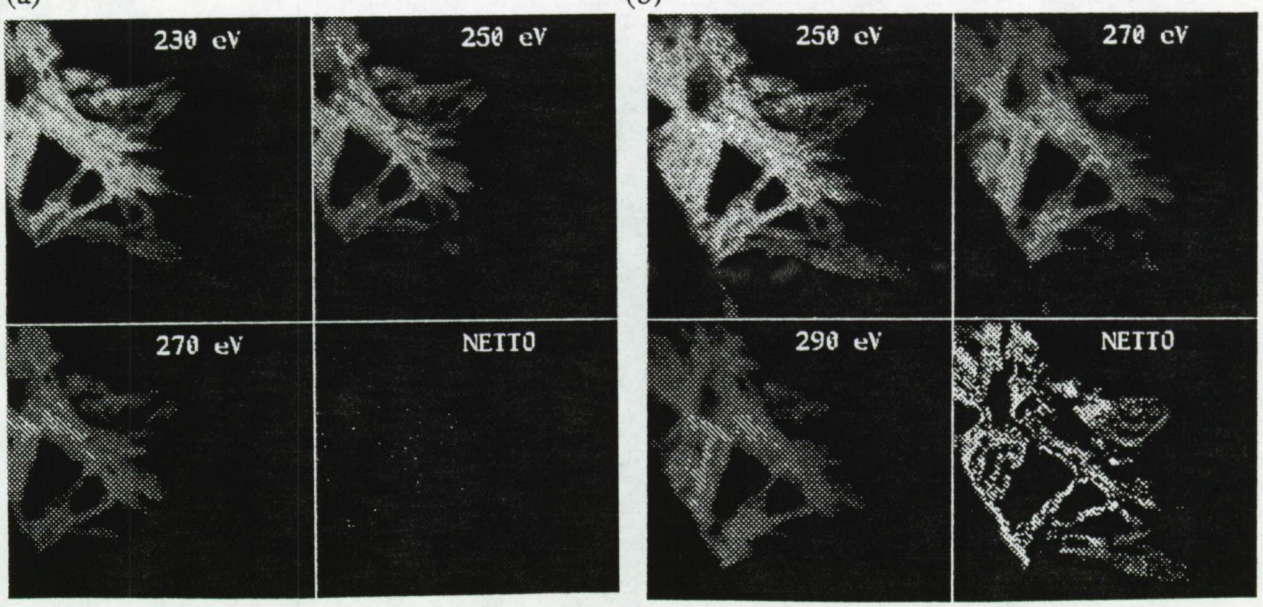

Figure 5.5: (a) Noise image as a result of background subtraction for a series of 3 images all taken in the pre-edge region before the C-onset of an organosilane treated asbestos fiber. (b) Net carbon distribution resulting from a normal three-image procedure.

As an approximation, a more statistically valuable net image can be obtained by subtracting the noise contribution. Subtraction of the noise is performed by setting a cut-off threshold above which the signal is accepted. The level of the threshold is chosen either as two times the maximum noise intensity from a pixel in a region where the element is absent, or as three times the mean of all noise contributions (Nys, 1992). However, thresholding results in the subtraction of one fixed pixel value for the whole image although the noise contribution normally varies from pixel to pixel. So finally, the difficulty in determing the reliability of the obtained element distribution still remains that of the estimation of the variance and its confidence level in each picture element of the net-EELS image.

5.5.3 Multi-image method

5.5.3.1 Statistical approach

The whole methodology of image collection and processing can be expanded to more than 2 images taken before the characteristic onset.

Consider Figure 5.6 and assume that the number of EELS images are recorded from energy-losses ΔE_{-J} to ΔE_{-1} before the edge (J images), one image at the edge energy ΔE_0 and K images after the edge at energy values $\Delta E_1,...\Delta E_K$.

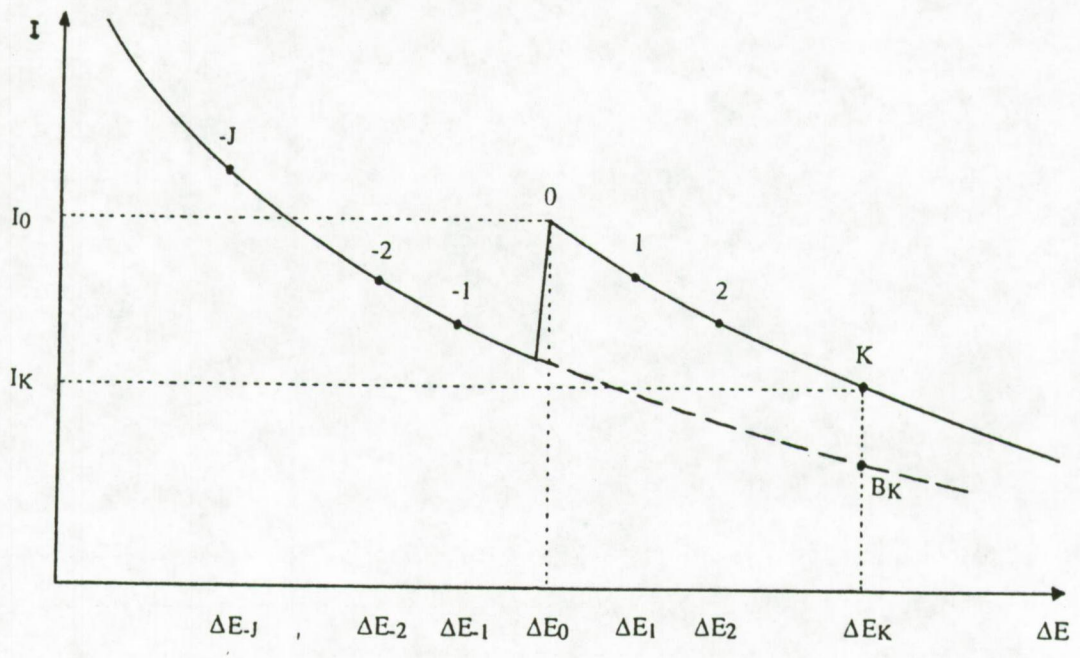

Figure 5.6: Definitions of the parameters used for multi-ESI imaging.

The total net area of the edge feature can be calculated as:

$$A = \sum_{k=1}^{K} N_k \tag{5.5}$$

where the index k runs over the energy losses at and after the edge.

The net signal N_k at each energy loss value ΔE_k can be calculated from:

$$N_k = I_k - B_k \tag{5.6}$$

where I_k is the recorded total intensity and B_k is the extrapolated background intensity at an energy loss ΔE_k.

The transformed background intersection can be calculated by fitting a straight line through the log-log transferred spectrum (I_j versus ΔE_j) before the absorption edge. This part of the spectrum follows a power law:

$$B_j = I_j = \alpha\ (\Delta E_j)^{-r} = \alpha' \left(\frac{\Delta E_j}{\Delta E_0}\right)^{-r} = \alpha'\ \varepsilon_j^{-r} \tag{5.7}$$

where $\varepsilon_j = \Delta E_j/\Delta E_0$ and where α, $\alpha' = \alpha(\Delta E_0)^r$ and r are constants.

The log transformed equivalent is a linear relation:

$$ln I_j = \ln\alpha' - r \ln\varepsilon_j \tag{5.8}$$

or

$$Y_j = a + b\ X_j \tag{5.8}$$

where $a = \ln\alpha'$, $b = -r$, $Y_j = \ln I_j$ and $X_j = \ln \varepsilon_j$.

For a series of (X_j,Y_j) pairs of images collected at different energies with associated uncertainty σ_j on each measured Y_j value and a standard deviation σ_j about the actual value, the best fitting values of a and b in equation 5.8 can be calculated via the method of Gauss using:

$$a = \frac{1}{\Delta}\left(\sum_{j=1}^{J}\frac{X_j^2}{s_j^2}\sum_{j=1}^{J}\frac{Y_j}{s_j^2} - \sum_{j=1}^{J}\frac{X_j}{s_j^2}\sum_{j=1}^{J}\frac{X_jY_j}{s_j^2}\right) \tag{5.9}$$

$$b = \frac{1}{\Delta}\left(\sum_{j=1}^{J}\frac{1}{s_j^2}\sum_{j=1}^{J}\frac{X_jY_j}{s_j^2} - \sum_{j=1}^{J}\frac{X_j}{s_j^2}\sum_{j=1}^{J}\frac{Y_j}{s_j^2}\right) \tag{5.10}$$

$$\Delta = \sum_{j=1}^{J}\frac{1}{s_j^2}\sum_{j=1}^{J}\frac{X_j^2}{s_j^2} - \left(\sum_{j=1}^{J}\frac{X_j}{s_j^2}\right)^2 \tag{5.11}$$

where all summations run over the J images collected before the edge (j = -J,...-1).

Assuming that the measurements at different ΔE_k energies are statistically independent, the uncertainty on the parameters a and b can be expressed as:

$$s_a^2 = \frac{1}{\Delta}\sum_{j=1}^{J}\frac{X_j^2}{s_j^2} \tag{5.12}$$

$$s_b^2 = \frac{1}{\Delta}\sum_{j=1}^{J}\frac{1}{s_j^2} \tag{5.13}$$

The least square fitting of the (X_j,Y_j) pairs assumes that the uncertainty in X_j (expressed as the variance between the images collected at different energy losses) is smaller than the uncertainty in Y_j (expressed as the variation in intensity observed in images collected at one energy position). When a linear uncertainty model is employed:

$$s(I_j) = \sigma\, I_j \tag{5.14}$$

it follows that:

$$s^2(Y_j) = \left(\frac{\partial Y_j}{\partial I_j}\right)^2 s^2(I_j) = \left(\frac{\partial \ln I_j}{\partial I_j}\right)^2 \sigma^2\, I_j^2 \tag{5.15}$$

$$s^2(Y_j) = \frac{1}{I_j^2}\,\sigma^2\, I_j^2 = \sigma^2 = constant \tag{5.16}$$

Since the variance is constant, the derivation of the expressions for a, b, Δ, s_a and s_b can be reduced to:

$$a = \frac{\sum_{j=1}^{J} X_j^2 \sum_{j=1}^{J} Y_j - \sum_{j=1}^{J} X_j \sum_{j=1}^{J} X_j Y_j}{J \sum_{j=1}^{J} X_j^2 - (\sum_{j=1}^{J} X_j)^2} \tag{5.17}$$

$$b = \frac{J \sum_{j=1}^{J} X_j Y_j - \sum_{j=1}^{J} X_j \sum_{j=1}^{J} Y_j}{J \sum_{j=1}^{J} X_j^2 - (\sum_{j=1}^{J} X_j)^2} \tag{5.18}$$

$$\Delta = \frac{1}{\sigma^4}\left(J \sum_{j=1}^{J} X_j^2 - (\sum_{j=1}^{J} X_j)^2 \right) \tag{5.19}$$

$$s_a^2 = \frac{\sigma^2 \sum_{j=1}^{J} X_j^2}{J \sum_{j=1}^{J} X_j^2 - (\sum_{j=1}^{J} X_j)^2} \tag{5.20}$$

$$s_b^2 = \sigma^2 \frac{J}{J \sum_{j=1}^{J} X_j^2 - (\sum_{j=1}^{J} X_j)^2} \tag{5.21}$$

Once the above entities are calculated, the background intensity B_k at energy ΔE_k can be transformed using equation (5.7) according to:

$$B_k = \exp\left(a + b \ln\frac{\Delta E_k}{\Delta E_0}\right) \tag{5.22}$$

Note that the background at ΔE_0 is simply given by: $B_0 = \exp(a)$

The uncertainty on the net intensity N_k can be expressed as:

$$s^2(N_k) = s^2(I_k) + s^2(B_k) \tag{5.23}$$

where $s^2(I_k) = \sigma^2 I_k^2$. The uncertainty on the background level B_k is defined by the uncertainties on the fitting coefficients a and b. According to error propagation rules, the variance for the variable B_k depending on other variables a and b, is given as a function of these variables, s_a^2 and s_b^2 each multiplied by the effect these variables have on the magnitude of the variable B_k.

$$s^2(B_k) = \left(\frac{\partial B_k}{\partial a}\right)^2 s_a^2 + \left(\frac{\partial B_k}{\partial b}\right)^2 s_b^2 \tag{5.24}$$

$$s^2(B_k) = B_k^2 s_a^2 + x_k^2 B_k^2 s_b^2 \tag{5.25}$$

Here,
$$x_k = \ln\frac{\Delta E_k}{\Delta E_0} = \ln\varepsilon_k \tag{5.26}$$

Substituting equation (5.26) into (5.23), the uncertainty on the total edge intensity $A = \Sigma N_k$ is then given by:

$$s^2(A) = \sum_{k=1}^{K} s^2(N_k) = \sum_{k=1}^{K} s^2(I_k) + s_a^2 \sum_{k=1}^{K} B_k^2 + s_b^2 \sum_{k=1}^{K} x_k^2 B_k^2 \tag{5.27}$$

Note that the index k runs over the images collected at energy losses ΔE_0 to ΔE_k starting respectively at and extending behind the edge.

Substitution of the expressions for $s^2(I_k)$ (eq. 5.14), s_a^2 (eq. 5.20) and s_b^2 (eq. 5.21) in equation (5.27) yields:

$$s^2(A) = \sigma^2 \left(\sum_{k=1}^{K} I_k^2 + \frac{\sum_{j=1}^{J} X_j^2 \sum_{k=1}^{K} B_k^2 + \sum_{k=1}^{K} x_k^2 B_k^2}{J \sum_{j=1}^{J} X_j^2 - (\sum_{j=1}^{J} X_j)^2} \right) \tag{5.28}$$

showing that the overall uncertainty is directly proportional to the constant σ.

When the summation of k is only limited to one image at the edge (k=0), the uncertainty on N_0 then reduces to:

$$s^2(N_0) = \sigma^2 \left(I_0^2 + \frac{\sum_{j=1}^{J} x_j^2}{J \sum_{j=1}^{J} X_j^2 - (\sum_{j=1}^{J} X_j)^2} B_0^2 \right) \tag{5.29}$$

The uncertainty of the net image is dependent on different factors that all can be calculated from the experiment except for the value of σ. At this point, the whole procedure is quite similar to spectrum analysis. The difference for EELS spectra is that σ can also be determined from the experiment itself by e.g. collecting the intensity at one energy-loss channel for several times. For each channel, its mean value is then calculated with the corresponding standard deviation. Because of limitations in time and data storage, this procedure is not straightforward for ESI applications. Therefore, it is advisable to collect either one series of images at a specific energy loss position and determine the σ to be used throughout the experiment, or search a value of σ for which the net signal in a region of no interest is eliminated interactively. Both methods give comparable results in the net image.

The time for processing 20 images (256x256) is less than 60 seconds. For changing the value of σ, the whole ESI calculation does not have to be repeated and one command is sufficient to obtain a new display of the net image within 5 seconds.

5.5.3.2 Worked example

The methodology, the processing and the result of the multi-image method is best illustrated by an example. Let us consider again the BN particle. The exact position of the absorption edges of boron and nitrogen are first determined in spectrum mode (Figure 5.7). The K-edge onset for boron is situated at 188 eV, for the nitrogen K-edge at 400 eV. Note that the presence of large intensities of the Π^* peaks in the near-edge structure of both boron and nitrogen clearly reveals a hexagonal structure (sp^2-bonding).

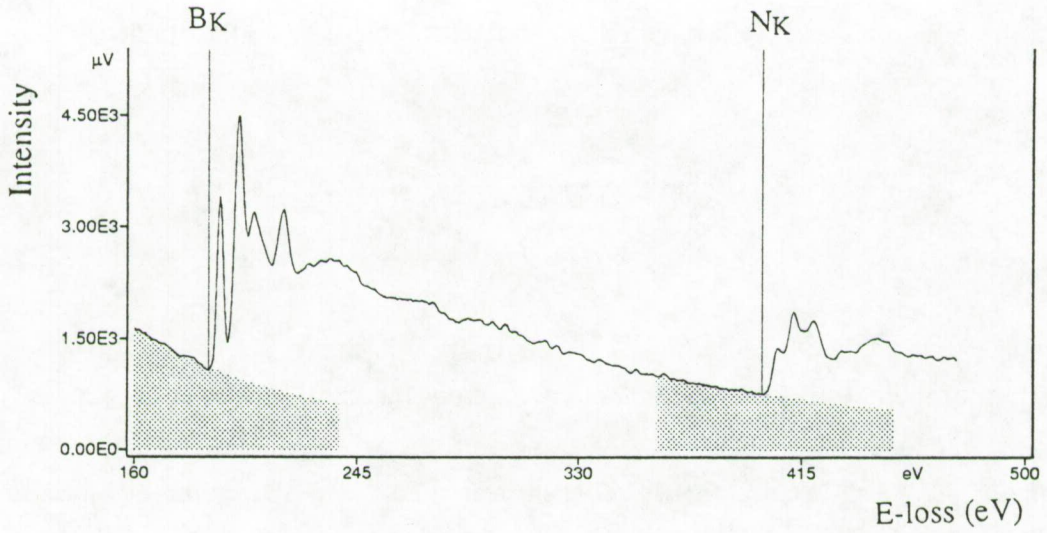

Figure 5.7: EELS spectrum of a sub-micrometer h-BN particle showing the B-K onset at 188 eV and the N-K onset at 400 eV.

A total of 20 images are taken around the boron edge starting at an energy-loss of 170 eV and increasing with energy intervals of 2 eV. The last image is thus collected at 208 eV loss. The same number of images are recorded for nitrogen starting at an energy-loss of 380 eV up to 418 eV. A least square fitting procedure is performed for every corresponding pixel position of the pre-edge images using a PV-WAVE program (Precission Visuals, Inc., Colorado, USA) operating on a UNIX network system. Just as for the three-image model, the extrapolated background image (artificial image) underneath the characteristic edge is subtracted from the edge image resulting in a net-element distribution. The net signal can be presented in two different ways. First, the result of only one edge image is taken (e.g. the edge at the most intense energy position). For boron this would be the net image at 196 eV, for nitrogen at 412 eV. Secondly, all difference images underneath the edge can be added and included in the element distribution. The two presentations are pictured in Figure 5.8 for the nitrogen distribution within the BN particle. Comparison of the two presentations reveals that more significant net-signal is obtained when the sum of net-images are displayed.

If we plot the estimated standard deviation (s_I) for each pixel of 8 images taken at the same energy-loss as a function of its intensity, a scatterplot is obtained as presented in Figure 5.9. From this plot it can be seen that most of the scatterpoints are positioned around a straight line. This indicates that the standard deviation increases linearly as the intensity in that pixel increases. This

was expected since the linear output response of the SIT Vidicon camera results from a gain amplification and thus, also variations in intensity are subjected to the same amplifications. The relation between the pixel intensity and the standard deviation is expressed by the slope ($tg\delta$) of the scatterplot and $tg\delta = \sigma$. Any vertical deviation of a scatterpoint to the scatter line reflects the contribution of extrapolation artefacts and instrumental effects.

In the case of the h-BN particle, all images are recorded at different energies and the scatterplot might slightly deviate from an exact linear relationship since variations in energy are to be considered. The scatterplot obtained from images collected at different energies (Figure 5.10) is quite identical to Figure 5.9. This allows us to accept the linear approximation model so that only variations in intensity have to be taken into account.

A calculation procedure was developed using the WAVE program in order to obtain all parameters necessary for the representation of significant net-elemental distributions. The WAVE processing routine allows the operator to display an energy-loss spectrum at each selected pixel position in the image. The number of data points selected for construction of this spectrum corresponds to the number of images collected and selected (in this case 20 data points). As an extra option, the intensity distribution across the X and Y directions for the chosen pixel position in the net-image can be displayed.

From the scatterplot of s_I versus the intensity (I), the value of $tg\delta$ can be derived. The meaning and effect of $tg\delta$ on the final net-image display can be seen from the following experiment. Let us consider in more detail the nitrogen distribution within the BN particle. Suppose the operator chooses a low value of $tg\delta = 5$. The resulting statistically significant net-distribution of nitrogen associated with this $tg\delta$ is presented in Figure 5.11a. The image spectrum of the pixel position as indicated by the arrow is presented in Figure 5.11b. From this spectrum it is clearly seen that a characteristic N-signal is present but does not show up in the map. The X- and Y-line intensity distributions for the specified pixel position are plotted in Figure 5.11c and 5.11d. The datapoints marked by a cross (+) represent the characteristic signal above the background for the selected slope level of $tg\delta$. The datapoints marked by a point (.) represent non-significant signal. The value of $tg\delta = 5$ is rather low if we compare the results with a slope level of $tg\delta = 10$ (Figure 5.12) as obtained from the scatterplot. Here the X- and Y-intensity distributions show only + marks across the BN particle, there where N is present. Consider a pixel position on the particle as indicated by the double arrow. The corresponding energy-loss clearly shows a nitrogen edge (Figure 5.12e), but the net signal is not plotted because it is statistically insignificant. The settings for $tg\delta = 20$ (Figure 5.13) is too high as there are a lot of pixels observed at background positions located outside the BN particle contour. So, false positive pixels are present at places where no

signal should be detected. Thus, by changing the value of tgδ, also the number of significant element specific pixels within the map is changed.

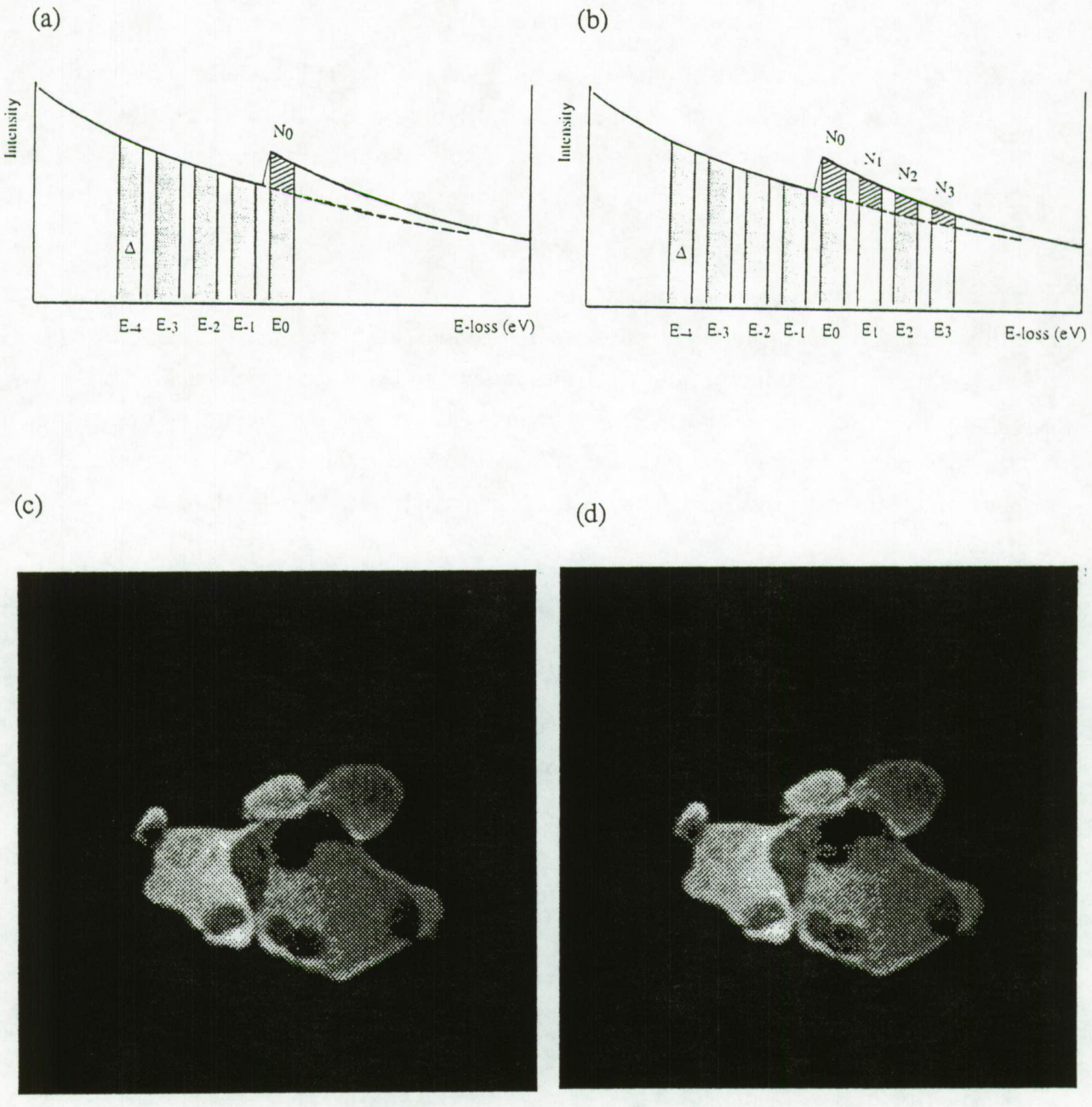

Figure 5.8: (a) and (b) are respectively illustrations for the net-element image presentations. (c) Net-nitrogen distribution within a BN particle using only the signal of one edge-image. (d) net-nitrogen distribution as the result of summation of all net-image intensities underneath the N-K peak.

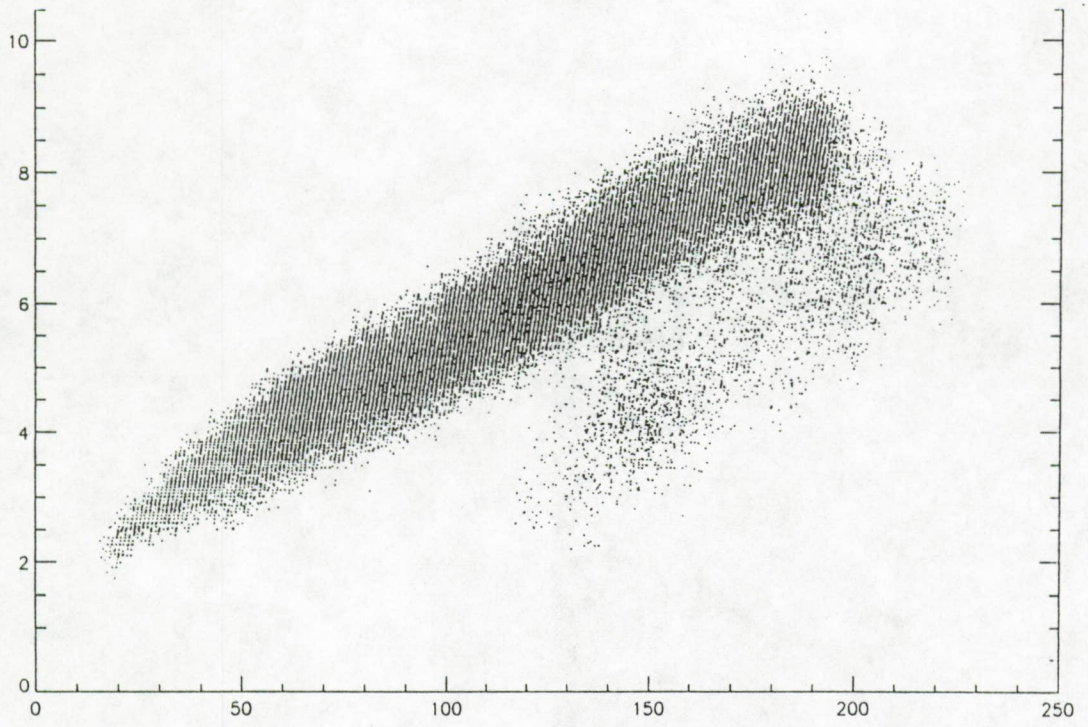

Figure 5.9: Scatterplot of the standard deviation versus intensity of each pixel in a series of 8 images recorded at the same energy-loss.

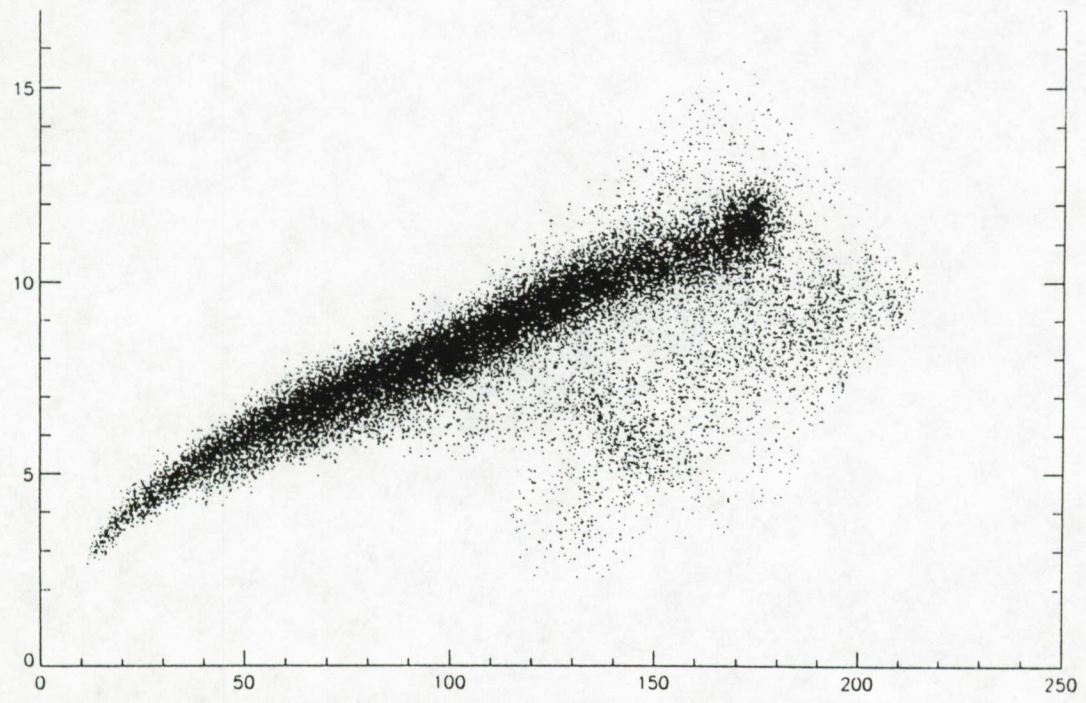

Figure 5.10: Scatterplot of the standard deviation versus intensity of each pixel in a series of 8 images recorded at energy-loss increments of 2 eV.

(a)

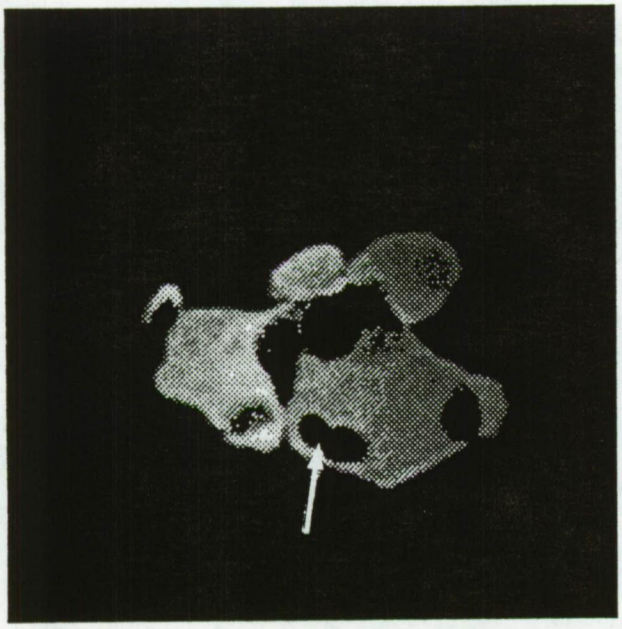

(b)

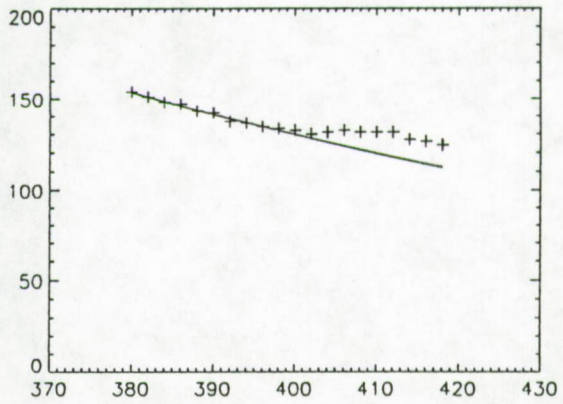

(c)

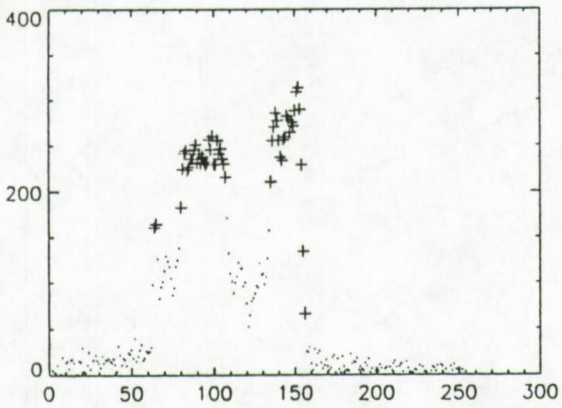

(d)

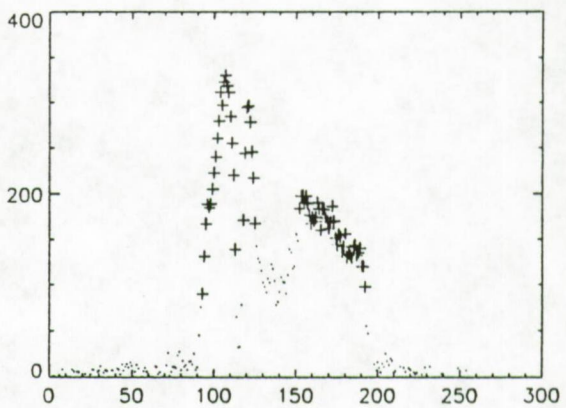

Figure 5.11: (a) Sum of the net-nitrogen distributions within a BN particle for a slope level tgδ = 5, (b) image spectrum at the pixel positions marked by the arrow, (c) and (d) are intensity distributions respectively across the X and Y direction at the marked pixel position.

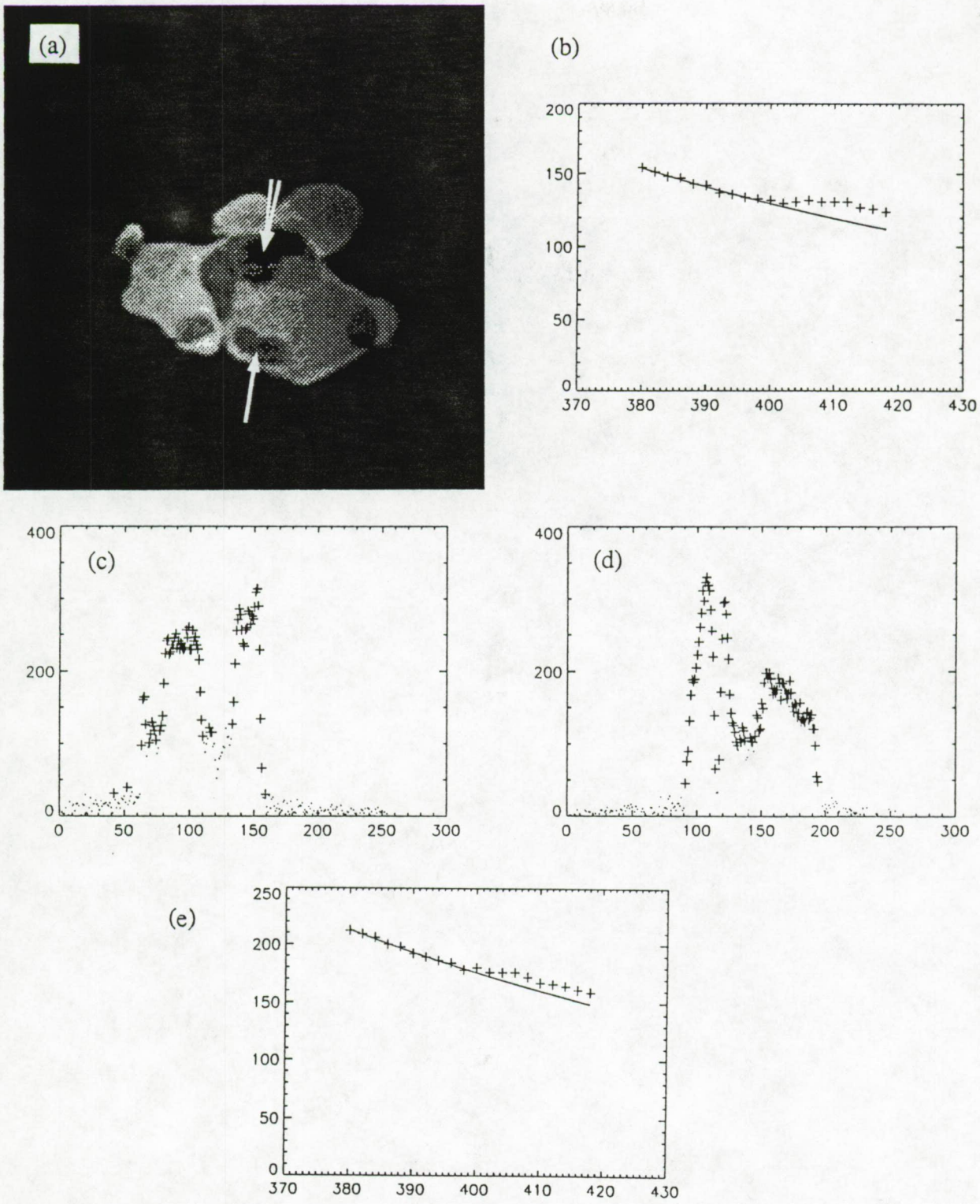

Figure 5.12: (a) Sum of the net-nitrogen distribution within a BN particle for a slope level tgδ = 10, (b) image spectrum at the pixel positions marked by the arrow, (c) and (d) are intensity distributions respectively across the X and Y direction at the marked pixel position. (e) Energy-loss spectrum generated at the pixel position indicated by the double arrow. The presence of nitrogen in not significant.

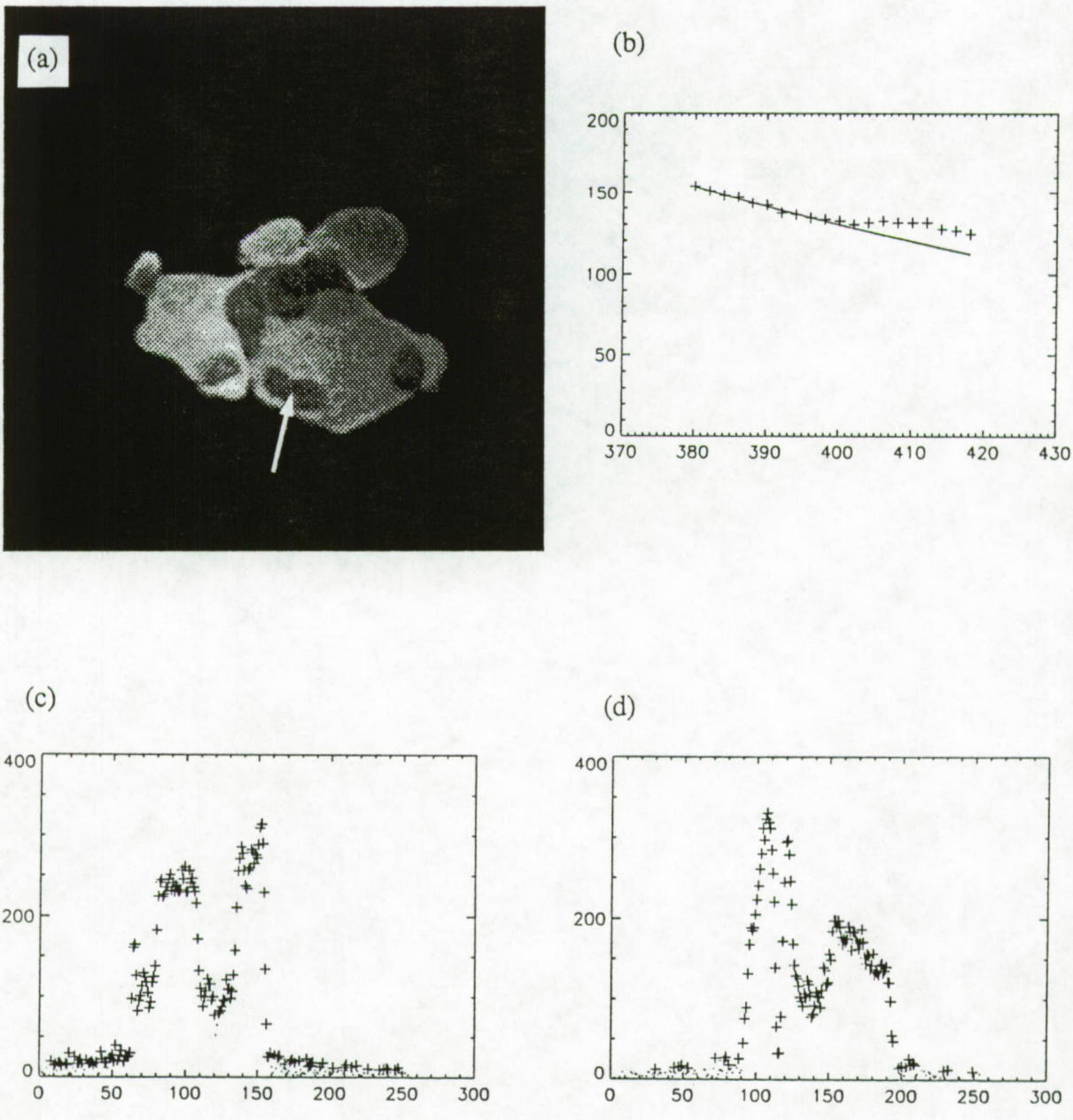

Figure 5.13: (a) Sum of the net-nitrogen distribution within a BN particle for a slope level tgδ = 20, (b) image spectrum at the pixel positions marked by the arrow, (c) and (d) are intensity distributions respectively across the X and Y direction at the marked pixel position.

Instead of taking for example 9 pre-edge images each at a relative energy increment, one can collect three times three images at one energy position. If this is done for the boron signal of the BN particle, the obtained result of the summation of net images looks like in Figures 5.14a and 5.14b. The net image shows less significant signal if the result is compared with a conventional 9-image background setting (Figures 5.14c and 5.14d). This can be explained when keeping in mind that three images collected at one energy-loss position of 170 eV have all equal or higher image pixel intensities when compared to three images collected at energy-losses of respectively 170 eV, 172 eV and 174 eV. The former series of images have higher standard deviations associated to their pixel intensities, and consequently, the parameters a and b of the background are determined less accurate. The final image is therefore of a minor quality.

The multi-ESI method can handle as many images as the operator prefers. At least two pre-edge images have to be collected, thus reducing the multi-ESI method to the 3-ESI method. So, the result of multi-imaging can be compared with the three-image method, both performed on the same set of BN images. Let us consider the boron specific element distribution. For the three image method, two boron pre-edge images are taken at 170 eV and 180 eV, respectively, and the edge signal at 196 eV loss. In case of the multi-ESI method, we have only to consider the net-distribution at one and the same edge position (196 eV). The results for the 3-ESI method and multi-ESI method are respectively shown in Figures 5.15 and 5.16. The spectra are collected at the same pixel position. In case of the 3-image mode, the extrapolation curve in the spectrum (Figure 5.15b) is of worse quality compared to that of Figure 5.16b. According to the X- and Y-intensity distribution, a slope value of $tg\delta = 23$ was selected for the multi-image mode and a $tg\delta = 30$ for the 3-image process. Even at a lower significance level (higher $tg\delta$ value) the net element distribution shows more noise and less significant signal.

In general, one has to be aware that the multi-image method is very sensitive to specimen drift occurring during the image collection. This effect is primarily caused by heating of the sample and is more severe when higher electron doses are used. The result of a shift in a series of images over three pixels results in a scatterplot is given in Figure 5.17. The scatterplot shows three straight lines with a high $tg\delta$ value. Each of these lines is composed of exactly 256 point corresponding with an array of 256 pixels from the edge of the image. However, the linearity between s_I and I is still valid because for the collection of an image, the intensity response for each pixel remains statistically independent.

Image shifts are also easily recognized by rapidly altering the view between the first and last collected image. To avoid specimen drift, cryo-cooling is recommended in order to stabilize the sample prior to image collection.

(a)

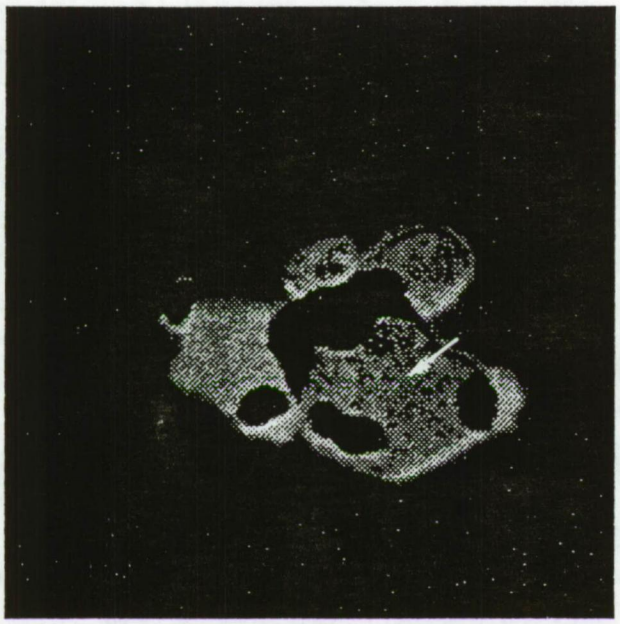

(b)

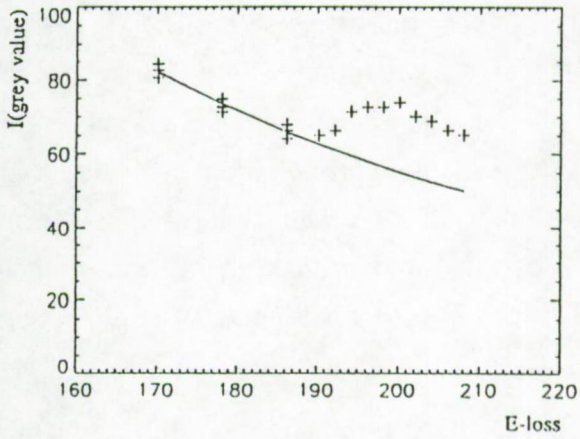

(c)

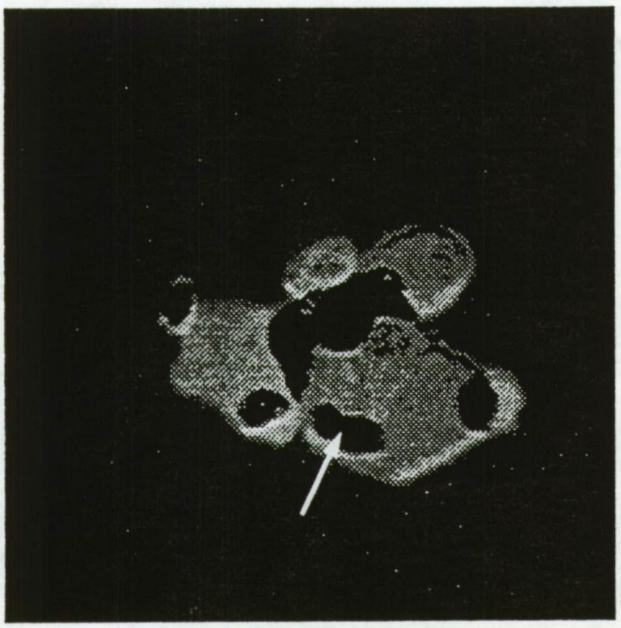

(d)

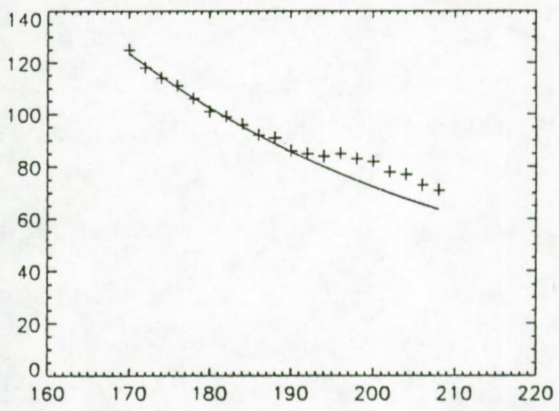

Figure 5.14: (a) Sum of the net-boron distribution for a BN particle when respectively three times three pre-edge images were collected, (b) image spectrum at the pixel positions marked by the arrow, (c) sum of the net-boron distribution when 9 different pre-edge images are collected, and (d) image spectrum at the pixel positions marked by the arrow.

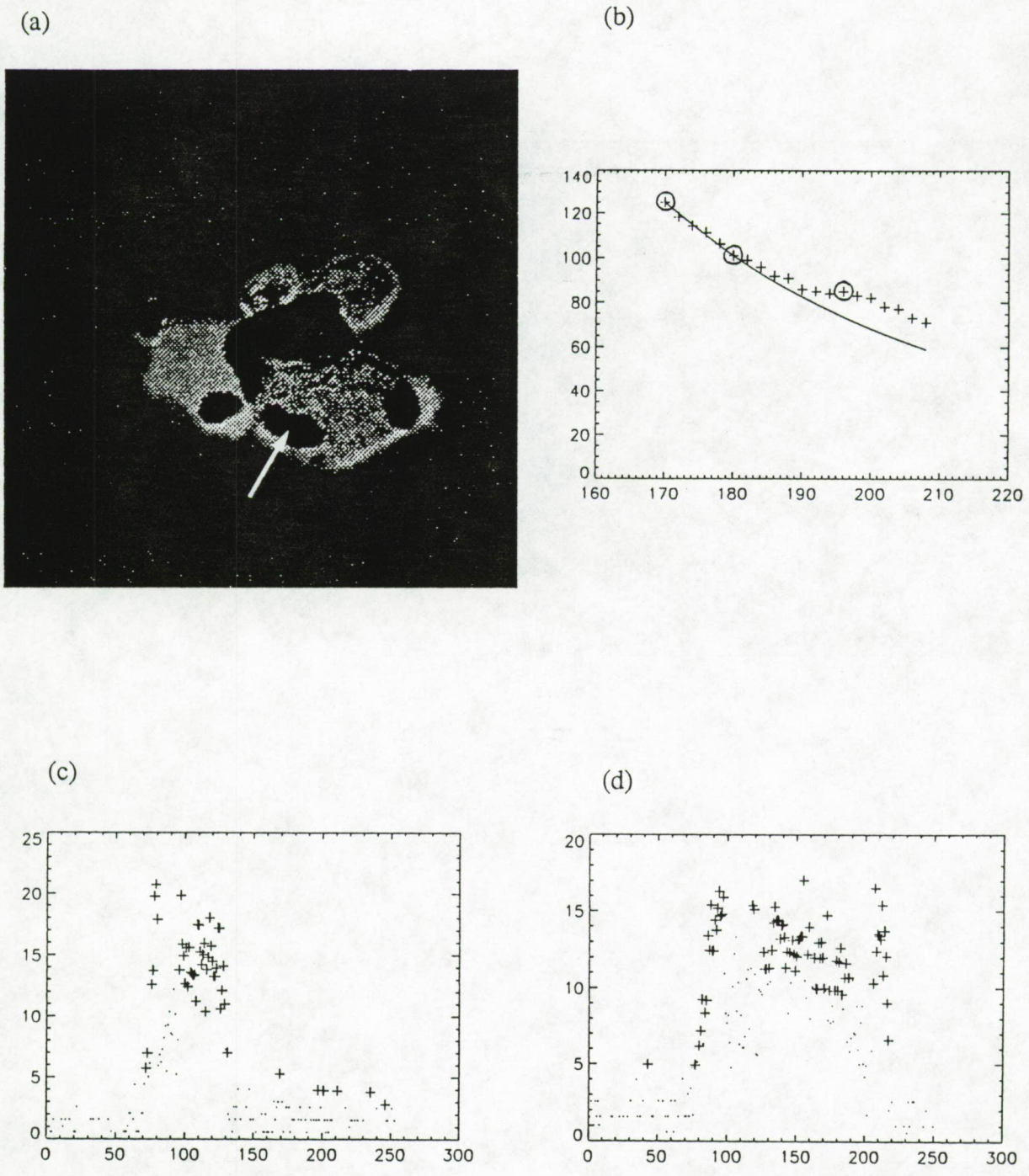

Figure 5.15: (a) net-images of boron obtained by the 3-ESI method (tgδ = 30). (b) spectrum obtained from the pixel position as indicated by the arrow. (c) and (d) are intensity distributions for the boron signal.

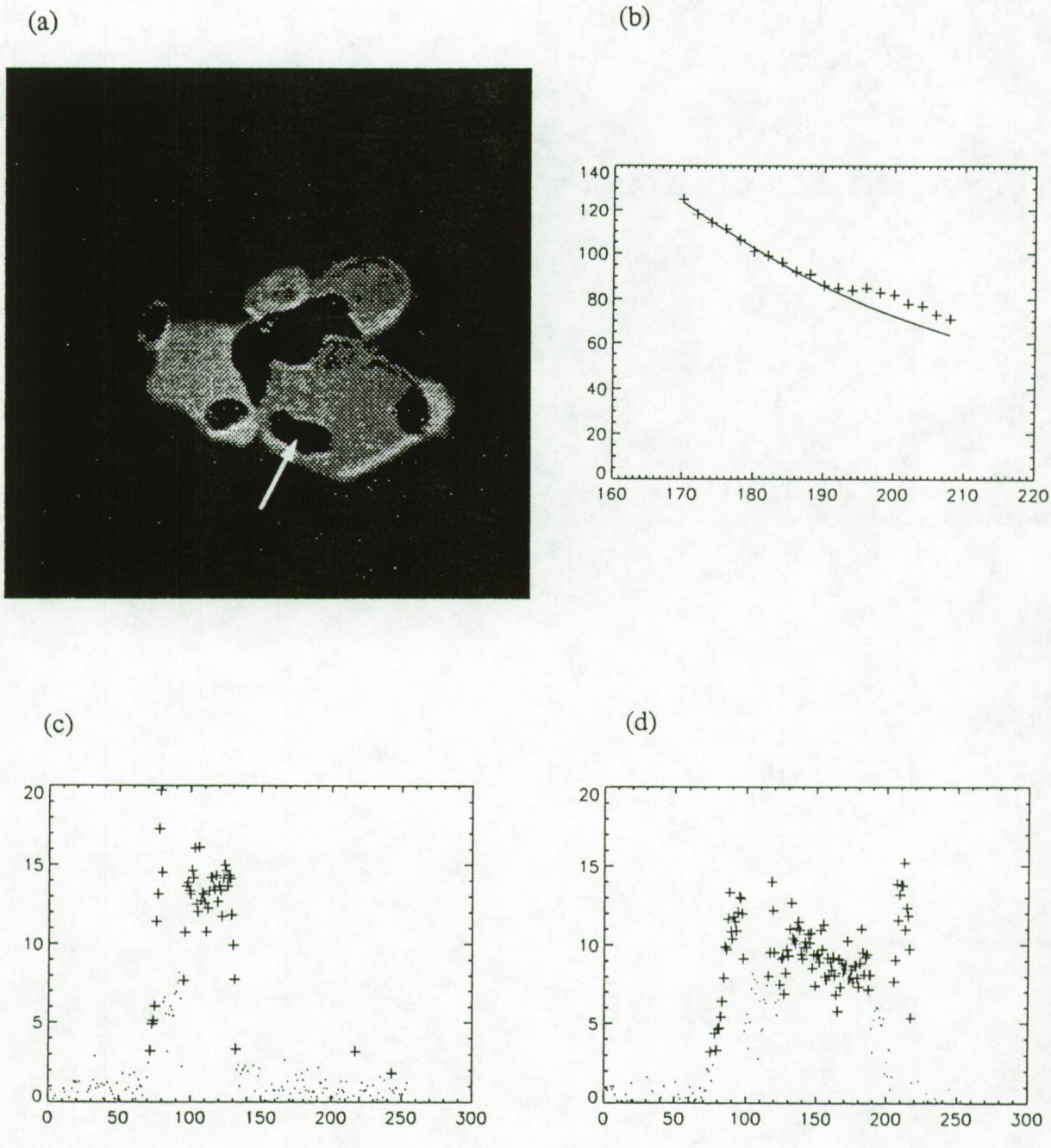

Figure 5.16: (a) net-images of boron obtained by the multi-ESI method (tgδ = 23). (b) spectrum obtained from the pixel position as indicated by the arrow. (c) and (d) are intensity distributions for the boron signal.

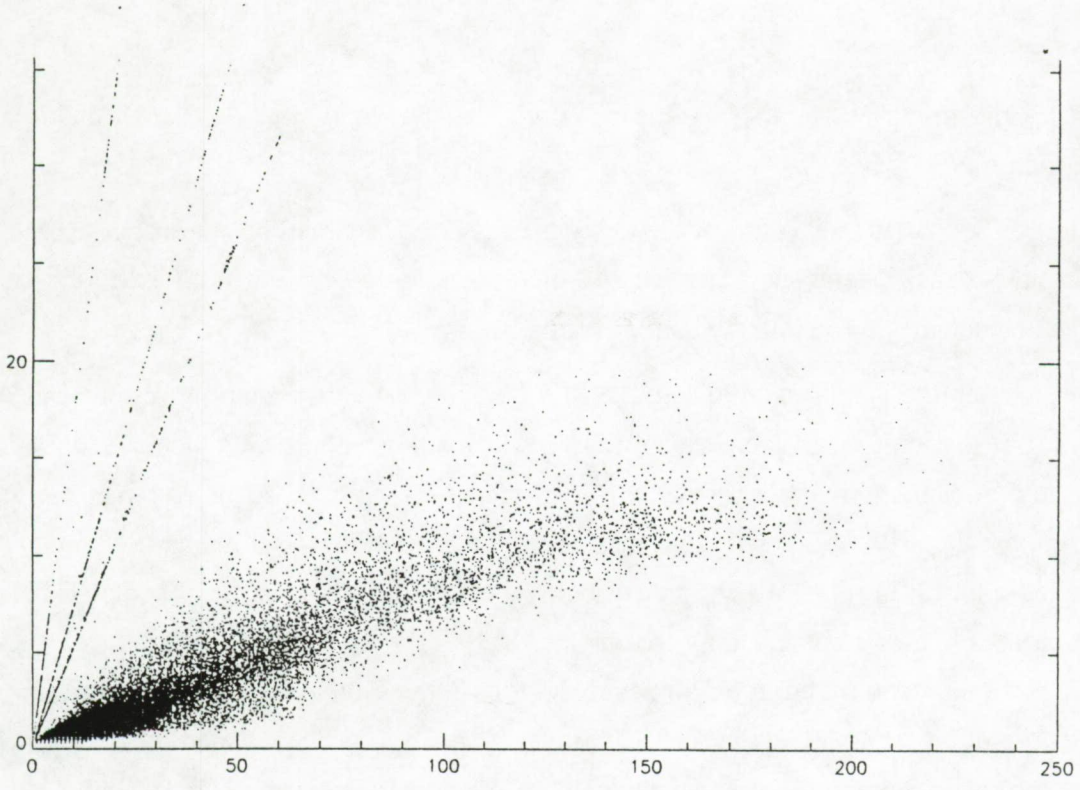

Figure 5.17: Scatterplot obtained from 10 images that suffered a drift over three pixels between the first and the last image.

5.6 Status about quantitative ESI

As for any kind of analytical system, the ultimate goal is to present results in a quantitative way.

The chemical images collected by the multi-image method correlate the intensity with the specific core loss signal and represent qualitative element distributions. The intensity of a net-characteristic electron energy loss image does not directly reflect a truly quantified chemical map, since effects of multiple elastic and inelastic scattering, or variation in incident energy are not considered. Multiple scattering may reduce the signal-to-background ratio and therefore complicates background subtraction. Based on the method of quantifying EELS-spectra (Egerton et al., 1976), the theory of quantitation can be extended to element specific imaging (Leapman et al., 1985). The number of atoms n, of an element detected by the core excitation K in one pixel at position coordinates (x,y), is then in analogy to equation (4.3) given as :

$$n(x,y) = \frac{I_K^{\beta,\Delta}(x,y)}{I_0^{\beta,\Delta}(x,y)\,\sigma_k^{\beta,\Delta}} \qquad (5.12)$$

where $I_K^{\beta,\Delta}$ is the measured core edge intensity for collection semi-angle β and energy-loss integration range,Δ; $I_0^{\beta,\Delta}(x,y)$ is the measured low-loss intensity. $\sigma_k^{\beta,\Delta}$ is the partial cross section for the parameters β and Δ.

Division by $I_0\beta,\Delta$ takes account of the decrease in core loss signal by plural elastic and inelastic scattering. So each characteristic processed image has to be divided by an extra elastic image - this has been clearly underlined by Butler et al. (1982).

In practice for the ZEISS EM902 and a SIT Vidicon camera detection system however, this procedure is difficult to realize because of two reasons. First, the simultaneous acquisition of the elastic and core loss image is prevented by strong differences in intensity range and cannot be recorded by the SIT Vidicon under the same camera setting. Reducing the intensity of the low-loss signal by introducing an intensity absorber or filter with known characteristics in front of the camera can overcome this problem (De Bruijn, 1992). Secondly, the output signal of the camera shows a response curve of higher sensitivity in the middle of the image and sloping down towards the outer regions (Figure 5.18). This effect cannot be compensated by simply subtracting a dark current image from the normal recorded image. Correction is only effective by dividing the net-image by the camera dark current image since the output signal of the camera is the result of a signal amplification process. However, the IBAS system only allows recording and processing of 8 bit images, so, the dynamic range of 256 grey level values is clearly insufficient for performing camera corrections by division of two images.

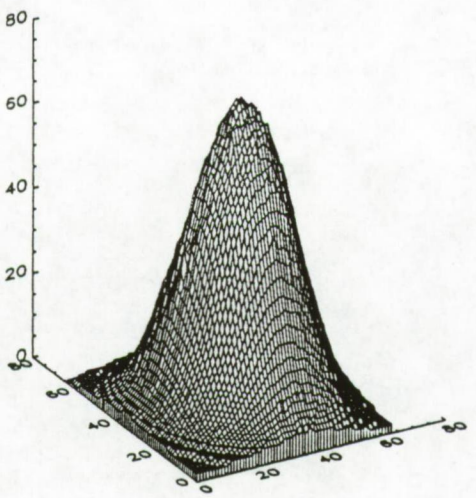

Figure 5.18: Camera respons curve showing the sensitivity of the camera as a function of position along the X and Y axes. The shading plane was recorded by homogeneously illuminating a carbon foil of uniform thickness.

In the present configuration of a TEM coupled with a SIT Vidicon camera and 8 bit image processor, the system remains inadequate for quantitative ESI applications.

5.7 Conclusion

Particle characterization has been demonstrated to be very succesful when the electron microscope with integrated electron energy filter is operated for zero-loss imaging. If contrast enhancement is insufficient, it can be further increased using adaptive image processing routines.

The thickness of the specimen will affect the signal-to-background ratio. At least two or more pre-edge images have to be taken in order to extrapolate the background signal.

For all the multi-ESI experiments, it is proven that this method improves the yield in characteristic net-signal while also reducing the uncertainty on the intensity at each pixel position, especially in comparison with the conventional 3-ESI method. The effect of multi-ESI is even more enhanced when summation of all net-intensities are considered in the final image.

Unfortunately, image acquisition for quantitative purposes is currently limited by the dynamic range of the silicone-intensified TV camera (Somlyo, 1984).

5.8 References

Butler J.H., Watari F., Higgs A.; Simultaneous collection and processing of energy filtered STEM images using a fast digital data acquisition system, *Ultramicroscopy*, 8, 327-334, 1982

Cermola M., Schreil W-H.; Size changes of polystyrene Latex particles in the electron microscope under controlled physical conditions, *J. Electron Microsc. Techn.* 5, 171-179, 1987

De Bruijn W.C.; oral communications, 1992

Egerton R.F., Rossouw C.J., Whelan M.J.; *Developments in Electron Microscopy and Analysis*, Academic Press, London, 129, 1976

Henkelman R.M., Ottensmeyer F.P.; An energy filter for biological microscopy, *J. Microsc.*, 102, 79-94, 1974

Leapman R.D., Fiori C.E., Gorlen K.E., Gibson C.C., Swyt C.R.; Combined elemental and STEM imaging under computer control, *Ultramicroscopy*, 12, 281-292, 1984

Leapman R.D., Gorlen K.E., Swyt C.R.; Digital processing of electron energy loss spectra and images, *Scanning Electron Microscopy* /1985/I, SEM Inc., AMF O'Hare, Chicago, 1-13, 1985

Michiels F.; Aspects of quantification in secondary ion mass spectrometry, Ph.D. Thesis, University of Antwerp (UIA), 1990

Nys, B.; The development of image processing and analytical techniques for applications in chemistry and biochemistry, PhD. Thesis, University of Antwerpen (UIA), 1992

Olesik J.W., Walters J.P.; The silicon-intensified target Vidicon detector: Operation, characterization and application in atomic spectroscopy research, in "*Multichannel Image Detectors*", 31-56, 1983

Ottensmeyer F.P., Andrew J.W.; High resolution microanalysis of biological specimen by electron energy loss spectroscopy and by electron spectroscopic imaging, *J. Utrastruct. Res.*, 72, 336-348, 1980

Reimer L., Ross-Messemer M.; Contrast in the electron spectroscopic imaging mode of a TEM: I Influence of zero-loss filtering on scattering contrast, *J. Microscopy*, 155, 169-182, 1989

Rez P., Ahn C.; Computer control for X-ray and energy cross profiles and images, *Ultramicroscopy*, 8, 341-350, 1982

Somlyo A.P.; Compositional mapping in biology: X-rays and electrons, *J. Ultrastruct. Res.*, 88, 135-142, 1984

Soria F., Artal P., Bescos J., Heinemann K.; Digital image processing of nanometer-size metal particles on amorphous substrates, *Ultramicroscopy*, 24, 19-26, 1988

Talmi Y.; Applicability of TV-type multichannel detectors to spectroscopy, *Anal. Chem.*, 47, 658-670, 1975

Trinick J., Berriman J.; Zero-loss electron microscopy with the Zeiss EM902, *Ultramicroscopy*, 21, 393-398, 1987

CHAPTER 6

Electron energy-loss spectroscopy and electron probe X-ray microanalysis of exhaust aerosols in slurry nebulization inductively coupled plasma atomic emission spectrometry for ceramic powders.

6.1. Introduction

Well-characterized refractory powders such as Al_2O_3, SiC and ZrO_2 are of increasing interest owing to the development of advanced types of ceramics. These powders are difficult to dissolve. Accordingly, direct ways for routine analysis using inductively coupled plasma - optical emission spectrometry (ICP-OES) were studied. In order to optimize such procedures the analyte volatilization processes but also the composition and properties of the analyte vapor produced have to be studied as reported in work on different sampling techniques for direct solid sampling in plasma spectrometry (Broekaert et al., 1988). In spark ablation ICP-OES, electron probe X-ray micro analysis (EPXMA) and X-ray fluorescence (XRF) measurements for Al, Cu and Fe alloys were used. For a medium voltage spark at low repetition rate, it was shown that the composition of the bulk and the particulate material produced in the spark were in good agreement (Raeymaekers et al., 1988b). When using slurry nebulization with a Babington-type nebulizer, it was experienced that fine ceramic powders could be directly analyzed by inductively coupled plasma atomic emission spectrometry (ICP-AES). However, it was found that very small differences in the composition of the produced aerosol occur with different nebulizer gas flows (Broekaert et al., 1988).

Temperatures of ICPs with Ar, N_2, O_2 and air as gases were found to be in the order of 5000 K (Raeymaekers et al., 1988b and 1988c). Modeling of the evaporation processes in a high temperature plasma used for spectrochemical analysis has pointed out that not all of the material is converted into atomic species that are subsequently excited or ionized. A fraction of the

material is only partly evaporated, leaving behind partly molten or remolten particles and fine particulate material as a result of either gas-to-particle conversion processes or cooling processes of a melt, hereafter denoted as residual particulate matter (Raeymaekers et al., 1988b). The evaporation efficiency has been calculated. It was found to be a function of the particulate material, the traveling time in the plasma and the gas temperature, which directly relates to the type of gas used and the respective gas flow rates.

From the literature it is known that the ICP produces individual μm-sized particles and sub-μm condensate particles when it is fed with slurries (Davies and Jeffries, 1986; Raeymaekers et al., 1988a). It was also found in earlier work that for particles sized below 5 μm, the nebulization and transport processes did not cause large changes of particle size distributions of the analyte (Raeymaekers et al., 1988b).

To give a better insight into the processes that occur in the plasma when slurries are nebulized, the residual material leaving the plasma has been sampled in this work for different types of gas and studied using electron energy-loss spectroscopy (EELS) and element specific imaging (ESI). It is complementary to previous work, which has mainly concentrated on the analytical aspects of slurry inductively coupled plasma spectrometry (Broekaert et al., 1988 and 1989), including sample preparation and nebulization (Van Borm et al., 1991) and noise analysis (Van Borm and Broekaert, 1990).

In the present work, EELS and EPXMA will be applied to the exhaust aerosols produced by ICP with Ar, N_2 and O_2 as outer gases, when slurries of Al_2O_3, ZrO_2 and SiC are nebulized by a Babington-type pneumatic nebulizer and analytically relevant working conditions are used. The results will supplement the nebulization and evaporation studies for better understanding of the breakdown mechanisms of the different matrices and to help defining better atomic spectrometric conditions in the application of slurry nebulization ICP techniques for the analysis of these materials.

6.2. Aerosol sampling and sample preparation

For this study, 10 mg ml^{-1} analyte slurries of Al_2O_3, ZrO_2 and SiC were pneumatically nebulized using a commercially available Babington-type G.M.K. nebulizer (Labtest Equipment Co., Ratingen, FRG) fed with a peristaltic pump (Gilson Minipuls II) via a PVC tube (inner diameter 1.0 mm) at a rate of 2.1 ml min^{-1}. The exhaust aerosols were collected on 700 mesh carbon-coated microscope grids that were directly mounted in a Batelle DCI-6 single jet cascade

impactor (Delron Inc.) (Mitchell and Pilcher, 1959). Only material deposited on the last stage, with a cut-off diameter of 0.25 μm, was used for analysis. The sampling equipment for the particulate material is shown in Figure 6.1. To avoid damage of the ca. 20 nm thin carbon foil by the hot gas leaving the ICP, the aerosol was collected by a glass funnel and conducted to the impactor by a 60-cm long silicone rubber tube. Two sampling runs were made. The location of the funnel above the ICP coil and the collection times used to get an optimum particle loading on the grids as well as the other sampling conditions are listed in Table 6.1.

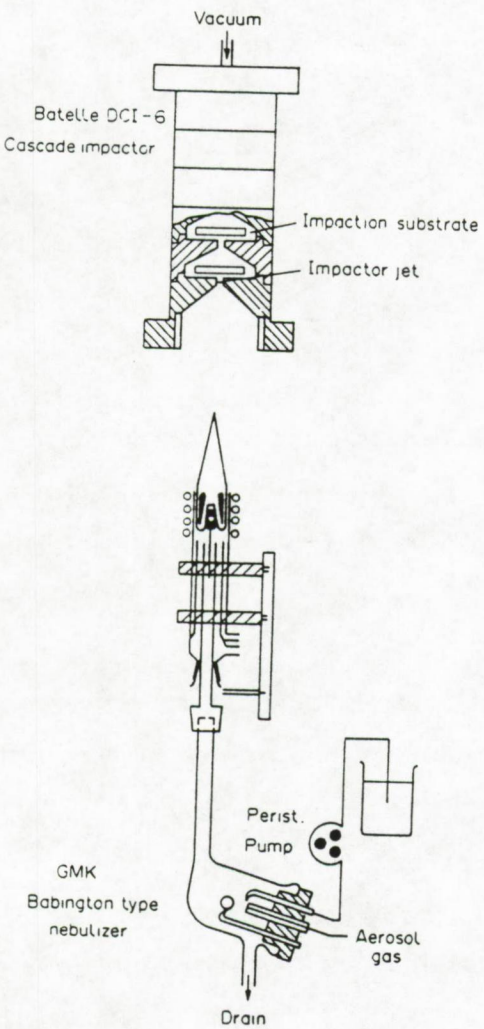

Figure 6.1. Experimental set-up for the sampling of exhaust aerosols produced by slurry nebulization of various ceramic suspensions into an ICP.

Table 6.1. Conditions for the two sampling experiments.

	First experiment		Second experiment	
Parameter	Al_2O_3	SiC	SiC	ZrO_2
Analyte concentration ($\mu g\ ml^{-1}$)	10000	10000	10000	10000
Sample uptake rate ($ml\ min^{-1}$)	2.1	2.1	2.1	2.1
Power (kW)	2.2	2.0	~2	~2
Outer gas ($l\ min^{-1}$)	Ar:22.0	Ar:26.8	Ar:22.0	Ar:22.0
	O_2:24.5	O_2:29.9	O_2:24.5	O_2:24.5
	N_2:26.4	N_2:32.2	N_2:26.3	N_2:26.3
Intermediate gas ($l\ min^{-1}$)	8.2	8.2	4.9	4.9
Aerosol gas ($l\ min^{-1}$)	0.6	0.6	0.5	0.5
Sampling time (min)	2–8	10	8	8
Sampling rate (exhaust aerosol) ($l\ min^{-1}$)	12	12	12	12
Pump rate (exhaust aerosol) ($l\ min^{-1}$)	45	45	45	45
Distance coil-funnel (cm)	40	48	40	40

6.3. Analysis conditions

100 particles were analyzed for 15 seconds each using an electron beam of 20 keV and a beam current of 1 nA. Besides the elemental composition, also the diameter and shape factor of each particle were recorded. For a detailed description of EPXMA with special interest to individual particle analysis, the reader is referred to chapter 1 of this work or to more specialized publications (Bernard et al., 1986; Raeymaekers et al., 1988b).

For EELS analysis, an energy region of about 50 to 70 eV was selected for extrapolation of the background. All EELS spectra were serially recorded at image magnifications between 12,000 and 50,000, the maximum scattering angle being 11 mrad and the energy resolution as measured on the elastic signal being 2.2 eV.

Element specific images (ESI) were collected by selecting an energy band of 7 to 8 eV (measured on the viewing screen). For ESI, two background images were taken at energy positions of about 15 and 25 eV preceding the edge, and an extrapolated image was calculated. This extrapolated image was then subtracted from the image taken at the edge resulting in a "difference" or "net" image showing the elemental distribution. Prior to element mapping, EELS spectra were recorded for verification of the elemental composition. The whole operation of recording and processing element specific images takes less than 3 minutes.

Size, shape factor and aspect ratio distributions of more than 1000 ceramic exhaust particles are obtained by processing zero-loss filtered images as explained in chapter 5. Data, such as the equivalent spherical diameter (D_S), minimum and maximum particle diameter (D_{min} and D_{max}), perimeter and pixel area were used as input data for the distributions.

The equivalent spherical diameter (D_S), shape factor (Shf) and aspect ratio (AR), respectively, are defined and calculated as follows.

$$D_S = 2(\text{area}/\Pi)^{1/2} \tag{6.1}$$

$$\text{Shf} = (\text{perimeter})^2/4\Pi\,\text{area} \tag{6.2}$$

$$AR = D_{max}/D_{min} \tag{6.3}$$

Both the Shf and AR have values equal or greater to one. Actually, the term "shape factor" can be interpreted as a measure of circularity, since it gives the deviation of the projected particle profile from a circle, regardless of the size of the particle. For spherical particles having very rough surfaces, the square of the perimeter rapidly increases and the numerical values of the shape factor diverge more as the shape becomes more irregular. Also the AR was calculated as it does not depend on the roughness but is rather a measure for the roundness of the particles.

6.4. Results and discussion

6.4.1 Al_2O_3

EPXMA and electron microscopy studies were performed on Al_2O_3 particles collected with an electrostatic point-to-plane precipitator. Using a point-to-plane potential of 6 kV and a gas flow rate of 1 ml/min, the collection efficiency for sub-micron particles can be safely assumed to be higher than 30% (Raeymaekers et al., 1988b). Electron microscopical observation of our carbon coated grids showed that the foil did not resist the impaction experiments. Changing the electrostatic impaction conditions negatively influenced the collection efficiency for the aerosol fraction. Therefore we substituted the electrostatic precipitator by a cascade impactor as sampling device. The experimentally observed aerodynamical diameter for the last impaction stage was in good agreement with the theoretical diameter of 0.25 μm.

A sampling time of 8 to 10 minutes and a distance of about 40 cm between the ICP torch and the sampling funnel were found to give the best sampling conditions, if the stability of the ICP versus time, the amount of slurry required and the particle loading on the grids are taken into account.

Electron microscopical examination of the loaded grids showed that most of the particles had a nearly spherical geometry. The diameter, shape factor and aspect ratio number distributions of more than 1000 particles are presented in Figure 6.2. The dimensions of the Al_2O_3 exhaust particles range between 0.05 and 1.6 μm. An exponentially decreasing number distribution is observed toward the larger diameters. A Gaussian distribution with a maximum around 0.35 μm is superimposed on it. A hierarchical cluster analysis was applied to the morphology data in order to classify all the measured particles into distinct groups or particle types. The classification was done by selecting only the spherical diameter and the aspect ratio, since these two variables are independent of each other. However, the spherical diameter and the shape factor are both based on the area determination and thus are correlated variables. Therefore, we preferred the aspect ratio over the shape factor. As a result of the multivariate analysis, three different particle morphologies were observed (Table 6.2), namely (a) spherical Al_2O_3-particles having a mean diameter of 0.4 μm (type 1); (b) larger irregularly shaped Al_2O_3-particles with a mean diameter of about 0.6 μm (type 2) and (c) Al_2O_3-particles with particle diameters smaller than 0.2 μm i.e. mean diameter of 0.09 μm (type 3).

Table 6.2: Results of the classification of more than 1000 Al_2O_3 exhaust particles into 3 different clusters (particle types) according to the variables D_s and AR.

Number	D_{max} (μm)	D_{min} (μm)	D_s (μm)	*Shf*	*AR*
291	0.11	0.09	0.09	1.4	1.3
583	0.55	0.42	0.42	1.3	1.2
209	0.91	0.41	0.60	1.7	1.8

Almost 30 % of all the exhaust particles have diameters below 0.12 μm. The smallest particles sometimes seemed to be attached to the larger ones. This fact was also observed for spark produced aerosols (Raeymaekers et al., 1988b). However, more often the small particles were found to surround the irregularly shaped particles according to a typical ring pattern (Figure 6.3). The aspect ratio for particle types 1 and 3 suggests a more rounded or spherical shape than for particles of type 2.

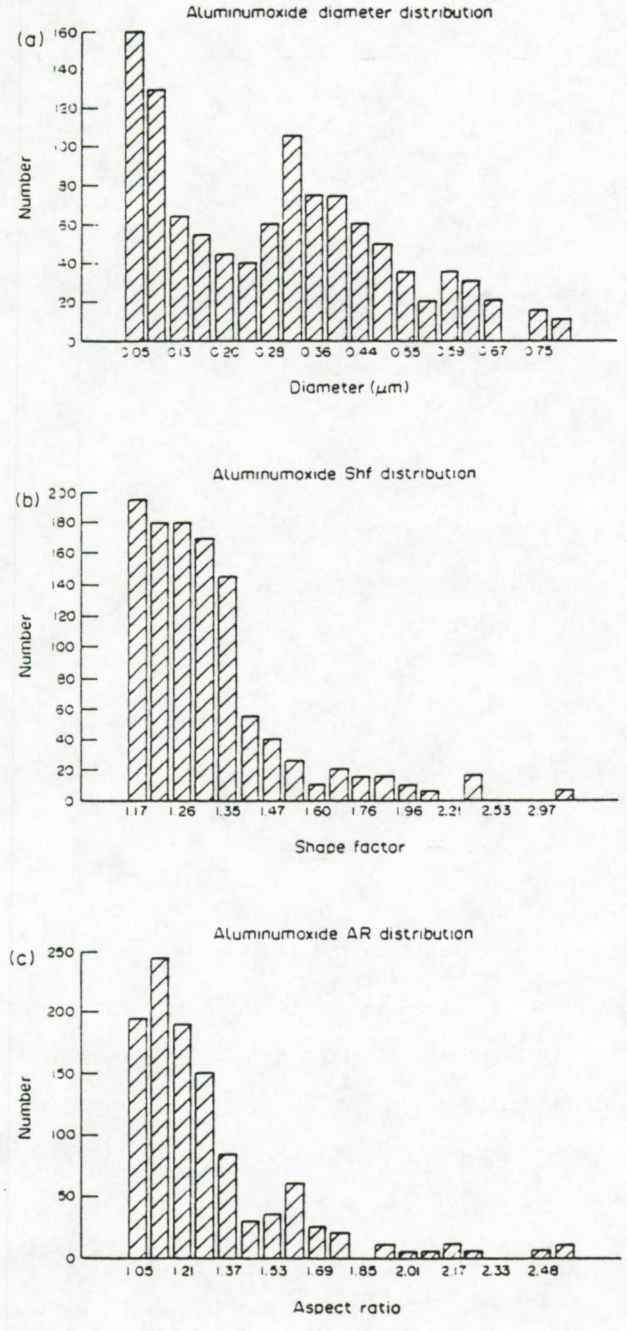

Figure 6.2: Number distribution plots of: (a) diameter, (b): shape factor and (c): aspect ratio of Al_2O_3 exhaust aerosols obtained from the first experiment.

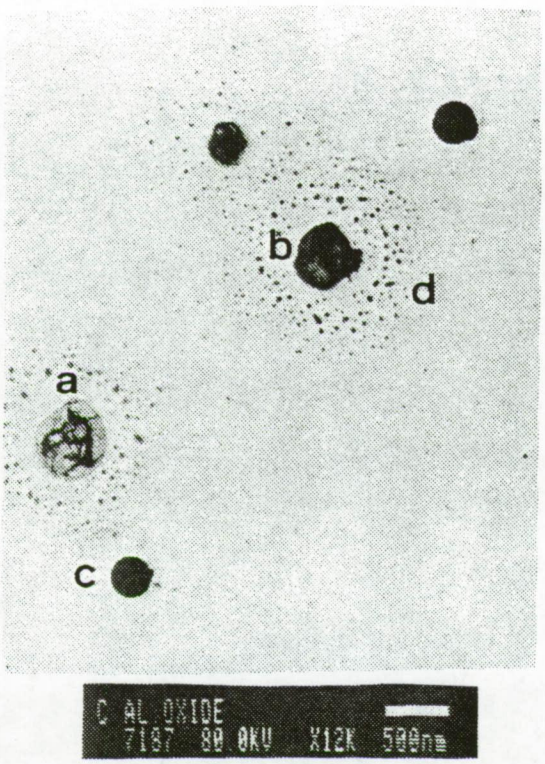

Figure 6.3: Sub-μm sized irregular and spherical Al_2O_3 exhaust aerosols of (a): an irregular Al_2O_3 particle after structure modification by the electron beam, (b): before structure modification, (c): spherical sub-μm Al_2O_3 aerosols and (d) very small particulate material surrounding the larger particles.

Electron microscopical inspection indicated that the spherical particles remained very stable to high electron beam irradiation doses, whereas both the irregular and the surrounding small particles noticeably suffered structure modifications, leaving behind spots with different transparency in the center of the structure. Figure 6.3 shows a picture of two irregularly shaped particles, one before (a) and one after (b) modification by the electron beam. Very small clusters can also be seen all over the carbon foil. These small clusters do not seem to be transformed, even under stringent electron beam conditions. Most of these very small particles are excluded from the distribution data because of insufficient contrast in the transmission image and therefore, they are almost totally suppressed by the threshold setting of the image background. Their chemical composition, however, is identical to that of the larger particles. An EELS spectrum showing the Al-L absorption edge from a 0.07 μm Al_2O_3 particle is shown in Figure 6.4.

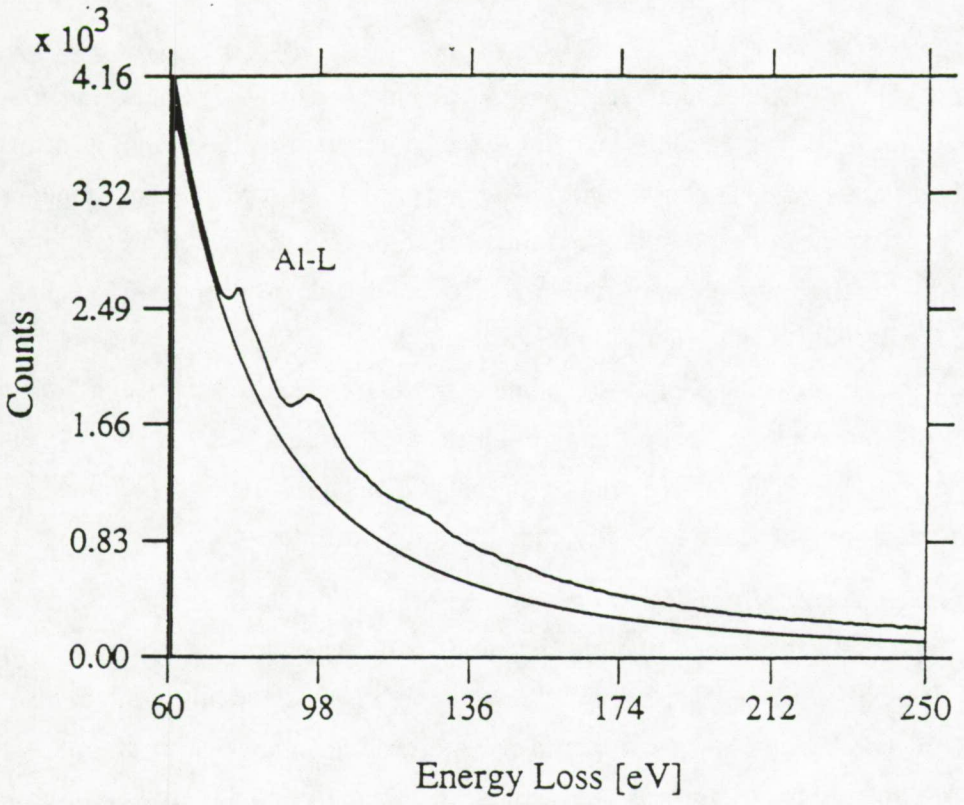

Figure 6.4: Serially recorded electron energy loss spectrum of a 0.1 μm Al_2O_3 exhaust particle showing the characteristic Al-L absorption edge at 75 eV above the extrapolated background (lower curve).

More detailed information about the shape and size of the particles with diameters larger than 0.3 μm was obtained by automated EPXMA measurements. The EPXMA measurements cover the analysis of the first two particle types because the dimensions of particle type 3 are much too small to be detected by the automated EPXMA. Hierarchical cluster analysis was applied to the EPXMA elemental composition results to classify the 100 particles in 3 different classes (Table 6.3).

Table 6.3: Characterization of 3 different exhaust Al_2O_3 particle types after a multivariate classification procedure according to the elemental composition variation as measured by EPXMA.

Particle type	Detected elements	Diameter (μm)	*Shf*	Abundance (%)
Al_2O_3	Al	0.4	1.1	66
Al_2O_3	Al	0.5	1.4	32
Diverse	Al,Si,S	0.8	2.3	2

About 65 % of all the particles analyzed by EPXMA have a nearly spherical shape (shape factor close to 1). Aluminium was the only element detected and particles belonging to this group are therefore identified as Al_2O_3. The second cluster or particle group with an abundance of 32 % has a slightly higher mean shape factor and thus contains particles which are slightly aspherical. Also here, Al was the only element detected. However, the difference in mean diameter, as compared to the particles of the first group, is too small to be significant. It is more probably due to limitations in the measuring process rather than real differences between the two particle groups. The difference in the shape factor might suggest a different particle morphology. The third group of particles has an abundance of only 2 % and contains particles with variable elemental composition; these are probably contamination particles.

As the aerosol generated from the slurry passes through the high temperature region of the plasma, the particulate suspended material becomes partially or totally molten. For the partially molten particles, only the outer parts are molten or more viscous and still contain a solid nucleus. The vertical injection of the suspension and the convection of the warm air masses above the plasma are responsible for the upward movement of the analyte material. The high temperature drop on their trajectory from the plasma toward the impactor is responsible for the cooling of the analyte material. The spherical particles observed are typically generated from combustion processes. During the cooling of a gas, which happens when the plasma is sampled with the cascade impactor, condensation occurs and gas-to-particle conversion is a very probable mechanism resulting in almost spherical particles and it often occurs besides vapor condensation. The first phenomenon is often observed in industrial burning processes such as the formation of fly-ash particles from power plants (Mamane et al., 1986) or Fe-oxide particles from iron foundries (Post and Buseck, 1983). As the spherical particles are the most abundant ones (2/3 of all particles), this mechanism would imply that most of the analyte is converted to the vapor phase.

A fraction of the larger irregularly shaped particles is surrounded by very small aggregates. These small aggregates are found as a regular ring pattern, but are never observed around the spherical particles. Most probably, the particles have relatively loose upper layers due to stress during the cooling process so that they splash out and give rise to the typically observed ring phenomenon as the particulate material impacts on the grid. This ring pattern could also be due to the fact that a fraction of the analyte (either in the form of a gas or in partially remolten forms) still has viscous parts before impaction. During the collection, the very small particles are then also formed by splashing out. These typical ring patterns are also found in other impaction experiments, when, e.g., H_2SO_4 droplets impact on a filter (Mamane and De Pena, 1978).

However, it is hard to believe that the analyte material is not fully condensed (i.e., is not cooled down completely to the solid state) as this would require still very high temperatures 40 cm away from the ICP torch. The fact that irregular particles show deformations during irradiation might be due to recrystallization in a more stable structure. It may even be so that some gas is entrapped during the cooling process and might be driven out of the particles, leaving back less dense areas within the particle. After transformation by the electron beam, these particles would become stabilized. In Figure 6.3, the smooth surface of the spherical type is seen in contrast with the rough and cleaved structure of the irregular particle type.

6.4.2 SiC

For the experiments with SiC powders, different ICP operating conditions were applied. Three outer gases were used, namely Ar, O_2 and N_2. The major particle types observed for all 3 outer gases also have morphologies corresponding to spherical SiC particles. However, a larger fraction of the exhaust particles have more irregular shapes. This can be clearly seen in Figures 6.5 and 6.6, presenting diameter, shape factor and aspect ratio distributions of SiC exhaust particles for O_2 and N_2 as outer gases, respectively.

A typical "satellite" SiC particle type was observed for all 3 outer gases used. They were found in both the first run of experiments and the second one. This type of particles was never observed for Al_2O_3. However, when changing the outer gas from Ar or N_2 to O_2, the number of these "satellite" type of particles seemed to increase. Almost 10 % of all the observed particles in the case of O_2 as an outer gas resembled satellites composed of a central body (core) having 1 to 3 long antennas (Figure 6.7). These antennas did not seem to have a preferential direction, ruling out the possibility that they may have been created by or as the result of the impaction process. Sometimes, very small particles were found which also surrounded these irregular ones. The diameter of the latter ranges between 0.3 and 0.8 μm. The tails have a width comparable to that of the very small particles. Their length varies between 0.05 μm and up to several micrometers. They can be much longer than the central body itself. Tables 6.4a and 6.4b, show the multivariate classification results for N_2 and O_2 as outer gas, respectively.

The size and morphological parameters showed that these typical "satellite" particles were the particle groups with the lowest abundance.

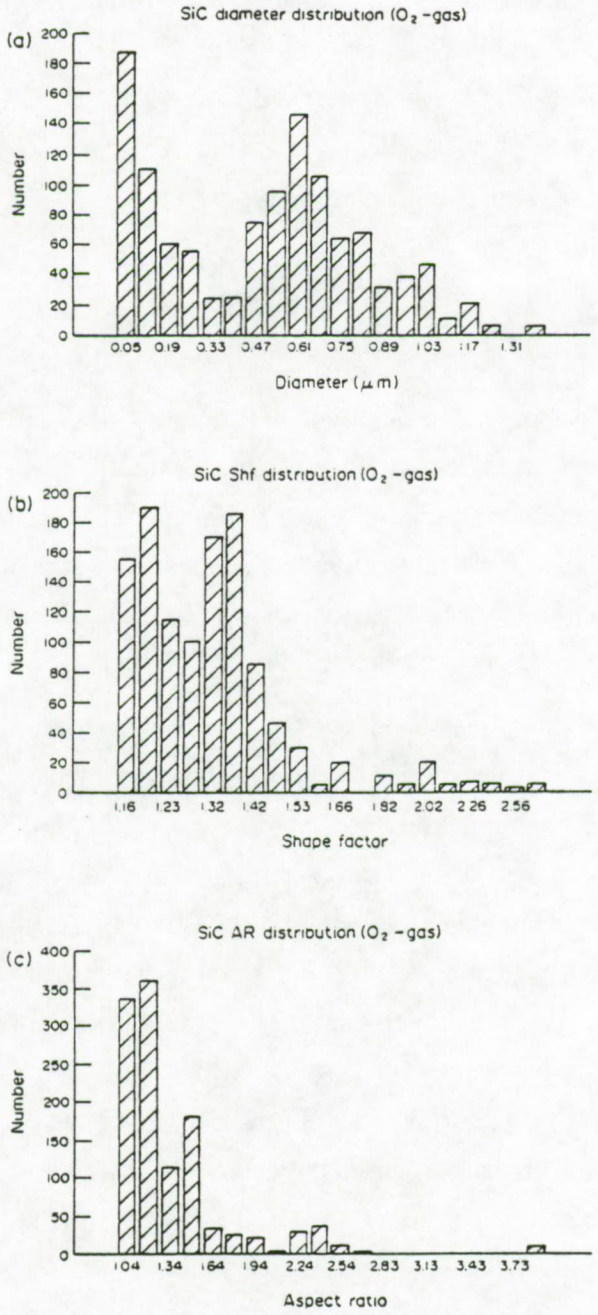

Figure 6.5: Number distribution plots for (a): diameter, (b): shape factor and (c): aspect ratio for SiC slurries using an ICP with O_2 as an outer gas (second sampling series).

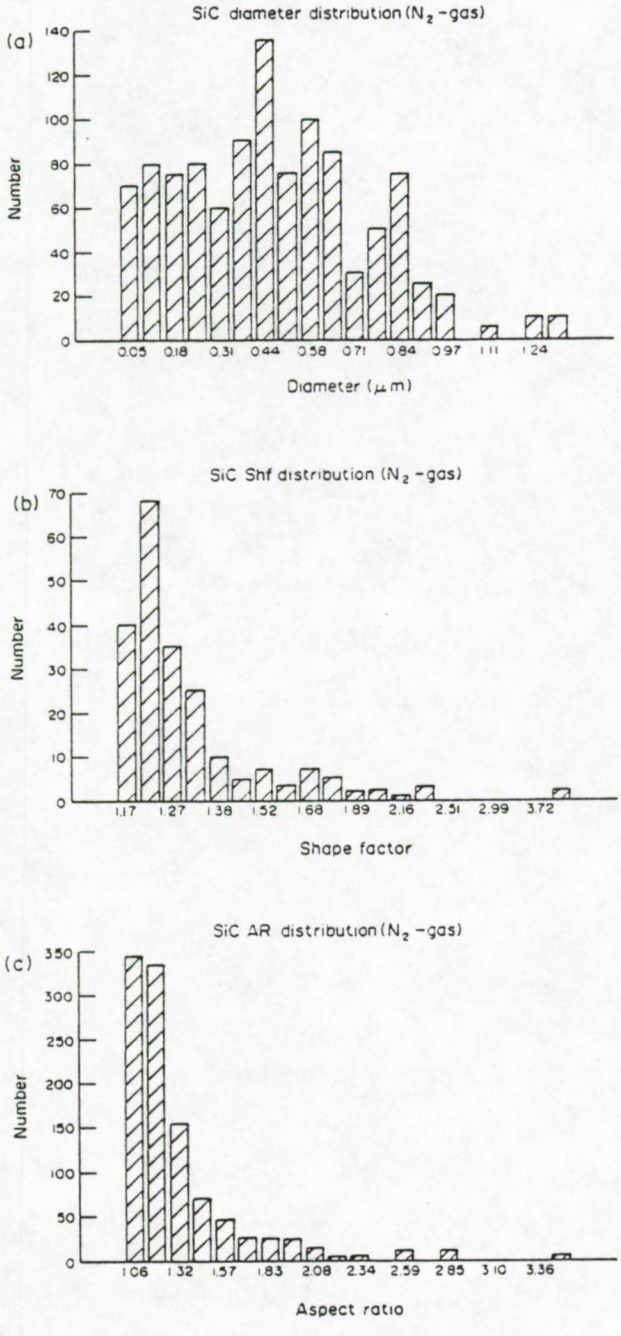

Figure 6.6: Number distribution plots for (a): diameter, (b): shape factor and (c): aspect ratio for SiC slurries using an ICP with N_2 as an outer gas (second sampling series).

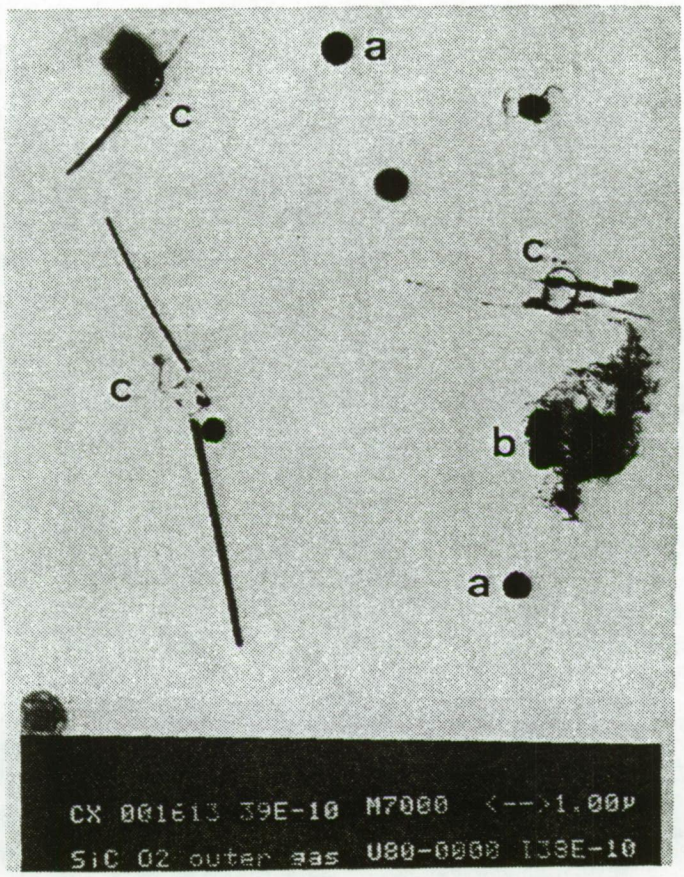

Figure 6.7: Sub-µm SiC exhaust aerosols collected when using O_2 as an outer gas (second sampling run). Different particle morphologies are observed such as (a): spherical, (b): irregular and (c): satellite particle types.

No differences in morphology or chemical composition were observed for the SiC powders sampled during each of the experiments. For the SiC samples, not only Si and C, but also N and O were detected in both the spectrum and imaging mode. N was only observed in a minor fraction of the SiC, namely in the satellite type and the irregular particle type. As the analyte trajectory passes through an area of air at room temperature, it cools down and can react with atmospheric O_2 and N_2. An EELS spectrum showing the Si-$L_{2,3}$, N-K and O-K edge is presented in Figure 6.8. The O-signal may represent either dissolved O_2 in the bulk of the particles or chemically bound O_2, as was also observed in Si_3N_4 powders (Jenett et al., 1989).

EELS can provide detailed information about the electronic state and chemical bonding of the sample. Indeed, the form of the characteristic E-loss structure depends sensitively on the bonding and coordination of the atom and thus, different forms of the same element can be distinguished (Joy, 1986). Figure 6.9 presents different net Si-$L_{2,3}$ absorption edges which were collected from various Si-standards.

Table 6.4: Results of the classification of more than 1000 SiC exhaust particles into 3 different clusters for the ICP operated with (a): O_2 as an outer gas and (b): N_2 as an outer gas, respectively.

Number	D_{max} (μm)	D_{min} (μm)	D_s (μm)	*Shf*	*AR*
(a)					
622	0.84	0.66	0.72	1.2	1.2
433	0.21	0.14	0.16	1.4	1.5
110	2.00	0.77	0.86	2.0	2.3
(b)					
618	0.59	0.50	0.58	1.2	1.2
403	0.23	0.18	0.20	1.6	1.8
54	2.05	0.68	1.05	2.2	2.6

(a)

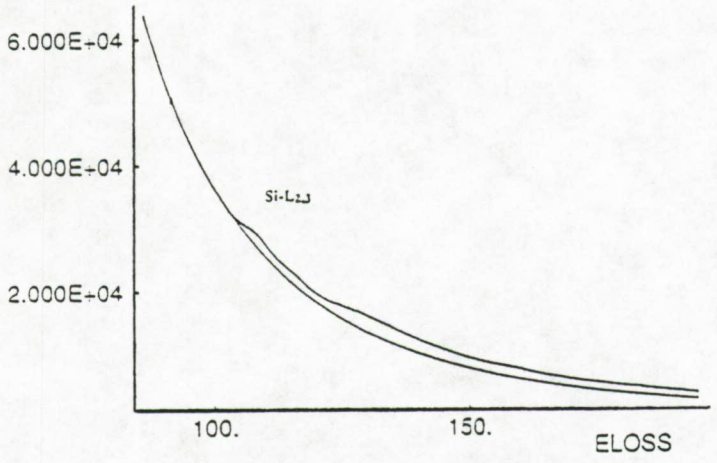

(b)

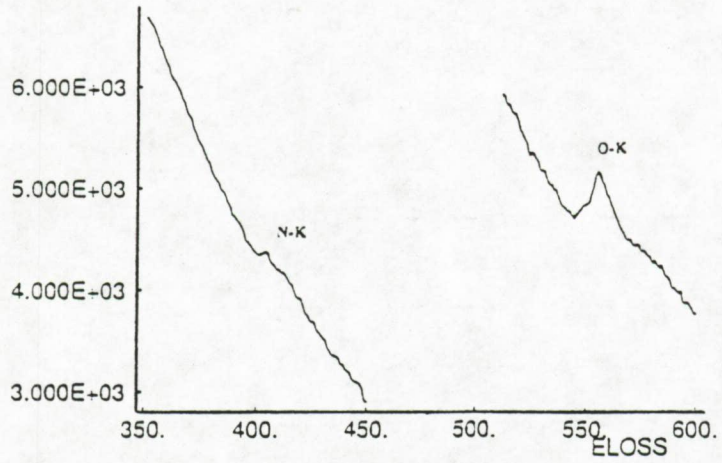

Figure 6.8: Serially recorded electron energy-loss spectrum of an ICP produced SiC exhaust particle for O_2 used as an outer gas. (a): detailed spectrum showing the Si-$L_{2,3}$ edge above the extrapolated background and (b) the N-K and O-K absorption edges, respectively.

After comparison with these three standards, we see a good similarity with the SiO_2-edge. This might be an indication that at least a part of the Si has chemically reacted with oxygen to form a Si-O-bond.

For all the different gases used, O_2 was observed in all SiC particles but N was often absent. Element-specific images of particles as small as 0.05 μm were recorded for the 3 different samples. Results of the ESI technique for a SiC exhaust particle show a homogeneous oxygen distribution (Figure 6.10). When showing the N, C and O results in overlay for a typical SiC particle (Figure 6.11), homogeneous distributions over the particles for all three elements are found.

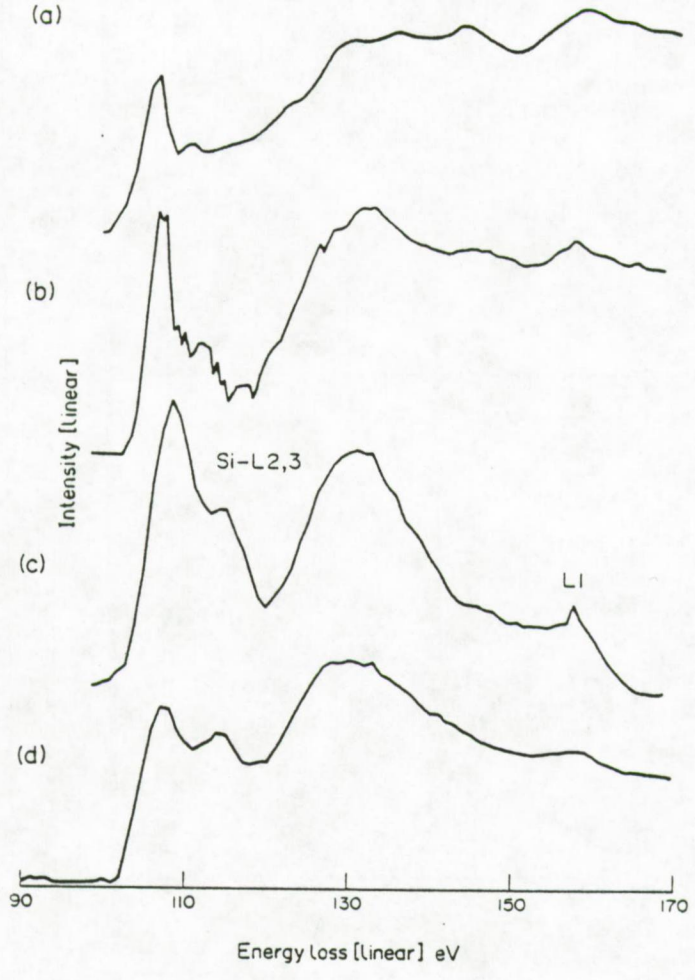

Figure 6.9: Nett-Si energy-loss spectra of (a): SiC standard, (b): Si_3N_4 standard, (c): SiO_2 standard and (d): SiC exhaust aerosols, respectively.

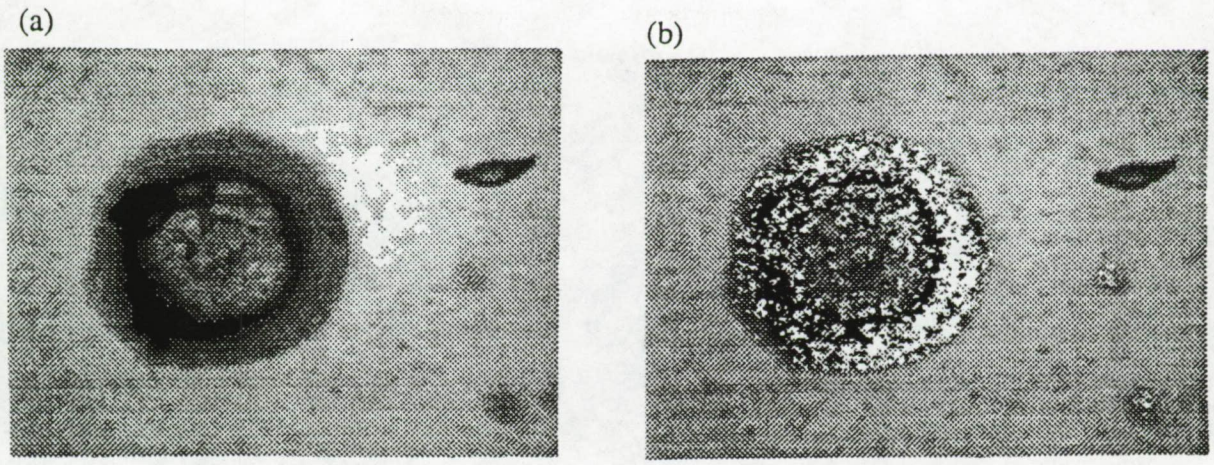

Figure 6.10: Element-specific images of SiC exhaust particles. Outer gas: O_2. (a): zero-loss image, (b): netto intensity distribution of O as an overlay on the zero-loss image.

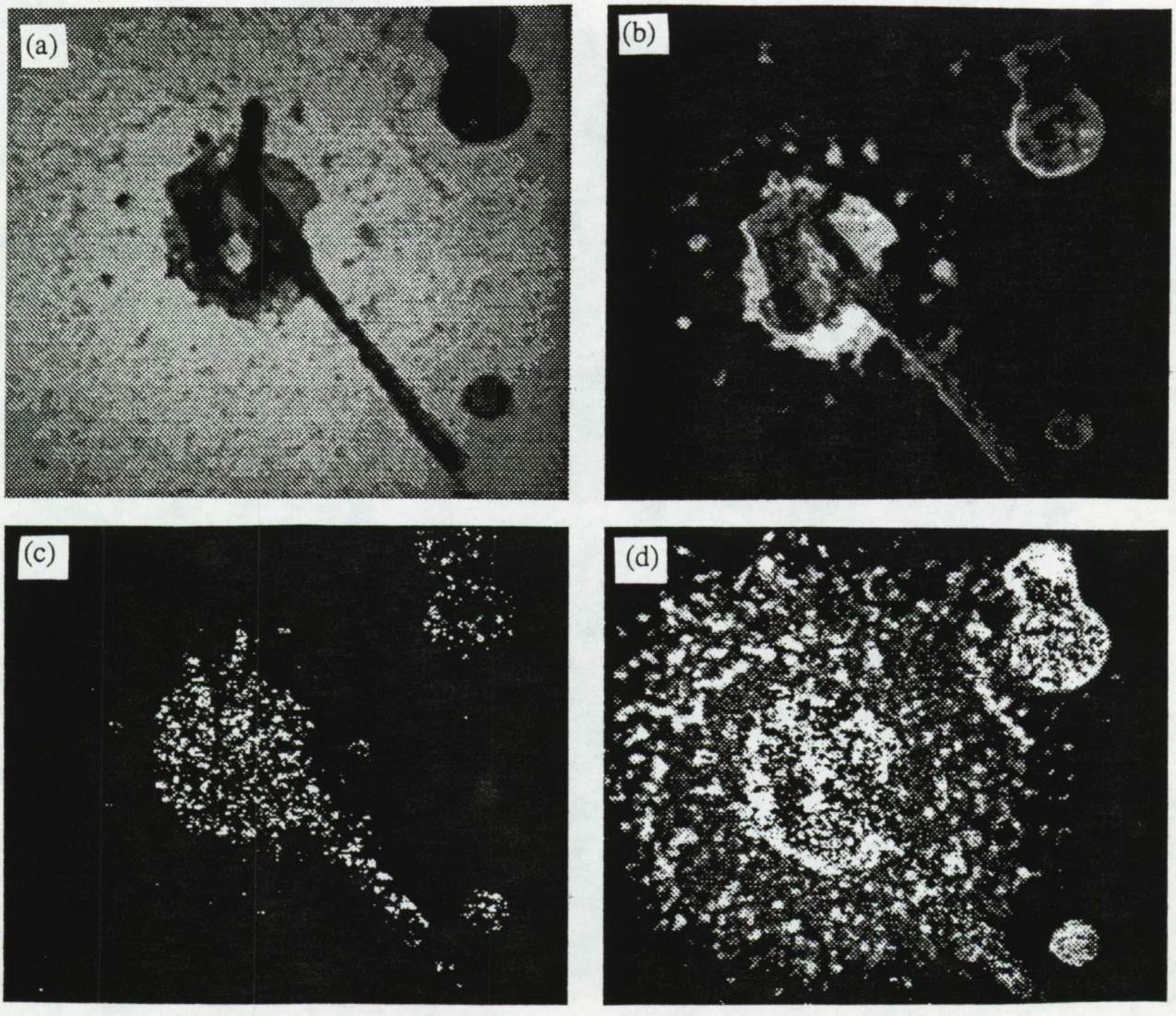

Figure 6.11: Element-specific images from SiC exhaust particles. Outer gas: O_2. (a): zero-loss image, netto-intensity distribution of (b): C (c): N and (d) O, respectively.

6.4.3 ZrO2

When using 3 different outer gases (Ar, N_2 and O_2) in the nebulization of ZrO_2 slurries into ICPs, no differences in shape, morphology and chemical composition of the produced ZrO_2 aerosols were found. A very large fraction of all particles is spherical with a mean diameter of 0.25 μm (Table 6.5).

Table 6.5: Results of the classification of more than 1000 ZrO_2 exhaust particles into 3 different clusters (particle types) according to the variables D_S and AR.

Number	D_{max} (μm)	D_{min} (μm)	D_s (μm)	*Shf*	*AR*
849	0.34	0.28	0.30	1.2	1.21
164	0.48	0.28	0.37	1.4	1.60
57	0.10	0.02	0.05	1.7	2.20

A small fraction of the ZrO_2 particles has an irregular shape. Size and morphology distributions for ZrO_2 exhaust particles for an ICP with Ar as an outer gas are shown in Figure 6.12.

ESI images were recorded at the energy loss of the M-edge of Zr, namely at 180 eV. From element specific mapping, it could be concluded that also the distribution of Zr and O is homogeneous over the whole particle for both the round and irregular ones. By EELS spectrum analysis of the exhaust particles for ZrO_2 slurries no elements other than Zr and O could be detected. EELS spectra (Figures 6.13a and b) of the Zr-M edge at 175 eV and the Zr-L_1 and Zr-L_2 edge at 2200 and 2300 eV, respectively, could be obtained from a ca. 0.1 μm ZrO_2 particle. These spectra were recorded in parallel mode using a JEOL 2000 FX scanning transmission microscope coupled to a Gatan spectrometer (model 666) and a Kevex 7000 multichannel analyzer. Element specific maps showed that Al and Zr also seemed to be distributed homogeneously over the whole particles just as O did.

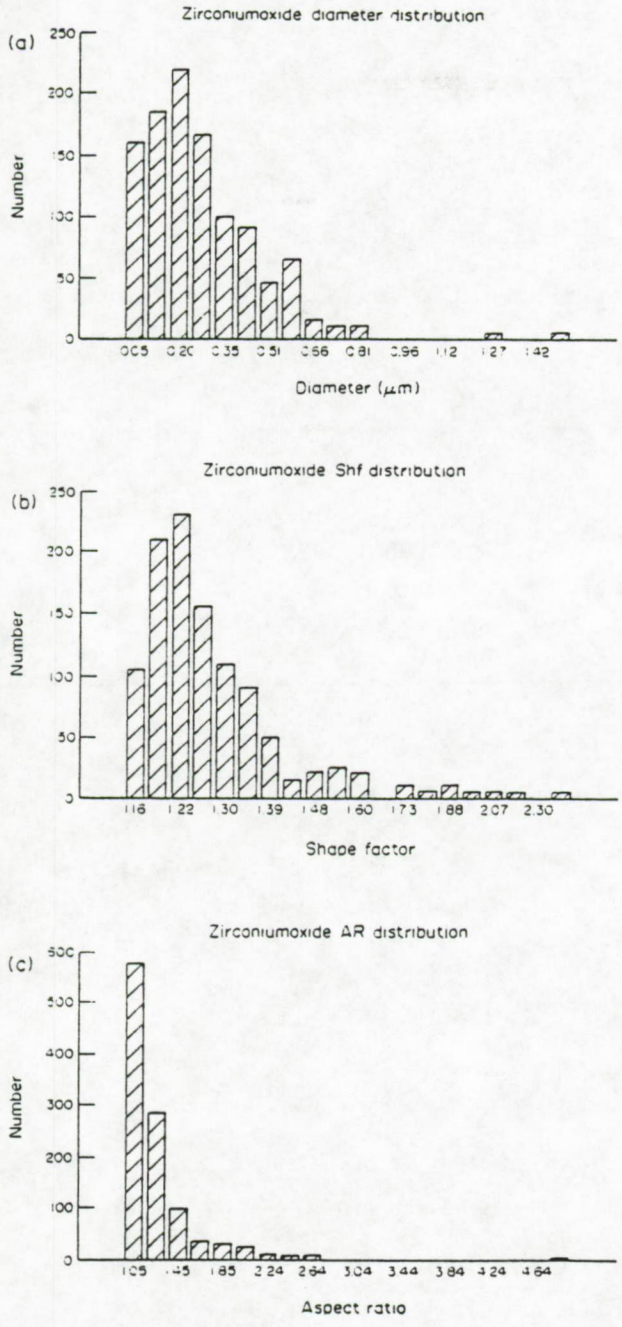

Figure 6.12: Number distribution plots of (a) diameter, (b) shape factor and (c) aspect ratio of the ZrO_2 nebulization experiment using an Ar-outer gas.

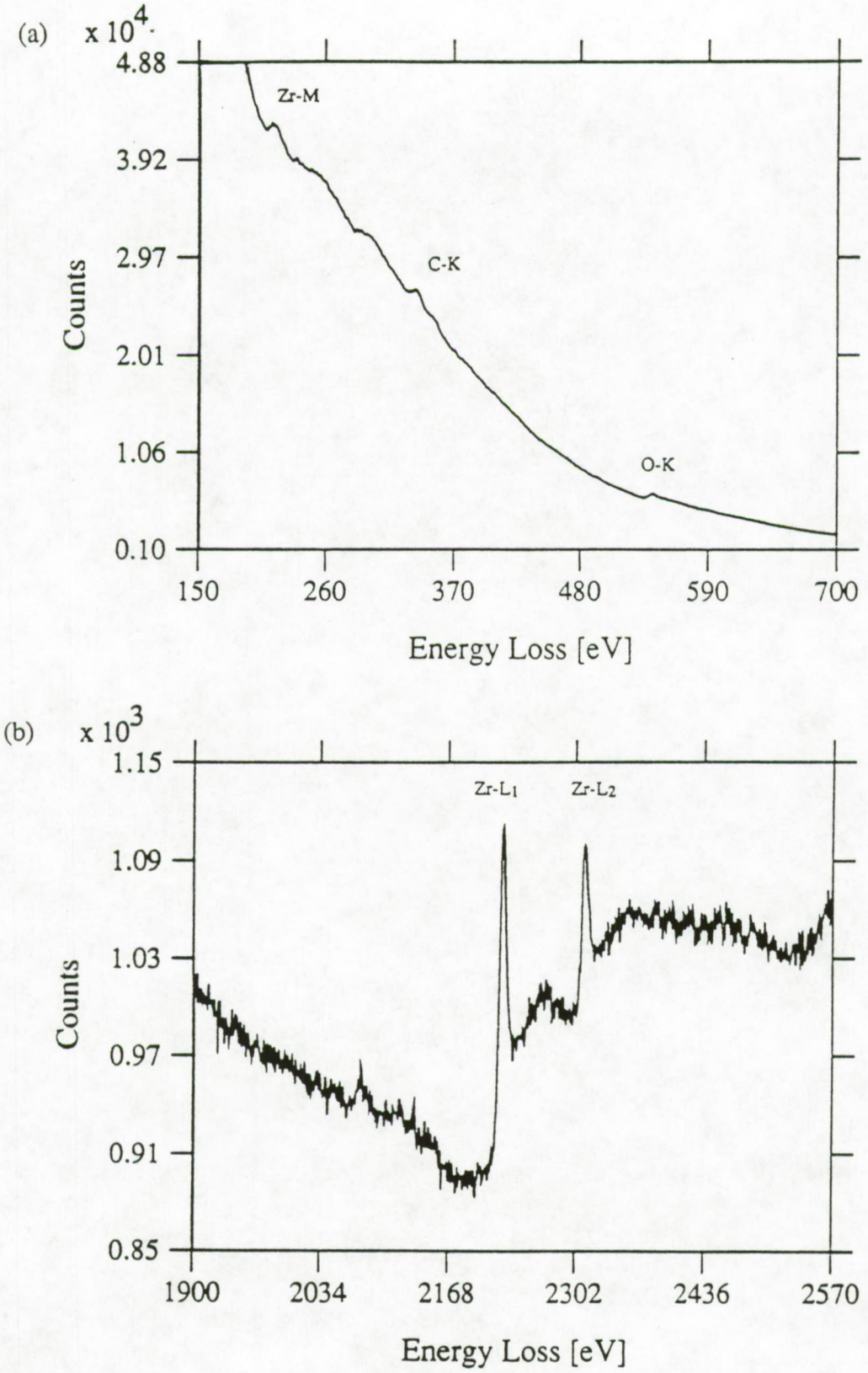

Figure 6.13: Parallelly recorded EEL-spectra of (a) the Zr-M edge at 175 eV and (b) the Zr-L_1 and Zr-L_2 edge at 2200 and 2300 eV.

6.5. Conclusions

The large spherical particle structures observed for Al_2O_3, SiC and ZrO_2 are formed during the cooling of the analyte by a gas-to-particle conversion mechanism. These particles formed the major fraction for Al_2O_3 and ZrO_2 but were less abundant in the case of SiC samples.

For Al_2O_3 and ZrO_2, no differences in morphology and chemical composition were observed when using different outer gases. The breakdown process of SiC may be understood to depend considerably on the choice of the outer gas. Of the three gases used, O could be detected in all particles; it is homogeneously distributed over the particles.

A comparison of the results of both experiments reveals that the use of various outer gases (N_2, O_2 and Ar) has no effect on the shape and morphology of the sub-μm aerosols. No unexpected chemical composition was observed for residual particulate matter in the case of Al_2O_3 and ZrO_2, but indeed, for SiC, O was present in all particles for the 3 different gases. The use of O_2 as outer gas for the ICP seems to affect the composition of the exhaust SiC particles in which N_2 was sometimes detected.

Slurries of different ceramic powders nebulized under the same operating conditions (experiment 2) may result in a different morphology, as shown for ZrO_2 and SiC. The element N was never detected in ZrO_2 exhaust aerosols. Probably the air column between the plasma and impactor leads to oxidation of the analyte material.

In the experiments performed, quantitative volatilization probably does not take place. However, some questions remain unanswered, such as why N is never detected when the ICP is operated with Ar and N_2 as outer gas or why N is not found on Al_2O_3 and ZrO_2 particles?

6.6. References

Bernard P.C., Van Grieken R., Eisma D.; Classification of estuarine particles using automated electron microprobe analysis and multivariate techniques, Environ. Sci. Technol. 20, 467-473, 1986

Broekaert J.A.C., Leis F., Raeymaekers B., Zaray Gy., A study of some techniques for direct solids sampling in plasma spectrometry, Spectrochim. Acta 43B, 4/5, 339-353, 1988

Broekaert J.A.C., Graule T., Jenett H., Tölg G., Tschöpel P.; Analysis of advanced ceramics and their basic products, Fresenius Z. Anal. Chem. 332, 825-838, 1989

Davies J.A., Jeffries A.C.; Size distribution of particulate matter in exhaust gasses in inductively coupled plasma atomic emission spectrometry, Analyst 111, 221-223, 1986

Jenett H., Bubert H., Grallath E.; Comparative surface and bulk analysis of oxygen in Si_3N_4 powders, Fresenius Z. Anal. Chem. 333, 502-506, 1989

Joy D.C.; The basic principles of EELS, in "Principles of Analytical Electron Spectroscopy", Eds. D.C. Joy, A.D. Romig Jr. and J.I. Goldstein, Plenum Press, New York, pp. 250, 1986

Mamane Y., De Pena R.G.; Quantitative method for detection of individual submicrometer size sulfate particles, Atmos. Environ. 12, 69-82, 1978

Mamane Y., Miller J.L., Dzubay T.G.; Characterization of individual fly ash particles emitted from coal- and oil-fired power plants, Atmos. Environ. 20, 2125, 1986

Mitchell R.I., Pilcher J.M.; Ind. Chem. Engng. 51, 1039, 1959

Post J.E., Buseck P.R.; Energy dispersive X-ray microanalysis of individual particles from two secondary iron foundries, Microbeam Analysis, 182-186, 1983

Raeymaekers B., Graule T., Broekaert J.A.C., Adams F., Tschöpel F.; Characteristics of nebulized suspensions of refractory oxide powders used for the production of ceramics and their evaporation behaviour in inductively coupled plasma, Spectrochim. Acta 43B, 923-940, 1988a.

Raeymaekers B., Van Espen P., Adams F., Broekaert J.A.C.; A characterization of spark-produced aerosols by automated electron probe micro-analysis, Appl. Spectrosc. 42, 142-150, 1988b

Raeymaekers B., Broekaert J.A.C., Leis F.; Radially resolved rotational temperatures in nitrogen-argon, oxygen-argon, air-argon and argon ICPs, Spectrochim. Acta 43B, 941-949, 1988c

Van Borm W.A., Broekaert J.A.C.; Noise characteristics in inductively coupled plasma optical emission spectrometry using slurry nebulization and direct powder introduction techniques, Anal. Chem. 62, 2527-2532, 1990

Van Borm W.A., Broekaert J.A.C., Klockenkämper R., Tschöpel P., Adams F.; Aerosol sizing and transport studies with slurry nebulization in inductively coupled plasma spectrometry, Spectrochim. Acta 46B, 1033-1049, 1991

CHAPTER 7

Semi-quantitative analysis of individual standard salt aerosol particles

7.1. Introduction

In this chapter we report on a study of individual particles of NaCl, $(NH_4)_2SO_4$, and KNO_3 analyzed using a ZEISS EM 902 instrument and a JEOL 2000 FX. Our interest in these salt particles is twofold; these aerosol standards can be easily prepared in the laboratory and there is need for low-Z element determination in environmental aerosol research. There is a growing interest in small particles for environmental studies since they might be initiators or catalysts for secondary reactions. They can also act as condensation nuclei and easily undergo further chemical transformation reactions. These environmental particles are mainly composed of elements such as carbon, nitrogen and oxygen that are difficult to detect with conventional X-ray analysis. Thus high spatial resolution combined with low-Z elemental analysis should favor EELS analysis over other electron-beam techniques.

7.2. Sample preparation

Standard test aerosols of NaCl, $(NH_4)_2SO_4$ and KNO_3 were generated by nebulization out of their respective aqueous solutions. The generation and sampling equipment for the preparation of standard particulate salt material is shown schematically in Figure 7.1.

The average aerosol diameter can be controlled by either changing the concentration of the solution or by varying the collection distance above the solution (Otten et al., 1986). To prevent the collection of droplets, the generated aerosol was passed through a diffusion dryer during the upward trajectory before impaction. Experiments showed that a reproducible aerosol particle

fraction is formed for an approximately 0.1M solution. The exhaust aerosols were collected on either 700-mesh amorphous carbon coated grids or on 400-mesh grids covered by a perforated Formvar foil and coated with a thin carbon layer. The microscope grids were mounted in a Batelle DCI-5 single-jet cascade impactor. To preserve the grids from contamination, the impactor was placed just above the diffusion dryer and operated at a reduced input flow relative to the diffusion dryer output. This nebulizing mechanism produces polydisperse aerosols (i.e., particles with various diameters). Only the last impactor stage, with a cut-off diameter of 0.25 μm, was used for EELS analysis. This aerosol-generation method allows us to control the size of the collected particles and to reduce aggregation of the particles. Also a homogeneous distribution is obtained over the entire collection area.

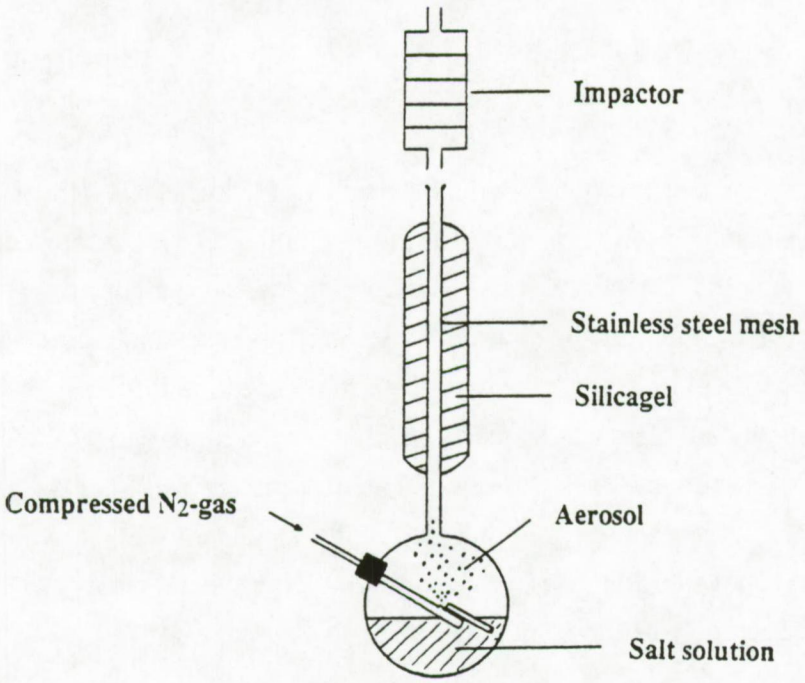

Figure 7.1: Apparatus used to simulate standard test aerosols.

7.3. Instrumentation and acquisition conditions

The ZEISS EM 902 (TEM) instrument has already been extensively discribed in chapters 4 and 5. The energy loss intensity per channel is an average of three individual recordings of one second. Typical acquisition times are then on the order of 10 minutes for an energy span of 400 eV in steps of 2 eV. Recording times can be reduced at the expense of the statistical reliability of the data.

Analogue analysis were performed on a scanning transmission electron microscope. The JEOL 2000 FX (STEM) is equipped with a Gatan 666 magnetic-sector spectrometer (Figure 7.2) coupled to a Kevex data storage and processing unit for parallel spectrum recording. The acronym "PEELS" is widely used to refer to parallel electron energy-loss spectroscopy. Here an array of diodes that are position sensitive (Chapman et al., 1980; Jenkins et al., 1980) and placed in the dispersion plane of the analyzer are used for single-electron counting. By using a low-noise scintillator and photomultiplier tube, shot noise that results from Poisson statistics of the arriving electrons (Egerton, 1982) is then the main noise component in the spectrum. The microscope was operated at a 200-keV acceleration voltage since Blake et al. (1988) observed that structural damage is reduced, at least in the case of fluorite, CaF_2, with using high voltages compared to lower voltages.

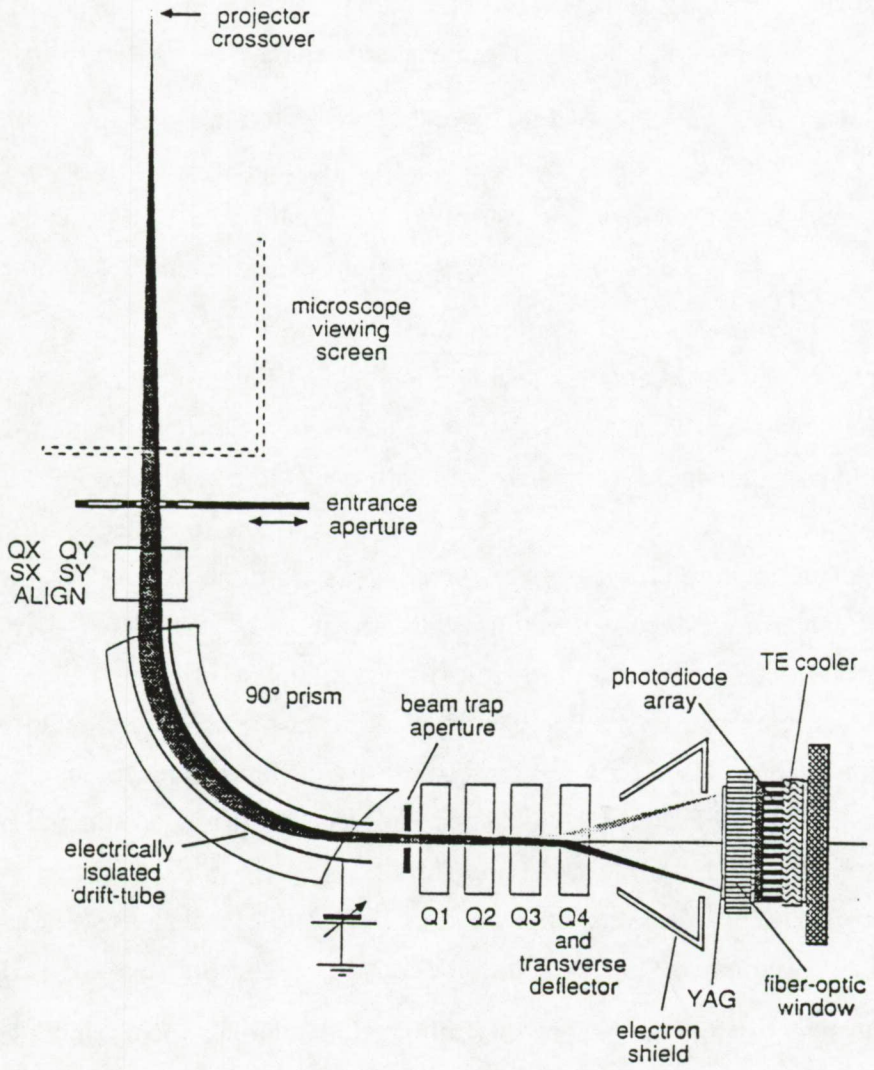

Figure 7.2: The main components of the Gatan 666 spectrometer.

The parallel spectra were acquired into 1024 channels, where each channel corresponds to an energy increment of 1 eV. A useful range of about 1000 eV may be achieved during one spectrum acquisition and only takes about 3 seconds. Thus, for comparable spectrum acquisition parameters (energy span of 2000 eV in steps of 2 eV) the parallel collection system is about 1000 times more efficient than the serial system of the ZEISS instrument. However, this factor is significantly reduced when smaller energy-loss spans are of interest, as is usually the case. This efficiency factor does not affect the obtained results significantly as we will show, unless time is a critical factor in spectrum acquisition.

For both instruments, a nitrogen-cooled cold stage was used since this can reduce the rate of mass losses of certain elements under electron-beam radiation (Hall and Gupta, 1974; Shuman et al, 1976; Somlyo et al., 1979; Egerton, 1980). The energy resolution in spectrum mode varied between 1.5 and 1.8 eV for both instruments as measured separately on the zero-loss signal.

All spectra obtained with the ZEISS EM 902 were recorded at a magnification of 30,000 times. The spectrometer acceptance angle is then limited by an objective aperture of 60 μm (β=11 mrad). Higher magnifications reduce the transmission signal and so statistically reliable data cannot be obtained. For the JEOL 2000 FX, magnifications of 30,000 to 50,000 times were used.

If the carbon signal from the supporting foil does not interfere with the characteristic-peak positions of other elements of interest, one should analyze particles supported by the carbon foil instead of those lying over the holes. Substrate conductivity can help protect the interaction volume from radiation damage during low-temperature electron microscopy (Jacobson et al., 1971; Lamvik et al., 1989). Therefore, analyses on the amorphous-C supporting foil were preferred because heat is more efficiently conducted away from the sample and out-diffusion of volatile species is thereby reduced (Egerton, 1980; Fryer and Holland, 1984; Egerton et al., 1987). The electron dose received by the specimen was calculated for the ZEISS by measuring the transmitted beam current using a Faraday cup located at the screen level (this is the object plane for the spectrometer). Table 7.1 gives an overview of the differences between the ZEISS EM 902 and the JEOL 2000 FX, as well as the conditions used for recording and processing the spectra. For these experiments, the background fitting region (Γ) was consistently set at 70 eV. However, for nitrogen determinations, both a Γ and a Δ of 50 eV were used, because problems can arise as the fitting region will interfere with the broad C-K edge or the K-$L_{2,3}$ edge.

Modelling of the background in the pre-ionization edge region and extrapolation below the ionization edge was done by an inverse power law (see equation 4.1) of the form:

$$I_i = A\, E_i^{-R} \qquad (7.1)$$

Table 7.1: Instrumental parameters and spectrum recording and processing conditions of the EELS spectra.

Parameter	ZEISS EM 902	JEOL 2000 FX
Acceleration voltage	50 to 80 keV	80 to 200 keV
Filament	W	LaB_6
Spectrometer	prism spectrometer	magnetic sector
Electron detector	PMT	YAG scint. + photodiode aray
Spectrum recording	serial scans	parallel mode
E-range	0 - 2000 eV	0 - 4000 eV
Step size	2 eV/channel	1 or 2 eV/channel
Acquisition time/channel	3 x 1s	3 x 1s
Total acquisition time	ca. 3 to 10 minutes	3 seconds
Magnification	30,000 times	30,000 - 80,000 times
Background fitting region (Γ)	70 eV	70 eV
Background extrapolation (Δ)	70 eV	70 eV
Fitting strategy	unweighted least squares	weighted least squares

After a logarithmic transformation, the coefficients A and R can be calculated by linear regression. Variance calculations of the intensity output of each channel strongly depend on the way electron energy-loss signals are recorded, and these differ for the ZEISS EM 902 and the JEOL FX 2000. For the ZEISS instrument, the signal intensity is obtained by converting the photomultiplier tube (PMT) anode current into a proportional voltage that is integrated by a digital voltmeter. The voltage output at a specific energy-loss is linearly proportional to the number of energy-loss electrons at that energy. In practice, if we record the spectrum for n times 1 second, the best estimation of the variance for channel i is given by:

$$s_i^2 = \frac{\Sigma (x_{ij}-x_i)^2}{(n-1)} \qquad (7.2)$$

where x_i is the mean of the n read-outs for channel i. In this case, an unweighted least-squares estimation can be used as a fitting strategy for the ZEISS spectra deconvolution. However, for the spectra obtained with the 2000 FX, the intensity distribution of the energy-loss electrons is obtained by counting the number of electrons that reach each channel of the detector. The variance on the intensity data is calculated by Poisson statistics and varies from channel to channel with the square root of the intensity. The signal-to-noise ratio is then proportional to S, where S represents the accumulated signal per channel. Therefore, for the 2000 FX measurements, a weighted least square estimation is preferred over an unweighted least square fit.

The net edge integral (I_k) is calculated according to equation (4.2). The ratio N^x/N^y for two elements X and Y in the same particle, giving rise to the characteristic edges, can then be calculated using the relation 4.3. For this equation, the assumption is that no mass losses occur during the acquisition of one spectrum so that the low-loss region remains the same for all elements and thus cancels out. This assumption is almost true for the fast parallel detection method but is not quite appliable for the more time consuming serial recordings at medium to high electron doses. However, applying this equation enables us to study the effect of mass losses in EELS analyses of salt particles.

For NaCl, serial recording needed special attention. The NaCl spectra were collected in three partial scans over a different energy region. The first and third regions correspond respectively to energy loss regions of chlorine and sodium. An approximately 2-fold electron radiation dose and a maximum detector gain was necessary for the collection of Na edges at about 1080-eV loss. The chlorine and sodium regions were matched by an energy-loss region extending from 250 to 1020 eV. This region of 780 eV was recorded by integrating the signal per channel for only 3 times 0.1 second in order to reduce the total acquisition time.

For monitoring mass losses of one specific element as a function of time or electron dose, the relative concentration of a particular element, N(R), can be defined as the ratio of the initial concentration of that element, N(0), to the concentration at higher dose, N(D), or after a specific time, N(t):

$$N(R) = \frac{N(D)}{N(0)} = \frac{I_k^D(\beta,\Delta)\ I_l^0(\beta,\Delta)\ G^0}{I_l^D(\beta,\Delta)\ I_k^0(\beta,\Delta)\ G^D} \qquad (7.3)$$

The superscripts 0 and D represent the initial values and their values at an electron dose D, respectively. It is possible that the thickness of the analyzed area changes as elemental losses occur. For this, the net areas under the characteristic edges are normalized by dividing them by the areas under the zero-loss peak. Dark-current corrections were performed on all spectra in order to reduce the effect of electronic noise.

Some 20 to 30 spectra were recorded for each standard particle type. Only those that have a characteristic signal-to-noise ratio exceeding 3, were selected for quantification. The reason some spectra show bad statistics is mainly because at very low electron doses, an insufficient number of transmitted electrons reached the detector.

7.4. Results and discussion

For all standards, severe electron-beam-induced radiation damage was observed within less than one minute at normal exposure (electron doses of approximately 0.5 to 5 $C.cm^{-2}$). The residual structure of NaCl was observed to mature into a stable configuration after 1-2 minutes and applying higher electron dose had no subsequent effect. The structural damage, as visible with the TEM, reflects the sputtering of the halogen atoms (Szymonski and de Vries, 1983; Szymonski et al., 1985; Nakayama and Itoh, 1985) rather than out-diffusion processes (Al Jammal et al., 1973). Different phenomena seem to occur for KNO_3 and $(NH_4)_2SO_4$ as they partly or totally sublimate and disappear. When liquid nitrogen temperatures are used and the beam current is reduced by a factor of 10 to 50 times (about 0.01 to 0.5 $C.cm^{-2}$), the visual damage did not appear in NaCl within the first 5 minutes of viewing time. For KNO_3 and $(NH_4)_2SO_4$, only slow morphological changes occured. The highest electron doses, still leaving the analyzed sample volume unchanged, were used to collect electron energy-loss spectra.

The mean element ratios determined from the quantitative EELS analyses are given in Table 7.2, as are the minimum and maximum determined ratios.

7.4.1 NaCl

Figure 7.3 shows a typical EEL spectrum of a sub-micrometer NaCl particle. It is important to start spectrum collection from chlorine toward the higher electron energy-losses of sodium. Figure 7.4 demonstrates that chlorine losses are greater than sodium losses, even when the latter

are collected at electron doses that are ten times greater. There is good agreement between the element ratios determined for NaCl by parallel and serial EELS.

Table 7.2: The mean elemental atomic ratio determined by serial and parallel EELS of three different inorganic standard salt particles. Also the minimum and maximum observed elemental ratio are given

	Sample	Ratio			Min-max observed ratio		
		Na/Cl			Na/Cl		
ZEISS	NaCl	1.2 ± 0.8			0.8-1.4		
JEOL	NaCl	1.1 ± 0.6			0.9-1.3		
		O/S	N/S	O/N	O/S	N/S	O/N
ZEISS	$(NH_4)_2SO_4$	2.1 ± 0.8	1.1 ± 1.2	2.9 ± 0.9	1.4-3.4	0.4-1.8	1.0-6.1
JEOL	$(NH_4)_2SO_4$	3.9 ± 0.9	1.2 ± 0.6	2.5 ± 0.7	1.5-7.7	0.6-2.1	2.2-3.6
		O/K	N/K	O/N	O/K	N/K	O/N
ZEISS	KNO_3	2.4 ± 0.5	0.7 ± 0.6	3.9 ± 2.9	1.9-2.6	0.2-1.2	2.1-8.8
JEOL	KNO_3	3.5 ± 0.7	1.0 ± 0.4	3.7 ± 2.1	2.1-4.6	0.3-1.9	2.4-6.4

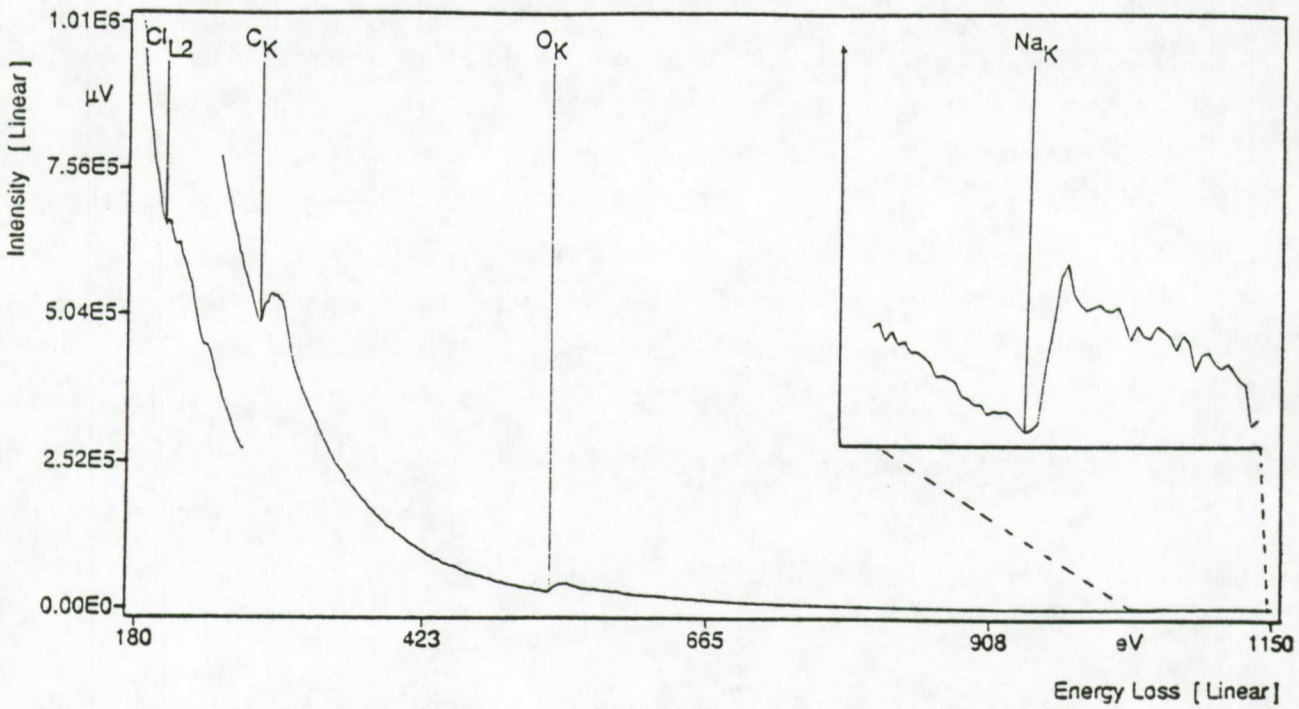

Figure 7.3: EEL-spectrum of a NaCl particle showing the Cl-L_2 ionization edge and the Na-K ionization edge (enlarged view in the upper right corner). A C-K edge from the supporting foil and an O-K edge as a result of an oxidation process are also shown.

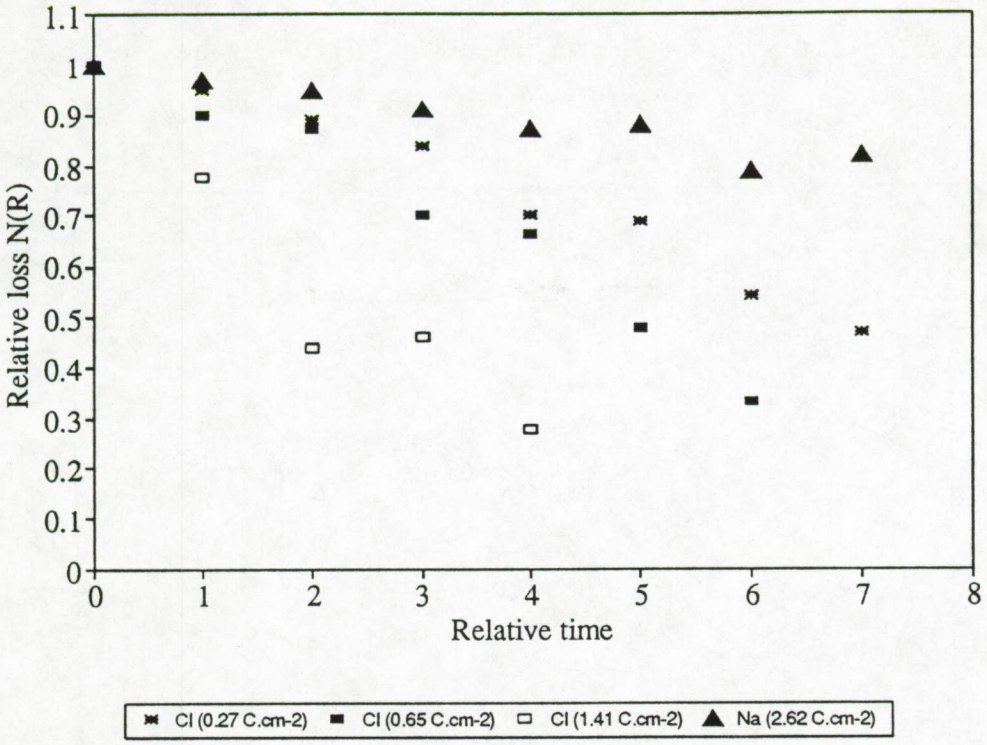

Figure 7.4: Relative loss N(R) of chlorine and sodium from NaCl as a function of time, collected at a constant electron iradiation dose. The relative loss is the ratio of the measured element intensity at constant time intervals (relative time) to the initial measured element intensity (relative time of zero).

For the relative loss measurements of specific elements, characteristic features were collected over an energy range of 160 eV for five times 0.1 second and per energy increment of 2 eV. The zero-loss region (1 eV per channel) and the intermediate region (2 eV per channel) were recorded for three times 0.1 second. This all corresponds to a total acquisition time of about 2.5 minutes. One minute intervals were used between the end and the start of a new spectrum to correspond with the time needed to store all information and to control all instrument settings.

The signal-to-noise ratio of the chlorine ionization edge above the extrapolated background did not exceed the value of one after a relative time interval of four minutes at a dose of 1.41 $C.cm^{-2}$.

Collection of serial spectra in reverse order, starting from the high energy-loss towards the low-loss region, results in a mean Na/Cl ratio of 1.8, which is far above the theoretical value of one. The reason for this difference is that Cl-losses had occurred before the signal was acquired. From Figure 7.5, it can be seen that chlorine losses occur more rapidly as the electron doses increase. Under much higher electron doses, the halogen atoms can be removed totally, but also

removal of the metallic component can occur either by diffusion or, in the case of alkali metal, by thermal desorption (Muray et al., 1984; Mankiewich et al., 1984).

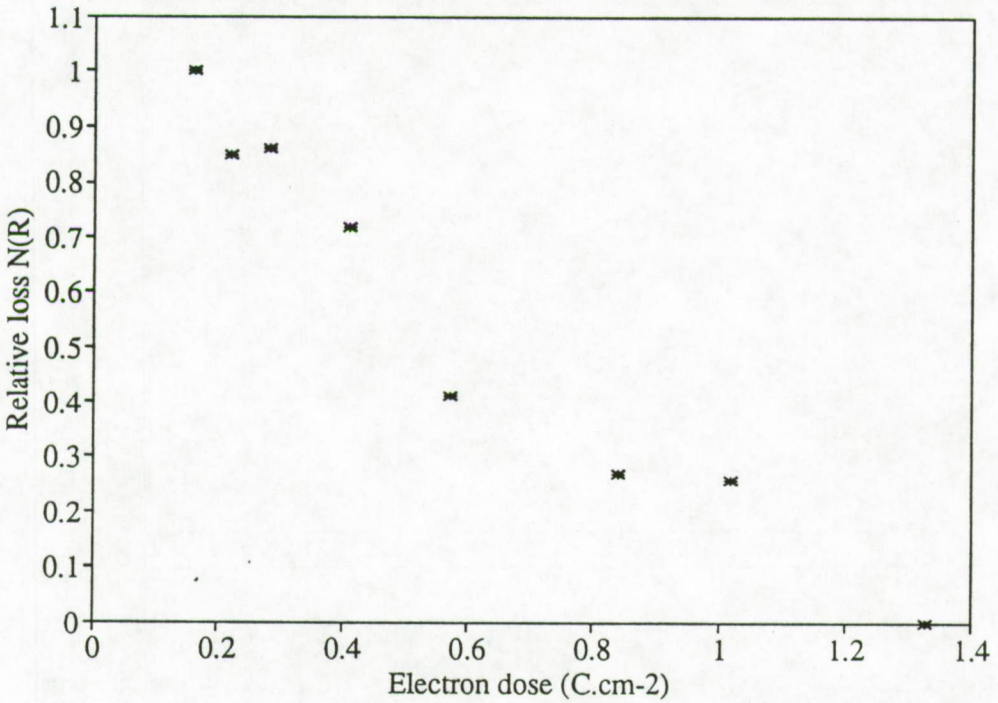

Figure 7.5: Relative loss of chlorine from NaCl as a function of electron iradiation dose.

There is evidence that radiation damage arises from inelastic scattering of the incident electrons resulting in excitation, decay, and reformation mechanisms (Hobbs, 1979). The remaining alkali atoms may segregate into a metallic phase that will be oxidized in a TEM (Egerton et al., 1987). The oxidation is shown in the NaCl spectrum (Figure 7.3) by the appearance of the O-K edge at 545 eV.

7.4.2 $(NH_4)_2SO_4$

A typical serially recorded $(NH_4)_2SO_4$ spectrum is shown in Figure 7.6. First the N-K and O-K signals were collected and then the S ionization edge was recorded at a reduced PMT gain. The sulfur energy-loss region was rescaled according to the gain setting used. Just as for NaCl, element losses determine the success of analysis, but for $(NH_4)_2SO_4$ degradation occurs more readily. Figure 7.7 shows the time dependency of nitrogen, oxygen and sulfur losses in $(NH_4)_2SO_4$.

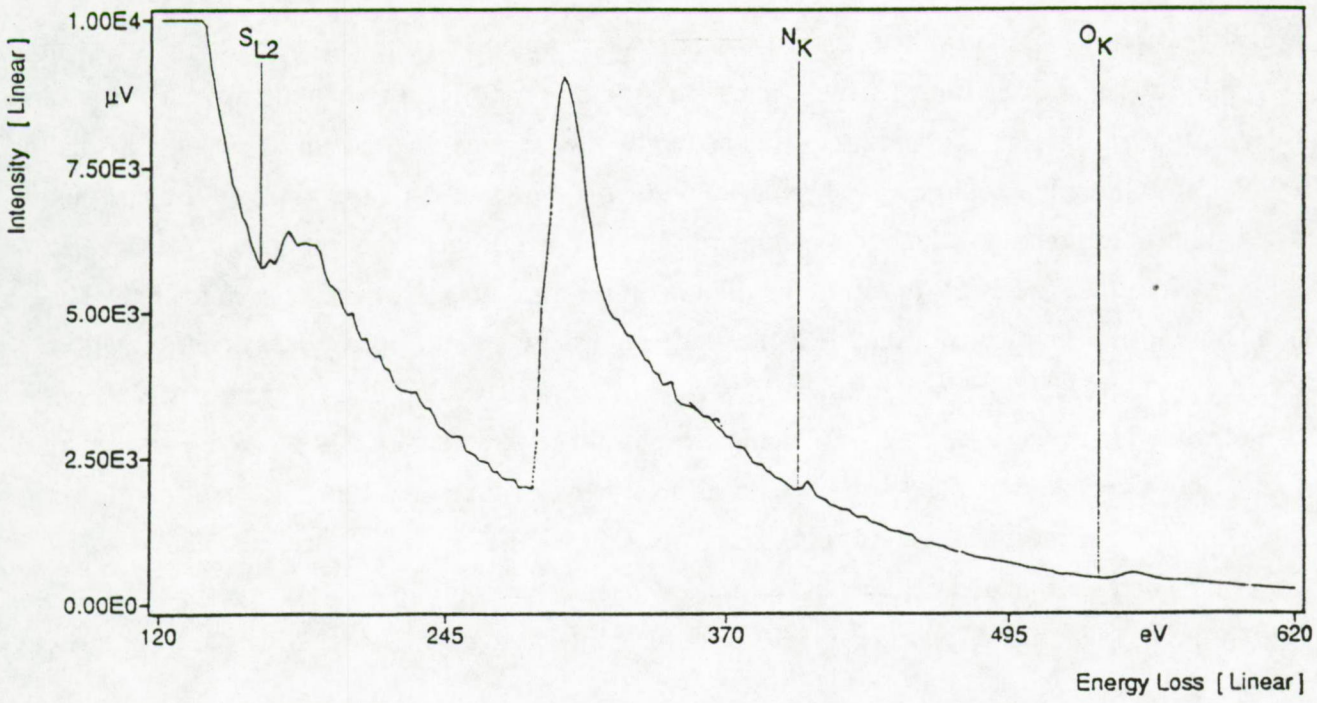

Figure 7.6: EEL-spectrum of an $(NH_4)_2SO_4$ aerosol that was collected in two scans; the first scan went from nitrogen, the most beam-sensitive element, to oxygen, while the second scan extends from sulfur to an overlapping energy-loss region with the first scan. The spectrum was reconstructed by increasing the intensities of the first region by the corresponding gain change.

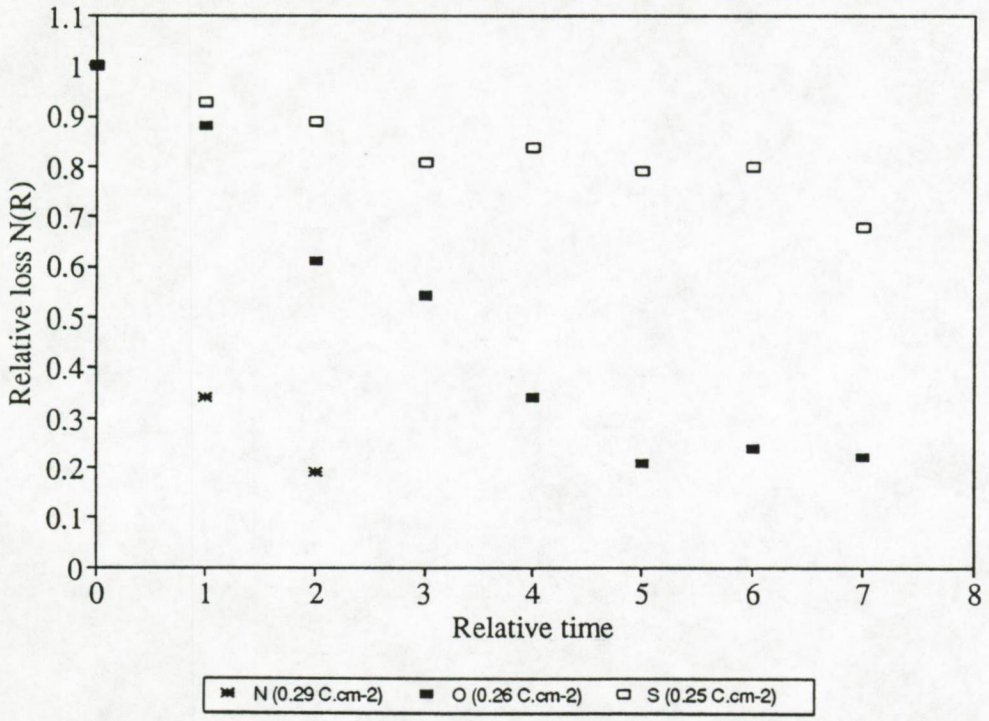

Figure 7.7: Relative loss of nitrogen, oxygen and sulfur from $(NH_4)_2SO_4$ as a function of time and collected at a constant electron dose.

Already after one spectrum acquisition, the relative nitrogen intensity dropped by a factor of three. After four relative time intervals, the signal-to-noise ratio for nitrogen did not even exceed the one sigma criterion. Oxygen losses seemed to be less severe, whereas for sulfur only a small relative loss in concentration was observed. Figure 7.8 shows the relative nitrogen, oxygen and sulfur concentrations as a function of electron dose. For nitrogen, the net intensity decreases rapidly with time. The effect of electron radiation on the nitrogen losses can be seen from the N/S and O/N ratios. The results of the PEELS experiments show that nitrogen losses occurred within the first few seconds of recording [mean N/S ratio of 1.2 for $(NH_4)_2SO_4$]. Oxygen loss is slower than nitrogen loss, and therefore O/N element ratios above the theoretically predicted values are found. However, oxygen mass losses occur as a function of time, and this also results in lower O/S ratio for the more time consuming serial recording. The small decrease in relative sulfur concentration as a function of time and radiation dose is probably the result of hydrogen sulfide formation, a phenomenon also observed in sulfur-containing aminoacids (Misra and Egerton, 1980).

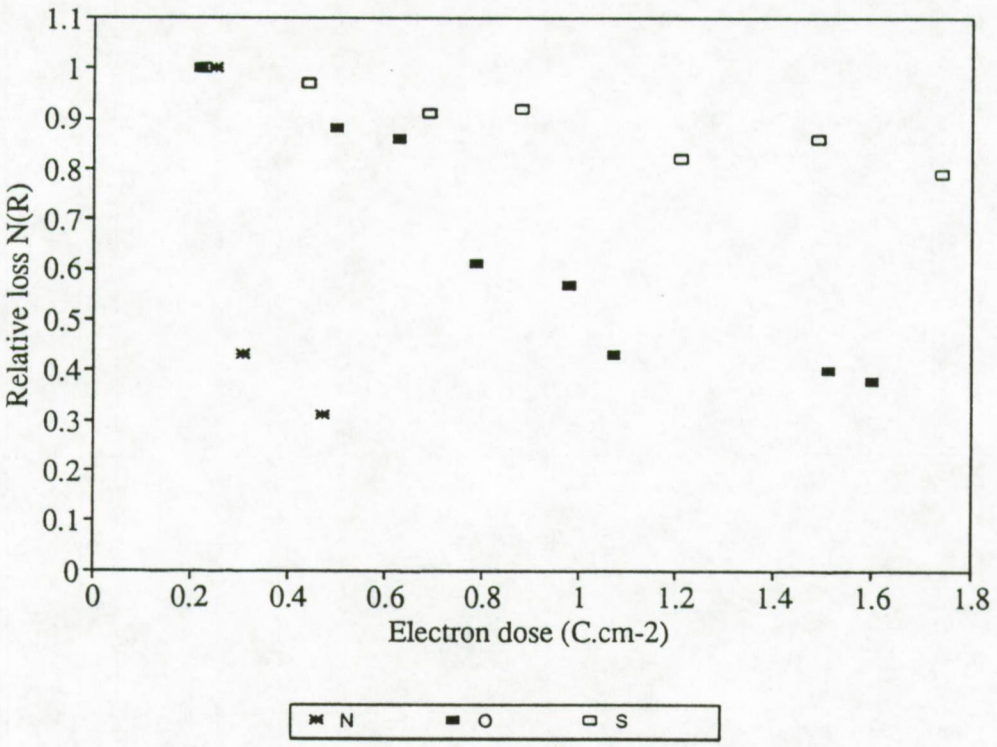

Figure 7.8: Relative loss of nitrogen, oxygen, and sulfur from $(NH_4)_2SO_4$ as a function of electron irradiation dose.

7.4.3 KNO_3

Figure 7.9 shows a PEELS spectrum of a KNO_3 particle. Since the broad C-K feature (C-K at 283 eV loss) of the carbon foil overlaps with the K-$L_{2,3}$ edge (K-$L_{2,3}$ at 294 eV loss), it is necessary to select and analyze particles that lie over holes in the supporting foil. For the serially recorded KNO_3 spectra, the gain does not need to be changed since all characteristic edges lie within an energy span of less than 300 eV. As nitrogen seems to be the most beam sensitive, it is advisable to start serial spectrum collection from nitrogen towards oxygen as a separately defined region from potassium. Figure 7.10 shows that the electron dose affects the relative loss of N > O > K.

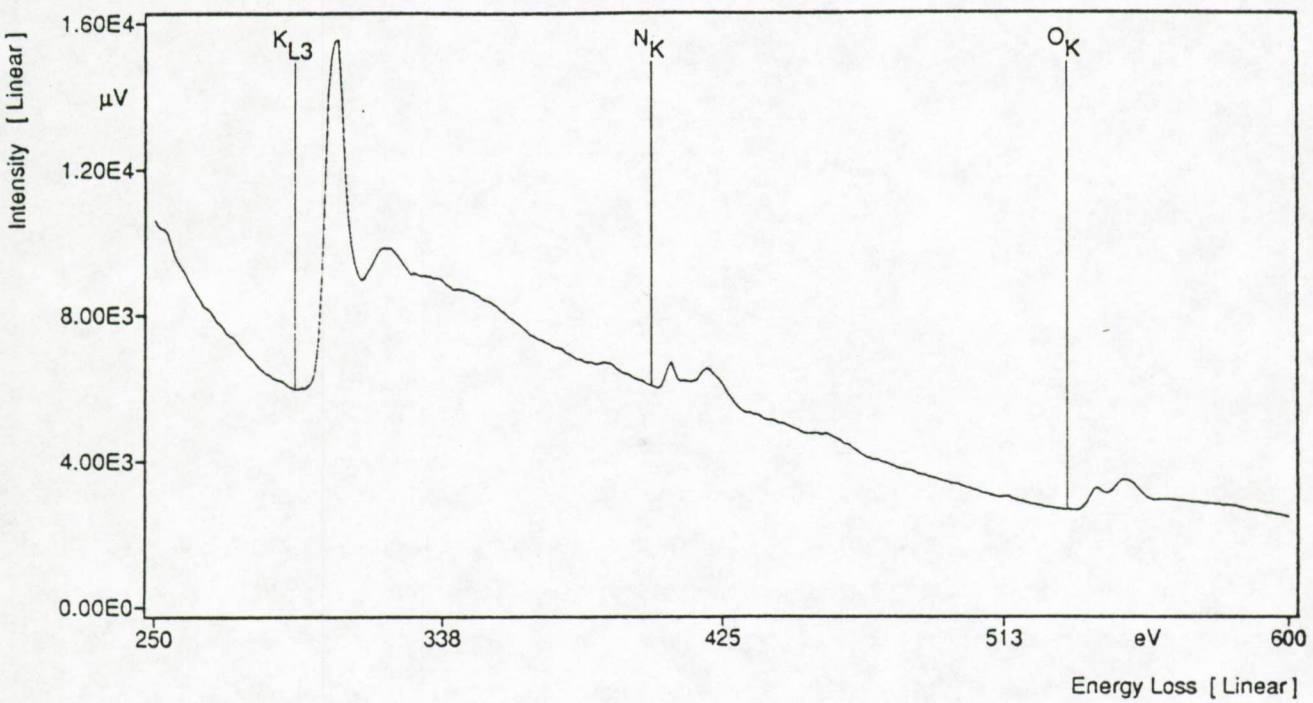

Figure 7.9: EELS-spectrum of a standard KNO3 particle showing the K-$L_{2,3}$, N-K, and O-K ionization edges.

For KNO_3, the elemental ratio differences between the serial and parallel recorded spectra are less extreme than for $(NH_4)_2SO_4$, but, just as for $(NH_4)_2SO_4$, nitrogen and oxygen losses limit the success of EELS analyses.

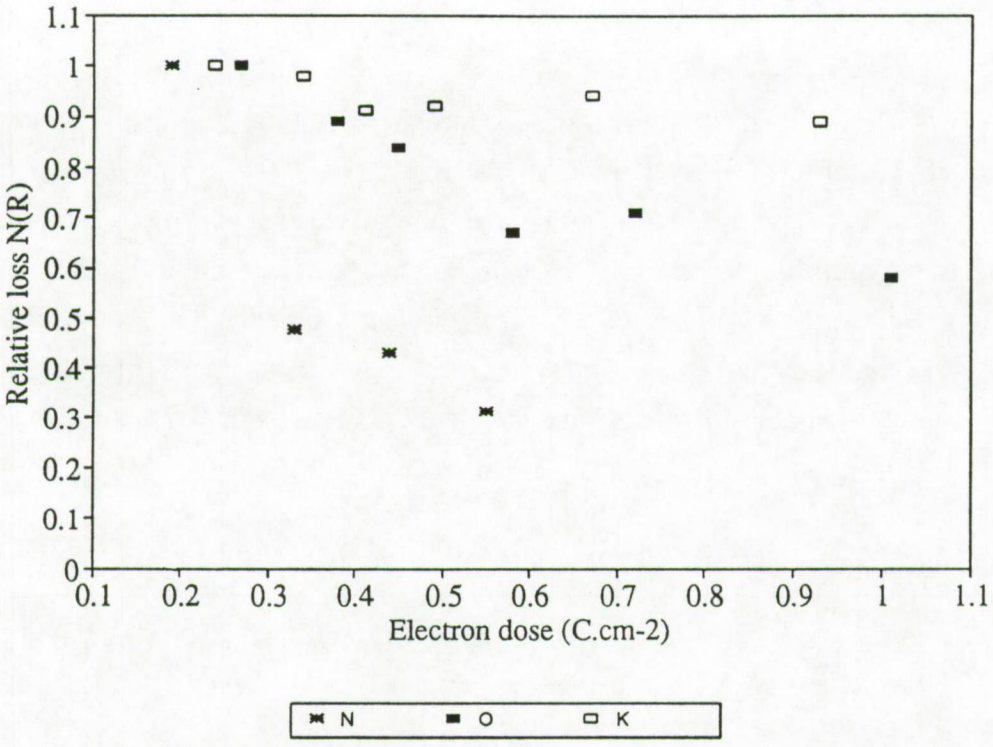

Figure 7.10: Relative loss of nitrogen, oxygen, and potassium from KNO_3 as a function of electron dose.

7.5 Conclusion

Preferential element losses and structure reorganization occur frequently in the electron microscope. These changes can lead to poor or even unsuccessful analyses. From the elemental ratios, we conclude that the volatile elements are released more rapidly than the others, resulting in a sequence of nitrogen before oxygen before chlorine, potassium, sodium and sulfur. Even at cryogenic temperatures, preferential losses and structure reorganization cannot be avoided.

The quality of the analyses is limited by counting statistics. High relative standard deviations were observed, ranging from 15 to 100%. Large counting times and high electron doses (lower detector gain necessary) favor good statistics as the signal-to-noise ratio is increased, but mass losses also become more important. A compromise should be made by using the lowest electron doses that still fulfill the signal-to-noise ratio requirements and that preserves the object as much as possible from structural changes. This can be done by analyzing some particles and directly process the energy loss spectra. Minor changes of electron dose or acquisition times can be made according to the statistics required.

Element ratios closer to the theoretical values are observed when EEL spectra are recorded in the parallel mode, indicating that the acquisition time is important. For analyzing beam-sensitive samples such as inorganic salt particles, a parallel recording device is therefore advantageous.

In general, EELS is only of limited use for quantitative particle determination. Analysis of inorganic salt particles, such as KNO_3 and $(NH_4)_2SO_4$, is best restricted to qualitative purposes.

7.6 References

Al Jammal Y., Pooley D., Townsend P.D.; The role of exciton diffusion in the electron induced sputtering of alkali halides; J. Phys. C, 6, 247, 1973

Blake D.F., Allard L.F., C.J. Echer, F. Freund; Characterization of electron-beam induced damage structures in natural fluorite, CaF_2, by analytical electron microscopy, in "Microbeam Analysis", Ed. D.E. Newbury, San Francisco Press Inc., San Francisco, 129-132, 1988

Chapman J.N., Roberts P.T.E., MacLeod A.M., Ferrier R.P.; Inst. of Phys. Conf. Series, 52, 77, 1980

Egerton R.F.; Chemical measurements of radiation damage in organic samples at and below room temperature; Ultramicroscopy 5, 521-523, 1980

Egerton R.F.; Principles and practice of quantitative electron energy-loss spectroscopy, in "Microbeam Analysis", Ed. K.F.J. Heinrich, San Francisco Press Inc., San Francisco, 43-53, 1982

Egerton R.F.; Electron Energy Loss Spectroscopy in the Electron Microscope; Plenum Press, New York and London, 1986

Egerton R.F., Crozier P.A., Rice P.; Electron energy-loss spectroscopy and chemical change; Ultramicroscopy 23, 305-312, 1987

Fryer J.R., Holland F.; The reduction of radiation-damage in the electron-microscope, Ultramicroscopy 11, 67 (1983) 67, Proc. Roy. Soc. (London) A393 353, 1984

Hall T.A., Gupta B.L.; Beam-induced loss of organic mass under electron-microprobe conditions; J. Micros., 100, 1193-1195, 1974

Hobbs L.W.; Application of transmission electron microscopy to radiation damage in ceramics, J. Am. Ceram., 62, 267-268, 1979

Jacobsen E.H., King J.G., Thomson M.G.R., Weaver J.C.; Electron and molecular microscopy - possibilities rather than limitations, Science, 173, 751, 1971

Jenkins D.G., Rossow C.J., Booker G.R., Fry P.W.; Inst. of Phys. Conf. Series, 52, 73, 1980

Lamvik M.K., Davilla S.D., Klatte L.L.; Substrate properties affect mass loss rate in collodion at liquid helium temperature; Ultramicroscopy, 29, 241-250, 1989

Mankiewich P.M., Craighead H.G., Harrison T.R., Dayem A.H.; High resolution electron beam lithography on CaF_2, Appl. Phys. Letters 44, 468, 1984

Misra M., Egerton R.F.; L-shell ionization of aluminium and silicon by 80 keV electrons, J. Phys. D., 13, L71-L73, 1980

Muray A., Isaacson M., Adesida I.; AlF_3-A new very high resolution electron beam resist, Appl. Phys. Letters 45, 589, 1984

Nakayama T., Itoh N.; Desorption induced by electronic transitions (DIET II), Ed. W. Brenig and D. Menzel; Springer, Berlin, 237, 1985

Otten P., Bruynseels F., Van Grieken R.; Nitric acid interaction with marine aerosols sampled by impaction; Bull. Soc. Chim. Belg., 95, 447-453, 1986

Szymonski M., de Vries A.E.; Desorption induced by electronic transitions (DIET I), Eds. N.H. Talk, M.M. Traum, J.C. Tully and T.E. Madey; Springer, Berlin, 216, 1983

Szymonski M., Ruthowski J., Poradzisz A., Postawa Z.; Desorption induced by electronic transitions (DIET II), Ed. W. Brenig and D. Menzel; Springer, Berlin, 160, 1985

Shuman H., Somlyo A.V., Somlyo A.P.; Quantitative electron probe microanalysis of biological thin sections: Methods and validity; Ultramicroscopy, 1, 317-339, 1976

Somlyo A.P., Somlyo A.V., Shuman H.; Electron probe analysis of vascular smooth muscle: Comparison of mitochondria, nuclei and cytoplasma; J. Cell. Biol., 81, 316-335, 1979

CHAPTER 8

Study of individual carbonaceous particles present in the Phoenix urban aerosol.

8.1 Introduction

Urban growth and expanded industrial activity are generally dependent upon the increased use of fossil fuels and their derivatives. The absence of commensurate emission controls will inevitably lead to higher ambient concentrations of matter and derived breakdown products.

Carbonaceous particles in the atmosphere contribute significantly to the total suspended particulate matter and can sometimes comprise more than 50% of the total submicron mass fraction. They exist mainly in the particle size range < 3 μm with major amounts in the size range below 1 μm. Atmospheric carbonaceous material consists of different types of particulate carbon fractions. For simplicity, it can be divided into three distinct groups namely: carbonates, elemental carbon (EC) and organic carbon (OC).

Although observed in atmospheric particles, carbonates form a minor component in the fine fraction of aerosols, at least in polluted urban atmospheres (Appel et al., 1989). Mueller et al. (1972) reported that carbonate carbon presents in aerosols from Pasadena, California, represent systematically less than 5% of the total carbon.

Elemental carbon (also denoted as black carbon or inorganic carbon) has a structure similar to impure graphite and is formed during combustion processes. Graphite itself is a mineralogical phase of C present in soot particles. Soot is known to be a chemically complex mixture of amorphous polymerized organic material plus graphite elemental carbon (Wagner, 1981). Elemental carbon is a prominent constituent of atmospheric aerosols and is present in urban areas (Pierson and Russell, 1979; Gray et al., 1984), and remote areas such as tropical oceans (Andreae et al, 1984; Clarke et al., 1984a) and the Arctic region (Rahn and McCaffrey, 1980; Clarke et al.,

1984b). The largest fractions are emitted in the accumulation mode (mean mass diameter = 0.2 μm) what explains their long atmospheric residence times (Japar et al., 1986). Elemental carbon is especially of interest since it is an extremely efficient absorber of visible light (Japar and Szkarlat, 1981). Even at the low concentrations at which it is found in rural and remote areas, it can contribute significantly to atmospheric visibility degradation (Charlson et al., 1978) and to perturbations of the atmospheric radiation balance (Cess, 1983). In urban areas, the elemental carbon fraction accounts for less than 44 % of the total carbonaceous content in the atmosphere (Appel et al., 1979).

As a third group, organic carbon can either be emitted directly as particles (primary OC) or can be formed by gas-to-particle conversion in the atmosphere (secondary OC). Among the primary OC, polycyclic aromatic hydrocarbons (PAH) are believed to be the most wide-spread in the environment and some of them have proven to be carcinogenic (Grover, 1986). Combustion of fossil fuels, vehicular emissions and wood burning are viewed as the major contributors to the ambient particles rich in PAH. The formation of secondary organic aerosols is believed to result from gas phase oxidations of organic gases (precursors) as olefins, aromatics, cyclic alkenes and long chain aliphatics (Grosjean, 1977). Organic carbon aerosol present in the Los Angeles area, has been found to account for roughly 65% to 70% of the fine particulate carbonaceous aerosol (Gray et al., 1986, Turpin and Huntzicker, 1991).

In general, different pathways exist for the formation of environmentally important sub-micrometer aerosols. The main pathways and processes leading to aerosol formation and growth of carbonaceous particles are illustrated schematically in Figure 8.1. Low volatility products either nucleate or condensate on the surfaces of pre-existing particles, even if their concentrations are below the saturation concentration (Pankow, 1987). The secondary aerosols are found mainly in the accumulation mode (particle diameter between 0.1 and 1.0 μm) (Whitby et al., 1972).

Characteristic proportions of elemental and organic carbon have been identified in numerous combustion and non-combustion processes as automobile exhaust, oil-fired boilers, fireplaces, meat-cooking operations, cigarette smoke and vegetation detritus (Hildemann et al., 1991).

Up to now, analysis of carbonaceous particles has mostly been limited to bulk analysis and only recently carbonaceous particles have been subjected to a single particle approach (Katrinak et al., 1992).

As discussed in chapter IV, EELS is a very promising technique for low-Z element analysis especially when good spatial resolution is required.

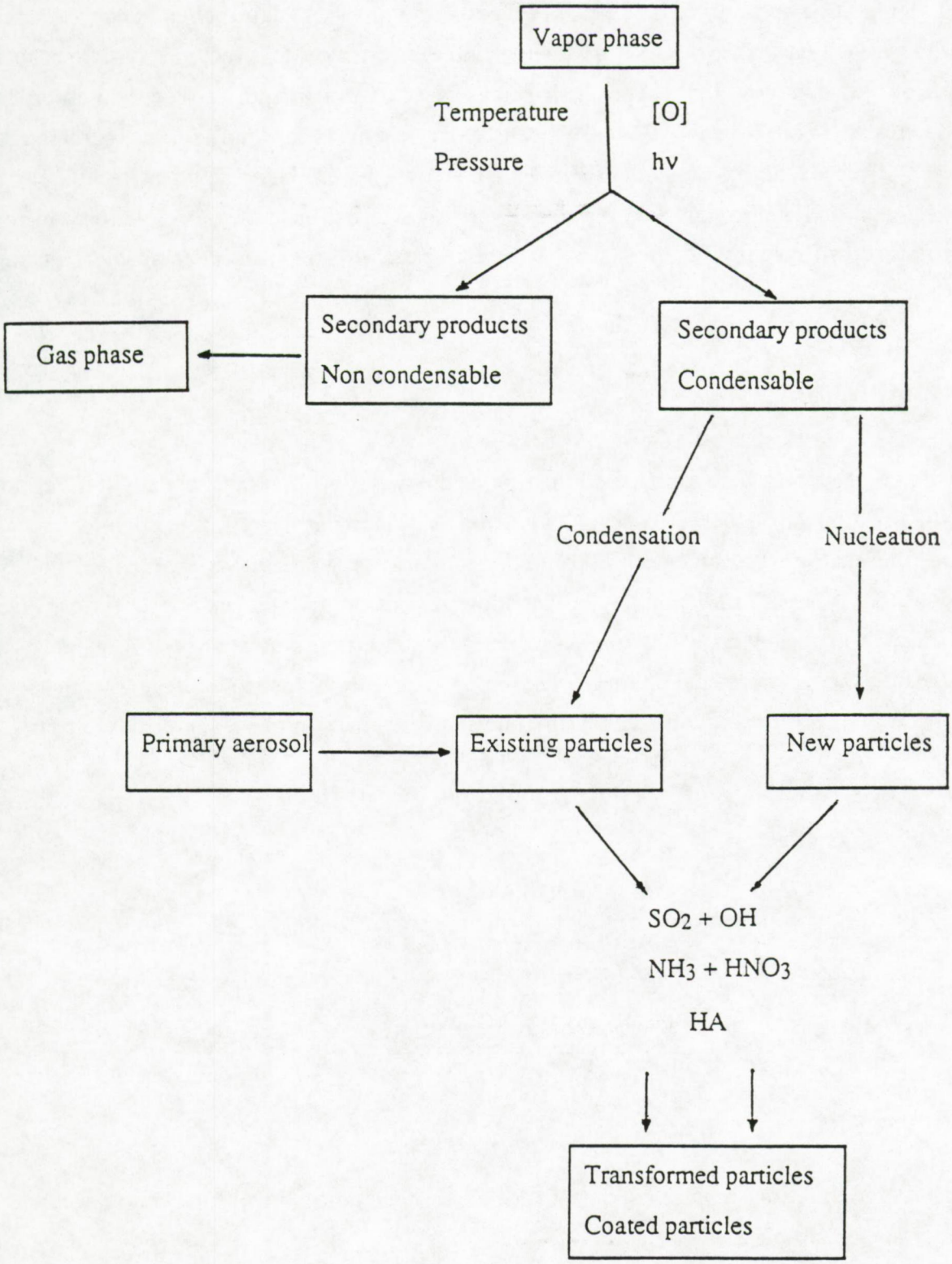

Figure 8.1: Different pathways and processes of aerosol formation and growth of carbonaceous particles out of a vapor phase.

Light elements have high ionization cross sections resulting in a high probability for observing core-loss transitions. The energy loss phenomenon is sensitive to structural variations in the sample as was demonstrated earlier on shapes of spectra for diamond, graphite and amorphous carbon (Egerton and Whelan, 1974). This can be very useful in the study for e.g. carbonaceous aerosols. The advantages of both EELS and ESI over other microanalytical techniques are demonstrated and applied to study structural variations (spectrum mode) and perform element specific images (imaging mode) of sub-micrometer particles present in the aerosol of Phoenix, Arizona, USA.

8.2 Sampling

Atmospheric particles were sampled on the roof of the two-story Maricopa County Air Pollution Control building at 1845 E. Roosevelt, Phoenix, AZ. Particles were collected on perforated carbon foils that are evaporated on 200 mesh electron microscope grids. The aerosol filtration unit consisted of a plastic 47-mm holder that allowed to mount two polycarbonate filters (Figure 8.2). Each grid rested on a 0.2 μm pore-size polycarbonate filter acting as a support and, underneath a 8.0 μm pore-size filter. The larger pore-size filter is needed to prevent large aerosol particles from deposition onto the grids, still allowing carbonaceous chain aggregates to pass.

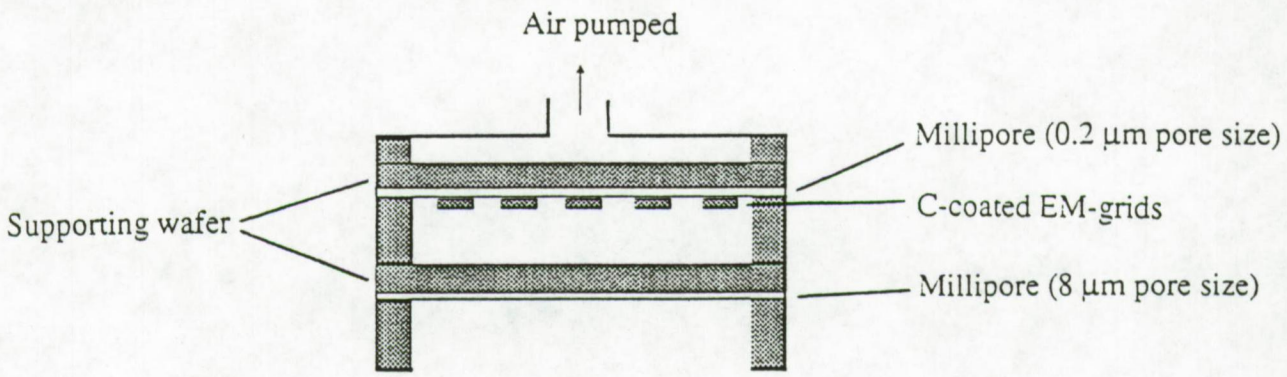

Figure 8.2: Schematic representation of the filter device used for sampling atmospheric sub-micrometer particles.

Approximately 1 m^3/h of ambient air was pumped for 2-10 h periods in September 1989, January 1990 and May 1990. Lower particle concentrations in the spring and autumn months

necessitated collection periods of up to 8 to 10 hours, compared with 2-3 hours for the January sample. Immediateley after collection, samples were stored at room temperature in a desiccator to avoid them from secondary reactions. Little or no change in sample composition was observed following this procedure (Katrinak et al., 1992).

Reference samples of graphite, boron carbonitride (BNC_4) and siliconcarbide (β-SiC) were powdered separately in an agate mortar and transferred onto evaporated carbon film supported by TEM grids.

8.3 Methodology

All energy-loss data were obtained at cryogenic temperatures (- 170 ^{0}C) by cooling the sample stage with liquid nitrogen. Magnifications of 30,000, 50,000 or 85,000 times were used at which the spectrometer acceptance angle is limited by the 60 μm objective aperture (β = 11 mrad). Then, the analyzed areas in spectrum mode (limited by the 50 μm selector aperture) correspond to respectively 0.05 μm^2, 0.03 μm^2 and 0.01 μm^2. The energy resolution of the system under these conditions is about 1.7 eV as measured from the full width at half-maximum (FWHM) of the zero-loss peak. Energy-loss spectra were collected starting from 0 eV up to 100 eV above the highest observable energy-loss edge in steps of 1 eV. The background for each spectrum was fitted and extrapolated according to an exponential function as given by equation (4.1). Elemental ratios were determined using formula (4.3). Detection limits L_D are calculated using an error level of 5%. The detection limit can be expressed in term of the signal-to-noise ratio by the equation (Van Puymbroeck, 1992):

$$SNR = \frac{L_D}{S_k} \tag{8.1}$$

where S_k is the standard deviation on the net signal I_k. For $\alpha = 0.05$ or a 95% confidence interval, SNR corresponds to 3.29. The mean calculated detection limits for the elements in a carbon matrix are 5.2 atom% for silicon, 15.1 atom% for phosphorus, 3.4 atom% for sulfur, 14.2 atom% for nitrogen, 10.1 atom% for oxygen, 6.9 atom% for iron, 10.2 atom% for copper, 14.7 atom% for zinc.

Element specific images were obtained at magnifications between 30,000 and 50,000 times. A selector diaphragm of 400 μm was chosen in order to enlarge the imaged field. The spectrometer slit width was set at approximately 9 eV, allowing to view the same field in image mode as

selected by the selector aperture. Energy specific images (512 x 512 pixel size) were recorded by a SIT Vidicon camera, integrated and stored on-line by an IBAS image processing system. At least 2 or more images were taken at different energy losses preceeding the edge. The number of pre-edge images depends on the stability of the sample to radiation damage and sample shifts. At least one image is taken underneath the maximum intensity of the characteristic energy loss edge. After transferring the images to a UNIX platform, an artificial pixel by pixel background image can be calculated using a PV-WAVE program. The element specific image is the difference of the edge image and the background image. Non-characteristic image pixels resulting from noise and extrapolation errors are determined and removed by the procedure as proposed in chapter 5. The remaining relevant pixels are represented as a white overlay (grey value of 255) on the zero-loss filtered image.

8.4 Results

Almost 90 % of the particles are present as long chained clusters. The length of these chains sometimes extends to 3 μm and they are composed of hundreds of individual spherules. A good example of such typical carbon chain aggregates, photographed at high magnification (Figure 8.3), clearly shows the spherical aggregate nature of this type of particles.

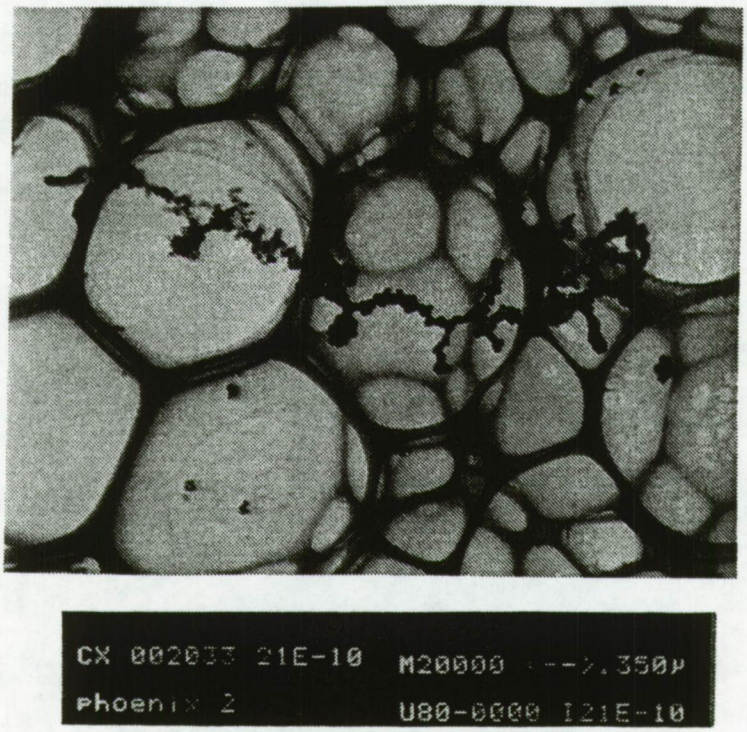

Figure 8.3: Zero loss filtered image of a typical carbonaceous particle chain aggregate.

Very large aggregates were observed for the January sample. This is not surprising since increased particle sizes, frequently associated with aged aerosols, have longer residence times in a stagnant atmosphere often observed during this period (Dodd et al., 1991). Some dense spherical particles (also identified as carbonaceous species) are more frequently observed for the May 1990 and September 1990 samples. No other remarkable differences in particle morphologies are observed upon visual inspection of the three samples. All different particle types are present in the three samples but their number abundances may vary from one another. Unless specified, no further distinction as a function of sampling period will be made.

More than hundred particles were subjected to EELS/ESI analysis. Some were selected randomly and some were chosen because of their special shape, size or morphology. Analysis reveals that large structural variations are present. For more than 95% of all particles, both carbon and oxygen were detectable. For about 50 to 55% of these carbonaceous particles, associations with other elements as silicon, sulfur, nitrogen, phosphorus or metals as Fe, Cu and Zn were observed (Table 8.1). Thus the particles present in the Phoenix aerosol can be classified into different particle types according to their chemical composition (element associations). The abundances presented in Table 8.1 are just estimations based on a combination of morphologic appearances and chemical analysis by EELS.

Table 8.1: Estimation of the abundances for different particle types found in the sub-micrometer particle fraction of the Phoenix aerosol. The elements between brackets are less frequently detected

Particle type	Elements detected	Abundances (%)
Carbonaceous particles	C, O (N)	
Graphitic form		8
Amorphous form		42
S-rich particles	S, C, O (N)	
$(NH_4)_2SO_4$ + C		5
H_2SO_4 + C		15
Si-rich particles	Si, C, O	15
Si-S-rich particles	Si, S, C, O (N)	7
Fe-rich particles	Fe, O	3
P-rich particles	P, C, O (S)	3
Cu-Zn-rich particles	Cu, Zn, O (P)	2

Each of the characteristic particle types will be discussed in more detail in the following paragraphs.

8.4.1 Carbon-rich particles

Although carbon is detectable in about 95% of all particles, the carbon-rich particle type denoted in this context only represents those particles that have carbon as only detectable element. Sometimes oxygen and very low concentrations of nitrogen were detected. It has been reported that soot surfaces are readily oxidized by common atmospheric gasses as O_3, NO_2 and SO_2 (Smith et al., 1989).

Based on the characteristic shape of the energy-loss spectra of carbon, further differentiation within the carbon-rich group can be made. The energy loss near edge fine structure (ELNEFS) of the C-K edge often reflects structural variations present in the analyzed matrix and can be determined by the relative amounts of Π^* and σ^* bonding. Figure 8.4 shows spectra collected from different types of carbon structures. As can be seen, graphite, BNC_4 and amorphous carbon show a characteristic absorption K-edge at 284 eV that is marked by two features.

The first feature resembles a transition from a 1s core state to the Π^* conduction band and is more pronounced for graphite and BNC_4 than for amorphous carbon since they have a more sp^2-type bonding character. For amorphous carbon, it is however known that the films reveal micro-crystalline graphitic regions within mostly amorphous areas (Iijima, 1980), therefore also showing a minor Π^* onset. For siliconcarbide, the Π^* onset is not visible since the atomic bindings are of a sp^3-form.

The second feature observed in the spectra corresponds with a 1s transition to the σ^* conduction band and occurs at 291 eV or higher. The tall and sharp σ^* peak in graphite and BNC_4 indicates a high degree of structural order (Comelli et al., 1988). For amorphous carbon, various randomly oriented binding configurations lead to a superimposed broad featureless σ^* onset. Thus, the more the analyzed area resembles the graphitic structure or is ordered, the more pronounced the Π^* and σ^* peak height ratios are in the spectrum (Katrinak et al., 1992). Intensities for the Π^* and σ^* peaks were measured as their peak-heights above the calculated background because peak areas become meaningless for the small Π^* edge. The energy difference between the Π^* and σ^* peaks were determined by their separation (in eV) at the highest point of their peaks (Figure 8.5). This energy-separation strictly indicates bond length variations as there are between single, double and triple bonds. Variations may also be caused by distorted or dangling bonds in a

distorted structure. The energy maximum of the σ^* peak for hydrocarbon gasses ranges from 291 eV for single bonds to 310 eV for triple bonds (Hitchcock et al., 1984).

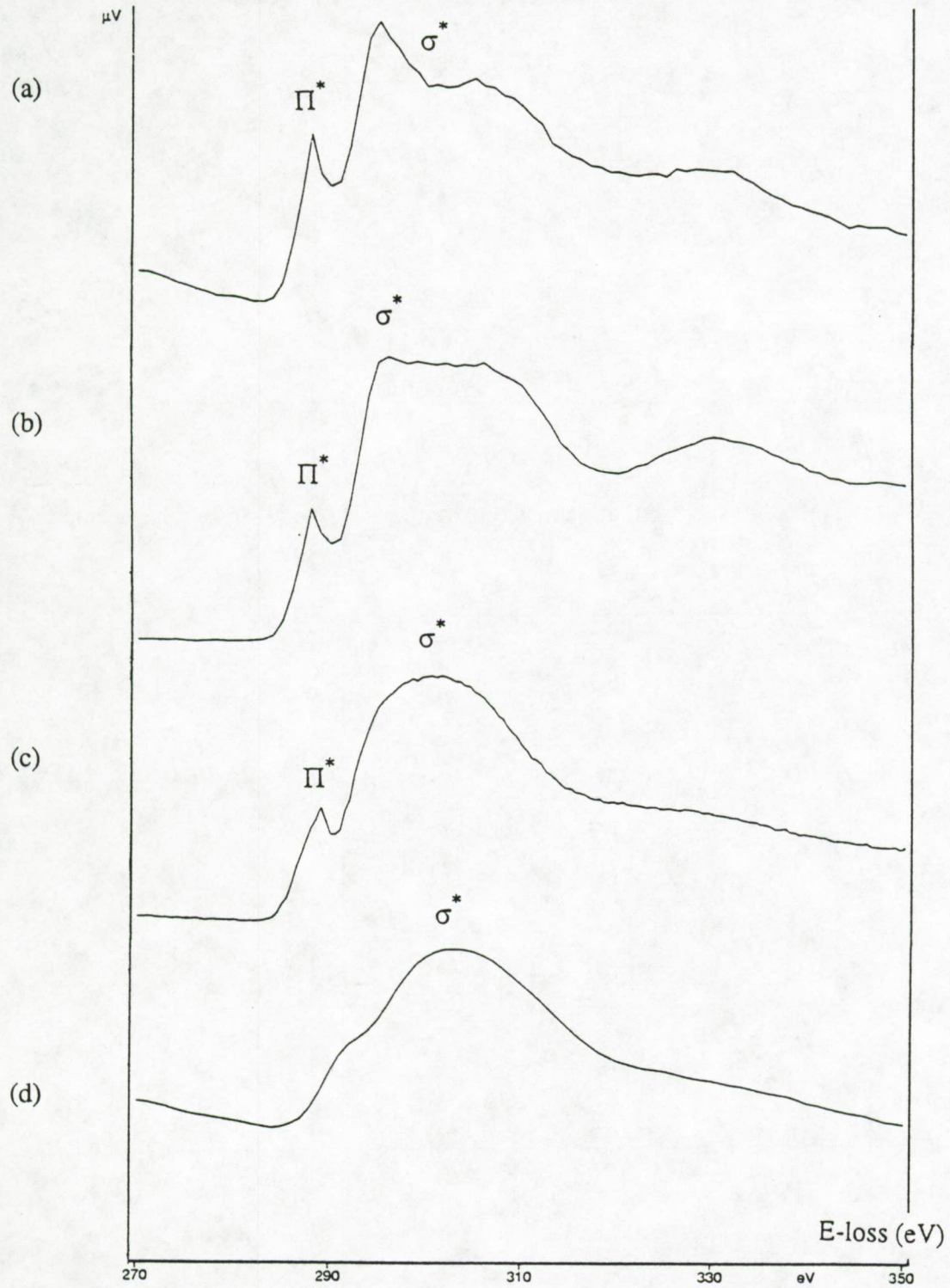

Figure 8.4: Electron energy loss spectra of (a) pure graphite powder, (b) boron carbonitride (BNC_4), (c) amorphous carbon foil and (d) siliconcarbide powder (β-SiC).

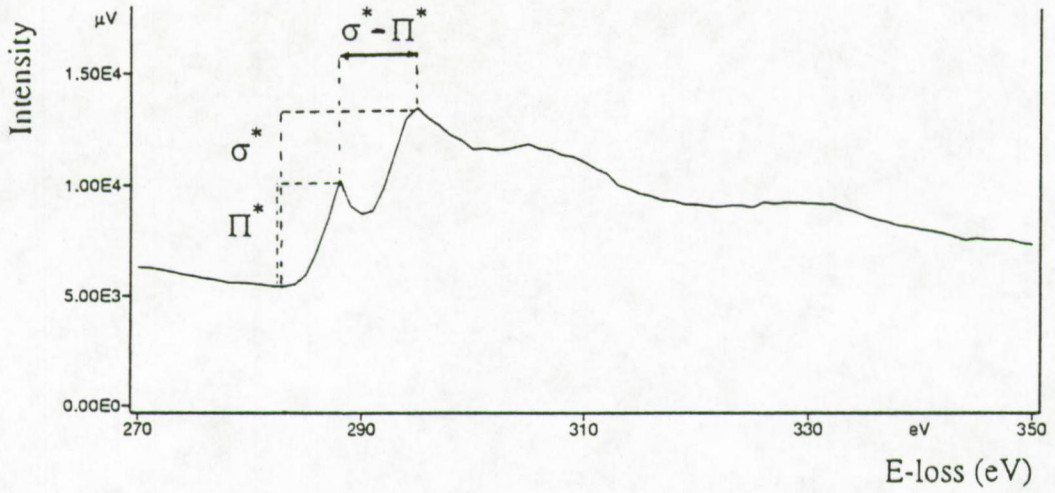

Figure 8.5: Definitions used for the calculation of Π^*/σ^* ratios and $\sigma^* - \Pi^*$ (eV) measurements.

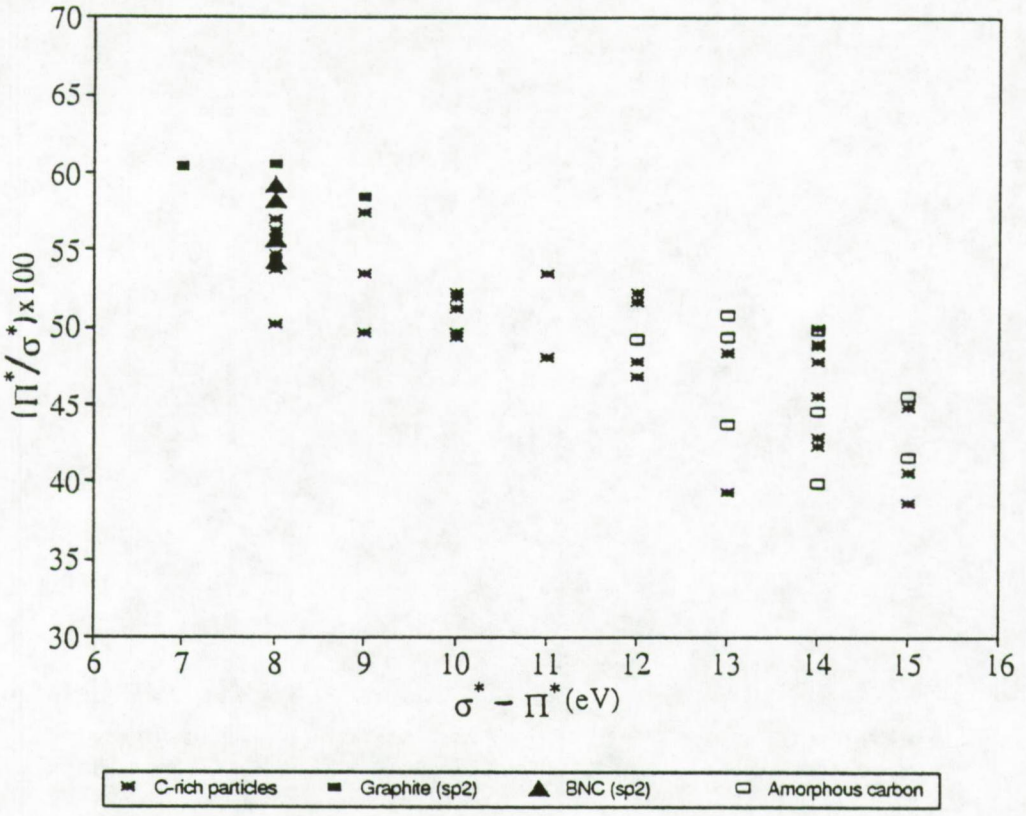

Figure 8.6: Plot of the peak-height ratio (Π^*/σ^*) versus the maximum energy loss difference of σ^* and Π^* peak. Also the data for boroncarbide, graphite and amorphous carbon are represented.

A possible linear relationship is tested between peak-height ratios and the energy difference for the σ^* and Π^* edges. The result is a negative linear correlation coefficient of 0.81 (Figure 8.6).

For 99% of confidence, there exists a correlation as was tested using a Fisher Z-transformation. Data of the reference samples where not taken into account for these calculations.

From the obtained plot, it is possible to classify carbon-rich particles according their resemblance to the graphitic or amorphous type of particles. However, interpretation of the obtained data is liable to statistical variations in the collected data and to a rather poor energy resolution available for such measurements. A slight overestimation of the pronounced graphitic structure is possible because of the dominant effect of the graphitic structure on the shape of the σ^* peak.

Some of the chain-type particles were classified as graphitic carbon-rich particles when the energy difference of σ^* - Π^* fell within the range of 8 to 10 eV. It is known that with increasing temperature (e.g. T > 1000 C), amorphous carbon can undergo structural changes from poorly stacked layers over intermediate structural steps, towards flat perfectly ordered layers. Other C-rich particles resemble more the amorphous C-edge with σ^* - Π^* ranging from 10 to 16 eV. Although it is not always evident, known combustion processes suggest that these species likely represent the hydrocarbon fraction. The energy difference observed in the samples indicates a range of bond lengths in the aggregates suggesting a mixture of graphite and hydrocarbons. Both the graphitic carbon-rich particles as well as the hydrocarbon particulate fraction can form a long chain of aggregates and they are randomly observed in the same carbon chains. Sporadically, a characteristic nitrogen K-onset at an energy loss of 400 eV is observed in spectrum mode. Only if nitrogen is detectable and if sulfur is absent, identification as nitrates is most probable. Nitrate coatings might be present on many more particles, but because of the high detection limit for nitrogen it may be unidentified.

8.4.2 S-rich particles

A fraction of the chain aggregates contain S, N and O (Figure 8.7) although carbon still remains the dominant element.

Quantitation of these spectra is not straightforward because of heavy mass losses. Spectra have been analyzed following the procedure explained in chapter 4. The power law fitting region was optimized by minimizing the χ^2 parameter between the model curve and the experimental data for each of the observed edges. The ratios determined for various Phoenix aerosol particle types and their statistical uncertainties are gathered in Table 8.2.

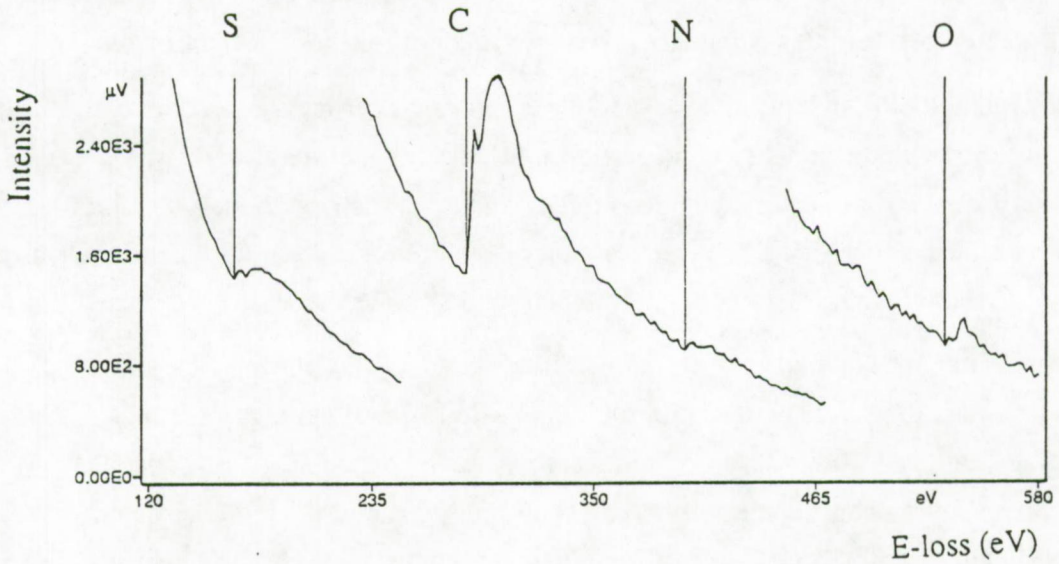

Figure 8.7: Electron energy loss spectrum of an ammonium sulfate particle showing the S, C, N and O edge.

Table 8.2: The mean elemental atomic ratio and their statistical uncertainty are determined by serial EELS for different particle types observed in the Phoenix aerosol.

Particle type	Element ratio Determination	Minimum - maximum ratio
S-rich		
$(NH_4)_2SO_4$	N/S	0.48 ± 0.09 - 1.2 ± 0.1
	O/S	1.3 ± 0.1 - 3.1 ± 0.3
H_2SO_4	O/S	1.5 ± 0.3 - 3.4 ± 0.4
S-rich	C/S	3.60 ± 0.07 - 32 ± 5
Si-rich	O/Si	1.7 ± 0.5 - 5.5 ± 0.3
	C/Si	14 ± 1 - 31 ± 4
Fe-rich	Fe/O	0.55 ± 0.01 - 0.62 ± 0.02
Cu-rich	Cu/O	0.55 ± 0.02 - 0.84 ± 0.09
P-rich	O/P	0.8 ± 0.1 - 1.3 ± 0.2

Atomic ratios were calculated for as many spectra as possible. Spectra possessing a signal-to-noise ratio for an element of interest above 4 are retained from quantization. The calculated element ratios of O/S and/or N/S sometimes correspond with $(NH_4)_2SO_4$ and sometimes with H_2SO_4 as determined from standards (see chapter VI). Just as for the ammonium sulfate rich particles, the H_2SO_4 particles often have much larger diameters and their morphology resembles closely to a solidified structure of a droplet. Figures 8.8 shows sulfur maps from H_2SO_4 and $(NH_4)_2SO_4$ particles, covering carbonaceous particles. Both the observed $(NH_4)_2SO_4$ and H_2SO_4 particles with their typical morphologies can easily be recognized from other particles. The N-K edge from $(NH_4)_2SO_4$ observable in spectrum mode is too low for ESI applications. Figure 8.9 shows a chain of S-containing pherules.

The elements S, O and/or N are also observed in several parts of chained soot particles. It seems that the presence of sulfur does not affect the chain aggregation. This points out that reactions of S-rich species with soot particles are secondary processes. The observed coatings are probably a combination of sulfates and nitrates deposited onto aggregates from the ambient air. The elements S and N are more often present in the organic carbon fraction and less frequently observed in the graphitic-like fraction. It is possible that the chemical reaction between soot particles and S- and N-rich species may alter the well-organized structure of graphite to a more random C-structure. According to Chang and coworkers (1982), H, N and O can be incorporated in the active sites (defects and dislocations) in hexagonal graphitic layers present in soot spherules.

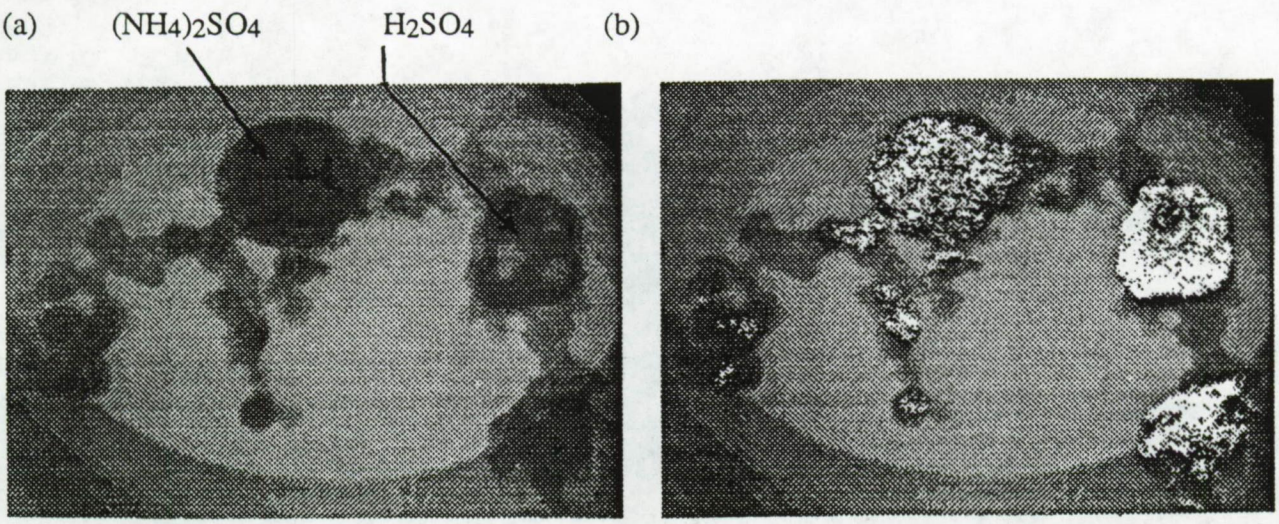

Figure 8.8: Zero-loss filtered images of (a) H_2SO_4 and $(NH_4)_2SO_4$ with their element specific S-signal in overlay in (b).

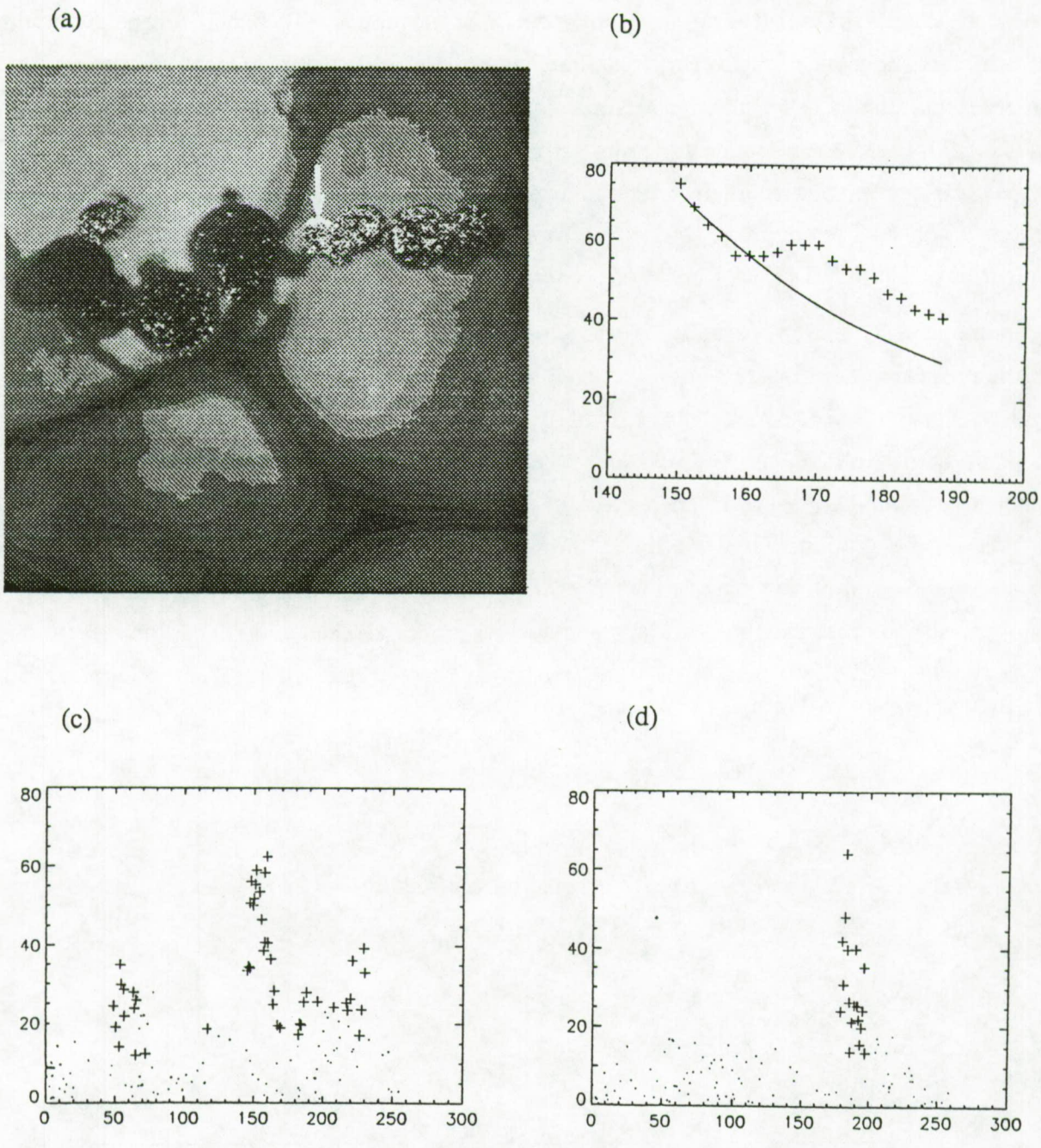

Figure 8.9: S-rich particles with (a) zero-loss image showing the S-signal in overlay, (b) generated energy-loss spectrum, (c) and (d) are respectively intensity distributions in X and Y direction across a pixel coordinate (the cross marks represent the statistically significant signal).

Also aerosol particles from south-central New Mexico were reported to contain nitrogen (Sheridan et al., 1993). Laboratory simulations for heterogeneous reactions of SO_2 and NO_2 with carbonaceous material has led to $HOSO_3^-$, HONO, NO and NO_2^- formation. The latter two are only observed on active carbon. Some researchers found that NO_2 enhances the deposition of SO_2 onto carbonaceous particles (Britton and Clarke, 1980). Others observed little or no effect of SO_2/NO_2 mixtures on transformation rates (Harrison and Pio, 1983). Nitrate is also a very reactive agens for secondary reactions on various particles as carbonaceous particles, sea salt particles and some mineral particles (Mamane and Gottlieb, 1992). However, much of the transformation reactions depend on the relative humidity present in the atmosphere (De Santis and Allegrini, 1992).

8.4.3 Si-C-rich particles

About 15 to 20% of the remaining fraction of particles have a different appearance. They are visible as rounded grains and are randomly mixed within the carbon-rich chain aggregates. Sometimes more dense structures, resembling nuclei, are visible. Such particles are more often enriched in Si, C and O (Figure 8.10) and are believed to represent the quartz and/or silicate fraction.

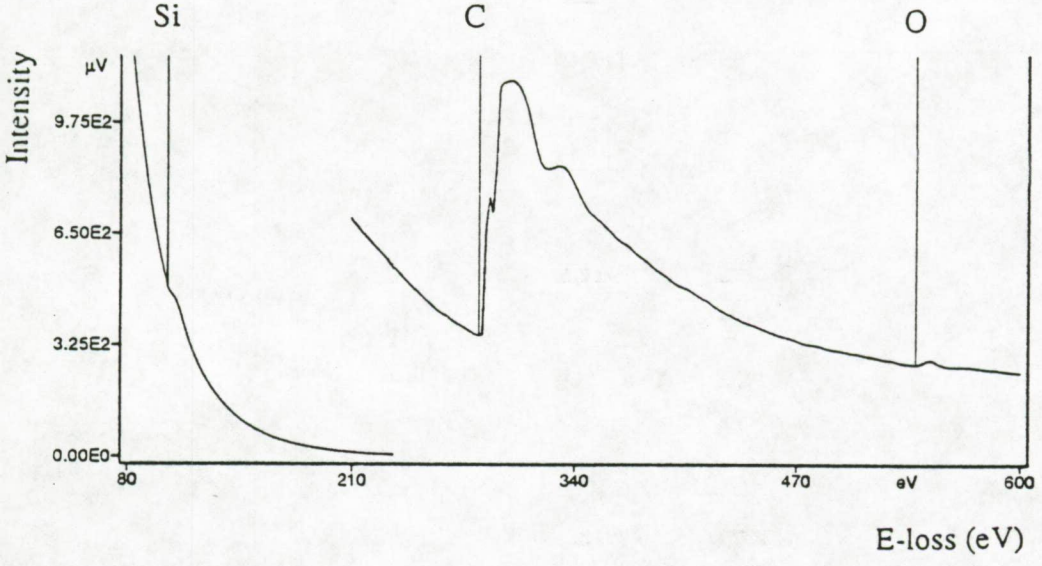

Figure 8.10: Electron energy loss spectrum of a Si-rich particle showing the silicon $L_{2,3}$-edge at 99 eV, the carbon K-edge at 284 eV and the oxygen K-edge at 532 eV.

Silicates are recognized and distinguished from quartz by the presence of a very weak Al-$L_{2,3}$ edge at 70 eV. However, the Al-concentration in silicate is generally quite low resulting in a very weak edge superimposed on an intense background and therefore difficult to observe. From the accompanying C-edges, it is observed that Si is not preferentially associated with either the graphitic-like (EC) fraction or the organic (OC) fraction.

The result of element specific imaging performed on Si-rich particles can be seen in Figure 8.11. The visible dense structures correspond to a specific Si-signal as derived from energy-loss spectra. The remaining statistically relevant signal in image mode indicates that some of the particles appear as small structures surrounded with a carbon-rich phase of various thickness. Although ESI only results in a two-dimensional projection of information, it is rather obvious that the Si-rich phase is coated with a carbon layer.

The presence of Si-rich carbonaceous particles and the C-rich particles within the same aggregates can only be explained when they are originating from the same emission sources since spherule formation and aggregation both occur prior to emission. It has previously been postulated by Andreae et al. (1986) that adsorption of gas-phase organics onto existing surfaces can occur resulting in carbon coated particles. This process could be very efficient during combustion processes. Silicates have much higher condensation temperatures, thus being the primary component to condensate during the cooling of the gas-phase. These new particles can then act as condensation nuclei upon which the more volatile components can condensate.

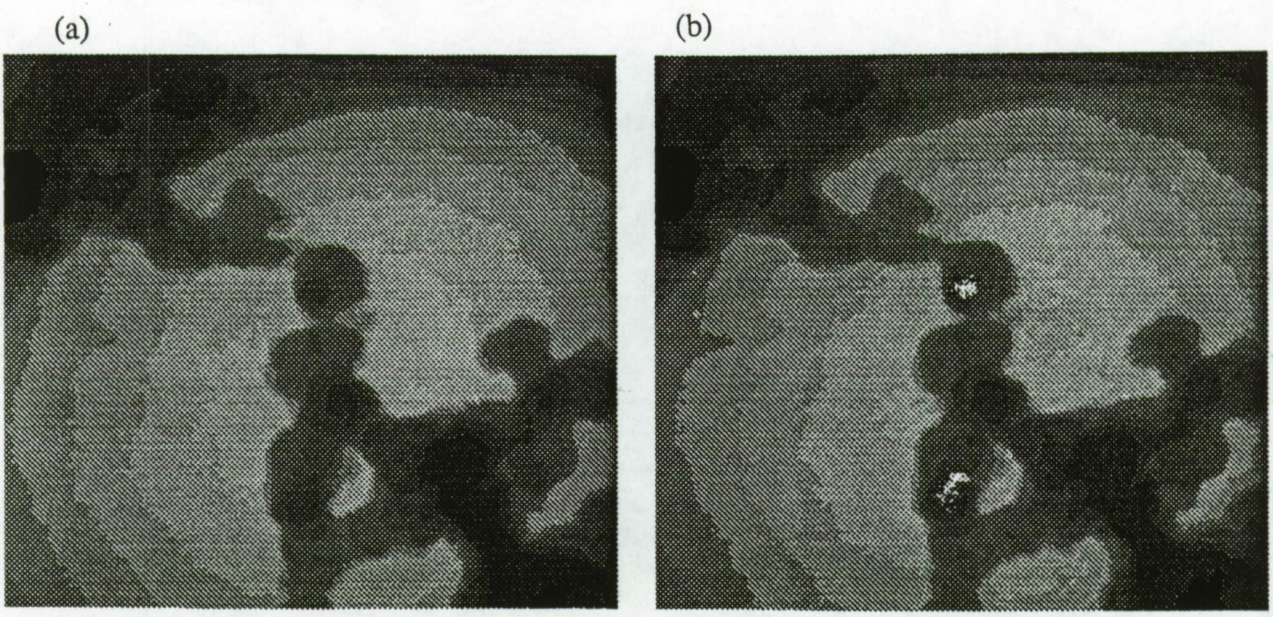

Figure 8.11: Element specific image representing the Si-specific signal (b) as an overlay on the zero-loss filtered image (a). The images were recorded at a magnification of 30,000 times.

8.4.4 Si-S-C-rich particles

Just as for the C-rich particles, secondary reactions between Si-rich components and S-rich species are likely to occur. Indeed, very often sulfur and rarely nitrogen could be detected in association with silicon (Figure 8.12). The signal to noise ratio in spectrum mode for Si (ratio between 3 and 5 are observed) is often too low to result in characteristic pixel intensities in image mode as compared to sulfur, carbon or oxygen. With the ESI technique it was not possible to obtain either sufficient Si- or S-characteristic signals within these S-Si-C-rich particles.

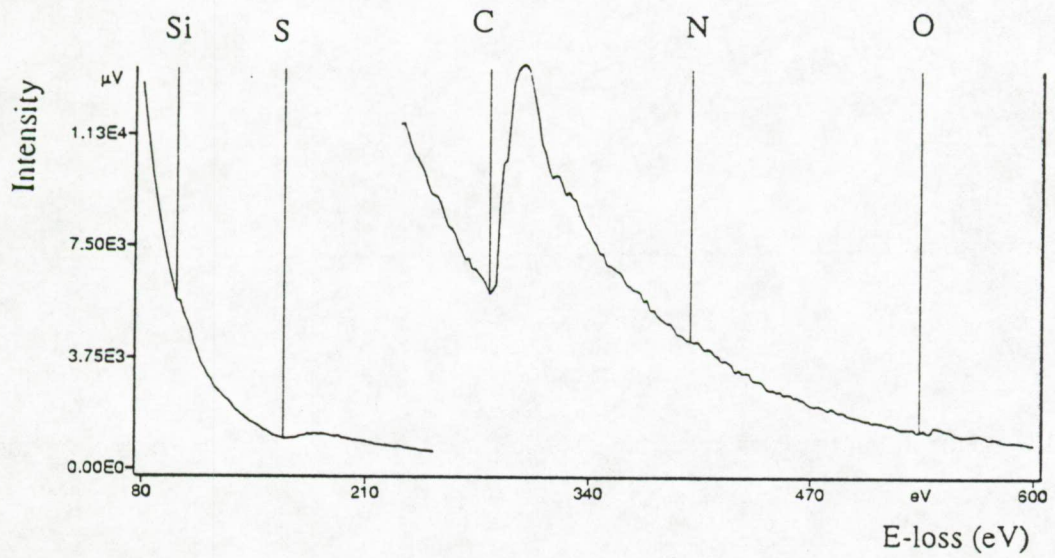

Figure 8.12: Electron energy-loss spectrum of a sub-micrometer particle composed of Si, S, C, N and O.

8.4.5 Minor particle types

8.4.5.1 Copper/zinc-rich particles

Copper-rich particles are the main metal-rich particles observed in the January 1990 sample. Their number contribution is estimated to be less than 3% of the total particulate fraction present in the Phoenix aerosol.

Sometimes zinc can be identified within CuO particles but zinc was never observed in the

absence of copper (Figure 8.13). These Cu- and/or Cu-Zn-rich particles have sizes and morphologies comparable with those of carbonaceous particles. These metal-rich particles can be entrapped within a carbonaceous aggregate structure.

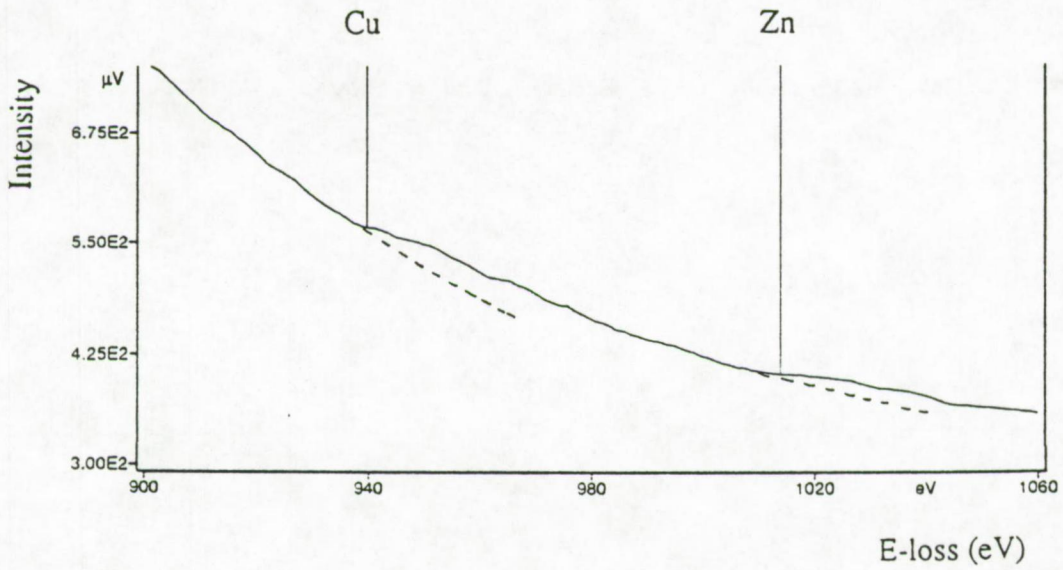

Figure 8.13: Electron energy-loss spectrum of a sub-micrometer Cu-Zn-rich particle detected in the Phoenix aerosol of May 1990.

The quantitative Cu/O ratio determination varies from 0.55 to 0.84 (Table 8.2) and can be explained by an electron-beam induced reduction of CuO to metallic Cu (Long and Petford-Long, 1986). The $L_{2,3}$ near edge fine structure of 3d transition metals are marked by prominent features at the threshold called "white lines". The structure of the L_2 and L_3 edges for Cu are only present for Cu^{2+} (Cu does not exhibit any white line structure as the 3d conduction band is filled) (Figure 8.14a). The EELS spectrum recorded from a Cu-rich particle present in the Phoenix aerosol (Figure 8.14b) resembles an intermediate form of CuO and metallic Cu.

Carbon is always the major detectable element in the Cu-Zn-oxide particles. The growth of carbon filaments encapsulating small metal catalyst particles probably occurs by catalytic decomposition of carbon-containing gases between 327 and 1,027 C (Baker et al., 1975; Bradley and Buseck, 1983). The mechanism of growth in these conditions is illustrated and explained in Figure 8.15.

(a)

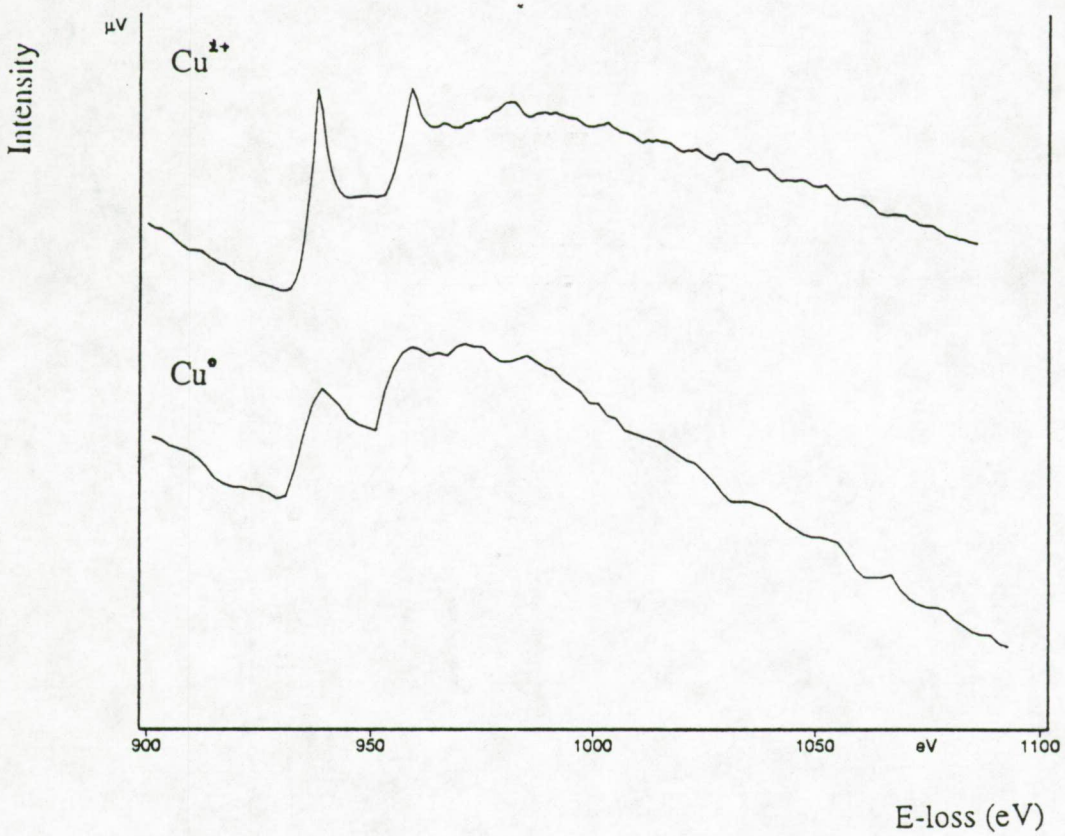

(b)

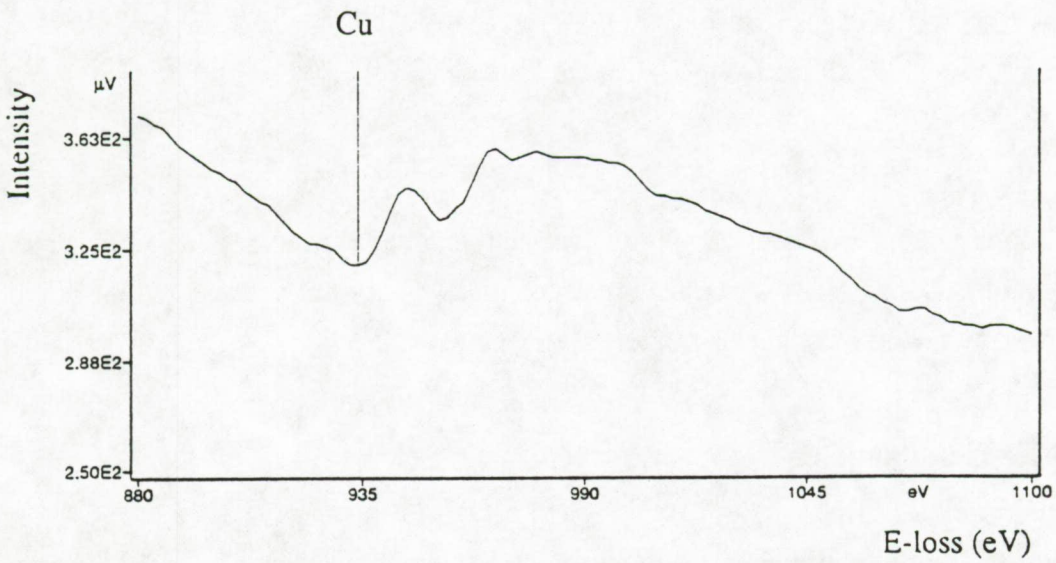

Figure 8.14: (a) Comparison between EELS spectra of a CuO powder standard at initial exposure to the electron beam (Cu^{2+}) and after 5 minutes of exposure (Cu). (b) EELS spectrum of a Cu-rich particle present in the Phoenix aerosol.

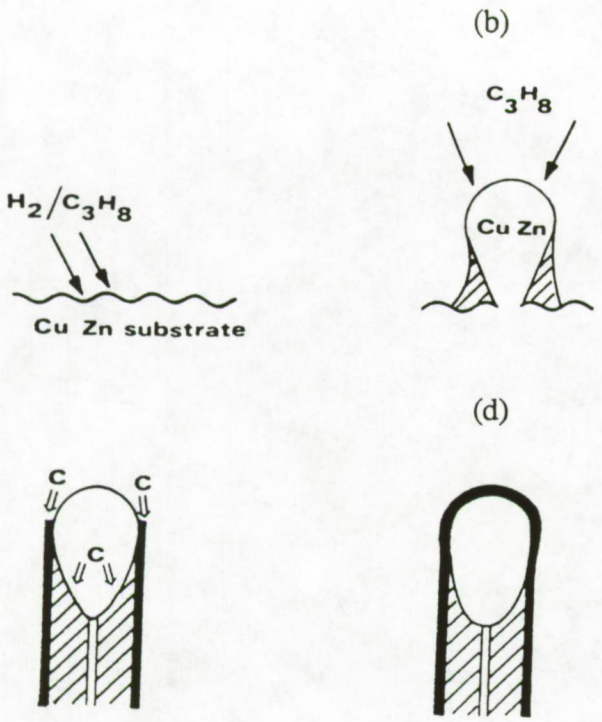

Figure 8.15: Stages in the growth of metal catalyst containing carbon filaments. (a) A carbon-containing gas (usually carbon monoxide or a hydrocarbon) decomposes on the exposed face (b) of a metal catalyst particle. (c) Carbon dissolves in alloy droplet, diffuses through droplet and is precipitated on rear face to form body of growing filament. (d) Growth of filament terminates when catalytically active face is no longer exposed (source: Bradley and Buseck, 1983).

Such complex intergrowths of carbon, copper and zinc correspond much with these reported by Bradley and Buseck (1983) who recovered such metal catalyst containing carbon-filaments from the plume downwind of a copper smelter.

8.4.5.2 Fe-rich particles

A few ironoxide-rich particles were found in the September 1989 and May 1990 samples. Their size was in the order of 0.3 μm and thus much greater than the carbonaceous particles. Only very thin sections of the irregularly shaped Fe-rich particles were selected for analysis. The atomic Fe/O ratio (Table 8.2) corresponds much with a Fe_2O_3 compound. A typical EELS spectrum of such an Fe_2O_3 particle is given in Figure 8.16.

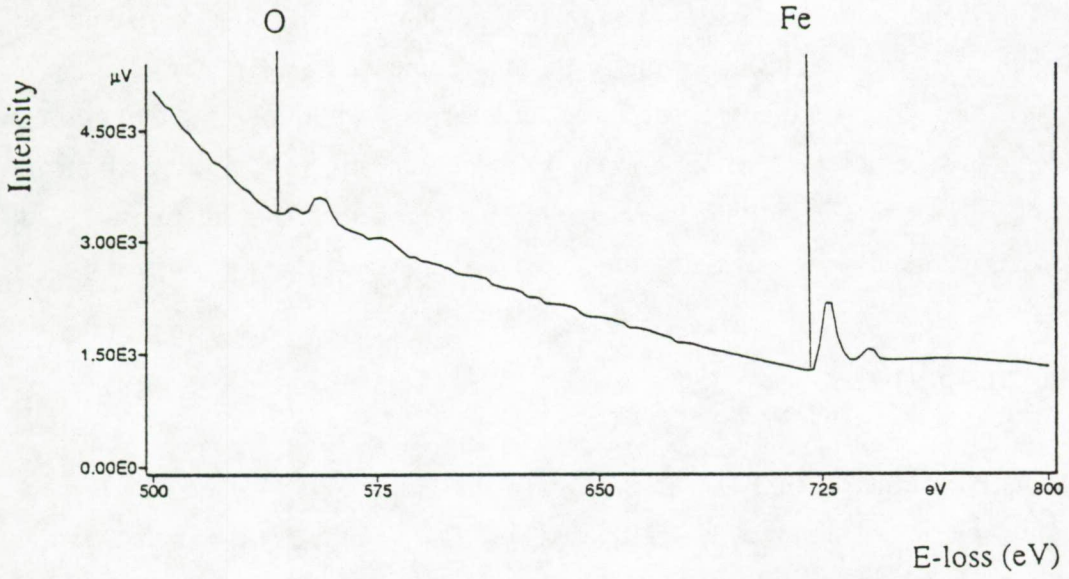

Figure 8.16: Electron energy-loss spectrum of a sub-micrometer thick section from a Fe_2O_3 particle present in the Phoenix aerosol.

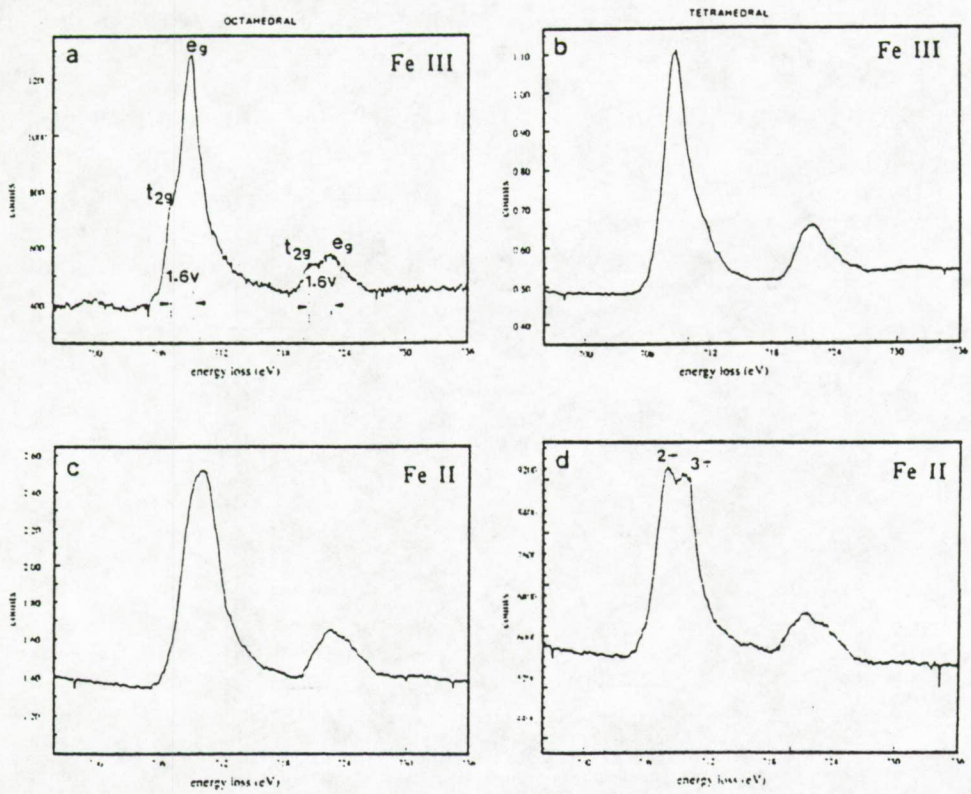

Figure 8.17: L_3 and L_2 edges of iron in four different compounds: (a) franklinite ($[Zn,Mn]Fe_2^{3+}O_4$), (b) hercynite ($Fe^{2+}Al_2O_4$), (c) fayalite (Fe_2SiO_4) and (d) iron analogue of leucite ($KFeSi_2O_6$) (source: Krishnan, 1990)

The L_3 and L_2 "white line" features for iron oxides are due to excitations of the electrons from the $2p_{3/2}$ and $2p_{1/2}$ spin-orbit split levels to the unoccupied 3d levels (Krishnan, 1990). The multiplet structure only becomes apparent at an energy resolution of 1 eV or better and accordingly cannot be observed within our energy resolution. Figure 8.17 shows typical L_3 and L_2 edges for Fe(III) and Fe(II) both in octahedral and tetrahedral coordinations. The detected Fe_2O_3 particles are believed to originate from abrasive and/or metallurgy processes.

8.4.5.3 Fibrous particles

Very unusual and distinctive fibrous particles were found in the May 1990 sample (Figure 8.18). Such fibrous particles are mainly composed of C, sometimes associated with minor concentrations of sulfur. The shape of the carbon K-edge cannot distinguish whether these particles resemble a graphitic or amorphous structure since they are always supported by an amorphous carbon foil (no fibers were found to overpass the holes). Analogous fibrous particles were observed by Bradley and Buseck (1983) near a copper smelter. These authors employed high resolution TEM and EELS to obtain high resolution images of single fibers. The measured fringe spacings of 0.34 nm and the shape of the carbon K-edge indicated that these fibers are composed of graphitic carbon.

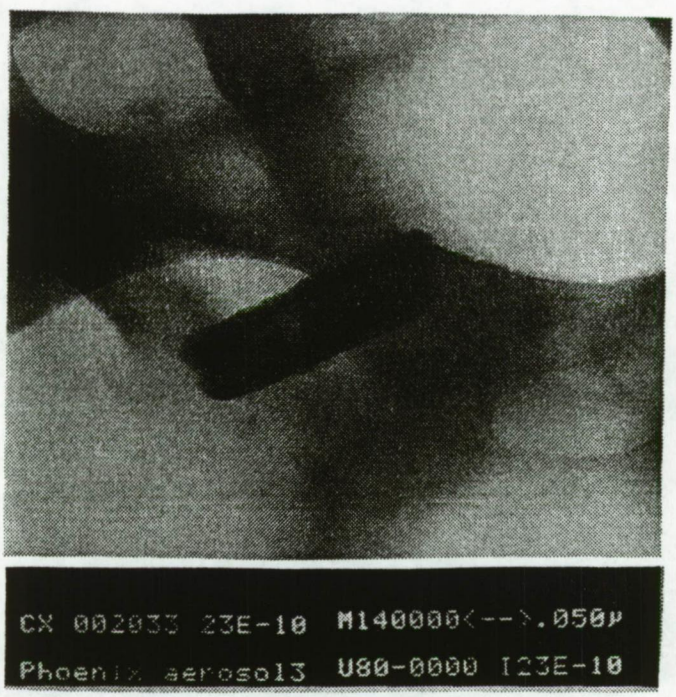

Figure 8.18: Energy-filtered zero-loss image of a fibrous particle present in the Phoenix aerosol of May 1990

8.4.5.4 P-rich particles

A few particles in the samples show the presence of the element phosphorus. These P-rich particles have slightly larger diameters than the carbonaceous particles and are less transparent to the electron beam. Again, both graphitic-like carbon and amorphous carbon were recognized. Sometimes associations with either sulfur (Figure 8.19) or copper (Figure 8.20) were observed.

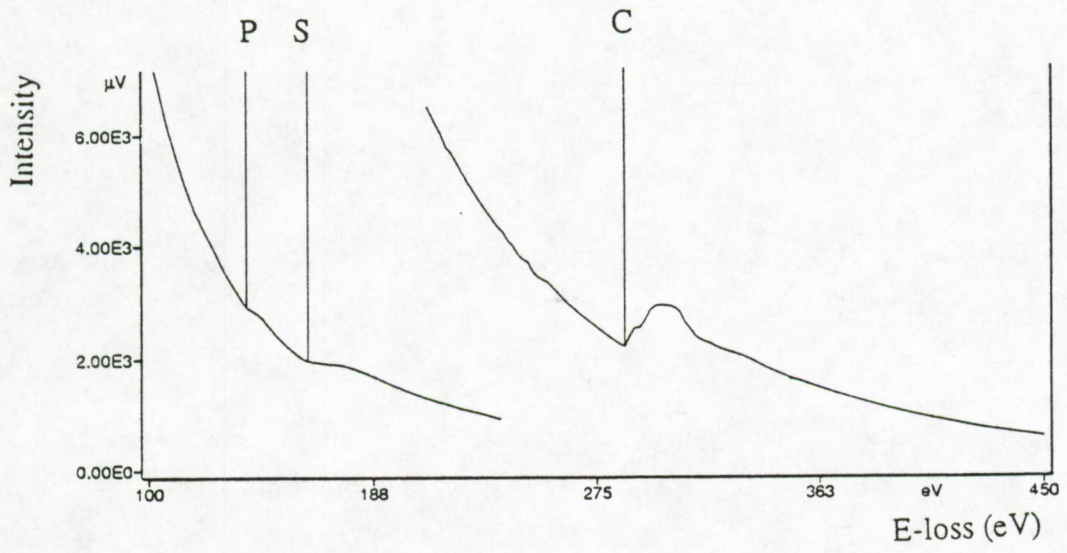

Figure 8.19: EELS spectrum of a sub-micrometer P-S-rich particle present in the Phoenix aerosol of September 1989.

The phosphorus edge is generally a weak broad signal and although detected in spectrum mode, it does not always result in a significant ESI map. Figure 8.21 is the result of a multi-image background correction showing only the significant pixels as an overlay on the zero-loss image (Figure 8.21b). For this, twenty images were collected starting from an energy-loss of 110 eV with energy increments of 2 eV and ending at 148 eV. The first seven images were used to fit and calculate the exponential background by a least square procedure. The reconstructed energy-loss spectrum through one significant pixel coordinate is shown in Figure 8.21a. Also intensity distributions across the X-direction (Figure 8.21c) and Y-direction (Figure 8.21d) are plotted. The cross marks represent all significant pixel net-intensities in contrast to the dots.

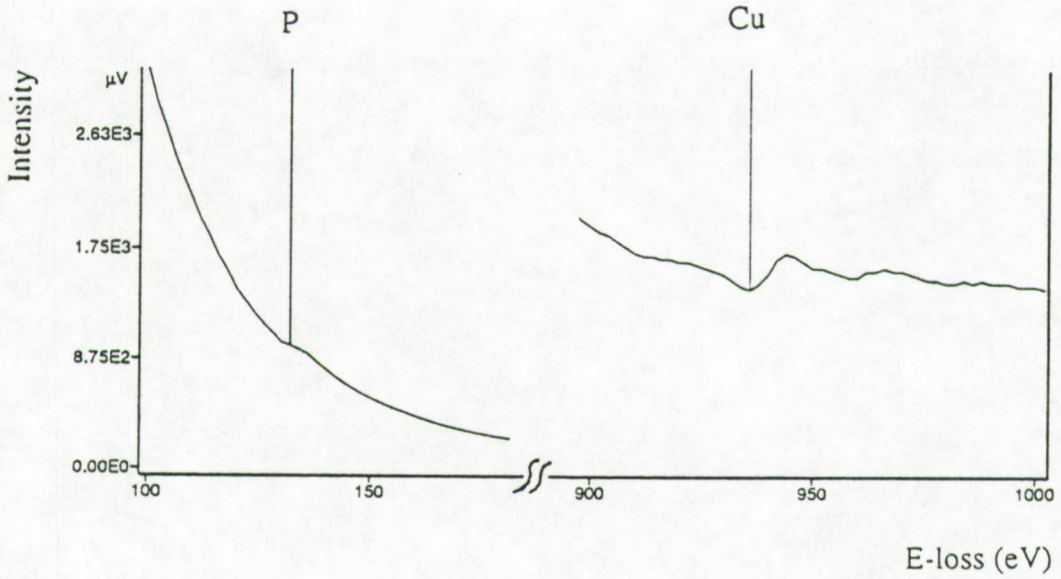

Figure 8.20: EELS spectrum of a sub-micrometer P-Cu-rich particle present in the Phoenix aerosol of September 1989.

A clear apportionment of the phosphorus-rich particles is not possible because of the variety of atmospheric emission sources. Phosphorus may be ejected into the atmosphere on soil particles as a result of erosion by wind, in spores, fungi and pollen as the result from biological activity, on sea salt particles derived from the oceans, and as emissions due to mans industrial and agricultural activities (Graham and Duce, 1979). The detection of Si and P within the same particle is hard to perform, if not impossible to obtain by EELS, especially when both elements comprise the minor atom fractions of the particle. The low, but broad Si-$L_{2,3}$ edge onset followed by its EXELF structure overlaps with the P-$L_{2,3}$ edge at 134 eV. Therefore crustal weathering components containing P cannot be identified and if they are present in the Phoenix aerosol, they will be classified into the Si-C-rich group. Since no sea salt or silicates are identified in the samples, industrial, biological and agricultural activities are all probable sources for particulate phosphorus in the Phoenix aerosol.

(a)

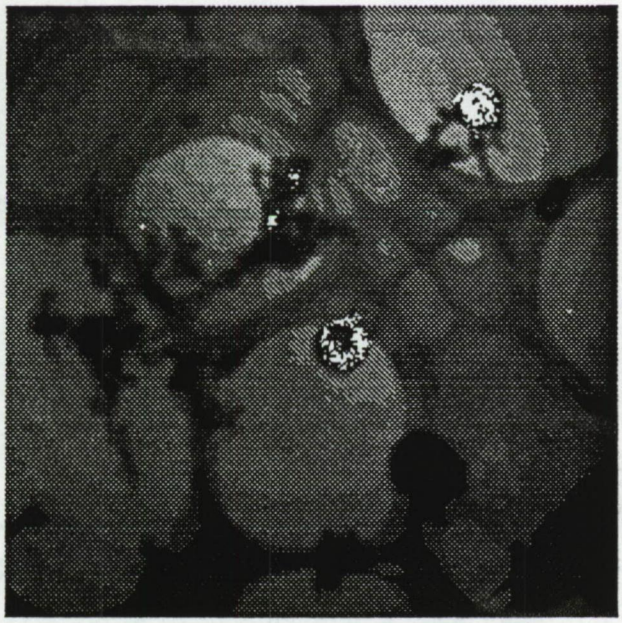

(b)

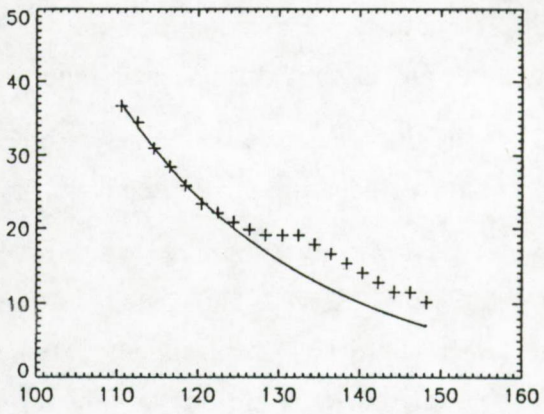

(c)

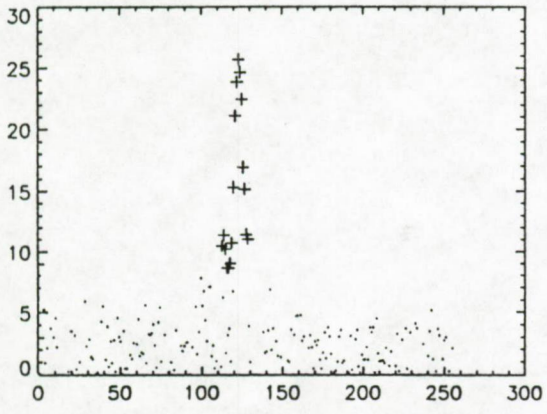

(d)

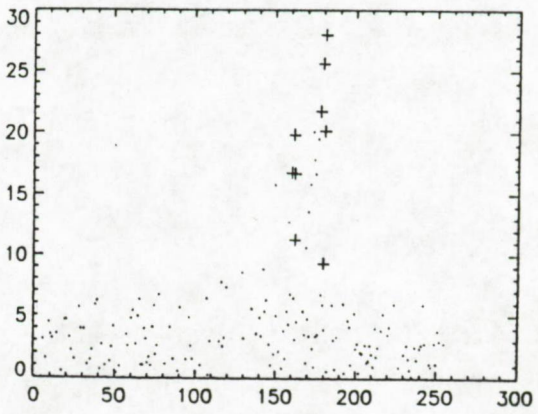

Figure 8.21: (a) Zero-loss image showing only the significant phosphorus distribution as a white binary overlay. (b) Reconstructed energy-loss spectrum through one characteristic pixel coordinate. (c) and (d) are respectively intensity distributions in X- and Y-direction across the pixel coordinate (the cross marks represent the significant signal).

8.5 Conclusion

Using EELS/ESI, the chemical and structural properties were investigated from single particles as small as 10 nm. EELS demonstrated how such analysis can be used to fingerprint some atmospheric pollutants to specific sources.

The compositional information (both qualitative and quantitative) permits the identification of graphite and organic carbon as an important component in the Phoenix aerosol.

The graphitic structures were interpreted as part of the primary soot spherules and the amorphous areas as hydrocarbons condensed during aggregation.

Secondary transformation reactions of carbonaceous particles in the presence of SO_2/NO_2 mixtures are observed. The coated aggregates have carbon structural variations similar to those in uncoated aggregates, suggesting both types of particles to form from similar preemission sources. The sulfate coatings are probably deposited from the ambient atmosphere following aggregate emission. ESI provided visual evidence of S and C coatings respectively present on the surfaces of carbonaceous and quartz particles identified in the Phoenix environment.

Although the copper mining industry in Arizona hass strongly been reduced the past 10 years, typical copper- and carbon-specific particles were observed to indicate minor contributions of such mining sources to the atmospheric aerosol.

Other particle types as Si-C-rich, Fe_2O_3 and P-rich particles were detected. It is not always evident to assign these particle types to unique sources, because many have multiple contributing sources. However, some of them carry detailed information about their organized subsequent evolution.

8.6 References

Andreae M.O., Andreae T.W., Ferek R.J., Raemdonck H.; Long-range transport of soot carbon in the marine atmosphere, *Sci. Tot. Environ.* 36, 73-80, 1984

Andreae M.O., Charlson R.J., Bruynseels F., Storms H., Van Grieken R., Maenhaut W.; Internal mixture of sea salt, silicates, and excess sulfate in marine aerosols, *Science* 232, 1620-1623, 1986

Appel B.R., Hoffer E.M., Kothny E.L., Wall S.M., Haik M.; Analysis of carbonaceous material in southern California atmospheric aerosols, *Envir. Sci. Technol.* 13, 98-104, 1979

Appel B.R., Cheng W., Salaymeh F.; Sampling of carbonaceous particles in the atmophere-II, *Atmos. Environ.* 23, 2167-2175, 1989

Baker R.T.K., Harris P.S., Henderson J., Thomas R.B.; Formation of carbonaceous deposits from reaction of methane over nikkel, *Chem. Phys. Carbon* 13, 17-22, 1975

Bradley J.P., Buseck P.R.; Catalytically grown carbon filaments from a smelter aerosol, *Nature* 306, 770-772, 1983

Britton L.G., Clarke A.G.; Heterogeneous reactions of sulfur dioxide and SO_2/NO_2 mixtures with a carbon soot aerosol, *Atmos. Environ. 14*, 829-839, 1980

Cess R.D.; Arctic aerosols: model estimates of interactive influences upon the surface-atmosphere clear-sky radiation budget, *Atmos. Environ.* 17, 2555-2564, 1983

Chang S.G., Brodzinsky R., Gundel J.A., Novakov T.; in "*Particulate Carbon: Atmospheric Life Cycle*" Eds. Wollf G.T., Klimisch R.L., Plenum Press, New York, 159-181, 1982

Charlson R.J., Waggoner A.P., Thielke J.F.; Visibility protection for class I areas: the theoretical basis, Report No. PB-288842, U.S. Department of Commerce (August), 1978

Clarke A.D., Weiss R.E., Charlson R.J.; Elemental carbon aerosols in the urban, rural and remote-marine troposphere and stratosphere: inferences from light absorption data and consequences regarding radiative transfer, *Sci. Tot. Environ.* 36, 97-102, 1984a

Clarke A.D., Charlson R.J., Radke L.F.; Airborne observations of Arctic Aerosol-IV. Optical properties of Arctic Haze, *Geophys. Res. Lett.* 11, 405-408, 1984b

Comelli G., Stohr J., Robinson C.J., Jark W.; Structural studies of argon-sputtered amorphous carbon films by means of extended X-ray absorption fine structure, *Phys. Rev. B* 38, 7511-7519, 1988

De Santis F., Allegrini I.; Heterogeneous reactions of SO_2 and NO_2 on carbonaceous surfaces, *Atmos. Environ.* 26A, 3061-3064, 1992

Dodd J.A., Ondov J.M., Tuncel G., Dzubay T.G., Stevens R.K.; Multimodal size spectra os submicrometer particles bearing various elements in rural air, *Environ. Sci. Technol.* 25, 890-903, 1991

Egerton R.F., Whelan M.J.; Electron energy-loss spectra of diamond, graphite and amorphous carbon, *J. Electron Spectrosc. Rel. Phenom.* 3, 232-236, 1974

Graham W.F., Duce R.A.; Atmospheric pathways of the phosphorus cycle, *Geochim. Cosmochim. Acta* 43, 1195-1208, 1979

Gray H.A., Cass G.R., Huntzicker J.J, Heyerdahl E.K., Rau J.A.; Elemental and organic carbon particle concentration: a long-term perspective, *Sci. Tot. Environ.* 36, 17-25, 1984

Gray H.A., Cass G.R., Huntzicker J.J, Heyerdahl E.K., Rau J.A.; Characteristics of atmospheric organic and elemental carbon particle concentrations in Los Angeles, *Environ. Sci. Technol.* 20, 580-589, 1986

Grosjean D.; *Ozone and other photochemical oxidants*, National Academy of Sciences, Washington D.C., 1977

Grover P. L.; Polycyclic aromatic hydrocarbons in cancer research, in "*Polynuclear Aromatic Hydrocarbons*" 9th Int. Symp., Eds. Cooke M., Dennis A.J., Columbus, Richland WA, 1-12, 1986

Harrison R.M., Pio C.A.; Kinetics of SO_2 oxidation over carbonaceous particles in the presence of H_2O, NO_2, NH_3 and O_3, *Atmos. Environ.* 17, 1261-1275, 1983

Hildemann L.M., Markowski G.R., Cass G.R.; Chemical composition of emissions from urban sources of fine organic aerosol, *Environ. Sci. Technol.* 25, 744-759, 1991

Hitchcock A.P., Beaulieu S., Steel T., Stohr J., Sette F.; Carbon shell electron energy-loss spectra of 1-butene and 2-butene, trans 1,3 butadiene, and perfluoro-2-butene-carbon carbon bond lengths from continuum shape resonances, *J. Chem. Phys.* 80, 3927-3935, 1984

Iijima S.; High resolution electron microscopy of some carbonaceous materials, *J. Microsc.* 119, 99-111, 1980

Japar S.M., Szkarlat A.C.; Real-time measurements of diesel vehicule exaust particulate using photoacoustic spectroscopy and total light extinction, *Soc. Automotive Eng. Trans.* 90, 3624-3631 (SAE paper No. 81184), 1981

Japar S.M., Brachaczek W.W., Gorse Jr. R.A., Norbeck J.M., Pierson W.R.; The contribution of elemental carbon to the optical properties of rural atmospheric aerosols, *Atmos. Environ.* 20, 1281-1289, 1986

Katrinak K., Rez P., Buseck P.R.; Structural variations in individual carbonaceous particles from an urban aerosol, *Environ. Sci. Technol.* 26, 1967-1976, 1992

Krishnan K.M.; Iron $L_{3,2}$ near edge fine structure studies, *Ultramicroscopy* 32, 309-311, 1990

Long N.J., Petford-Long A.K.; In-situ electron-beam-induced reduction of CuO: A study of phase transformations in cupric oxide, *Ultramicroscopy* 20, 151-160, 1986

Mamane Y., Gottlieb J.; Nitrate formation on sea-salt and mineral particles - a single particle approach, *Atmos. Environ.* 26, 1763-1769, 1992

Mueller P.K., Mosley R.W., Pierce L.B.; Carbonate and non-carbonate carbon content in photochemical aerosols as a function of size, *J. Colloid Interface Sci.* 39, 235, 1972

Pankow J.F.; Review and comparative analysis of the theories of partitioning between the gas and aerosol particulate phases in the atmosphere, *Atmos. Environ.* 21, 2275-2283, 1987

Pierson W.R., Russell P.A.; Aerosol carbon in the Denver area in November 1973, *Atmos. Environ.* 13, 1623-1628, 1979

Rahn K.A., McCaffrey R.J.; On the origin and transport of winter Arctic aerosols, Ann. N.Y. Acad. Sci. 338, 486-503, 1980

Sheridan P.J., Schell R.C., Kahl J.D., Boatman J.F., Garvey D.M.; *Atmos. Environ.*, in press, 1993

Smith D.M., Akhter M.S., Jassim J.A., Sergides C.A., Welch W.F., Chughtai A.R.; Studies of the structure and reactivity of soot, *Aerosol Sci. Technol.* 10, 311-325, 1989

Turpin B.J., Huntzicker J.J.; Secondary formation of organic aerosol in the Los Angeles Basin: a descriptive analysis of organic and elemental carbon concentrations, *Atmos. Environ.* 25, 207-215, 1991

Van Puymbroeck J.; Electron energy-loss spectrometry: Development of methodology and software for the acquisition and processing of spectra, Ph.D. Thesis, University of Antwerp (UIA), 1992

Wagner H.G.; *Particulate Carbon: Formation during Combustion*, Eds. Siegla D.C., Smith G.W.; Plenum Press, New York, 1-29, 1981

Whitby K.T., Husar R.B., Liu B.Y.H.; The aerosol size distribution of Los Angeles smog, *J. Colloid Interface Sci.* 39, 117-204, 1972

Summary and conclusions

Among the many techniques available at the Micro and Trace Analysis Center (MiTAC) for the observation and analysis of individual particles, electron probe X-ray microanalysis (EPXMA) in combination with multivariate classification techniques allows the most advanced characterization of individual particles in a fast and efficient way.

All facilities of EPXMA were used for the source apportionment of more than 25,000 individual aerosol particles detected above the North Sea, the English Channel and the Celtic Sea. The North Sea aerosol is predominantly composed of sea salt, sulfur-rich particles, silicates and calcium sulfate particles. Their abundance is dependent on meteorological conditions and sample location. Differences were studied on the basis of the abundance variations by using principal component analysis. The first component represents the marine-derived aerosol fraction and is more important as wind speed increases or at more remote locations. The second component differentiates anthropogenically derived $CaSO_4$-rich samples. Their relative abundance is more pronounced as the sampled air masses spend longer residence times over the South of England. The samples of the third cluster are related to high silicate and sulfur abundances. Two different clusters separate mixed marine/continental samples from pure continental-derived silicate and sulfur-rich particulate samples. On the average, of all samples taken during various locations and periods, about 60 % have a marine source. The other 40 % of the particles have a continental or mixed marine/continental origin.

Five pairs of North Sea bulk waters and their corresponding surface microlayer samples were investigated for their particulate matter content and chemically analyzed and characterized by EPXMA and laser microprobe mass analysis (LAMMS). Multivariate techniques as hierarchical and non-hierarchical clustering in association with principal component analysis was performed on a data set containing more than 3000 individual particles. The classification procedure yielded eight different particle types. Differences in particle type abundances for the microlayer and bulk water were observed. They were apportioned to their most probable sources. The results were compared with atmospheric and riverine particle data. The domination of the major particle groups (aluminosilicates,

Ca-rich aluminosilicates, $CaCO_3$, silicates and organic particulate matter) suppresses the relative abundance of the metal-rich particles (Fe-rich, Ti-rich and others). A conditioned classification was performed using selection criteria derived from riverine suspensions and atmospheric particulate North Sea data. Similar particle abundances were observed for both the multivariate and the conditional particle classification procedures.

Chemical characterization of very small substances is of increasing interest in many domains of research. The ability of electron energy-loss spectrometry (EELS) to perform qualitative and quantitative information of light elements combined with a high spatial resolution, is one of the innovations of the late seventies. Beside spectrum analysis, an energy filter integrated in a transmission electron microscope offers the possibility of elemental specific imaging (ESI). In this work, an attempt is made to explore the characteristics of EELS for single particle analysis. Optimization of the instrumental parameters is discussed and the advantage of energy filtering is demonstrated for the localization and sizing of particles. ESI gives direct evidence of the localization of specific elements in a matrix and has major advantages over an X-ray mapping. Despite of this, the ESI-technique is not fully exploited and still suffers from shortcomings. To obtain reliable element specific images, the net intensity of the elemental edge must be determined. The net intensity is obtained by subtracting a background image. This background image needs to be determined by extrapolation out of images taken before the characteristic onset. The conventional three-image method is expanded to many pre-edge images in order to reduce the uncertainties of the background parameters. A linear model is proposed to determine the variance of the intensity in every image pixel. It is observed that the standard deviation increases linearly as the intensity in that pixel increases. From this, an accurate estimation of the uncertainty of the net intensity could be evaluated. The multi-ESI method is advantaged over the 3-ESI method as it allows with a higher degree of certainty to gain more characteristic signal, thus improving the quality of the element distribution map. This was demonstrated by directly comparing the two techniques.

The totality of the EELS and ESI methodology, together with its typical problems, were illustrated within different domains of individual particle analysis.

Exhaust aerosols in inductively coupled plasma (ICP) atomic emission spectrometry generated from different ceramic powder suspensions (Al_2O_3, ZrO_2 and SiC) were investigated by EELS and EPXMA. Differences in morphology, size and elemental composition of sub-micrometer residues of these refractory powders, collected above ICPs operated with different gasses, were found to depend on the outer gas (N_2, O_2 and Ar), the distance between the impacting stage and the plasma, and on the ceramic powder introduced as a slurry into a suitable nebulizer. Identical exhaust types of particles were observed in the case of Al_2O_3 and ZrO_2 slurries, also when different outer gases and different operation conditions were used. For SiC, much depends on the outer gas used, as shown by morphological and chemical composition studies. Nitrogen could sometimes be detected on SiC aerosols, but only when the ICP used O_2 as an outer gas. EELS and ESI were used for the elemental analysis of the individual exhaust particles and the localization of the detected elements (Al, Zr, Si, C, O and N).

Polydisperse standard aerosols of NaCl, $(NH_4)_2SO_4$, and KNO_3 were generated from their solutions by a pneumatic nebulizer. These aerosol particles are beam sensitive and therefore special precautions are necessary. A methodology is proposed for serially recording electron energy-loss spectra from sub-micrometer salt particles. The results of quantification are compared with those obtained by parallel electron energy loss spectroscopy (PEELS).

Standard deviations of the element ratios derived by the two EELS instruments were calculated in a different way because of the difference in counting statistics and recording procedure of the energy-loss signals.

Experimental conditions such as the intensity of the primary beam, time of radiation and temperature are responsible for large deviations from the theoretical values. These deviations arise because heavy mass losses occur, especially during the serial spectrum acquisition. The more time consuming serial EELS is therefore at a disadvantage relative to the parallel method. The best results were obtained for NaCl since halogen loss could be reduced more efficiently than nitrogen and oxygen losses. The results show that N-loss occurs within the first few seconds of the experiment at normal radiation doses. Even at cryogenic temperatures, losses of volatile elements cannot be avoided.

Carbonaceous particles in the Phoenix urban atmosphere have widely diverse origins and, as a consequence, a considerable range in structures and morphologies. A significant amount of coagulation between particles of anthropogenic and non-anthropogenic origin were found in ambient air samples.

Examination of EELS spectra indicates that many carbonaceous spherules have structures that range somewhere between essentially amorphous and graphitic. Of these, the apparently amorphous state is far more common among carbonaceous particles. The extent to which these details can be correlated with origin remains to be established. If such correlations become possible with a high degree of confidence, then it may eventually be possible to obtain significant environmental information from the character of individual particles of airborne carbonaceous matter. For all this, comparison is necessary with selected samples from a range of sources as e.g. gas, oil and wood combustion as well as selected industrial processes.

The carbon-rich particles seem to be very sensitive to secondary tansformation reactions. The identification of SO_2/NO_2 coatings on parts of the aggregates, suggest that these coatings are probably deposited from the ambient atmosphere following aggregate emission. Although carbon is the major element detected in more than 95% of the particles, the presence of minor elements as Cu, Zn, Fe, Si and P in the Phoenix aerosol is sometimes indicative for source.

EELS affords the opportunity of exploring sub-micrometer sized materials in far greater detail than was previously possible. The applications described above indicate the type of information that becomes available when performing single particle analysis. Such information cannot be obtained from bulk elemental analysis only. It is therefore advised that such techniques can serve as an aid for helping with specific problems connected to particle studies. EPXMA and EELS should supplement analytical techniques routinely used in chemistry.

Samenvatting en conclusies

Het Micro and Trace Analysis Center (MiTAC) is rijk aan technieken die speciaal ontwikkeld zijn voor de observatie en analyse van individuele deeltjes. Elektronenprobe X-straal microanalyse (EPXMA) in combinatie met multivariate classificatietechnieken laten op een zeer efficiente en snelle manier de karakterisatie van individuele deeltjes toe.

Nagenoeg alle faciliteiten van EPXMA werden benut voor de chemische karakterisatie van meer dan 25000 individuele aerosol deeltjes gedetecteerd boven de Noordzee, het Engels Kanaal en de Ierse Zee. De luchtmassa's boven de Noordzee en omgeving bevatten voornamelijk zeezout, zwavelrijke deeltjes, silikaten en calciumsulfaat deeltjes. Hun abundanties zijn sterk afhankelijk van meteorologische omstandigheden en van de monsterlocatie. Verschillen in samenstelling werden bestudeerd aan de hand van variaties in elementabundanties door gebruik te maken van "principal component analysis". De eerste component vertegenwoordigt de mariene afgeleide aerosolfractie en is meer belangrijk wanneer de windsnelheid toeneemt of wanneer de bemonsteringslocatie meer afgelegen is. De tweede component staat voor de industrieel afgeleide calciumsulfaatrijke monsters. Hun relatieve abundanties zijn meer uitgesproken luchtmassa's afkomstig van boven Zuid Engeland. De monsters toegeëigend aan de derde component komen overeen met hoge abundanties aan silicaten en zwavelrijke deeltjes. Twee verschillende clusters onderscheiden gemengde mariene/continentale monsters van continentaal afgeleide silicaten en zwavelrijke deeltjes. In het algemeen kunnen we stellen dat ongeveer 60% van alle deeltjes een mariene oorsprong hebben. De resterende 40% hebben een continentaal of een gemengde mariene/continentale oorsprong.

Vijf paren van bulk- en microlaag-watermonsters afkomstig van de Noordzee, werden onderzocht naar deeltjessamenstelling en chemisch geanalyseerd door EPXMA en laser microprobe massaanalyse (LAMMS). Multivariate technieken zoals hiërarchische en niet-hiërarchische clusteringen in combinatie met principal componenten analyse werden uitgevoerd op een dataset van meer dan 3000 deeltjes. De klassificatie leverde acht verschillende deeltjestypes op. De chemische samenstelling van de deeltjesgroepen werd vergeleken met atmosferische- en rivier-gegevens. De dominantie van de belangrijkste

deeltjesgroepen (aluminosilikaten, Ca-rijke aluminosilicaten, $CaCO_3$, silikaten en organische deeltjes) onderdrukten de relatieve abundantie van de metaal-rijke deeltjes (Fe-rijke deeltjes, Ti-rijke deeltjes en anderen). Een conditionele classificatie werd uitgevoerd, gebruik makend van selectiecriteria afgeleid van gegevens van riviersuspenties en atmosferische deeltjes boven de Noordzee. Gelijkaardige deeltjesabundanties werden geobserveerd voor zowel de multivariate als de conditionele deeltjesclassificatie.

In vele onderzoeksdomeinen vertoont men een stijgende interesse voor de chemische karakterisatie van zeer kleine deeltjes. De mogelijkheid van elektronen-energieverliesspektrometrie (EELS) om kwalitatieve en kwantitatieve informatie te bekomen over lage-Z elementen en dit bij hoge spatiale resolutie, is één van de innovaties van de zeventiger jaren. Een energiefilter ingebouwd in de kolom van een transmissiemikroskoop laat toe om naast spectrumanalyse ook elementspecifieke beelden (ESI) te genereren. In dit werk is de mogelijkheid onderzocht om de karakteristieken van EELS en ESI aan te wenden voor individuele deeltjesanalyse. De optimalisatie van intrumentele parameters werd onder de loep genomen en de voordelen van energiefiltering werden gedemonstreerd aan de hand van localisatie en groottebepaling van deeltjes. ESI geeft informatie over de localisatie van specifieke elementen in een matrix en heeft grote voordelen vergeleken met X-straal mappingen. Desondanks is de ESI-techniek nog niet volledig geëxploiteerd en leidt het nog aan enkele tekortkomingen. Om betrouwbare elementspecifieke beelden te bekomen moet men de netto-intensiteit onder een ionisatierand bepalen. Dit wordt bereikt door van het totale energiespecifiek signaal een achtergrond af te trekken. Om het achtergrondsignaal te berekenen moet men allereerst een lineaire regressie doorvoeren op een serie van beelden genomen voor de karakteristieke ionisatierand om vervolgens te extrapoleren tot onder de ionisatierand. De onzekerheid op de regressieparameters bepaalt de onzekerheid op de achtergrond. De conventionele drie-beeldmethode werd uitgebreid tot meerdere beelden voor de piek om alzo onzekerheden op de achtergrondparameters te reduceren. Een lineair model werd voorgesteld om de variantie op de intensiteit voor elke pixel te bepalen. De standaarddeviatie stijgt lineair met de pixelintensiteit. Uitgaande van dit kan een akkurate schatting van de onzekerheid op de netto-intensiteit bekomen worden. Bij vergelijking van de twee methodes kan men stellen dat de multi-beeldmethode sterk bevoordeligd is boven

de conventionele drie-beeldmethode. De onzekerheid op het netto-signaal is verlaagd voor een verbeterd element specifiek beeld.

De gehele EELS en ESI methodologie, tesamen met hun specifieke problemen, werden geïllustreed binnen verschillende domeinen van individuele deeltjeskarakterisatie.

Verbrandingsaerosolen gegenereerd door het vertuiven van verschillende keramische suspensies (Al_2O_3, ZrO_2 ans SiC) in een een induktief gekoppeld plasma (ICP), werden onderzocht met EPXMA en EELS/ESI. Verschillen in morfologie, grootte en elementaire samenstelling van het verbrande residu zijn afhankelijk van o.a. het gebruikte ICP buitengas (N_2, O_2 en Ar), de afstand tussen het impactiemedium en het plasma en de aard van het keramisch materiaal. Nagenoeg identieke deeltjestypes werden geobserveerd voor Al_2O_3 en ZrO_2 suspensies, ook wanneer verschillende buitengassen werden aangewend. Voor SiC is dit enigszins anders. Reakties met zuurstof treden op onder alle condities. Soms werd stikstof gedetecteerd maar dit enkel bij aanwenden van een O_2-buitengas. Uit de experimenten kunnen we tevens besluiten dat er geen volledige omzetting van de keramische fractie naar de gasfase optreed. Verder werden EELS en ESI met succes aangewend voor de analyse en localisatie van Al, Zr, Si, C, O en N in individuele deeltjes.

Standaard aerosolen van NaCl, $(NH_4)_2SO_4$, en KNO_3 werden gegenereerd door pneumatische verstuiving van een oplossing. Deze aerosoldeeltjes blijken stralingsgevoelig te zijn en daardoor moeten speciale maatregelen getroffen worden vooraleer men deze kan analyseren. De kwantitatieve resultaten van seriële EELS werden vergeleken met deze van parallelle EELS.

Experimentele conditites zoals de elektronendosis op het monster, de duur van bestraling en de temperatuur zijn verantwoordelijk voor grote afwijkingen in elementaire samenstelling tussen berekende en theoretische waarden. Deze afwijkingen zijn het gevolg van massaverliezen, vooral wanneer spectra serieel opgenomen worden. De beste resultaten werden bekomen voor NaCl omdat het effect van massaverlies voor chloor veel kleiner is dan voor stikstof of zuurstof. Zelfs bij cryogene temperaturen kan het verlies van sommige elementen in vluchtige verbindingen niet tegengewerkt worden.

Koolstof-rijke deeltjes aanwezig in de atmosfeer van de stad Phoenix (USA) hebben een gevarieerde oorsprong en verschillen onderling sterk in struktuur en morfologie. Onderzoek van EELS spectra toont aan dat deze deeltjes struktureel variëren tussen een amorfe an grafiet-achtige struktuur. The amorfe fase is echter wel het sterkst vertegenwoordigd. Er is echter geen eenduidig verband gevonden tussen de struktuur van een deeltje en zijn oorsprong. Daarvoor dienen vergelijkende analyses uitgevoerd te worden op monsters die bronspecifiek zijn.

De deeltjes aanwezig in de stadsatmosfeer zijn zeer gevoelig aan secundaire transformatiereakties. De identifikatie van SO_2/NO_2 coatings op sommige deeltjes doet vermoeden dat de vorming van deze coatings onstaat uit de omgevingslucht nadat deeltjesaggregatie is opgetreden. Ondanks dat koolstof het hoofdelement is in meer dan 95% van de gedetecteerde deeltjes, worden ook kleinere bijdragen aan Cu, Zn, Fe, Si en P waargenomen die soms ook bronspeciek zijn.

EELS/ESI laat toe om zeer kleine deeltjes meer in detail te karakteriseren dan voordien mogelijk was. De toepassingen hoger vermeld, tonen het type van informatie aan dat bekomen kan worden. Zulke informatie kan moeilijk of niet door bulkanalysemethoden ingewonnen worden. Soms laat de techniek toe om specifieke problemen op te lossen. Soms is het aangeraden om zowel EELS/ESI als EPXMA in combinatie met andere technieken te gebruiken. Vanwege de hoge elektronendosissen nodig om EELS met succes uit te voeren, dienen voorzorgen genomen te worden teneinde monsterbeschadinging tegen te gaan.

List of publications

Articles

Application of electron energy-loss spectroscopy to aerosols.

C. Xhoffer, W. Jacob and R. Van Grieken

J. Aerosol Science, 20, 1617-1619, 1989, Special Issue: European Aerosol Conference 1989, Vienna-Austria, September 18-23, 1989

Micro-analysis of individual environmental particles

R. Van Grieken, P. Artaxo, P. Bernard, L. Leysen, Ph. Otten, H. Storms, A. Van Put, L. Wouters and C. Xhoffer

Chemia Analityczna, 35, 75-89, 1990

A method for the characterization of surface modified asbestos fibres by electron energy-loss spectroscopy and electron spectroscopic imaging

C. Xhoffer, P. Berghmans, I. Muir, W. Jacob, R. Van Grieken and F. Adams

J. Microscopy, 162, 179-184, 1991

Chemical characterization and source apportionment of individual aerosol particles over the North Sea and the English Channel using multivariate techniques

C. Xhoffer, P. Bernard, R. Van Grieken and L. Van der Auwera

Environ. Sci. Technol., 25, 1470-1478, 1991

Micro-analysis techniques for the characterization of individual environmental particles

R. Van Grieken, C. Xhoffer, L. Wouters and P. Artaxo

Analytical Sciences, 7, 1117-1122, 1991

Electron energy-loss spectroscopy and electron probe X-ray microanalysis of exhaust aerosols in slurry nebulization inductively coupled plasma atomic spectrometry for ceramic powders

C. Xhoffer, C. Lathen, W. Van Borm, J. Broekaert, W. Jacob and R. Van Grieken

Spectrochimica Acta, 47B, 155-172, 1992

Characterization of individual particles into the North Sea surface microlayer and underlying seawater: Comparison with atmospheric particles

C. Xhoffer, L. Wouters and R. Van Grieken

Environ. Sci. Technol., 26, 2151-2162, 1992

Micro-analysis techniques for the characterization of individual environmental particles

R. Van Grieken, C. Xhoffer, L. Wouters and P. Artaxo

in "Environmental Particles" Volume I, Environmental Analytical and Physical Chemistry Series, Eds. J. Buffle and H. Van Leewen, Lewis Publishers, Boca Raton, FL., 107-143, 1992

X-ray microprobe studies of Hungarian background and urban aerosols

Sz. Török, Sz. Sándor, C. Xhoffer, R. Van Grieken, K.W. Jones, S.R. Sutton and R.L. Rivers

in "Advances of X-Ray Analysis, 35", Eds. C.S. Barrett et al., Plenum Press, New York, 1183-1188, 1992

Micro-analysis of individual environmental particles

R. Van Grieken and C. Xhoffer

J. Anal. Atom. Spectr., 7, 81-88, 1992

Sources and composition of aerosol from Khartoum, Sudan

M.A.H. Eltayeb, C. Xhoffer, P. Van Espen, R. Van Grieken and W. Maenhaut

Atm. Environ., in press

Environmental aerosol characterization by single particle analysis techniques

C. Xhoffer and R. Van Grieken

in "Environmental Particles" Volume II, Environmental Analytical and Physical Chemistry Series, Ed. J. Buffle, Lewis Publishers, Boca Raton, FL., in press

Analysis of individual salt aerosol particles using electron energy-loss spectroscopy

C. Xhoffer, R. Van Grieken, W. Jacob and P.R. Buseck

submitted to Microbean Analysis

Single particle analysis of Hungarian background aerosol

Sz. Török, Sz. Sándor, C. Xhoffer, R. Van Grieken, E. Mészáros and A. Molnár

Idöjárás, in press

Proceedings

Characterization of individual environmental particles.

R. Van Grieken, P. Artaxo, P. Bernard, F. Bruynseels, Ph. Otten, H. Storms and C. Xhoffer

"Chemistry for the Protection of the Environment 1987", L. Pawlowski, E. Mentasti, W.J. Lacy and C. Sarzanini, Eds., Elsevier, Amsterdam-Oxford-New York-Tokyo, 307-316, 1988

Chemical composition, source identification and quantification of the atmospheric input into the North Sea.

Ph. Otten, H. Storms, C. Xhoffer and R. Van Grieken

Progress in Belgian Oceanographic Research - 1989, G. Pichot, Ed., Prime Minister's Services of Sience Policy Office & Ministry of Public Health and Environment, Brussels, 1989

Atmospheric deposition of heavy metals over the North Sea.

R. Van Grieken, Ph. Otten and Ch. Xhoffer

"Environmental Quality and Ecosystem Stability", ISEEQS Publications, Jeruzalem, Vol. IV, 87-88, 1989

Single particle analysis of particulate environmental samples.

R. Van Grieken, P. Bernard, Ph. Otten, C. Rojas, A. Van Put, Ch. Xhoffer and L. Wouters

Proceedings of the 3th Beijing Conference and Exhibition on Instrumental Analysis, BCEIA, Beijing, A83-A84, 1989

Karakterisering van individuele deeltjes in de Noordzee.

C. Xhoffer, Ph. Otten and R. Van Grieken

IZWO jaarvergadering, Brugge, 23 juni 1989

Individual coal flyash particles by EPMA

Sz. Sándor, Sz. Török, C. Xhoffer and R. Van Grieken

Proceedings of the XIIth International Congress for Electron Microscopy, L.D. Peachy and D.B. Williams, Eds., San Francisco Press, San Francisco, 254-255, 1990

Electron energy-loss spectroscopy and its application to individual particle analysis

C. Xhoffer, W. Jacob, R. Van Grieken, J.A.C. Broekaert and P.R. Buseck

"Electron Microscopy 92", Proceedings of the 10th European Congress on Electron Microscopy, Vol. I, A. Rios, J.M. Arias, L. Megias-Megias and A. Lopez-Galindo, Eds., Secretariado de Publicaciones de la Universidad de Granada, Granada, Spain, 283-284, 1992

Automated EPXMA of individual environmental particles

R. Van Grieken, P. Artaxo and C. Xhoffer

Proceedings of the 50th Annual Meeting of the Electron Microscopy Society of Amerika / 27th Annual Meeting of the Microbeam Analysis Society / 19th Annual Meeting of the Microscopical Society of Canada, G.W. Bailey, J. Bentley and J.A. Small, Eds., San Francisco Press, San Francisco, CA, 1482-1483, 1992

Source apportionment of individual aerosol particles: possible contribution to subproject Genemis

Sz. Török, Sz. Sándor, C. Xhoffer and R. Van Grieken

Proceedings of the 1992 EUROTRAC Symposium, in press

Environmental North Sea aerosol characterization by single particle techniques

H. Van Malderen, L. De Bock, J. Injuk, C. Xhoffer and R. Van Grieken

Submitted to "Progress in Belgian Oceanographic Research", Proceedings of the North Sea symposium, Ed. J.C.J. Nihoul

Abstracts

Micro-analysis of individual environmental particles.

R. Van Grieken, P. Bernard, L. Leysen, Ph. Otten, S. Scholdis, H. Storms, A. Van Put, L. Wouters and C. Xhoffer

10th Conference on Analytical Atomic Spectroscopy, Torun, Poland, September 5-6, 1988

Application of EELS on aerosols.

C. Xhoffer, W. Jacob and R. Van Grieken

EMAS: European Microbeam Analysis Society: 1st European Workshop on Modern Developments and Application in Microbeam Analysis, Antwerpen, 8-10 March 1989

X-ray emission spectroscopy: Recent trends and environmental applications

R. Van Grieken, C. Rojas, V. Van Alsenoy and C. Xhoffer

VII th Spectroscopy Symposium, Samsun, Turkey, 6-9 September, 1989

Application of electron spectroscopic imaging (ESI) for the surface characterization of sub-micron particles and fibers

C. Xhoffer, W. Jacob and R. Van Grieken

Second European Workshop on Spectroscopic Imaging and Analytical Techniques, Dortmund, Germany, 17-18 May, 1990

Interpretation of individual particle EPXMA data by principal component analysis

C. Xhoffer, P. Bernard, L. Brugmann and R. Van Grieken

European Workshop on Energy Dispersive X-ray Fluorescence (EDXRF), Antwerp, Belgium, 20-22 June, 1990

Single particle analysis of environmental samples

R. Van Grieken, P. Artaxo, F. Belmans, C. Rojas, H. Struyf, H., Van Malderen, A. Van Put, C. Xhoffer and L. Wouters

First Buenos Aires Workshop on Analytical Chemistry, Buenos Aires-Argentina, 12-16 November, 1990

Study of exhaust aerosols in slurry nebulization inductively coupled plasma atomic spectrometry for ceramic powders

C. Xhoffer, W. Van Borm, R. Van Grieken, W. Jacob and J. Broekaert

1991 European Winter Conference on Plasma Spectrochemistry, Dortmund-Germany, 14-18 January, 1991

Micro analytical characterization of various ceramic powders using electronprobe X-ray micro analysis and electron energy-loss spectroscopy

C. Xhoffer, W. Dorriné, R. Van Grieken, F. Adams and H. Jenett

EMAS: European Microbeam Analysis Society: 2nd European Workshop on Modern Developments and Application in Microbeam Analysis, Dubrovnik-Yugoslavia, 13-17 May, 1991

Micro-analysis of individual environmental particles

R. Van Grieken, C. Rojas, A. Van Put, C. Xhoffer and L. Wouters

XXVII Colloquium Spectroscopicum Internationale, Bergen, Norway, 9-14 June, 1991

Possibilities of cryo-EELS on individual salt particles: Comparison of the ZEISS EM 902 with the JEOL 2000 FX

C. Xhoffer, W. Jacob, R. Van Grieken and R. Buseck

Third European Workshop on Spectroscopic Imaging and Analysis Techniques, Martinsried, Germany, 27-28 June, 1991

Quantitative characterization of ceramic materials

J. Van Puymbrouck, C. Xhoffer, R. Riedel, W. Jacob and P. Van Espen

Third European Workshop on Spectroscopic Imaging and Analysis Techniques, Martinsried, Germany, 27-28 June, 1991

Micro-analysis techniques for the characterization of individual environmental particles

R. Van Grieken, C. Rojas, H. Van Malderen and C. Xhoffer

IUPAC, ICAS'91 International Congress on Analytical Sciences 1991, Chiba, Japan, 25-31 August, 1991

Micro-analysis of individual environmental particles

R. Van Grieken, H. Van Malderen and C. Xhoffer

3rd International Environmental Chemistry Congress in Brazil, Salvador, Bahia, Brazil, 30 September - 4 October, 1991